A proposal for an experiment to measure $\nu_\mu \to \nu_e$ oscillations and ν_μ disappearance at the Fermilab Booster: BooNE

December 7, 1997

E. Church, I. Stancu, G. J. VanDalen
University of California, Riverside, CA 92521

R. A. Johnson, V. Wu
University of Cincinnati, Cincinnati, OH 45221

J. M. Conrad,* J. Formaggio, T. Ochs, M. H. Shaevitz, E. G. Stern, B. Tamminga
Columbia University, Nevis Labs, Irvington, NY 10533

D. Smith
Embry Riddle Aeronautical University, Prescott, AZ 86301

C. Bhat, L. Bugel, R. Ford, I. Kourbanis, A. Malensek, W. Marsh, P. Martin, A. Russell, R. Stefanski
Fermi National Accelerator Laboratory, Batavia, IL 60510

G. T. Garvey, W. C. Louis,* G. B. Mills, V. Sandberg, B. Sapp, R. Tayloe, D. H. White
Los Alamos National Laboratory, Los Alamos, NM 87545

R. Imlay, H. J. Kim, A. Malik, W. Metcalf, M. Sung, N. Wadia
Louisiana State University, Baton Rouge, LA 70803

Z. D. Greenwood
Louisiana Tech University, Ruston, LA 71272

* *Co-spokespersons: J. M. Conrad and W. C. Louis*

Contents

Chapter 1

Executive Summary

The MiniBooNE experiment will be capable of observing both $\nu_\mu \to \nu_e$ appearance and ν_μ disappearance. In addition, if neutrino oscillations are observed, the experiment will be able to measure Δm^2 and $\sin^2 2\theta$ and search for CP violation in the lepton sector. By using the phototubes and electronics from the LSND experiment, the detector cost is estimated to be \$2.21M (\$3.07M with contingency and escalation). The neutrino beam line cost is estimated to be \$3.92M (\$6.25M with contingency and escalation).

This proposal describes a search for neutrino oscillations motivated by the LSND observation, which has been interpreted as $\bar{\nu}_\mu \to \bar{\nu}_e$, and by the atmospheric neutrino deficit which may be ascribed to ν_μ oscillations. The BooNE (Booster Neutrino Experiment) program will have two phases. The first phase, MiniBooNE, is a single detector experiment designed to:

- Obtain $\sim$ 1000 events per year if the LSND signal is due to $\nu_\mu \to \nu_e$ oscillations. This establishes the oscillation signal at the $\sim 8\sigma$ level.
- Extend the search for $\nu_\mu \to \nu_e$ oscillations significantly beyond what has been studied previously if no signal is observed.
- Search for ν_μ disappearance to address the atmospheric neutrino deficit. The signal is a suppression of the reconstructed 500,000 $\nu_\mu C \to \mu N$ events per year.
- Test CP-violation in the lepton sector if oscillations are observed by running with separate ν_μ and $\bar{\nu}_\mu$ beams.

The second phase of the experiment introduces a second detector, with the goal to:

- Accurately measure the Δm^2 and $\sin^2 2\theta$ parameters of observed oscillations.
- Compare the oscillation parameters in $\nu_\mu \to \nu_e$ and $\bar{\nu}_\mu \to \bar{\nu}_e$ to test for CP violation in the lepton sector.

This proposal focuses on the MiniBooNE experiment (phase 1). This experiment would begin taking data in 2001. By using phototubes and electronics from the LSND experiment, the MiniBooNE Detector is relatively inexpensive and can be constructed on a short time scale. The detector would consist of a spherical tank 6 m in radius. An inner structure at 5.5 m radius would support 1220 8-inch phototubes (10% coverage) pointed inward and optically isolated from the outer region of the tank. The vessel will be filled with 769 t of mineral oil, resulting in a 445 t fiducial volume. The outer volume will serve as a veto shield for identifying particles both entering and leaving the detector, with 292 phototubes mounted on the support structure facing outwards. The cost for the detector is estimated to be \$2.21M (or \$3.07M with contingency and escalation). The detector would be located 500 m from a Booster neutrino source.

The neutrino beam, constructed using the 8 GeV proton Booster at FNAL, would service both phases of the experiment. The neutrino beam line would consist of a target within a focusing system, followed by a $\sim$50 m long pion decay volume. The low energy, high intensity and 1 μs time-structure of a neutrino beam produced from the Booster beam are ideal for this experiment. The Booster is a highly reliable machine, with a downtime of $\sim 1.5\%$, thus we assume that the Booster can reliably deliver protons for a typical run which is two-thirds of a calender year. The sensitivities discussed in this proposal assume the experiment receives 5 Hz for 2×10^7s running at 5×10^{12} protons per pulse. The cost of this beam line is projected to be \$3.92M for materials, construction and installation (\$6.25M when EDIA, contingency and escalation also are included).

This Booster experiment is compatible with the Fermilab collider and MI programs. The Booster must run at 7.5 Hz to accommodate the MiniBooNE, NUMI and collider programs simultaneously. The FNAL Booster is capable of running at 15 Hz.

The MiniBooNE experiment represents an opportunity to resolve several interesting neutrino oscillation questions on a short-time scale. In particular, within the upcoming five years, no existing or approved experiments will be able to address conclusively the LSND signal region. Thus MiniBooNE represents an important and unique addition to the Fermilab program.

Chapter 2

Overview of the MiniBooNE Experiment

The MiniBooNE experiment is motivated by the evidence for neutrino oscillations from the LSND and atmospheric neutrino experiments. The detector will be similar to that in the LSND experiment and will be located 500m from a neutrino beam line fed by the 8 GeV proton Booster.

This chapter provides a brief introduction to the physics motivation and expectations for the MiniBooNE Experiment, the competition for searching for $\nu_\mu \to \nu_e$ oscillations, the design issues of the experiment, and the place of this experiment within the existing and future Fermilab programs. Each of these topics is further elaborated in later chapters of this proposal:

Chapter 3 considers the physics of neutrino oscillations.

Chapter 4 describes the BooNE beam line, including expected ν_μ fluxes and ν_e backgrounds and systematics.

Chapter 5 covers the detector design, detector simulation and event analysis technique, including backgrounds and systematic errors expected due to particle misidentification.

Chapter 6 provides both qualitative and quantitative discussion of the event reconstruction in the detector.

Chapters 7 and 8 describe the MiniBooNE $\nu_\mu \to \nu_e$ and ν_μ disappearance searches in detail.

Chapter 9 provides a brief overview of the non-oscillation physics topics which can be studied with MiniBooNE.

Chapter 10 considers the path to future upgrades for this experiment.

Chapter 11 provides an overview of the cost and schedule for the MiniBooNE experiment. Further details are supplied in appendix C.

2.1 Motivation

The MiniBooNE experiment is motivated by two important pieces of evidence for neutrino oscillations. The first is the observation of events by the LSND collaboration that are consistent with $\bar{\nu}_\mu \rightarrow \bar{\nu}_e$ oscillations. The second is the observed deficit of atmospheric neutrinos which may be attributed to ν_μ disappearance through oscillations.

In 1995 and 1996, the LSND experiment at Los Alamos reported evidence [1] for $\bar{\nu}_\mu \rightarrow \bar{\nu}_e$ oscillations at the level of $\sim 0.3\%$. The allowed values of Δm^2 and $\sin^2 2\theta$ corresponding to this evidence are indicated in Fig. 2.1 by the grey region. Previous oscillation searches have not seen oscillations in the region allowed by LSND with $\Delta m^2 > 4$ eV^2, as shown in Fig. 2.1. This isolates the most favored region at low Δm^2.

Since the original LSND publication, the KARMEN experiment at the ISIS facility and the LSND experiment have obtained further results that strengthen the case for a $\bar{\nu}_\mu \rightarrow \bar{\nu}_e$ oscillation signal. KARMEN observes an excess of events in their data taken through 1996 consistent with the LSND $\overline{\nu}_\mu \rightarrow \overline{\nu}_e$ oscillation signal, but only at the 1σ level due to low luminosity and high rates of cosmic-ray background.[2] Therefore, KARMEN prefers to quote a limit, as appears on Fig. 2.1. LSND has released preliminary results from the 1996-1997 run consistent with the previous LSND results.[3] LSND also is able to search for $\nu_\mu \rightarrow \nu_e$ oscillations using π^+ that decay in flight. This decay-in-flight oscillation search has different backgrounds and systematics than the decay-at-rest search, and the results are consistent with the decay-at-rest signal.[4] These results are described in detail in chapter 3.

If the LSND signal is due to neutrino oscillations, MiniBooNE expects between 800 and 1000 events per year, depending on the Δm^2 and $\sin^2 2\theta$ values of $\nu_\mu \rightarrow \nu_e$ oscillations. The expectations are shown in Fig. 2.2. The MiniBooNE systematics are significantly different to the LSND experiment. Thus MiniBooNE will be able to verify or disprove the LSND result. The full BooNE two-detector system can accurately measure the oscillation parameters if a signal is observed.

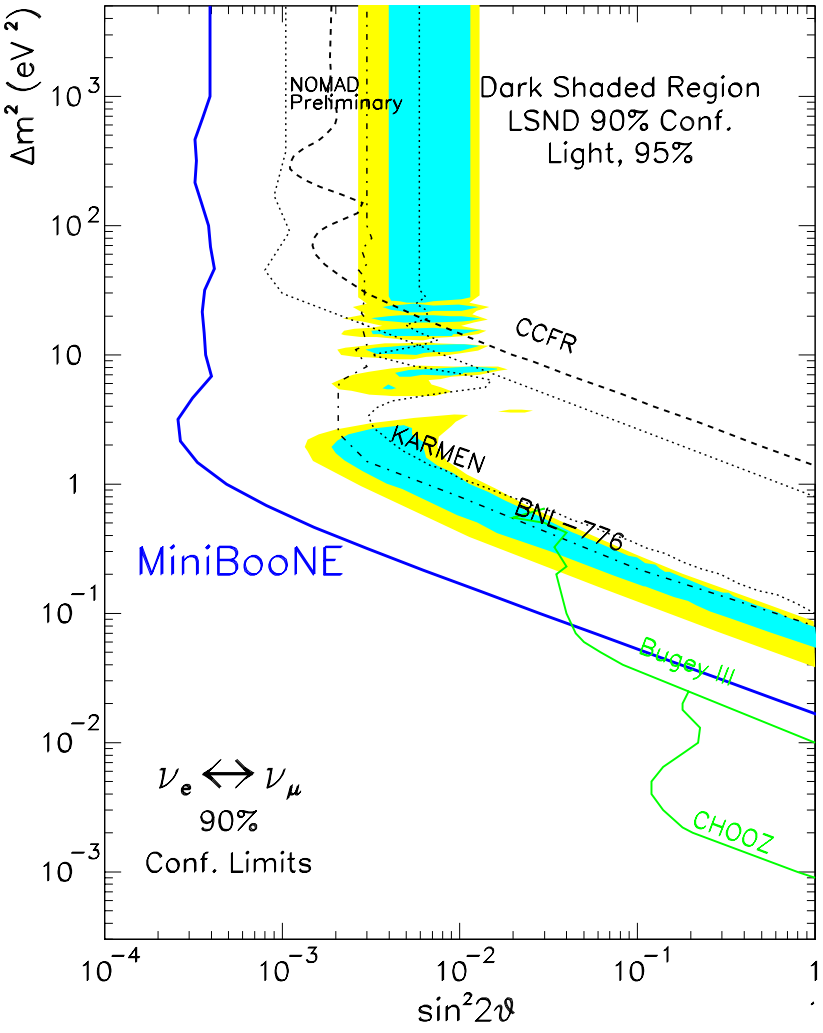

Figure 2.1: 90% C.L. limit expected for MiniBooNE for $\nu_\mu \to \nu_e$ appearance after one year of running, including systematic and statistical errors (see section 2.2), if LSND signal is not observed (solid line). Results from past experiments through December, 1997, also are shown.

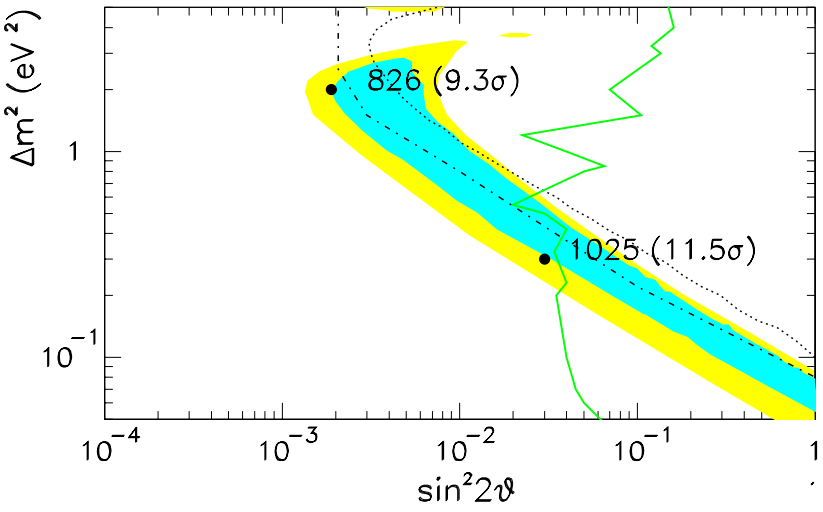

Figure 2.2: If LSND signal is observed, this plot shows the number of events expected in 1 year of running for MiniBooNE for the low Δm^2 favored region for LSND (shaded). Significance includes combined systematic and statistical errors (see section 2.2). Lines indicate regions excluded by past experiments (see Fig. 2.1).

If the LSND signal is not observed by MiniBooNE, then the expected sensitivity is shown in Fig. 2.1. This experiment extends significantly in Δm^2 and $\sin^2 2\theta$ beyond previous limits.

MiniBooNE is unique in its ability to make a definitive statement on the LSND signal within the next five years; however, there are two other approved experiments seeking to investigate this signal: the KARMEN2 experiment, which is presently running, and the MINOS experiment, which will begin taking data in 2002. There are two experiments in the design stage which have been submitted as Letters of Intent to CERN. There are also discussions of experiments at future neutron spallation facilities.

Fig. 2.3 shows the expectations for $\nu_\mu \to \nu_e$ oscillation experiments through 2005. MiniBooNE will begin running in 2001, coinciding with the completion of the KARMEN2 experiment. MiniBooNE can make a clear statement on the LSND signal by 2002, as shown in the figure. If an oscillation signal is observed, then the BooNE (2 detector) experiment will be proposed. BooNE and MINOS may be expected to run simultaneously and to have initial results in 2005. Here we summarize the expectations for the future (a more detailed discussion is presented in chapter 3):

- KARMEN2 will have insufficient statistics to verify fully the LSND result,[5,6] although this upgrade to KARMEN has achieved a significant improvement in their cosmic-ray background rate. So far, KARMEN2 has seen no events with a correlated neutron, however their expectation based on the LSND signal is ~ 1 observed event. Because KARMEN2's neutrino source and experimental signal are so similar to that of LSND, KARMEN2 will not provide the systematic check required.

- Because of their large L/E, MINOS will be unable to measure Δm^2 for the LSND signal region, but can contribute if there is a signal in the region below 0.1 eV^2. Fig. 2.3 shows the $\sin^2 2\theta$ limit based on the P875 (MINOS) proposal.[8] This collaboration is in the process of developing new particle identification techniques which may increase the $\sin^2 2\theta$ reach,[7] although the details of this method are, as yet, somewhat vague and must be adjusted to reflect the new detector design, which has significantly less segmentation and tonnage than their older design. At this point, we believe that MINOS will not be able to fully cover the LSND region at small $\sin^2 2\theta$ ($< 10^{-2}$).

- A Letter of Intent has been submitted to CERN to perform a low energy neutrino experiment similar to MiniBooNE with detectors at 128 m and 850 m.[9] This experiment claims slightly worse capabilities and a similar

time-scale to MiniBooNE. A second Letter of Intent has been submitted to CERN to search for $\nu_\mu \to \nu_e$ oscillations with the existing SPS neutrino beam.[10] Sensitivity and time-scale for this experiment were not presented.

- In the far future, neutrino oscillation experiments may run at three possible new neutron spallation facilities: Savannah River, Oak Ridge and NESS. These experiments are not expected to take data before 2005. The systematics of these experiments can be expected to be similar to LSND and KARMEN.

The second important hint for neutrino oscillations comes from experiments which indicate a deficit of muon neutrinos from cosmic ray production in the atmosphere. The Kamioka and IMB experiments [11,12] measure the ratio of μ/e to be only about 60% of the expected ratio for energies below $\sim$1 GeV, independent of the visible energy of the charged lepton and the projected zenith angle of the atmospheric neutrinos. Interpreting the shortfall as arising from oscillation of muon neutrinos requires a large mixing angle ($\sin^2 2\theta \sim 0.5$) and a $\Delta m^2 > 10^{-3}$ eV^2. The Kamioka group has observed a zenith angle dependence of the high energy (greater than 1 GeV) atmospheric neutrino sample [14] which indicates that $\Delta m^2 << 0.5$ eV^2 (Kamioka prefers a $\Delta m^2 \sim 10^{-2}$ eV^2), although the uncertainties are large. However a recent publication from the IMB collaboration[13] reports no zenith angle dependence. The recent Super Kamiokande results are confusing to interpret. The overall ratio-of-ratios favors a high value of Δm^2, while the new zenith angle analysis favors $\Delta m^2 < 10^{-2}$.[15] The Super Kamiokande results may be also consistent with no zenith angle dependence, although this is not the most-favored solution. If there is no zenith angle dependence, then the data indicate $\Delta m^2 > 0.15$ eV^2 at large $\sin^2 2\theta$, which is within the sensitivity of MiniBooNE. Upper limits on the possible Δm^2 range come from previous accelerator-based experiments and the zenith angle dependence of the atmospheric neutrino deficit. The CDHS search for ν_μ disappearance indicates $\Delta m^2 < 0.5$ eV^2 for large mixing.[18]

The atmospheric problem can be attributed to $\nu_\mu \to \nu_e$, $\nu_\mu \to \nu_\tau$ or oscillations to a sterile neutrino. We will consider the case of only three neutrino species in this proposal. The Bugey,[16] and CHOOZ[17] results, shown in Fig. 2.1, exclude most of the atmospheric neutrino deficit region for $\nu_\mu \to \nu_e$. Therefore, $\nu_\mu \to \nu_\tau$ oscillations are often considered to be the more likely possibility.

Fig. 2.4 shows an overview of past experiments (narrow dashed and dotted lines) and expectations for future approved experiments (wide dashed lines) for $\nu_\mu \to \nu_\tau$ searches. In light of the changing situation concerning the zenith

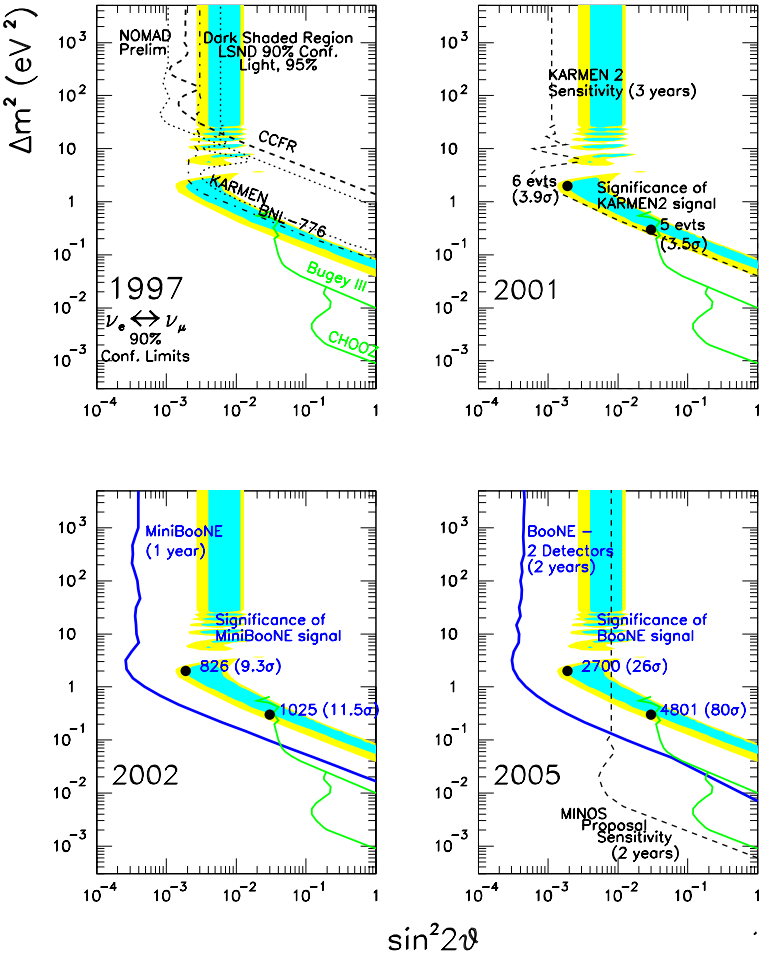

Figure 2.3: $\nu_\mu \rightarrow \nu_e$ oscillation results as of December, 1997, and expectations from upcoming approved experiments compared to MiniBooNE and BooNE in 2001 (MiniBooNE start), 2002 (MiniBooNE first results), and 2005 (BooNE first results).

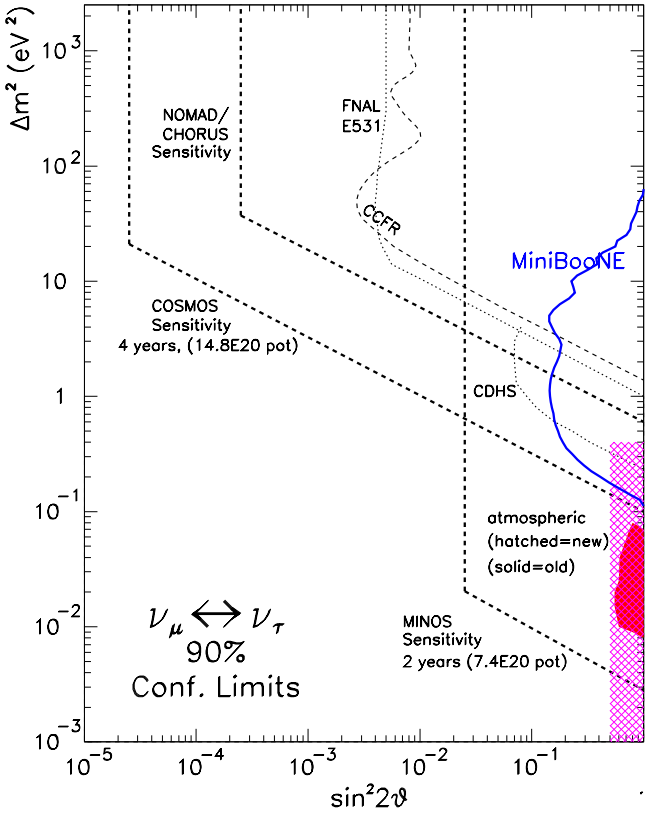

Figure 2.4: Summary of results from past experiments (narrow, dashed and dotted), future approved experiments (wide, dashed) and 90% C.L. limit expected for MiniBooNE (solid) for ν_μ disappearance. Solid region indicates the favored region for the atmospheric neutrino deficit from the Kamioka experiment. No zenith angle dependence would extend the favored region to higher Δm^2 as indicated by the hatched region.

angle dependence, Fig. 2.4 shows the allowed region if there is a zenith angle dependence in agreement with the Kamioka results (solid) and if the zenith angle is disregarded (hatched). In the higher Δm^2 scenario, MiniBooNE (solid line) can address the atmospheric neutrino oscillation question by searching for ν_μ disappearance. MiniBooNE is sensitive to variations in the flux with energy that are consistent with oscillations. Statistical and systematic errors were included in this determination.

The case where the Δm^2 values from atmospheric neutrino experiments are compatible with LSND provides a useful example of a three-generation mixing formalism which may be applied to explain the present pieces of evidence for neutrino oscillations. If Δm^2 for $\nu_\mu \rightarrow \nu_e$ from LSND is approximately the same as Δm^2 from $\nu_\mu \rightarrow \nu_\tau$ in the atmospheric case, then three-generation mixing models [19] with only two mass values for the mass eigenstates, *i.e.*, $m_3 \gg m_1 \approx m_2$, apply. In this case, the LSND result is explained via $\nu_\mu \rightarrow \nu_3 \rightarrow \nu_e$ while the atmospheric result is explained through $\nu_\mu \rightarrow \nu_3 \rightarrow \nu_\tau$. The solar neutrino results are also accommodated through $\nu_e \rightarrow (\nu_1, \nu_2) \rightarrow (\nu_\mu, \nu_\tau)$. This and other examples of three generation mixing models are discussed in this proposal.

In addressing the question of neutrino oscillations and neutrino mass, it is also possible to address current astrophysical issues as well. Neutrino mass, for example, may contribute to dark matter in the universe. Current limits allow neutrino masses in the Δm^2 range between 1 and 10 eV^2 [20]. Neutrino oscillations also address the issue of the nucleosynthesis of heavy elements in supernovae[21]. Current r-process nucleosynthesis models are highly sensitive to the neutron/proton ratio which, in turn, is highly sensitive to the neutrino energy distributions. Neutrino oscillations, therefore, may play a significant role in the r-process in supernovae, and current limits already have been set[22].

2.2 MiniBooNE Capabilities and Design Issues

As shown in the previous section, there is a need for experiments to probe $\nu_\mu \rightarrow \nu_e$ oscillations in the $0.01 - 10.0$ eV^2 mass region with mixings down to $\sin^2 2\theta \approx 10^{-3} - 10^{-2}$. For $\Delta m^2 = 1$ eV^2, an experiment needs an L/E value of about 1.0. Since the rate from a neutrino source falls as $1/L^2$, the most cost effective way to probe this region is with the smallest L for the available E_ν value. A neutrino beam from the 8 GeV Fermilab Booster is almost optimal for this region using an L value of ~ 500 m combined with $0.1 < E_\nu < 1.0$ GeV. In addition, a sensitive search for $\nu_\mu \rightarrow \nu_e$ oscillations requires low intrinsic ν_e background in the beam. A Booster ν beam would have a low ν_e background ($\nu_e/\nu_\mu \approx 10^{-3}$) for two reasons. First, the kaon production rate is low due the

low primary proton energy. Second, a short decay pipe can be used, thereby minimizing μ decay.

A low-energy Fermilab ν experiment is possible due to the very high proton fluxes available from the Booster. The FNAL Booster is capable of providing an additional 5 pulses per second at $\sim 5 \times 10^{12}$ protons per 1 μ sec pulse at 8 GeV. The duty factor of the Booster beam with single turn extraction reduces cosmic ray background enormously compared to LSND and makes the data acquisition problem much simpler than for LSND. The proposal presents results for 2×10^7 s of Booster running, which is obtainable in one calender year.

As 3 GeV pion production is copious from an 8 GeV beam, we propose building a focusing system capable of producing a parallel beam of pions centered on 3 GeV/c. The secondary pion beam has a relatively short decay length which can be varied from 25 to 50 m. The short decay length keeps the fraction of ν_e in the beam from the $\pi \to \mu \to e$ decay chain at a low level. Varying the decay length provides a test of signal versus background if an excess of ν_e events are observed. The MiniBooNE sensitivities and event rates shown in Figs. 2.1 - 2.4 assume 1×10^7 s of running at 25 and 50 m, respectively. The focusing system will be capable of operation in either positive or negative polarity, which opens further opportunities for verifying a signal. Combining the high proton flux with a high efficiency horn focused secondary beam will provide over 1,000,000 ν_μ events/.5 kt-yr at 500 m from the source.

The high intensity and rapid cycling of the Booster put important requirements on the beam design. There needs to be significant shielding to meet radiation safety and ground water requirements. The beam elements including the high-current horn need to be reliable at cycle rates of ≈ 5 Hz. A new underground enclosure must be constructed to house and provide access to the beam, the 50 m decay region and the dump. The neutrino beam will be directed horizontally at 6.0 m below the ground level, thereby minimizing any surface radiation. To achieve low cost, the enclosure needs to be made with conventional construction techniques and existing shielding materials when possible.

The proposed experiment would start with a single detector, MiniBooNE, to probe the LSND mass region and establish definitive evidence for neutrino oscillations. If a positive signal is observed, this first stage would be followed by a two detector experiment, BooNE, in the same neutrino beam. The second detector is expected to be located $\sim$ 1km from the neutrino source. The beamline and detectors are shown in figure 2.5.

For the initial single detector MiniBooNE experiment, accurate ν flux and background determinations will be needed. Modern simulation tools can ac-

Figure 2.5: Southwest region of the Fermilab site. The BooNE neutrino beam line originates at MI10 and points almost due north. Targeting and Dump Halls are located north of the MI cooling ponds. The MiniBooNE detector is located near the Lederman Science Center between Giese Road and Pine Street. The distance from the neutrino source to the detector is 500 m. A possible site for a second detector (the BooNE experiment) also is shown.

curately model beam transport and scraping but need to be augmented and checked using direct measurements. A primary ingredient for the simulation is the particle production spectrum from the 8 GeV proton interactions in the thick production target. The data are discussed in Section 4.4.1. Position and profile monitors similar to those used by NuTeV and BNL 776 in the primary beam, decay pipe, and post-dump region will provide important constraints on the beam simulation. Analysis methods have been developed in previous neutrino experiments to use the measured neutrino spectrum in the detector to determine the secondary particle fractions. For example, this technique has been successfully used to fix the charged π/K fraction in the NuTeV experiment. In addition, as presented in Section 4.4.4, the observed ν_μ event spectrum in MiniBooNE is highly correlated with the decaying pion spectrum due to the small solid angle subtended by the detector. Thus, the observed ν_μ events constrain the decaying pion spectrum and subsequent muon decay spectrum. Using this information, the systematic uncertainty on the ν_e background from muon decay can be reduced to the 5% level.

The MiniBooNE experiment needs a detector with a large fiducial mass and good particle identification for neutrino events in the $0.10 < E_\nu < 2.0$ GeV energy region. At these low energies, a totally active detector is necessary. A detector based on a large volume of mineral oil is both cost effective and very powerful for particle identification using the techniques developed for the LSND experiment. Mineral oil has several advantages over distilled water as a detection medium: a) more Čerenkov light, b) no purification requirements, c) longer radiation length, d) less μ^- capture probability, and e) the ability to use, for better particle identification, the inherent scintillation light of pure oil or enhanced light associated with a dilute scintillator mixture .

Many of the critical detector components are available from the LSND experiment including the 1220 eight-inch photomultiplier tubes (PMTs) with readout and data acquisition system. The mineral oil will be contained in a spherical tank 12 m in diameter, leading to a fiducial volume corresponding to $\sim$ 445 tons. The phototubes will be located at a radius of 5.5 m, and the 50 cm veto region between the outer wall and phototubes will be optically isolated from the main volume and viewed by an additional 292 phototubes facing outward. In order to minimize costs, the tank will use standard commercial oil/water tank technology and safety standards and be buried with its center at 6.0 m below the ground, the beam elevation.

Particle mis-identification is an important limitation for the $\nu_\mu \to \nu_e$ oscillation measurement. Using the techniques developed and tested in the LSND experiment, the mis-identification of ν_μ events as ν_e events can be reduced to the $\approx 10^{-3}$ level while keeping the ν_e and ν_μ efficiency $\sim$50% . The identifica-

tion techniques are based on the spatial and time correlation of the detected Čerenkov and scintillation light by the PMTs lining the walls of the detector. A further strength of the experiment is the ability to measure these backgrounds from the preponderance of events which are identified correctly. For this proposal, we have used χ^2-based particle identification for all simulations. (For the actual experimental analysis, we plan to apply a likelihood method similar to the recent LSND analysis that has significantly reduced background and increased efficiencies.)

Muon neutrino events are identified by observing an exiting μ or a decay electron with the correct time and position correlation with the μ. For ν_μ events, $8 \pm 0.1\%$ of the outgoing μ^-'s are captured before decay and must be identified by the spatial and time signature of the Čerenkov and scintillation light. In this type of detector, a μ has a sharper Čerenkov ring and relatively more scintillation light than an e or γ interaction. (Scintillation light can be isolated due to its much broader time distribution.) The signature for a ν_e event is a diffuse Čerenkov ring with relatively low scintillation light. This signature can also be satisfied by $\nu_\mu N \to \nu_\mu \pi^0 X$ events where the γ's from the π^0 decay are misidentified as electrons. The cross section and E_ν threshold for the π^0 production reduces the rate substantially for this process with respect to $\nu_\mu N \to \mu X$ scattering, but a rejection factor of 100 is still needed to reduce this background to the 10^{-3} level. This rejection is available for the MiniBooNE detector by detecting the second γ or by detecting late scintillation light from an energetic recoil proton.

The 8 GeV Booster ν beam using a focusing horn system and running for 2×10^7s first with a 25 m and then with a 50 m decay pipe will provide $\sim 1,000,000\,(200,000)$ $\nu_\mu(\overline{\nu}_\mu)$ events/yr in the 445 ton MiniBooNE detector. For the $\nu_\mu \to \nu_e$ oscillation measurement, the beam ν_e background is expected to be at the 0.3% level with a systematic uncertainty of 5(10)% for $\mu(K)-$ decay. The mis-identification backgrounds can be held to less than 0.2% and be known with an uncertainty of 5%. These statistics and systematic uncertainty estimates were used to obtain the sensitivity curves shown in Fig. 2.1 and the signal significance plot shown in fig. 2.2. For the ν_μ disappearance sensitivity calculation, a 25% uncertainty in the overall normalization and a 10% bin-to-bin shape uncertainty in the energy distribution was assumed. When determining the sensitivity and significance, the energy dependences of the expected signal, efficiency, and backgrounds were included.

For oscillations at the LSND level, MiniBooNE should see approximately one thousand anomalous ν_e events over a beam-related (mis-identification) background of 1700 (1200) events, establishing the signal at the $\sim 8\sigma$ level. If no oscillation signal is observed, the experiment will exclude $\nu_\mu \to \nu_e$ os-

cillations with $\sin^2 2\theta > 3.8 \times 10^{-4}$ for large Δm^2 and $\Delta m^2 > 0.02$ eV^2 for $\sin^2 2\theta = 1$.

2.3 MiniBooNE as a Component of the Fermilab Program

MiniBooNE is compatible with the presently approved FNAL program and opens new opportunities for additional low energy experiments. The Booster is capable of providing the MiniBooNE request for protons while supplying the collider and NuMI experiments. The neutrino beam which is produced for MiniBooNE could be used by other neutrino experiments. One example is a νp elastic scattering experiment dedicated to measuring the strange axial form factor, which has been discussed at several workshops.[23] An anti-hydrogen experiment could make use of the BooNE beam line.[24] Possibilities for a $\mu^- N \to e^- N$ experiment are already under investigation by the MECO collaboration.[25] The extracted 8 GeV proton beam could also feed a series of experimental studies required for technical development of the First Muon Collider.[26] Technical R&D on target production, capture, decay and ionization cooling for the muon collider is required. The muon collider requires an upgraded Booster, with higher intensity and 16 GeV energy. The BooNE beam line is designed to accommodate these plans. Other experiments using protons from the upgraded Booster were under discussion at a recent workshop on Physics at the First Muon Collider and at the Front End of a Muon Collider.[27] The BooNE site at FNAL was chosen to have sufficient space for a future 8 GeV program of experiments and to coordinate with the muon collider plans.

MiniBooNE is an experiment which can and should begin running soon. Construction of MiniBooNE can be completed by 2001. The data-taking and analysis presented above is expected to be completed by 2002. The cost of the BooNE beam line is expected to be \$3.92M and the cost of the MiniBooNE detector is \$2.21M. (These costs are \$6.25M and \$3.07M, respectively, when contingency and escalation also are included.)

MiniBooNE represents a unique opportunity for Fermilab to pursue a definitive study of the LSND Δm^2 region. In the following proposal, we present the conceptual design for the MiniBooNE beam and detector and detail the expectations for this experiment.

Chapter 3

Status of Neutrino Oscillation Experiments

Evidence for neutrino oscillations comes from the solar neutrino experiments, the atmospheric neutrino experiments, and the LSND experiment. These results can be interpreted within three-generation neutrino mixing models. Although future experiments are planned, MiniBooNE fulfills a unique niche in addressing the present evidence for neutrino oscillations.

3.1 Neutrino Oscillation Formalism

It is likely that the interaction responsible for mass will have eigenstates which are different from the eigenstates that are associated with weak decays. In this model, the weak eigenstates are mixtures of the mass eigenstates and lepton number is not strictly conserved. A pure flavor (weak) eigenstate born through a weak decay will oscillate into other flavors as the state propagates in space. This oscillation is due to the fact that each of the mass eigenstate components propagates with a different frequency if the masses are different, $\Delta m^2 = \left|m_2^2 - m_1^2\right| > 0$. The most general form for 3-component oscillations is

$$\begin{pmatrix} \nu_e \\ \nu_\mu \\ \nu_\tau \end{pmatrix} = \begin{pmatrix} U_{e1} & U_{e2} & U_{e3} \\ U_{\mu 1} & U_{\mu 2} & U_{\mu 3} \\ U_{\tau 1} & U_{\tau 2} & U_{\tau 3} \end{pmatrix} \begin{pmatrix} \nu_1 \\ \nu_2 \\ \nu_3 \end{pmatrix}$$

This formalism is analogous to the quark sector, where strong and weak eigenstates are not identical and the resultant mixing is described conventionally

by a unitary mixing matrix. The oscillation probability is then:

$$\text{Prob}\,(\nu_\alpha \to \nu_\beta) = \delta_{\alpha\beta} - 4 \sum_{j>i} U_{\alpha\, i} U_{\beta\, i} U^*_{\alpha\, j} U^*_{\beta\, j} \sin^2 \left(\frac{1.27\, \Delta m^2_{i\, j}\, (\text{eV}^2)\ L\,(\text{km})}{E_\nu\,(\text{GeV})} \right) \tag{3.1}$$

where $\Delta m^2_{i\,j} = \left| m^2_i - m^2_j \right|$. Note that there are three different Δm^2 (although only two are independent) and three different mixing angles. The oscillation probability also depends upon L, the distance from the source, and E_ν, the neutrino energy.

Although in general there will be mixing among all three flavors of neutrinos, two-generation mixing is often assumed for simplicity. If the mass scales are quite different ($m_3 >> m_2 >> m_1$ for example), then the oscillation phenomena tend to decouple and the two-generation mixing model is a good approximation in limited regions. In this case, each transition can be described by a two-generation mixing equation:

$$P = \sin^2 2\theta\ \sin^2(1.27 \Delta m^2\ L/E_\nu) \tag{3.2}$$

where θ is the mixing angle. However, it is possible that experimental results interpreted within the two-generation mixing formalism may indicate very different Δm^2 scales with quite different apparent strengths for the same oscillation. This is because, as is evident from equation 3.1, multiple terms involving different mixing strengths and Δm^2 values contribute to the transition probability for $\nu_\alpha \to \nu_\beta$.

3.2 LSND Results

The LSND experiment uses a detector composed of 167 tons of dilute liquid scintillator placed 30 m from the beam stop of the LAMPF 800 MeV proton beam.[1] Neutrinos are produced from stopped $\pi^+ \to \mu^+ \nu_\mu$ and $\mu^+ \to e^+ \nu_e \bar{\nu}_\mu$ decays. The signature for a $\bar{\nu}_\mu \to \bar{\nu}_e$ oscillations in the detector is the reaction $\bar{\nu}_e p \to e^+ n$ followed by $np \to d\gamma$ (2.2 MeV). A likelihood ratio, R, is employed to determine whether a γ is a 2.2 MeV photon correlated with a positron or is from an accidental coincidence. R is the likelihood that the γ is correlated, divided by the likelihood that it is accidental. As shown in Fig. 3.1, R depends on the number of hit phototubes for the γ, the reconstructed distance between the positron and the γ, and the relative time between the γ and positron. Fig. 3.2 shows the R distribution, beam on minus beam off, for events with positrons in the $36 < E < 60$ MeV energy range. The dashed histogram is the result of the R fit for events without a recoil neutron, and the solid histogram

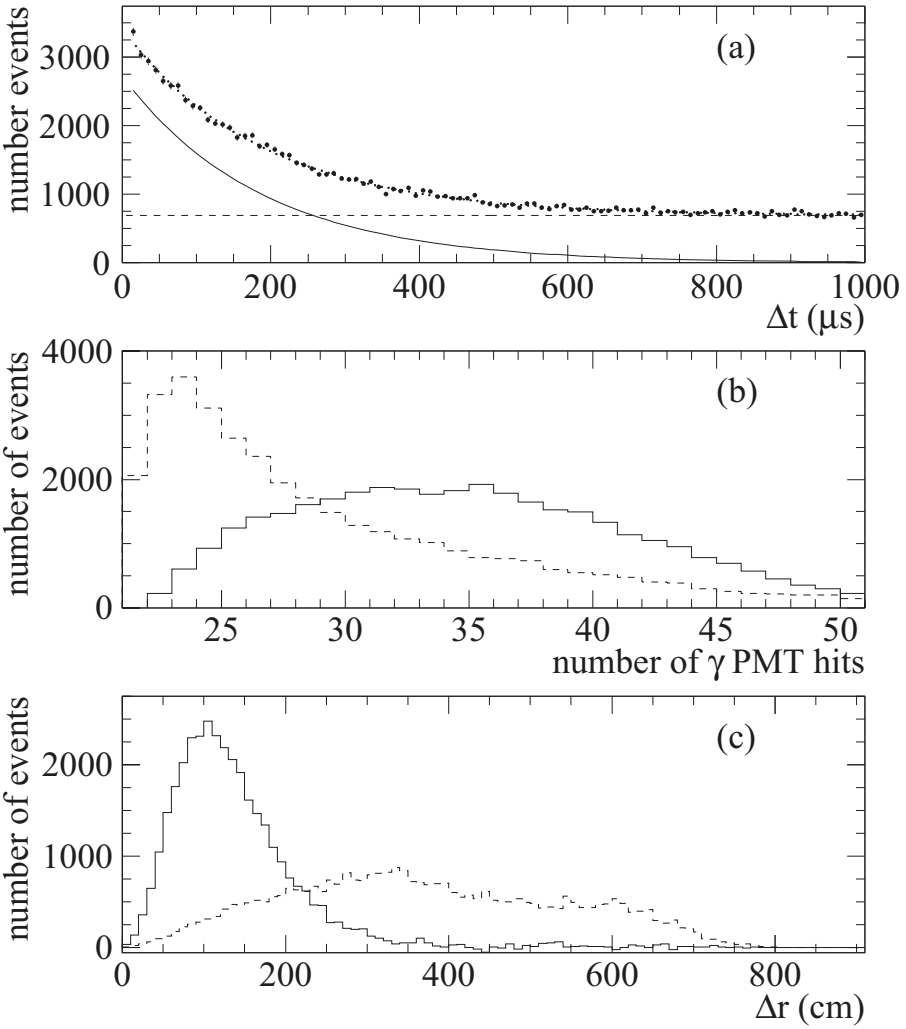

Figure 3.1: Associated γ distributions in (a) time, (b) PMT hits, and (c) distance for associated (solid) and accidental (dashed) γ's.

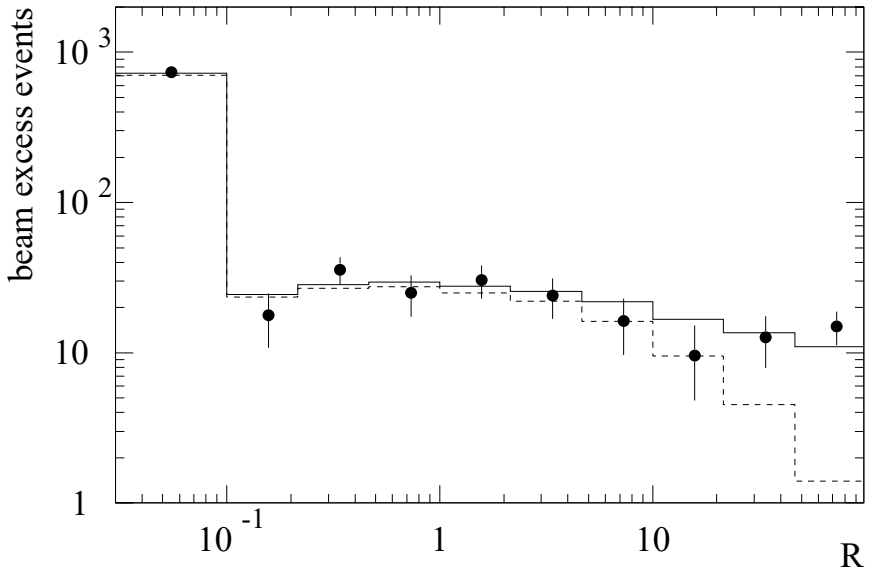

Figure 3.2: The R distribution, beam on minus beam off excess, for events that have energies in the range $20 < E_e < 60$ MeV. The solid curve is the best fit to the data, while the dashed curve is the component of the fit with an uncorrelated γ.

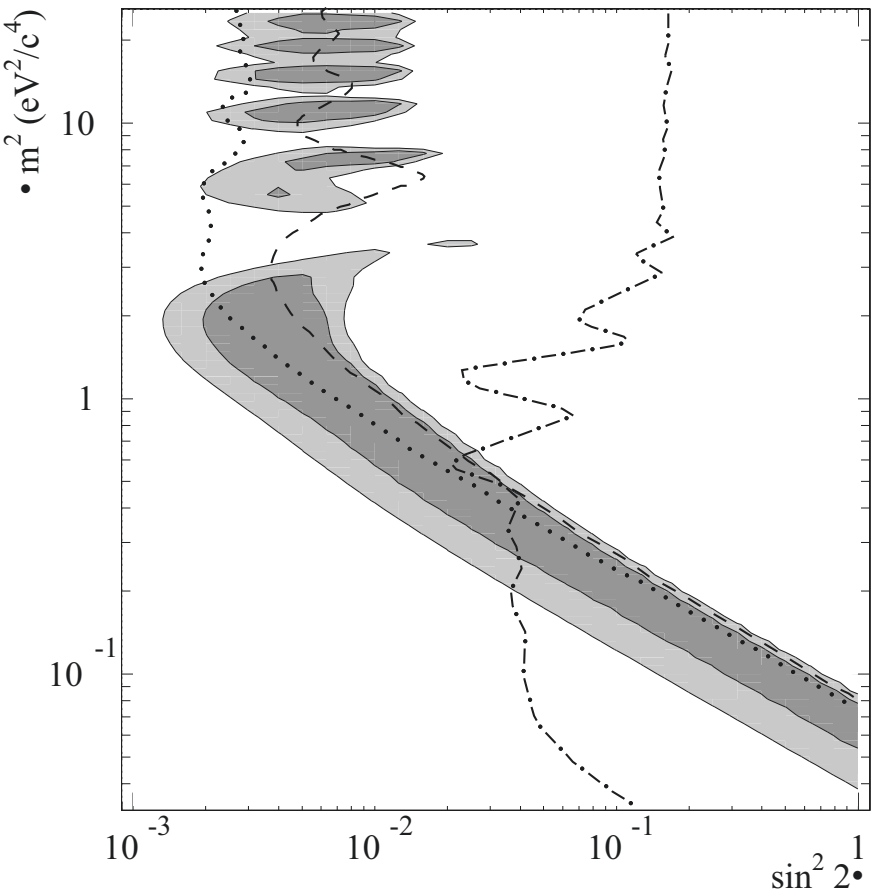

Figure 3.3: Allowed regions in the Δm^2 vs $\sin^2 2\theta$ parameter space from the LSND $\bar{\nu}_\mu \to \bar{\nu}_e$ appearance experiment. Also shown are 90% C.L. limits from KARMEN at ISIS (dashed curve), E776 at BNL (dotted curve), and the Bugey reactor experiment (dot-dashed curve).

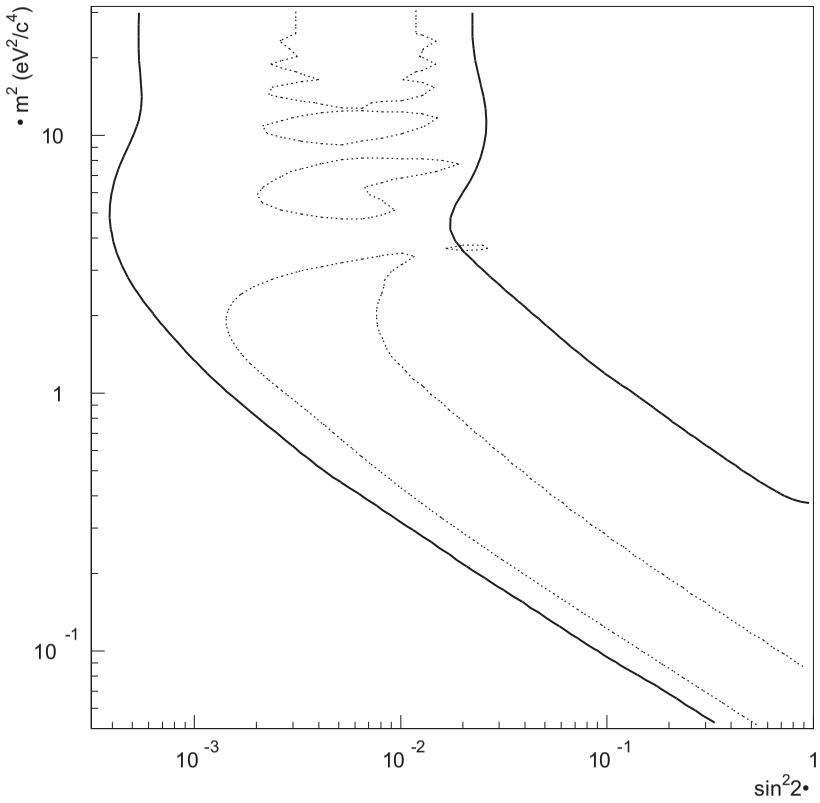

Figure 3.4: The 95% confidence region for $\nu_\mu \to \nu_e$ oscillations (solid curve) along with the favored regions for $\bar{\nu}_\mu \to \bar{\nu}_e$ oscillations (dotted curve).

Table 3.1: Preliminary numbers of "gold-plated" $\bar{\nu}_\mu \to \bar{\nu}_e$ LSND events with $R > 30$ from the entire 1993-1997 data sample.

e^+ Energy	Events Beam On	Events Beam Off	ν Background	Total Excess
$20 < E_e < 60$ MeV	61	15.6 ± 1.0	11.5 ± 1.5	33.9 ± 8.0
$36 < E_e < 60$ MeV	29	5.2 ± 0.6	3.0 ± 0.6	20.8 ± 5.4

Table 3.2: Preliminary numbers of $\bar{\nu}_\mu \to \bar{\nu}_e$ excess LSND events and the corresponding oscillation probabilities from fits to the R distributions for the running periods 1993-1995, 1996-1997, and 1993-1997.

Data Sample	Fitted Excess	ν Background	Total Excess	Oscillation Probability
1993-1995	63.5 ± 20.0	12.5 ± 2.9	51.0 ± 20.2	$(0.31 \pm 0.12 \pm 0.05)\%$
1996-1997	35.1 ± 14.7	4.8 ± 1.1	30.3 ± 14.8	$(0.32 \pm 0.15 \pm 0.05)\%$
1993-1997	100.1 ± 23.4	17.3 ± 4.0	82.8 ± 23.7	$(0.31 \pm 0.09 \pm 0.05)\%$

is the total fit, including events with a neutron. After subtracting the neutrino background with a recoil neutron there is a total excess of $51.8^{+18.7}_{-16.9} \pm 8.0$ events. This corresponds to an oscillation probability of $\text{Prob}(\bar{\nu}_\mu \to \bar{\nu}_e) = (0.31 \pm 0.11 \pm 0.05)\%$ and to an oscillation parameter allowed region shown in Fig. 3.3. Due to the low 800 MeV proton energy of the LAMPF beam, the neutrino backgrounds are quite small and well understood. The largest background is from μ^- decay at rest in the beam stop, which is suppressed by a factor of 7×10^{-4} relative to μ^+ decay at rest. The suppression results from the following three factors: the ratio of π^- to π^+ (0.12) times the probability that the π^- decays in flight (0.05) times the probability that the μ^- decays at rest (0.12).

The above results correspond to the 1993-1995 data sample. Preliminary $\bar{\nu}_\mu \to \bar{\nu}_e$ LSND results from 1996 and 1997 are given in Tables 3.1 and 3.2. Table 3.1 shows the number of "gold-plated" events with $R > 30$ from the entire 1993-1997 data sample, while Table 3.2 shows the total numbers of excess events and the corresponding oscillation probabilities from fits to the R distributions for the running periods 1993-1995, 1996-1997, and 1993-1997. The preliminary oscillation probability for the entire data sample is $(0.31 \pm 0.09 \pm 0.05)\%$.

The LSND signal is strengthened by a complementary $\nu_\mu \to \nu_e$ oscillation search,[4] which has completely different systematics and backgrounds than the

$\bar{\nu}_\mu \to \bar{\nu}_e$ oscillation search. The neutrinos for this search come from pion decay in flight and are of higher energies than those produced by stopped muons. The signature for $\nu_\mu \to \nu_e$ oscillations is an electron from the reaction $\nu_e C \to e^- X$ in the energy range $60 < E_e < 200$ MeV. Using two independent analyses, a total of 40 beam-related events and 175 beam-unrelated events are observed, corresponding to a beam on-off excess of 27.7 ± 6.4 events. The neutrino-induced backgrounds are dominated by $\mu^+ \to e^+ \bar{\nu}_\mu \nu_e$ and $\pi^+ \to e^+ \nu_e$ decays-in-flight in the beam-stop and are estimated to be 9.6 ± 1.9 events. Therefore, a total excess of $18.1 \pm 6.6 \pm 3.5$ events is observed above background.

The excess events are consistent with $\nu_\mu \to \nu_e$ oscillations with an oscillation probability of $(0.26 \pm 0.10 \pm 0.05)\%$. A fit to the event distributions yields the allowed region in the $(\sin^2 2\theta, \Delta m^2)$ parameter space shown in Fig. 3.4, which is consistent with the allowed region from the $\bar{\nu}_\mu \to \bar{\nu}_e$ search. These two searches have completely different backgrounds and systematic errors, and together they provide strong evidence that the observed event excesses are indeed due to neutrino oscillations.

3.3 Solar Neutrino Experiments

Since the first observation of ν_e interactions in a Cl target in the Homestake mine by Davis and collaborators,[28] four additional experiments have measured solar neutrino interactions and have determined that there are fewer neutrinos from the sun than are expected from the Standard Solar Model. There have been two experiments using Ga as target, GALLEX and SAGE, and the experiments at Kamioka, Kamiokande and Super Kamiokande, in which neutrinos are scattered from electrons in water. The Ga experiments [29] have the lowest energy threshold, while Kamiokande [30] is limited by the ~ 7 MeV detection energy threshold for electrons. Hata and Langacker published [31] a thorough analysis of the data three years ago. They considered experimental errors in detail as well as possible variations in the Standard Solar Model which is used to predict the flux of neutrinos that is expected from the sun in the absence of neutrino oscillations. Each of the experiments is sensitive to different parts of the neutrino spectrum. These sensitivities are shown in Table 3.3 using the Standard Solar Model of Bahcall and Pinsonneault [32]. The experimental results are shown in Table 3.4, where it is clearly seen that the measured solar neutrino flux is below the prediction of the Standard Solar Model.

Hata and Langacker conclude that the experimental data cannot be explained by variations in solar physics and that neutrino oscillations are strongly favored. Also, resonant transformation of ν_e to other flavors through the MSW effect is preferred, leading to the allowed region in the Δm^2 - $\sin^2 2\theta$ parame-

Table 3.3: Sensitivities of the three types of solar neutrino experiments on the expected reactions in the Standard Solar Model.

	Kamiokande	Homestake	GALLEX/SAGE
pp			0.538
^{7}Be I			0.009
^{7}Be II		0.150	0.264
^{8}Be	1	0.775	0.105
pep		0.025	0.024
^{1}3N		0.013	0.023
^{1}5O		0.038	0.037

Table 3.4: The measured rate from the three types of solar neutrino experiments compared to the Standard Solar Model.

Experiment	Rate
GALLEX/SAGE	0.62 ± 0.10
Homestake	0.29 ± 0.03
Kamiokande	0.51 ± 0.07

ter space shown in Fig. 3.5. Although we have stressed that three generations of neutrinos must be considered in general, that need not apply to the solar neutrino discussion as long as the masses m_1, m_2, m_3 are described by $m_3 >> m_2, m_1$. As the small mixing solution is favored, a value for θ_{12} of about 3×10^{-2} is implied. It is worth emphasizing that these data have been gathered over an extended period of time and that many systematic checks have been performed. Furthermore, the solar model is very much constrained by the solar luminosity, particularly in the case of the Gallium reaction. The Kamiokande result has been confirmed by preliminary Super Kamiokande results with significantly better statistics. Also, the neutrino oscillation hypothesis will be tested by the SNO experiment, which will measure both charged and neutral current solar neutrino interactions. Overall, the solar neutrino experimental observation appears firm, although uncertainties in solar dynamics are still a cause for concern as shown by the ^{3}He diffusion model of Cumming and Haxton. [33]

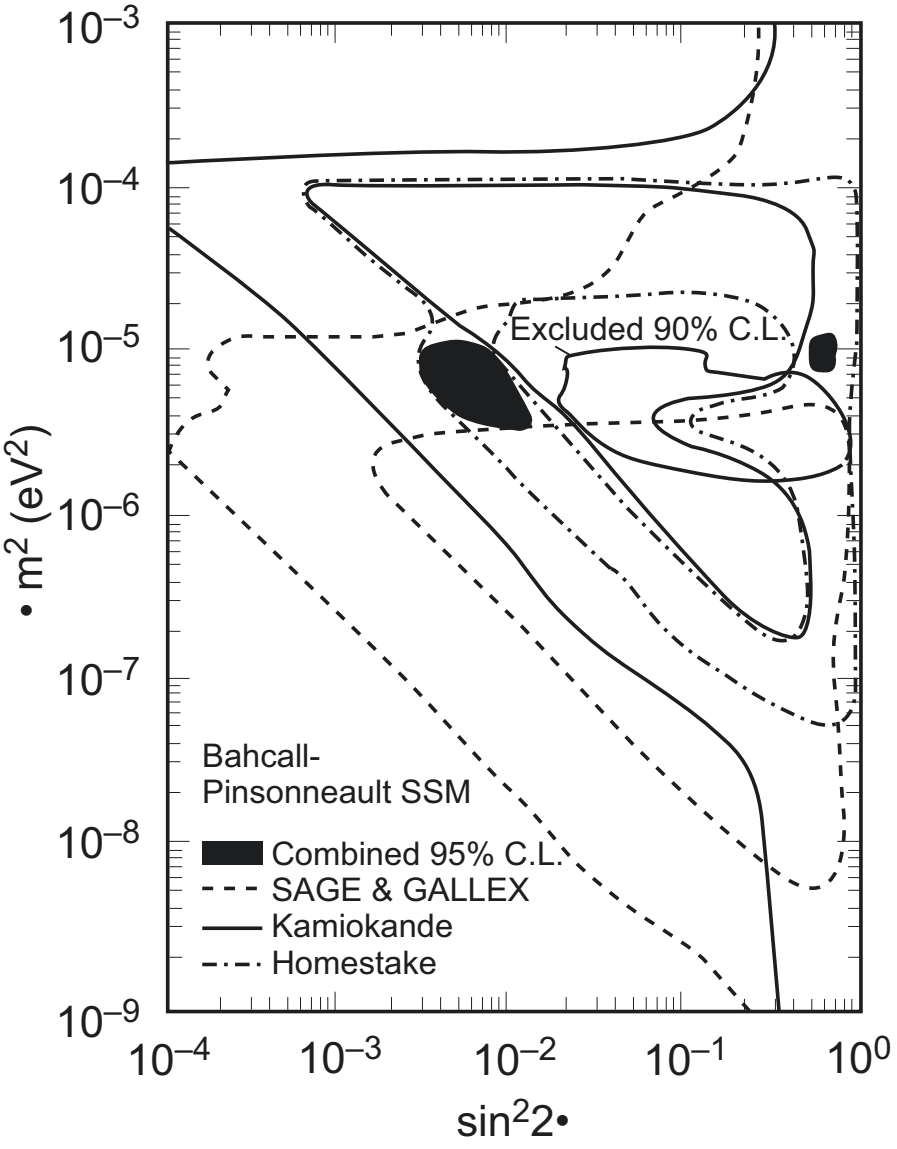

Figure 3.5: Allowed regions in the Δm^2 vs $\sin^2 2\theta$ parameter space from the four solar neutrino experiments.

3.4 Atmospheric Neutrino Experiments

Cosmic rays interacting in the upper atmosphere produce pions that decay into muons and neutrinos. In approximate terms, this decay chain produces two muon neutrinos for each electron neutrino. Charged-current reactions from these neutrinos have been observed in a number of detectors. The sensitivity of these detectors to electrons and muons varies over the observed energy range, and so the experiments depend on a Monte Carlo simulation to determine the relative efficiencies. For example, electron events are mostly contained in the detector, while muon events have longer range and escape the detector at the higher energies. The experiments report the observed ratio of muon to electron events divided by the ratio of events calculated in a Monte Carlo simulation. The experiments also model the absolute neutrino flux. A recent summary of the experimental situation is discussed by Gaisser and Goodman[34] and shown in Table 3.5. Several experiments measure the ratio of observed events to expected events to be less than one. For Kamiokande the data is divided into low and high energy samples. The low energy events have a muon (with energy typically less than 1 GeV) that is contained in the detector. Muons are identified in two ways by both Kamiokande and IMB. The first way involves identification of the Čerenkov ring, which is significantly different for electrons and muons. (There is also a significant difference between the efficiency for detection of electrons and muons, but this is presumably in the detector simulation.) The second method uses the fact that muons that stop in H_2O usually decay, allowing the observation of decay electrons to facilitate identification of the muon. The ratio is consistent using both methods of identification.

For the fully contained events the muon energy is sufficiently low that the cross section is over predicted by the Fermi gas model[35] used by all experiments. This is a valid concern but seems unlikely to explain the large and persistent effect observed. Moreover, this problem should not afflict the second sample of partially contained events for which the energy is typically ~ 5 GeV. It is our view, and that of the experimenters, that the ν_μ/ν_e ratio is suppressed, although some systematic effects are still to be understood.

The Kamiokande group has reported a zenith angle dependence of the apparent atmospheric neutrino deficit [14] based on their examination of higher energy atmospheric neutrino events (visible energy greater than 1.3 GeV and average energy equal to 6 GeV). In this instance the observed ν_μ/ν_e ratio was $0.57 \pm 0.08 \pm 0.07$, consistent with the earlier observations, but with a strong dependence of the ratio on the zenith angle of the projected neutrino direction. The ratio for these high energy neutrinos coming from directly

Table 3.5: Ratio of ν_μ to ν_e observed events divided by the ratio of expected events for the different atmospheric oscillation experiments.

Experiment	Exposure	Flavor Ratio
	kT - year	μ / e
IMB1	3.8	0.68 ± 0.08
Kamiokande Ring	7.7	0.60 ± 0.06
Kamiokande Decay		0.69 ± 0.06
IMB - 3 Ring	7.7	0.54 ± 0.05
IMB - 3 Decay		0.64 ± 0.07
Frejus Contained	2.0	0.87 ± 0.13
Soudan	1.0	0.64 ± 0.19
NUSEX	0.5	0.99 ± 0.29

overhead (zenith angle of about 0^0) was reported as 1.3 ± 0.4. Thus, the high energy muon neutrinos coming from large distances (zenith angle greater than 90^0) evidenced large depletion, while high energy muon neutrinos coming from overhead showed no such loss. The ν_μ and ν_e distributions are shown in Fig. 3.6, and the ratio of these two distributions is shown in Fig. 3.7. The probability of ν_μ disappearance is given by equation 3.2, which depends upon L, the distance from the neutrino's origin in km and E_ν, the neutrino energy in GeV. The fact that little disappearance effect is observed for a zenith angle of $\sim 0^0$ means that

$$\sin^2(1.27\Delta m^2 L/E_\nu) \sim 0$$

or

$$L/E_\nu << 1/1.27\Delta m^2.$$

With $L \sim 30$ and $E_\nu \sim 6$, one finds that $\Delta m^2 << 0.1$. This small value for Δm^2 has greatly influenced a number of subsequent proposals using large detectors at hundreds of kilometers from the neutrino source to investigate the phenomena associated with the atmospheric observations.

The significance of the reported dependence is not large, and the observed zenith angle dependence reported by Kamiokande has not been proven. A publication from the IMB collaboration[13] reports no such dependence. The Super Kamiokande preliminary results are confusing at present. As shown in Figs. 3.8 and 3.9, the zenith angle dependence favors a value of $\Delta m^2 \sim 10^{-2} - 10^{-3}$ eV^2; however, the overall ratio-of-ratios is the same at low and high energy and favors a higher value of $\Delta m^2 > 10^{-2}$ eV^2. Averaged over the neutrino energy, $< \sin^2(1.27\Delta m^2 L/E_\nu) > \sim 0.5$. If the zenith angle distribution were

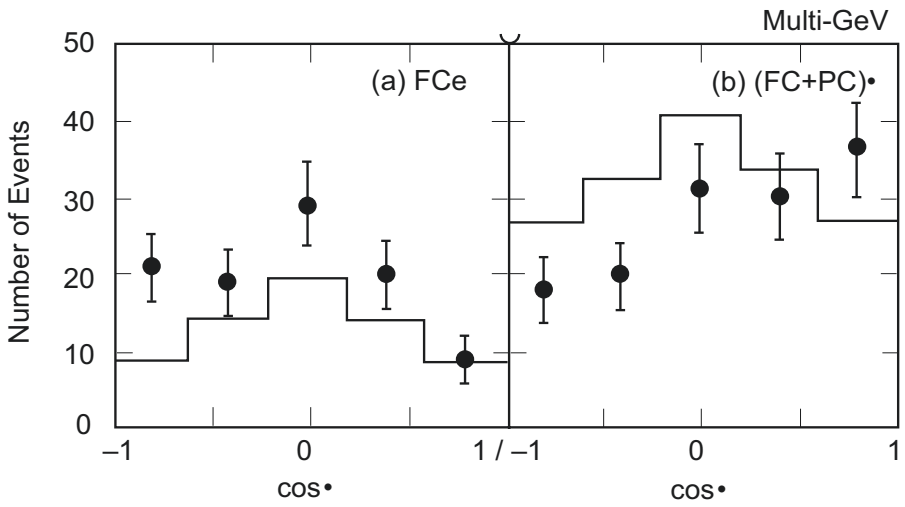

Figure 3.6: Zenith-angle distributions from the Kamiokande experiment for (a) the electron-like events and (b) the muon-like events. The circles with error bars show the data and the histogram the MC simulation (without oscillations).

flat, then

$$L/E_\nu > \pi/4(1.27\Delta m^2) = 0.62/\Delta m^2$$

which leads to $\Delta m^2 > 0.15$ eV^2. This value of Δm^2 is compatible with the LSND observation and would imply that there may be a common value of Δm^2 for ν_μ disappearance and for $\nu_\mu \to \nu_e$ oscillations (see section 3.5).

In this proposal we assume that the evidence for a discrepancy in the ratio of ν_μ events to ν_e events over that expected is significant enough to receive serious attention. However, we also assume that the value of Δm^2 that is deduced from the Kamiokande and Super Kamiokande zenith angle distribution may be taken with caution. The atmospheric neutrino problem makes the ν_μ disappearance measurement an important part of the BooNE proposal.

3.5 Theoretical Interpretation of the Data

It is difficult to make a fit to the experimental evidence described above with the general form given by Eq. 3.1. Therefore, simplifications must be made, resulting in various models with different assumptions. For example, the "max-

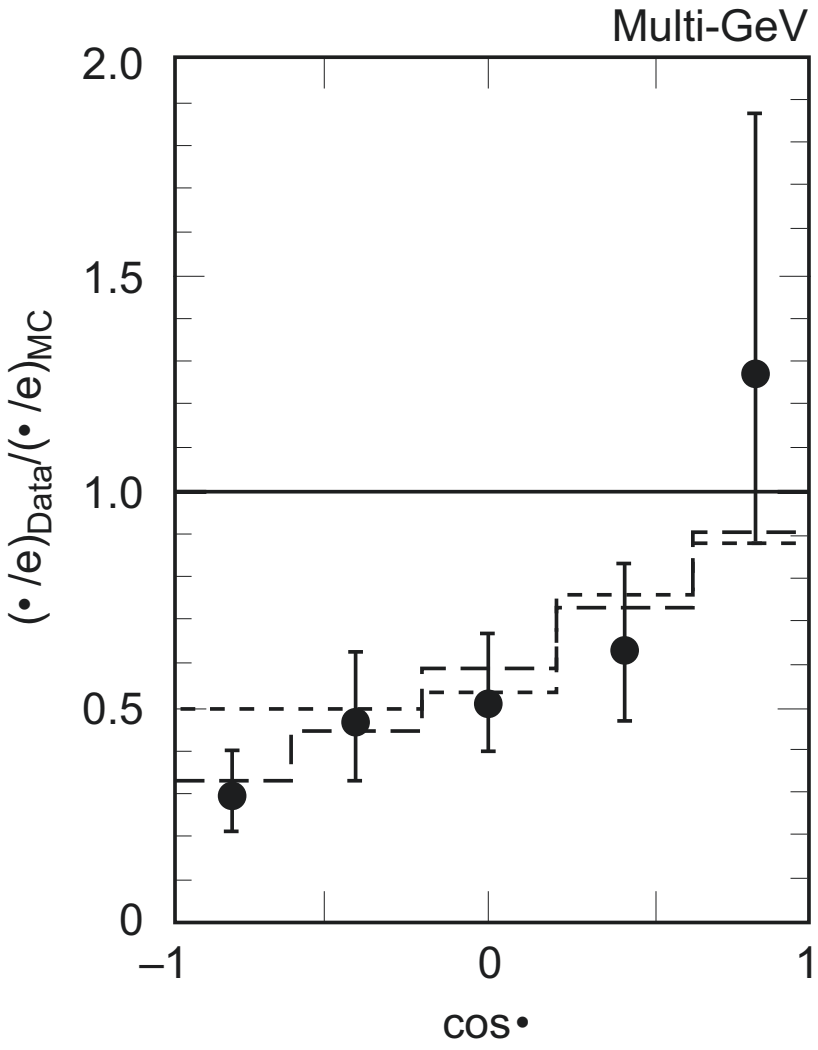

Figure 3.7: Zenith angle distribution of $(\mu/e)_{data}/(\mu/e)_{MC}$ from the Kamiokande experiment. The circles with error bars show the data. Also shown are the expectations from the MC simulations with neutrino oscillations for parameter sets $(\Delta m^2, \sin^2 2\theta)$ corresponding to the best-fit values to the multi-GeV data for $\nu_\mu \to \nu_e$ ($(1.8 \times 10^{-2}$ eV^2, 1.0), dashes) and $\nu_\mu \to \nu_\tau$ ($(1.6 \times 10^{-2}$ eV^2, 1.0), dots) oscillations.

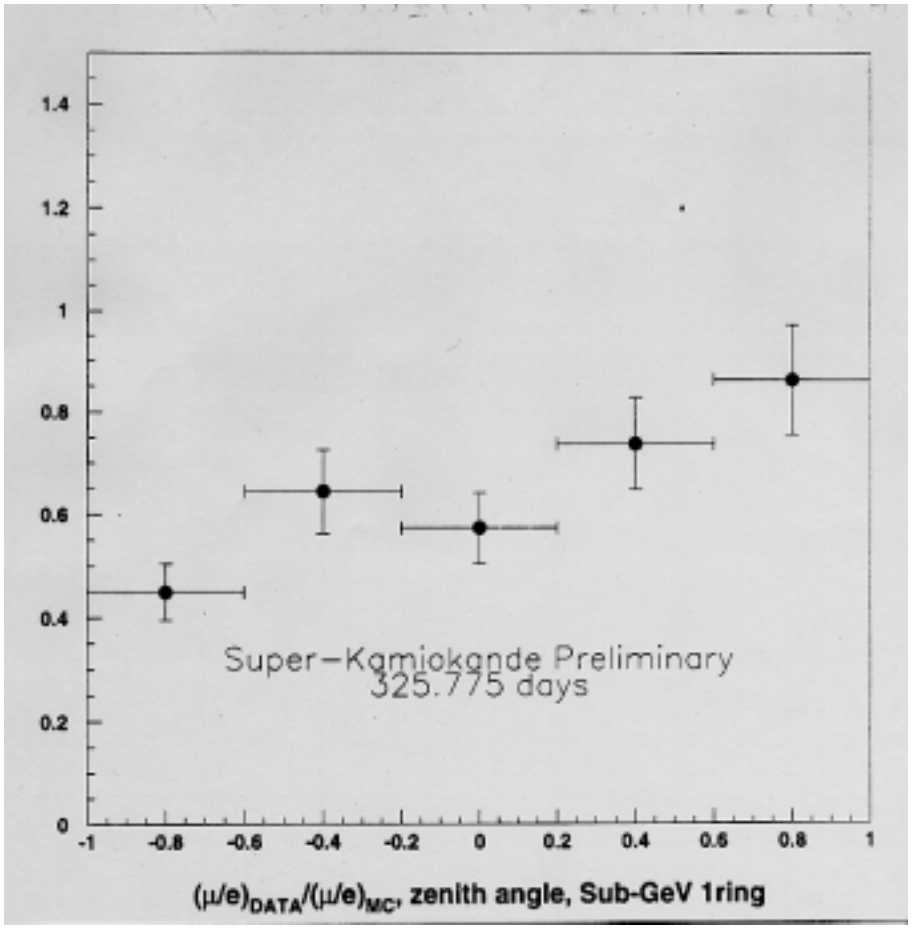

Figure 3.8: The Super Kamiokande preliminary zenith angle distribution for the sub-GeV contained events.

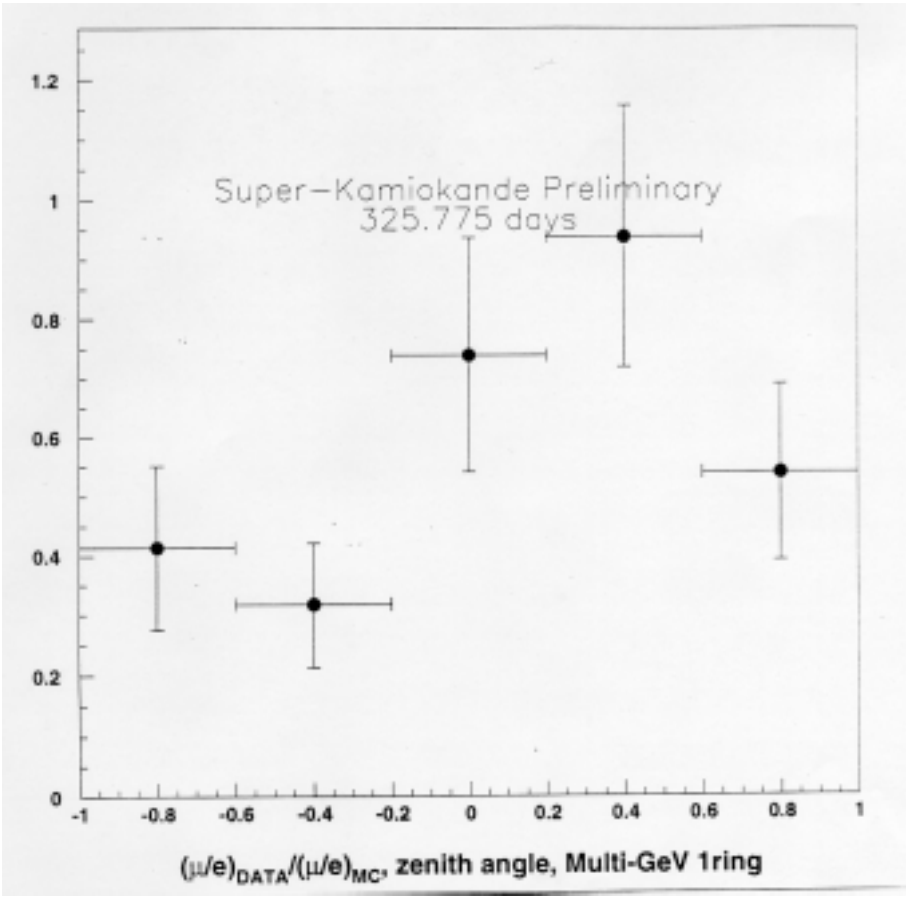

Figure 3.9: The Super Kamiokande preliminary zenith angle distribution for the multi-GeV contained events.

imal mixing" model[36] has a mixing matrix given by

$$U_{ij} = \frac{1}{\sqrt{3}} \begin{pmatrix} \omega_1 & \omega_2 & \omega_3 \\ \omega_1 & \omega_2 & \omega_3 \\ \omega_1 & \omega_2 & \omega_3 \end{pmatrix} \quad \text{where} \quad \omega_i = \begin{pmatrix} Complex\ Cube \\ Roots\ of\ Unity \end{pmatrix}$$

With $\Delta m^2_{12} < 10^{-11}\text{eV}^2$ and $\Delta m^2_{23} \approx 10^{-2}\text{eV}^2$, this model can accommodate the solar, atmospheric and reactor measurements but not the LSND signal.

Various models with two of the masses being "almost degenerate" can produce interesting oscillation patterns. In these models, the mixing matrix has large mixing between the degenerate partners and would be given approximately by

$$|U_{\alpha i}| = \begin{pmatrix} 0.99 & 0.03 & 0.03 \\ 0.03 & 0.71 & 0.71 \\ 0.03 & 0.71 & 0.71 \end{pmatrix}$$

An example of such a model is one with $m_1 \approx m_2 \ll m_3$ which leads to two Δm^2 scales given by a small Δm^2_{12} and a larger $\Delta m^2_{13} \approx \Delta m^2_{23}$. In this model, each oscillation channel ($\nu_\alpha \to \nu_\beta$) can be treated using the two-generation formalism with $\sin^2 2\theta \approx 4\,|U_{\alpha\,3}|^2\,|U_{\beta\,3}|^2$and the appropriate Δm^2. With effectively only two mass scales, it would seem hard to explain the three Δm^2 scales associated with solar ($\Delta m^2 \approx 10^{-5}$ eV^2), atmospheric ($\Delta m^2 \approx 10^{-2}$ eV^2), and LSND ($\Delta m^2 \approx 10^{-1}$ eV^2) experiments. Cardall and Fuller[19] have suggested that the atmospheric and LSND Δm^2 values could be similar if one discounts the zenith angle dependence. The common value would be in the range $0.1 < \Delta m^2_{LSND,\,atmos} < 0.5$ eV^2. The solar oscillation signal is accommodated by having $\Delta m^2_{12} \approx 10^{-5}$ eV^2. With the above mixing matrix and mass hierarchy, the solar, atmospheric and LSND data can all be explained by oscillations through the various mass eigenstates.

LSND:	ν_μ	$\to$	$\begin{pmatrix} \nu_1 \\ \nu_3 \end{pmatrix}$	or $\begin{pmatrix} \nu_2 \\ \nu_3 \end{pmatrix}$	$\to$	ν_e	$\Delta m^2 \approx 0.1 - 0.5$ eV^2 $\sin^2 2\theta \approx 5 \times 10^{-3}$
Atmospheric:	ν_μ	$\to$	$\begin{pmatrix} \nu_2 \\ \nu_3 \end{pmatrix}$		$\to$	ν_τ	$\Delta m^2 \approx 0.1 - 0.5$ eV^2 $\sin^2 2\theta \approx 1$
Solar:	ν_e	$\to$	$\begin{pmatrix} \nu_1 \\ \nu_2 \end{pmatrix}$		$\to$	ν_μ	$\Delta m^2 \approx 10^{-5}$ eV^2 $\sin^2 2\theta \approx 3 \times 10^{-3}$

The MiniBooNE experiment has the sensitivity to test for both $\nu_\mu \to \nu_e$ and $\nu_\mu \to \nu_\tau$ oscillations in the $\Delta m^2 = 0.1 - 0.5$ eV^2 mass region at the above mixing levels and, thus, offers an opportunity to explore this possible inclusive scenario.

3.6 MiniBooNE and Future Experiments

MiniBooNE will address the LSND result and the atmospheric neutrino deficit questions. Two other approved accelerator-based experiments are aimed at addressing these results; however, neither are likely to have definitive results within the next five years. These experiments are KARMEN/KARMEN2 and MINOS.

The KARMEN experiment[2] is of similar design to LSND. It has a total mass of 56 tons and is located about 17.5 m from the 200 μA proton source, compared to the 167 ton mass of LSND, which is located about 30 m from the 1000 μA LAMPF source. Fig. 3.10a shows the number of excess events as a function of Δm^2 that KARMEN has observed after 5 years of data taking, where the shaded band is the $\pm 1\sigma$ allowed region. Also shown in the figure is the expected number of events due to the LSND central value. Fig. 3.10b gives the 90% confidence level limit (KARMEN1) for neutrino oscillations as a function of Δm^2 and $\sin^2 2\theta$ [6]. As shown in Fig. 3.10a, KARMEN observes a one sigma excess of events that is consistent with the LSND signal at low Δm^2 ($\Delta m^2 < 2$ eV^2). The KARMEN2 experiment has completed an important upgrade of their veto detector shielding which has reduced the cosmic ray background by a factor of $\sim$ 40 from previous running. However, despite greatly reducing their chief background with the new veto shield, KARMEN2's event sample will be less than the LSND sample due to the accelerator intensity and small detector size. As a result, KARMEN2 may be able to address the LSND signal over the $\Delta m^2 > 1$ eV^2 range after 2-3 years of data taking (as shown by the KARMEN2 sensitivity in Fig. 3.10), but the signal will be less significant than the LSND signal. MiniBooNE will cover the full LSND range, particularly the $\Delta m^2 < 1$ eV^2 region with an expectation of $\sim 8\sigma$ for a signal. Furthermore, because KARMEN2's neutrino source and experimental signal are so similar to that of LSND, KARMEN2 will not provide the systematic check required. One wants to verify the LSND oscillation signal with high statistics in a new energy region where the backgrounds and systematic effects are completely different.

The MINOS experiment, scheduled to begin taking data in 2003, has sensitivity over only part of the LSND signal range. For this experiment, $\nu_\mu \to \nu_\tau$ oscillations can be detected through three "disappearance" measurements: the absolute CC rates, the NC/CC ratio, and the E_ν distribution in the two detectors. With two years of data, the experiment will cover the $\nu_\mu \to \nu_\tau$ region with $\sin^2 2\theta > 2 \times 10^{-2}$ and $\Delta m^2 > 10^{-2} - 10^{-3}$ eV^2 as shown in Fig. 2.4. MINOS was specifically designed to address the atmospheric neutrino deficit and has limited sensitivity for $\sin^2 2\theta < 0.02$. If the mixing is above about 0.1,

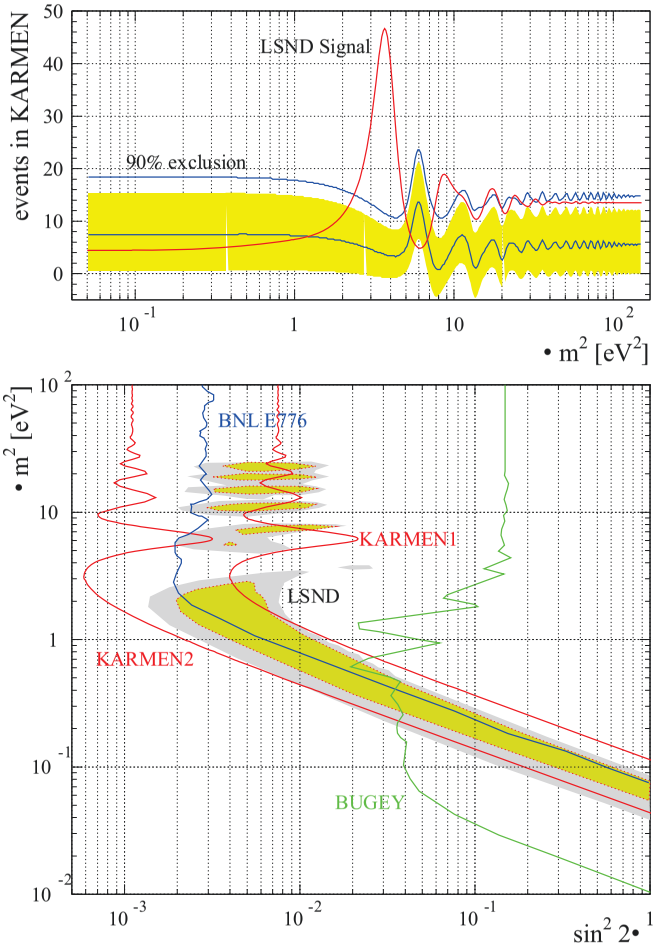

Figure 3.10: (a) The number of excess events as a function of Δm^2 that KARMEN has observed after 5 years of data taking. (b) The 90% confidence level limit for neutrino oscillations as a function of Δm^2 and $\sin^2 2\theta$ that has been obtained so far by KARMEN (KARMEN1) and that will be obtained by KARMEN after three years of data taking with the upgraded veto system (KARMEN2).

MINOS will be able to determine the $\nu_\mu \to \nu_\tau$ oscillation parameters from the E_ν dependence of the observed effects.

We base our understanding of the MINOS $\nu_\mu \to \nu_e$ search capabilities on those presented in the P875 (MINOS) proposal.[8] For $\nu_\mu \to \nu_e$ oscillations in the LSND signal region, the MINOS experiment will see an effect if $\sin^2 2\theta 0.01$ but will only be able to determine oscillation parameters if $\sin^2 2\theta 0.1$. The $\sin^2 2\theta > 0.05$ region of the LSND signal has already been ruled out by the Bugey and CHOOZ reactor experiments,[16,17] which means that the MINOS experiment will not have sensitivity to address the LSND signal region in any detail. This collaboration is in the process of developing new particle identification techniques which may increase the $\sin^2 2\theta$ reach.[7] The details of this method are, as yet, not publicly available. Preliminary expectations which were presented during summer, 1997,[37] must adjusted to reflect the final detector design, adopted in September, 1997,[38] which has significantly less segmentation and tonnage than their older designs. At this point, we believe that MINOS will not be able to fully cover the LSND region at small $\sin^2 2\theta$. It is unlikely that MINOS will present definitive results on either the LSND or atmospheric neutrino problem before 2005.

A Letter of Intent has been submitted to CERN [9] to search for $\nu_\mu \to \nu_e$ oscillations in the LSND Δm^2 region. The experiment would restore the neutrino line from the CERN-PS and would consist of three detector modules consisting of fine grained tracking calorimeters followed by electron and muon catchers. One module would be located in the "near" location at a distance of 128 m, while two modules would be located in the "far" location at a distance of 850 m. Each module would have a mass of 128 t. The experiment claims a sensitivity that is slightly worse than MiniBooNE and that would reach down to $\sin^2 2\theta < 10^{-3}$ at $\Delta m^2 = 2$ eV^2 and to $\Delta m^2 = 0.03$ eV^2 at $\sin^2 2\theta = 1$.

A second Letter of Intent for an experiment designed to address the LSND signal has also been submitted to CERN.[10] This experiment proposes to use the SPS to produce a neutrino beam which emerges from the Jura mountains at 17km from the source. This LOI is based on a 1981 proposal for the Jura Oscillation Experiment[39] and on a 1997 Letter of Intent to CERN for a Jura-based medium baseline experiment.[40] This LOI does not provide details on the beam design and flux expectations. Several detector technologies are under consideration, including a fine-grained calorimeter or one Icarus module (liquid argon TPC) followed by the CDHS muon spectrometer. Expected sensitivities are not yet determined, but may be expected to be comparable to MiniBooNE.

Chapter 4

The BooNE Beam

The neutrino beam will be fed by the 8 GeV proton Booster operating at a rate of 5 Hz with 5×10^{12}*ppp. Extraction uses EPB dipoles and permanent quadrupoles. Focusing is provided by a horn system based on the BNL design.*

This chapter provides a description of the beam design and expectations. Because the beam will service both MiniBooNE and future phases of the experiment, it is referred to as the BooNE beamline. The primary beam will be extracted from the Booster at MI10 and transported to the BooNE Target Hall, as shown in figure 4.1. Decays of secondary pions and kaons in the decay region of the Target Hall produce the neutrinos used by this experiment. The first section of this chapter addresses issues related to operating the FNAL Booster at MiniBooNE intensities. This is followed by an initial design for the primary proton beam extraction and transport. The third section addresses the secondary beam design, providing technical details on the horn. Civil construction issues for the primary and secondary beams are considered in the second and third sections of this chapter. The Project Design Report written by FNAL FESS is available upon request and the figures detailing the civil design are included as Appendix B. In the final section of this chapter, the expected neutrino fluxes are presented and the systematic error is considered.

Several criteria were used to design the neutrino beam. The first is to maximize the low energy flux, which provides sensitivity to the appropriate Δm^2 and $\sin^2 2\theta$ regions to study the LSND signal, while maintaining the detector on the Fermilab site. The second criteria is to maintain a small ($< 3 \times 10^{-3}$) ratio of ν_e ($\bar{\nu}_e$) to ν_μ ($\bar{\nu}_\mu$) while still obtaining high statistics. The ν_e beam background results mainly from muon decays, as kaon production is

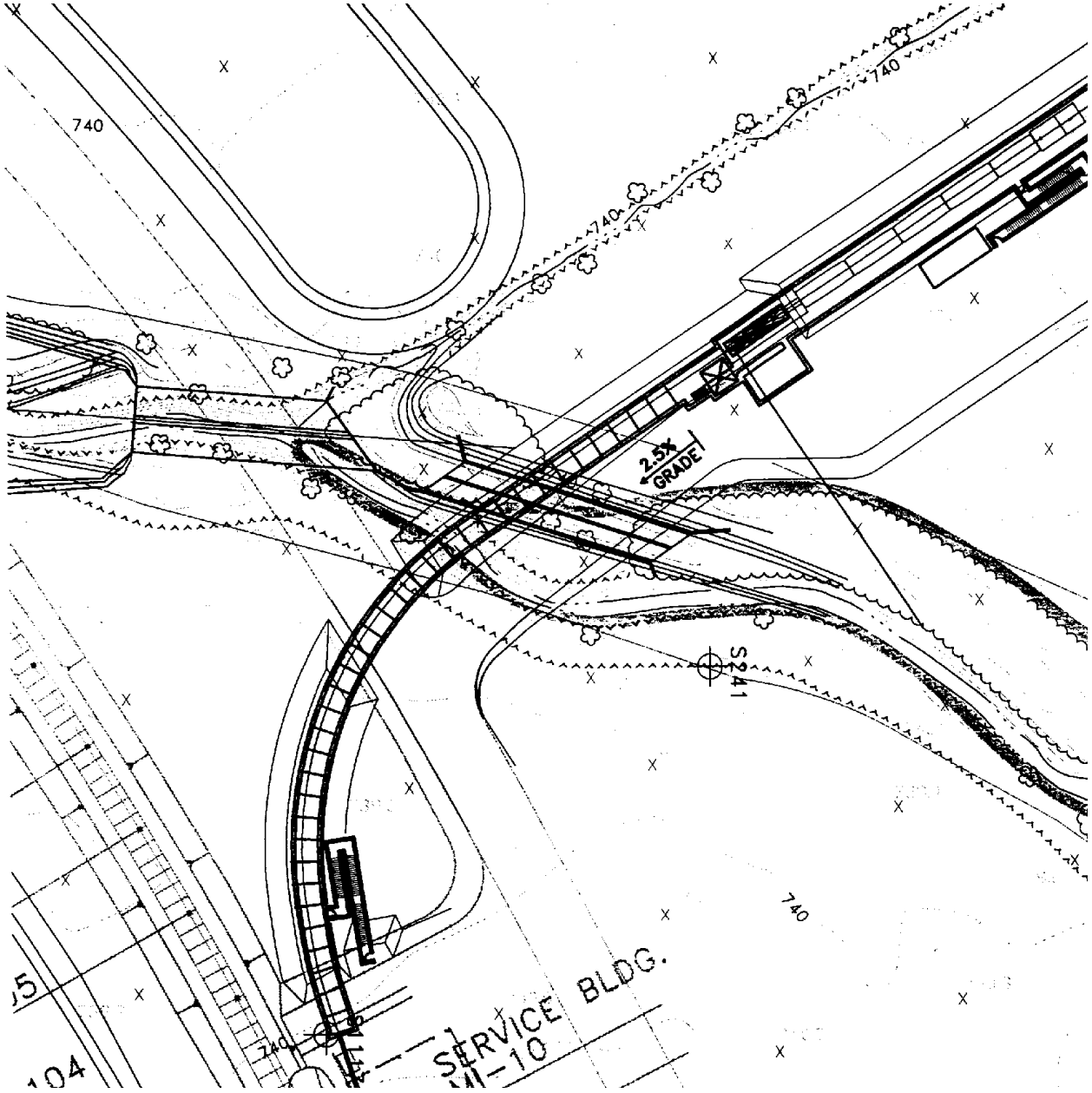

Figure 4.1: Layout of the BooNE beam line. FNAL Project North is to the right.

suppressed by the low proton beam energy. The solution is a low energy beam made from 8 GeV proton interactions in a target, producing pions and kaons which are focused using a horn system. For this proposal we present a beam using focusing elements of the same design as the horn at Brookhaven,[41] which we refer to as the "BNL" horn below.

4.1 Running the Booster at MiniBooNE Intensities

We are faced with two separate issues when considering running the Booster at high intensities. The first is the set of operational questions related to MiniBooNE running. The second is radiation safety. These issues are addressed below using the assumption that MiniBooNE, NuMI and Collider Running must be accommodated simultaneously. Although MiniBooNE plans to begin running before the NuMI program starts, in the future there is likely to be running with all three programs, and therefore we must design for this scenario. In the text below, "MiniBooNE intensity" refers to the intensity required to operate all three programs simultaneously. The Booster must operate at ~7.5 Hz to supply these three programs with a total beam delivery of 1.4E17 protons/hour.

4.1.1 Booster Operation

It is assumed that MiniBooNE will use ten Booster cycles under a typical NuMI Main Injector ramp that is 1.9 sec long, or eight Booster pulses under a stacking Main Injector ramp which is 1.467 sec long for an average running rate of 5 Hz. The ten or eight Booster pulses used can be consecutive or can be separated by a null Booster cycle (66.66 msec). The first case seems preferable since the second case requires a modification of the Main Injector ramps and can also lead to power supply regulation problems. A switch magnet needs to be used in order to bend the Booster beam in the MiniBooNE beam line. It is assumed that an existing magnet can be used, so the additional cost of the power supply is estimated to be around $50K.

The Booster can run at an average rate of 7-7.5 Hz with no additional modifications (except maybe two new septum magnets). However, in the future, if 15 Hz continuous operation is desired, additional modifications, totaling $728K, are needed for major power supply and magnet modifications in order for the Booster to operate reliably. Starting from upstream:

- the chopper kicker power supply needs to be modified. Estimated cost $15K.

- The ORBMP (orbit bump) power supply is currently rated for operation at 7.5 Hz so it needs to be replaced. Estimated cost $400K.

- The two septum magnet power supplies are also rated at 7.5 Hz and need to be replaced. We assume that for MiniBooNE operations the long 13 extraction point does not need to get upgraded in order to run at 15 Hz so only one septum supply needs to be replaced. Estimated cost per supply is $100K.

- The three septum magnets do not have enough cooling for operation at 15 Hz so they need to be replaced by new magnets. For MiniBooNE operation two new magnets will need to be built (one operational magnet and one spare) with an estimated cost of $80K per magnet. These magnets will also be required for NuMI operation.

- The Booster radio-frequency system (RF) was built to run CW. However there are some power issues that need to be resolved.

- It has been observed that there is not enough yard power available on the west side to run the bias supplies of the 10 RF stations connected to it. It is estimated that the main breaker on the west side needs to be replaced with a new one that has a higher current rating. Estimated cost $50K.

- About half of the individual station breakers also need to be upgraded to a higher current rating. Estimated cost $3K ($300 per breaker).

- The bias supply transformer cooling at the higher rep rates required needs to be checked.

- The RF cavities may also require additional cooling, which is available, in order to run at 15 Hz.

- Most of the power supplies required would probably be redesigned versions of the existing supplies, and the turnaround time would be 1-1.5 years per supply. The septum magnets need to have a design for additional water cooling and can be built in about a year.

The Booster is expected to be highly reliable based on past operational experience. From a study of the recent collider running (2/94-8/95) the Booster downtime (excluding scheduled shutdown) was 1.5% and the Linac downtime was 1.8%. The main source of the Booster downtime was the RF, largely due to water leaks. The typical Booster duty cycle during the collider run was 9%.

The neutron therapy facility is presently requesting 100% of the linac beam for 6 hours per day and 4 days per week, which is 14% of a calendar year. Thus it is feasible to assume that MiniBooNE can run for 2×10^7 s or 63% of the time in one calendar year.

4.1.2 Booster Radiation

Beam losses in the Booster with respect to the radiation shielding of personnel as well as irradiation that impacts the groundwater are being addressed. The losses can be classified into three types–(a) extraction at the region known as Long 3, (b) global (around the ring), and (c) localized (presently at Short 3).

Radiation measurements have been made and will continue for the next few months to characterize the losses. Preliminary plans at this point indicate that the above ground radiation due to extraction losses for MiniBooNE intensities can be reduced to acceptable levels. This is accomplished by adding steel shielding inside the tunnel, adding steel shielding above the tunnel (civil construction), and by putting a notch in the beam. The purpose of the notch is to prevent losses while the septum current is ramped up.

Global losses will be dealt with by using several interlocked detectors around the ring. Their placement will depend on the results of studies in conjunction with moving localized losses to those places in the tunnel where it's easiest to add internal steel - places of minimal equipment or high ceilings.

The groundwater issue is more difficult because added material is needed on the sides of the tunnel as well as underneath it. Last month, three boreholes were taken in the Booster floor at MP01 to determine the amount of activity in the soil. Results will be available in early 1998.

Radiation Shielding and Operational Solutions

The neutrino beam for the MiniBooNE experiment will be produced using 8 GeV protons from the Fermilab Booster at a rate of 5 Hz. The Booster beam is also used in the Main Injector for Tevatron collider operation, and fixed target experiments. The Booster is capable of operating at 15 Hz and will operate at about 7.5 Hz for the combined operations of pbar production, NuMI and MiniBooNE with a total beam delivery of 1.4E17 protons/hour.

The Booster accelerator is in a horizontal plane at an elevation of 726.5 ft and its enclosure ceiling is at 730.5 ft. The floor of the Booster gallery (along with the West and East Booster Towers) and that of the surrounding areas are at an elevation of 744 ft with a vertical soil-equivalent shielding of about 13.5 ft. Since the Booster gallery is located about 11 ft interior, but, off

from the vertical plane of the Booster, the soil equivalent shielding between the walk-way in the Booster gallery and the Booster beam is over 18.5 ft.

In the past, typical Booster operation was at 0.5 Hz with a total proton delivery of up to 9E15 protons/hour at 8 GeV. Beam is lost during the beginning of the acceleration cycle, at transition energy and at extraction. The beam-loss points at 8 GeV in the Booster were very localized, namely at the extraction region MP01 IN "Long-13", "Short-2" and at the "Short-3" sections. The radiation level in the gallery was kept below regulatory limits by using a combination of added steel over the Booster accelerator magnets and interlock detectors.

During the MiniBooNE era, the 8 GeV beam extraction to the MI-8 beam line will take place at MP02 in "Long-3". This extraction region is near the West Booster Tower building. The soil equivalent shielding under this building is 15.25 ft (including a 3.5 ft thick heavy concrete). The normal operating beam loss at the extraction location is estimated to be about 2%. This loss may pose a radiation problem in the West Booster Tower and in the ground water.

The extracted Booster beam will be transported via the MI-8 beamline and will be bent towards the MiniBooNE Target Hall at about the MI-851 location. For a short distance the beam will be transported using a buried beam pipe under the MI-10 service building. The MI-8 beamline enclosure is built with a total soil equivalent shielding of 24.5 ft and is capable of holding up to 26 ft of soil equivalent shielding. There are no anticipated problems seen regarding beam losses in the 8 GeV transport line.

Booster radiation shielding studies conducted at the extraction region showed that with the existing shielding one expects radiation dose of about 200 mrem/hr with the MiniBooNE operating conditions. But the allowed radiation dose (Fermilab Radiological Control Manual, FRCM) is 0.050 mrem/hr in unlimited occupancy region and less than 5 mrem/hr in the minimum occupancy region. To eliminate radiation problems in the West Booster Tower building different radiation shielding scenarios have been investigated by the Beams Division using the Monte Carlo code CASIM. These studies show that one needs about 5.5 ft of steel shielding to attain the unlimited occupancy limit. The Fermilab Beams Division has undertaken detailed accelerator studies and is looking into the possibility of inserting about 4.5 ft of steel under the West Booster Tower above the enclosure ceiling and adding the remaining steel over the MP02 extraction septum to comply with the FRCM requirements.

To estimate ground water contamination, Fermilab uses a specific model for groundwater mobility, referred to as the Concentration model. To comply with DOE and EPA regulations may require an addition of about 2.25 ft of steel under the Booster Beam extraction region or to add a notch in the Booster

beam to completely eliminate any beam loss during extraction for MiniBooNE. Concentration model assumes that the produced 3H nuclei migrate downwards at a rate of about 0.5ft /year. Recent soil samples extracted under MP01 area indicated the migration rate assumed in the concentration model is an over estimation. In view of these results, further investigations of different shielding options are underway.

At other locations of the Booster, the Beams Division shielding criteria[a] requires 25.5 ft of earth shielding for unlimited occupancy without interlock detectors and 14.5 ft with interlock detectors. Since adding passive shielding to meet FRCM requirements may be prohibitively expensive, the Beams Division use a combination of interlocked detectors around the Booster gallery to control the beam losses.

We conclude that the radiation shielding of the Booster and the MI-8 Beam line does not seem to be a major problem for MiniBooNE operation, provided that sufficient steel shielding can be added at the major loss points in the Booster. Further work will be required to fully understand the groundwater shielding requirements, but work done to the present would indicate that the problem can be solved by conventional means. The resolution of these issue is crucial for MiniBooNE to nearly the same degree as it is for the already approved Fermilab fixed target program.

The BooNE collaboration will continue to collaborate with the FNAL Booster group to resolve the Booster radiation issues. We believe that we can contribute in a number of ways, including preparing applications programs and helping to improve diagnostics.

4.2 The 8 GeV BooNE Beamline

This section describes the 8 GeV proton beam transport system from the Main Injector 8 GeV Beamline to the BooNE target station.

4.2.1 Transport Design

The BooNE 8 GeV beamline is designed to separate from the Main Injector 8 GeV Booster to Main Injector transfer line starting at station (quad) 851. The heading (measured ccw from site east) of the proton beam into Q851 is $-150.29°$. The heading of the ray from the target to the detector(s) is $-245.68°$ and the total required bend is $-150.29°$. A pulsed magnet will bend the beam by -0.045 r to deflect it into the BooNE beamline. Subsequently, the bend per

[a] Dugan's criteria for accidental beam loss or a continuous beam loss for one hour at a point in the Booster accelerator.

dipole will be 0.081 r (4.6°), assuming that EPB's or other 10′ (3 m) dipoles are used throughout. One pulsed dipole and 20 dipoles running dc are required. Powered and permanent magnet quadrupoles are used to provide focusing.

The first element is a switch magnet which is off for Booster to Main Injector transfers and is energized to direct the beam to the MiniBooNE experiment. Two additional dipoles are needed in the MI-10 enclosure to bend the extracted beam away from the Main Injector sufficiently quickly.

The beam passes out of the Main Injector enclosure near location 101 and travels under the MI-10 service building. To minimize the impact on the service building, it is proposed to use directional drilling techniques to install a 18″ diameter carrier pipe under MI-10 from the exit from the Main Injector enclosure to the beginning of the FODO arc, a distance of approximately 40 m. This pipe is a drift space and contains no beamline elements. Six powered quadrupoles, three at each end, are required to define the optics through the long drift region.

Beyond the drift, the beamline comprises a series of FODO cells, both bending and straight. The first 3 FODO cells each contain 6 EPB dipoles which direct the beam toward the detector.

The final few cells constitute a FODO channel and matching section to transport the beam to the horn and target and to define the final focus on the target. The details have not been worked out at this writing.

4.2.2 Magnet selection

We propose to use EPB dipoles through out the BooNE beamline. The maximum bend, ≈ 0.08 r, is defined by both the tolerable sagitta through the magnet and the desire to be able to operate this beamline at energies up to 16 GeV when a Booster upgrade is realized. A secondary benefit is that the power required for 8 GeV operation is relatively modest.

We propose to use SQA quadrupoles, mostly individually powered, to match the beam from the 8 GeV line into the long drift and from the drift to the arc, and to control the beam spot at the target.

The arc is a regular structure bracketed by matching sections. It is therefore very cost-effective to use permanent magnet quadrupoles similar to those used in the 8 GeV line and proposed for the Recycler ring in the arc.

4.2.3 The switch magnet

The only unusual magnet required for the beamline is the switch magnet located near Q851. It must be able to select ≤ 10 Booster batches from the ≈ 30 available in each Main Injector cycle. This suggests that a resonant power

supply operating at 15 Hz is appropriate. The parameters of EPB magnet suggest that it may a suitable candidate to adapt to this application [43].

4.2.4 Layout and optics

The beamline layout is shown in Fig. 4.2. The BooNE beamline starts with the switch magnet immediately downstream of 8 GeV line station 851 and ends near the entrance to the target hall.

The beamline optical functions β and η are shown in Fig. 4.3. The beam envelope is shown in Fig. 4.4. The envelope is calculated assuming invariant emittance $\epsilon_N = 40\pi$ mm·mr for the the beam from the Booster. This is the conservative estimate used for Main Injector design work. It is more likely that an emittance of about 20π mm·mr or less will be realized and the beam size will be smaller by a factor of more than $\sqrt{2}$.

4.2.5 Primary Beam Monitoring

The primary beam position, profile, and intensity will be monitored to maintain the highest possible flux, to constrain beam simulations, and to prevent losses. The high intensity of the Booster beam precludes the continuous use of standard beam line SWICs and SEMs. BPMs will be used to measure beam position, and a beam current toroid will measure beam intensity (BPMs can also measure intensity, but the toroid is necessary for an initial calibration). Approximately ten BPMs of one plane only will be placed at various positions in the beam line for beam tuning. Two x,y BPM pairs are needed, one close to the target and one downstream of the last magnet to measure the targeting angle and position.

We are considering using several low precision retractable wire SEMs or multiwires located at strategic places in the beam line to check beam shapes. This will be especially useful for commissioning.

There will also be approximately eleven loss monitors along the beam line to monitor beam losses. The loss monitors will trip the beam when a prescribed threshold is reached to prevent equipment damage. Since loss monitors are not used on each device and it is possible to lose the beam within one magnet, there needs to be a system to trip the permit if beam is detected at the upstream end of the beam line and not the downstream end. Otherwise, loss monitors must be placed to detect the beam wherever it can be lost. We will also install a beam halo monitor.

Two precision SEEDs (wire secondary emission monitors) or equivalent will be used to measure beam profiles and targeting angle. They will be retractable in order to keep radiation backgrounds low and they will be read

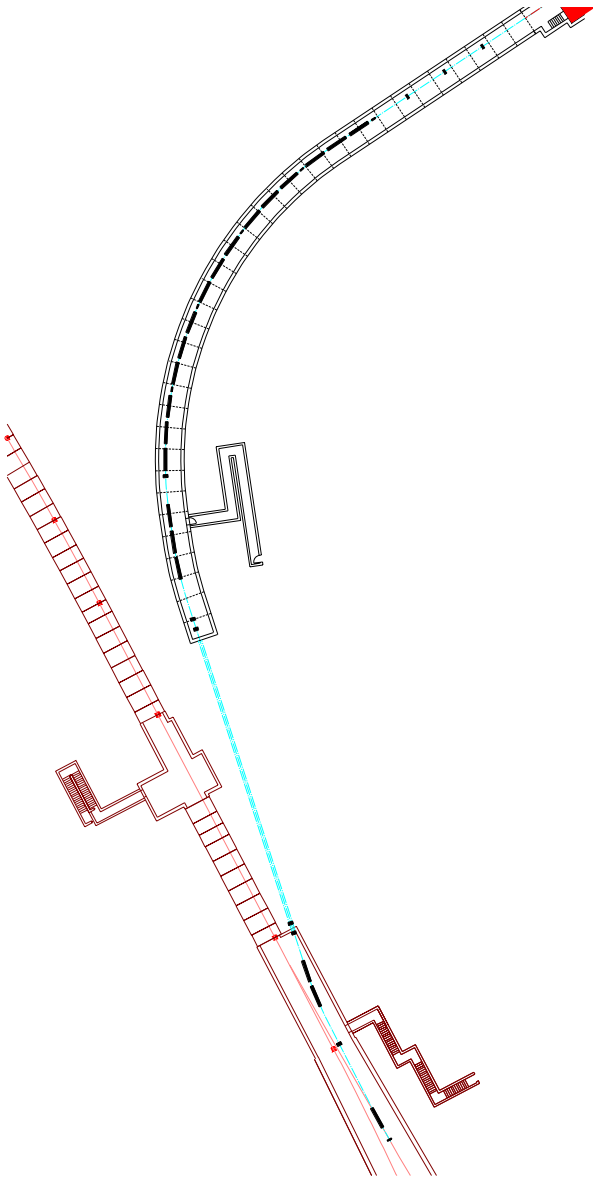

Figure 4.2: Layout of the BooNE beamline from the 8 GeV line station 851 to the target hall.

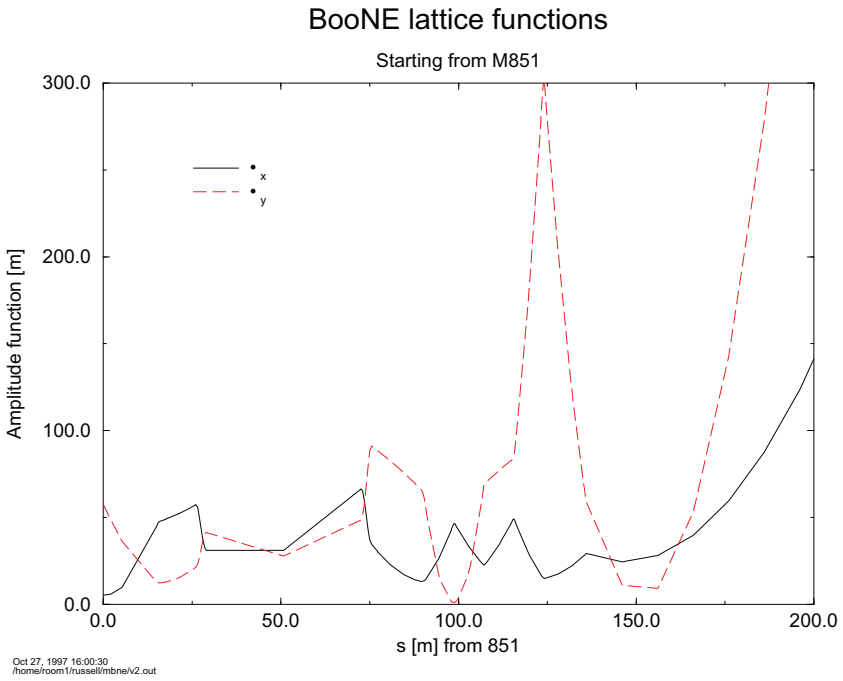

Figure 4.3: BooNE 8 GeV beamline optical functions β

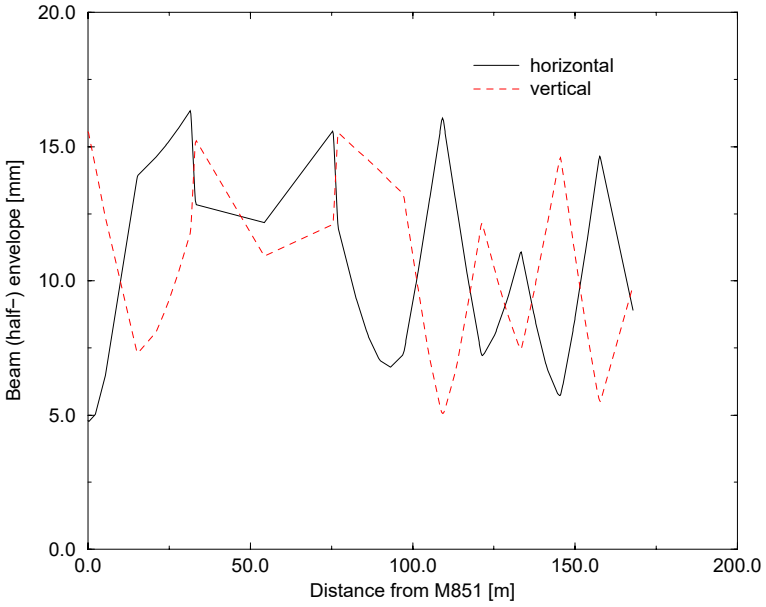

Figure 4.4: Beam envelope through the BooNE beamline for 40π mm·mr beam.

out using standard switchyard SWIC scanners. Experience at KTeV [44] and at CERN [45] has shown that secondary emission efficiency is reduced by 20-30% for integrated flux densities in excess of 10^{20} p/cm^2, which is sufficient for profile monitoring at BooNE.

Wire heating and shock were modeled[46] on the E815 SEEDs with 5×10^{12} ppp and 1.6 μs, 5 Hz Booster spill structure for a 1 cm FWHM and a 1 mm FWHM beam spot. Heating and shock criteria passed for the 1 cm beam, but tension loss due to heating exceeded criteria for the 1 mm beam. Current thinking is that the spot size on target will be about 1.5mm σ, so the model was recalculated. Peak temperature and tension loss was 200 °C and 40 g, respectively, which is acceptable provided that solder rather than epoxy is used to maintain tension. However, the thermal conductivity between the pads on the printed circuit board and the board itself is still uncertain. Also, the SEED will not be placed where the beam is smallest, which is at the target. We continue to investigate these issues.

The magnets and horn of the beam line will be controlled via Beams Division Accelerator Controls Department Internet Rack Monitors (IRMs). The BPMs, loss monitors, and standard SWIC scanners will also be read out via IRMs. The TeV clock and computer networking necessary for the IRMs will be present at MI10, the target service building, and the detector electronics room. There will be one IRM at each location.

The IRM installed in the detector electronics room will provide TeV clock decoding and a "beam present" signal for gating the detector. This IRM will also be the data server for the experiment's data acquisition of beam line information (BPMs, SEEDs, magnet currents, etc.). It will collect this information on a pulse by pulse basis from the other IRMs, time stamp each pulse with a Global Positioning System (GPS) derived time stamp, and send the data at some convenient rate to the experiment's data acquisition computer via the internet. The IRM collected data will be received via TCP/IP and stored by a separate process running on the main data acquisition computer at the MiniBooNE detector.

4.3 The Secondary Beam

The secondary beam is contained entirely within the Target Hall. The beam consists of three sections: the beam focusing system, a helium filled decay region, and the beam absorber. Collimator and radiation shielding is provided in the beam region. The focusing horns also have a power supply enclosure within the hall, and a Porta Kamp is located at the surface for small electronics and power supplies. Beam instrumentation is read out at the surface Porta

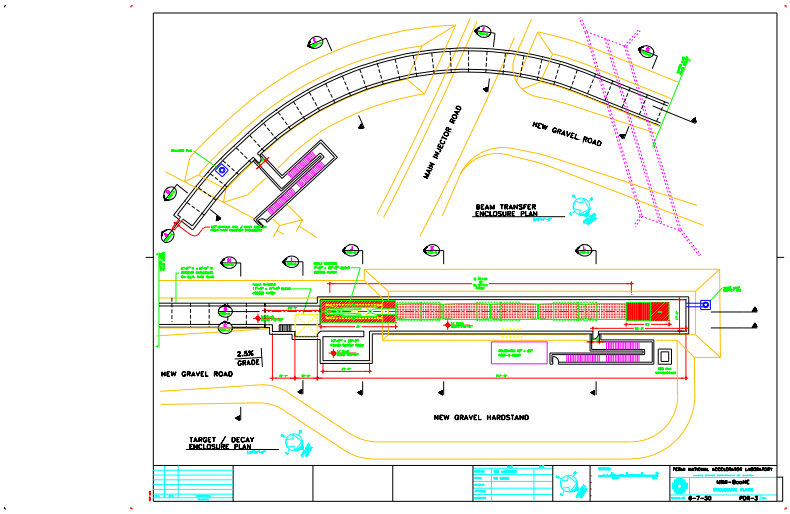

Figure 4.5: Design of the 8 GeV Line, Target Hall and Service Alcove and Porta Kamp

Kamp.

4.3.1 Target Hall Design

The BooNE Target Hall is designed to contain the three elements: the target-horn, the decay region, and the beam absorber. The hall contains the horn power supply and serves as a main access point for the beam enclosures. An associated service building (Porta Kamp) will house the dc supply for the horn, control system electronics, and personnel access electronics. Each of these has independent requirements, but the hall and service building are intended to integrate these functions and thereby minimize cost.

In Fig. 4.5 we show a plan view of the Target Hall with service alcove and Porta Kamp. The Hall is at beam elevation, with the roof covered by approximately 24 feet of overburden. The three main regions of the hall - the Target Stack, the decay region with helium bags, and the beam absorber - are delineated in the figure. The location of the horn power supply room is fixed by the need to place the pulsed supply as near as possible to the horns. Road access to this area, parking areas, and a hardstand for crane access will consist

of gravel and be accessible from the Main Injector road.

The Target Hall will have a containment system for groundwater. Consultation with environmental engineering firms has given us preliminary parameters for the system. Located approximately 10 feet below the floor and extending at a 45 degree angle up the sides and end of the hall, the containment will consist of two layers of plastic material. The layers will be separated by a fabric material, and additional fabric will lie on the top layer of plastic. Eighteen inches of either gravel or geotech will sit on the fabric and plastic barrier. The containment system will incline toward one end of the hall, where a drainage and monitoring pipe will be located. This is accepted practice for landfill design and will minimize groundwater shielding requirements within the Target Hall itself.

At present the final design of the horns is not complete. Their transverse size is the determining factor in the aperture of the Target Station end cap. A four foot diameter hole in this end cap along with a second steel collimator (also having a 4 ft diameter) about 9 meters further down the Decay Region gives a star density of about 1E-9 stars/cc on the inside of the tunnel walls. Because we have added containment to the enclosure, the design is satisfactory at this level using the Concentration Model. A factor of ten more would be required to achieve a satisfactory groundwater limit without the groundwater containment. Work will continue to see if additional collimator(s) will improve groundwater shielding. The four foot diameter limiting apertures may decrease as more GEANT studies are completed to fix the size and shape of the horns. In any event, it is clear that the groundwater containment system will satisfy requirements.

4.3.2 Target & Horn Region

Radiation shielding in this region requires a steel enclosure called a Target Stack. Within this enclosure, accessible from the top, is a slot that will house the target and horn system. The slot is filled with steel plates to provide shielding during operations. The entire assembly is accessible through a hatch located directly above the shield. The hatch is covered with concrete blocks during operations.

The utility connection to the horns is made from the top of the Target Pile. Access to the horns for assembly or repair is made by a 30 ton external mobile crane through the top of the hatch. Past experience at Fermilab indicates that this is the more cost efficient way to build this kind of structure. The utilities are supplied from the Service Alcove and Porta Kamp.

The target system is an integral part of the front horn assembly. It will

have its cooling water supplied through the face of the dump. These systems will be housed in the small area upstream of the Target Pile.

Secondary pions and kaons from a production target are focused by the series of two horns. A Brookhaven National Laboratory [41] horn design and target is used for the results presented in this proposal. However, the following modifications to the BNL design are being pursued to make it more appropriate for our application: (a) slightly increase the diameter of the inner conductor of Horn 1 for higher reliability, (b) possibly change the target from titanium to nickel to decrease the overall length of Horn 1 (titanium is assumed for the simulations in this proposal), (c) add water cooling to Horn 1 to accommodate the increased repetition rate, (d) add a collimator between the two horns to help mitigate the star density in the decay region that contributes to groundwater irradiation and (e) alter/simplify the conductor shapes to make fabrication less costly.

Horn Power Supply

The power supply proposed for powering the two series connected focusing horns for BooNE is of the direct coupled design. Energy is stored in a capacitor bank and switched via a parallel array of two HCT (high current thyristor) switches into the horn load. A parallel strip transmission line is used to connect the power supply to the focusing horns. The neutrino horns require a train of 250 kA pulses with a repetition period of 67 ms. An operating pulse width of 140 μs was chosen so that the power supply operating voltage is under 10 kV and within the realm of semi-conductor switching devices and planar transmission lines. They will be pulsed from 10 to 15 times at the 15 Hz rate in one second followed by a rest period of one second, repeating the sequence on a continuous basis. This results in a system load current of 4730 A(RMS).

Circuit Requirements

A LC discharge circuit will be used as shown in Fig. 4.6, which will achieve the peak current when the HCT switch releases stored energy from the capacitor bank into the horns via the stripline. The estimated circuit parameters are listed in Table 4.1.

Current and voltage waveforms of a typical cycle of power supply operation are shown in Fig. 4.7. The capacitor bank is initially charged to a positive voltage appropriate to 250 kA of output current. Upon command the stored energy is switched into the focusing horns that make up the load. After the discharge of energy into the horns the capacitor bank will have reversed its polarity. To recover this energy the capacitor bank is allowed to "ring" through

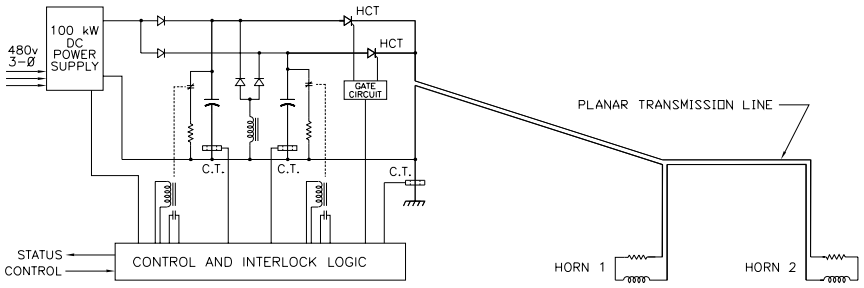

Figure 1. Basic horn power supply circuit with charge recovery.

Figure 4.6: A LC discharge circuit that will achieve the peak current when the HCT switch releases stored energy from the capacitor bank into the horns via the stripline.

a separate inductor via free wheeling diodes, after which the capacitor bank polarity is in the forward direction. At the end of the recovery cycle the energy lost from the capacitor bank is replaced by the charging power supply in time for the next discharge cycle to begin.

Capacitor Bank

From the inductance and resistance values projected for the two focusing horns and estimates for the balance of the circuit, the capacitance required for the bank is 1,350 μF at 10 kV. The total energy stored within the capacitor bank during operation is 48 kJ. This will be made up of an array of individual energy storage capacitors connected in parallel but separated electrically into at least two cells. The number of capacitors in each cell will be chosen to limit the amount of stored energy for that cell to a value that can be safely contained within an individual capacitor case, without rupture, in the event of an internal fault.

Charging System

The capacitor bank will be recharged by a 30 kW switch-mode power supply available from commercial sources. The calculated power consumption during operation of the horns is 25 kW. The required voltage for operation based upon present values for the circuit elements is 8.7 kV. Diodes are used between the

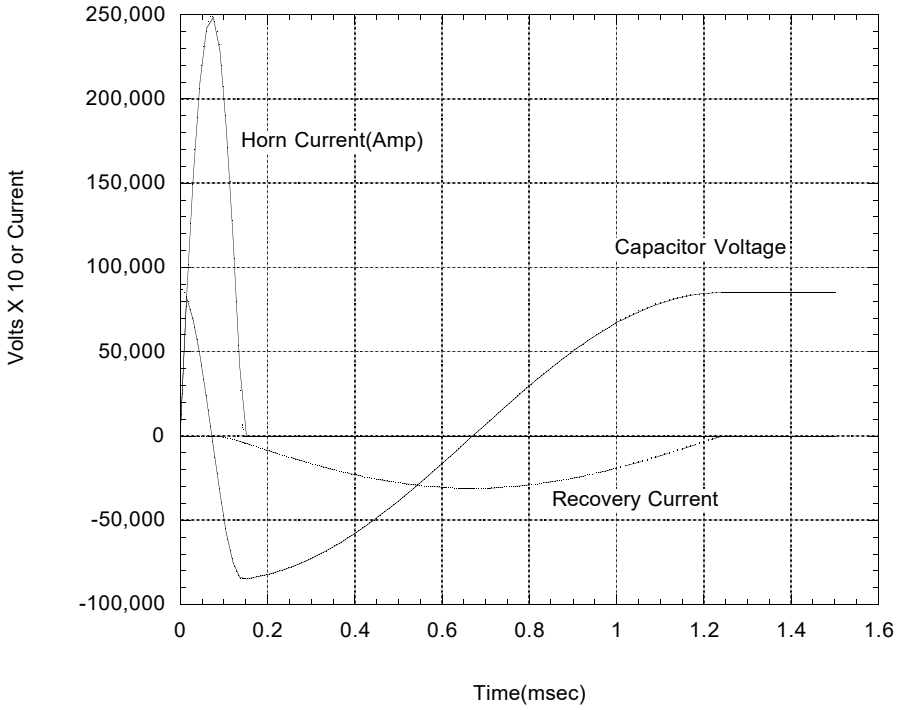

Figure 4.7: Current and voltage waveforms of a typical cycle of power supply operation

Table 4.1: Tabulation of neutrino horn circuit inductance L, resistance R, and power P.

Horn 1	0.455 μH	0.300 mΩ	6.7 kW
Horn 2	0.300 μH	0.050 mΩ	1.1 kW
Transmission line			
Power supply to beam line, 15 m.	0.450 μH	0.488 mΩ	10.9 kW
Distance between horns, 6 m.	0.180 μH	0.195 mΩ	4.36 kW
P.S. Cap. Bank plus connections (rough estimate)	0.2μH	0.100 mΩ	2.24 kW
Total	1.585 μH	1.133 mΩ	25.3 kW

charging power supply and the two separate sections of the capacitor bank. This permits charging of each half of the capacitor bank while keeping them isolated from one another for safety. The series diodes also prevent capacitor bank stored energy from being delivered backwards to the charging power supply in the event of a fault internal to the charging supply. These diodes are rated for the charging current level and twice the capacitor bank operating voltage. Diodes meeting these requirements are readily available from commercial sources.

Discharge resistors and safety system

A safety system will monitor operating parameters of the power supply and will shut it down if out of tolerance conditions are detected. Parameters to be monitored include over voltage and over current conditions of the charging supply, over voltage and over current conditions of the capacitor bank, ground fault currents, excessive temperatures, loss of cooling to the power supply or horns, personnel entry, etc. When fault conditions are detected the charging supply will be turned off and the capacitor bank discharged via a redundant arrangement of dump resistors and shorting relays to remove the stored energy. The dump resistors shall be rated to absorb the maximum stored energy capability of the capacitor bank, 68 kJ.

Discharge Switch

The discharge of stored energy from the capacitor bank to the horns is performed by HCTs. Each switching element shall consist of four HCTs in a series

assembly. Two such assemblies working in parallel will share in switching the total load current.

Current Transducers

A passive current transformer will be used to monitor the output current from the supply. This can be done in two possible ways: a single monitor located on the stripline to read the total current or two smaller monitors, one associated with each half of the capacitor bank, with outputs summed together to read total current. The latter method has the advantage of allowing the monitoring of the performance of each capacitor bank cell/HCT combination.

Transmission line

A transmission line consisting of two parallel plates will be used to connect the output of the power supply to the horns. Power losses in the transmission line are roughly double that of the two horns combined, 15.2 kW. It will be constructed to carry 4,730 A and capable of dissipating the resultant heat. A design allowing convective air cooling may be possible but further investigation and modeling is needed. In addition, it must have minimal inductance and resistance, be insulated for 10 kV operation, allow for thermal expansion and contraction at the horn connections, have insulation tolerant of the radiation flux, and permit rapid but reliable connection/disconnection at each horn terminal. If induced radioactivity is a concern, consideration needs to be given to the choice of material for the line, copper or aluminum.

Water Cooling

The HCTs will require water cooling at a flow rate of 2 gpm. Water cooling of the safety dump resistors may be desirable. Water cooling of the capacitors will depend on manufacturer specifications.

Cabinets

A cabinet similar to that used for the recently completed TESLA Modulators would be well suited for this power supply. It measures 6.25' high $\times$ 17.5' long $\times$ 5.75' deep.

Target Region Shielding

The secondary beam inside the Target Stack will be shielded with steel of outside dimension of 12' $\times$ 12' $\times$ 40' long. This design has a recessed entry

at the front, a water cooled collimator near the middle, and an endcap at the back so that as much radiation as possible is kept within the Target Station. CASIM results for this arrangement show that the highest residual dose rate at any point on the outside surface of the steel (infinite irradiation and zero cooloff) is less than 100 mr/hr.

4.3.3 Decay Region

The decay region will consist of a series of helium bags. Their dimensions will be approximately 15 ft x 15 ft x 30 ft . The helium gas system will be located at the service building to avoid irradiating gas cylinders and associated equipment that might occur if this equipment were located in the hall. Flow rates and helium requirements will be very low, as judged by the experience of a similar system used in NuTeV.

4.3.4 Beam Absorber

The Beam Absorber at the end of the Decay region also satisfies the condition of being less than 100 mr/hr at the surface of the steel. Since the beam intensity striking the Absorber is large, there is no re-entrant cavity at the front because it would decrease the solid angle very little. To service instrumentation that may be near the upstream face of the Absorber, a sheet of high Z material would be rolled in front of it during access.

The beam absorber is constructed of 10' × 10' × 2" steel plates as shown in Fig. 4.8. This object weighs 250 tons and is 10' × 10' × 21'. At a kinetic energy of 8 GeV, and because the beam passes through a thick target making the beam spot very large at the absorber face, cooling can be accomplished via natural convection. Intake air ducts for the Target Hall will be located near the Absorber. Almost all of the energy deposition occurs in the first half of the Absorber, so the 2 inch air gaps between the steel plates in the downstream half may be used for instrumentation.

To study ν_e backgrounds and other systematics associated with the neutrino beam, the absorber will be movable so that it can be placed anywhere along the length of the Target Hall downstream of the Target Stack. This will require that the absorber be mounted on Thompson bearings, and that a steel plate be installed for the absorber to roll over. The design provides for this capability. Since we anticipate a need to work at or near the absorber, its dimensions are chosen to provide approachable radiation levels at the steel surface even after extensive exposure. The hall dimensions are sufficient to provide room for access to and around the absorber.

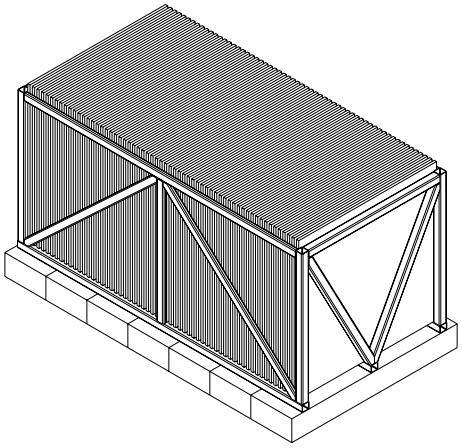

Figure 4.8: The steel absorber will be entirely air cooled, and movable along the beam axis.

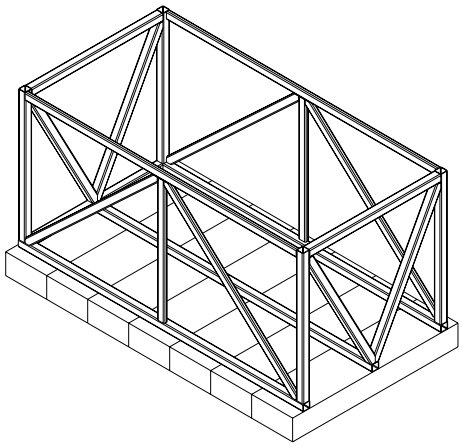

Figure 4.9: The steel absorber frame

In Fig. 4.8 we show an isometric view of the absorber. It will be constructed of steel plates taken from the Lab E detector. A 2 inch gap will separate each plate to provide for air cooling. The construction of the absorber will take place prior to the installation of the roof over the Target Hall by using an external mobile crane. The air cooling requirement makes modest demands on the enclosure's HVAC system. In Fig. 4.9 we show the framing fixture for the absorber. The 10' × 10" × 2" plates will be mounted vertically in the frame.

4.3.5 Secondary Beam Monitoring

There are four parameters which need to be measured in the secondary beam: targeting efficiency, intensity, beam profile, and accidentals.

The current plan to measure the absolute secondary intensity is with a large diameter beam toroid which will be positioned behind the steel of one

of the collimators to prevent halo from corrupting the measurement. These devices are available commercially (as special order) with electronics included. The intensity will be determined by subtracting the primary beam intensity measured before the target and correcting for target interactions.

Since the proton beam just upstream of the absorber is projected to be 1 m in diameter due to multiple scattering, it is unclear how the pion profile can be isolated as is done in NuTeV. The current NuTeV "yard" SWIC used for that purpose has an active region of 36". The "yard" SWIC will, however, be useful for understanding targeting angles and stability monitoring and will remain in the proposal.

The targeting efficiency will be monitored with a small triple coincidence set of counters mounted at 90° to the target. The scintillator is a special radiation hard material which has been used in the past for this purpose. These counters will be able to "see" the target through a small ∼1/8" hole in the target pile.

A standard paddle counter telescope will be used to measure accidental activity.

Although there are no plans to instrument the absorber, we have made provision for this. It is possible to install a large (approximately one meter square) Segmented Wire Ion Chamber (SWIC) mounted on the back face or inserted into the last meter of absorber. These devices can be difficult to manipulate but are small enough that they do not need a lot of room. A small hoist arrangement may be needed to move the SWICs into position in the absorber. This should not affect the size of the enclosure. These devices would be brought into the hall through the service building access.

4.4 Neutrino Fluxes

In this section we present the expected neutrino fluxes. Fig. 4.10 shows the expected ν_μ flux (solid histogram) from a 50m decay length beam line at 500 m and 1000 m from the target. The expected ν_e background is shown by the dashed histogram. For the initial single detector experiment, MiniBooNE, accurate ν flux and background calculations will be needed. Below, we first consider the production models of the Monte Carlo, providing evidence that our flux calculations, and therefore our expectations, are understood. Second, we present the horn simulation and, third, the ν_μ expectations and associated systematic error. Finally, we consider the ν_e beam content and systematics.

The beam simulation for this proposal uses the GEANT 3.21/FLUKA transport code. The fluxes presented here are based on the BNL horn design. The Monte Carlo includes all shielding in the Target Hall (hence it includes

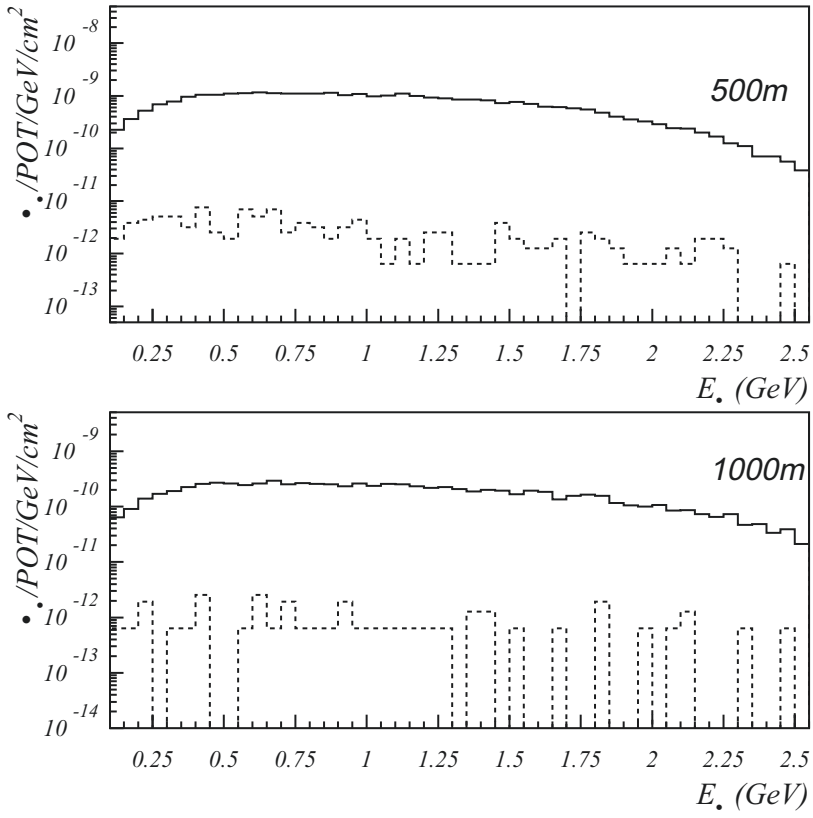

Figure 4.10: Flux of ν_μ (solid histogram) and ν_e (dashed histogram) from a 50m decay length beam line at 500 m and 1000 m from the target.

Table 4.2: For 8 GeV protons on Pb target, ratio of π^+ yield at 0° to 5° for various momenta.

p (GeV/c)	Ratio of Yields
0.85	1.05 ± 0.18
1.00	0.94 ± 0.23
1.50	0.95 ± 0.13
2.00	1.16 ± 0.10
2.50	1.74 ± 0.10
3.00	2.05 ± 0.10

beam scraping).

Position and profile monitors similar to those used by NuTeV and BNL 776 in the primary beam, decay pipe, and dump region will provide important constraints on the beam simulation. The primary and secondary beam monitoring has been described above.

4.4.1 Production Monte Carlo

A primary ingredient for the simulation is the particle production spectrum from the 8 GeV proton interactions in the thick production target. In this section we demonstrate that our flux expectations are based on realistic simulation of 8 GeV production using experimental production data.

Recent work by Mokhov and Striganov[47] consolidates what is known about particle production with 8 GeV protons. A large number of experiments have studied particle production in this energy range (selected papers are given in references 46 through 50). In Fig. 4.11 a comparison is shown for pion production by 6 GeV protons interacting in a thick copper target. In Fig. 4.12 we give distributions for 12 GeV protons in a copper target. Because titanium (our choice of target) and copper have similar A and Z, the excellent agreement with measurements gives confidence that our simulations are correct.

8 GeV production has less dependence on production angle than higher energy production because the events are much more isotropic. Thus MiniBooNE does not face the stringent requirements on primary beam angle faced by such experiments as NuTeV. Nevertheless, the incoming primary beam angle can be determined to roughly the same accuracy as in NuTeV (approximately 1 degree). Measurements with an accuracy of 10-20% have been made of pion production between 0 and 15 degrees.[48,49] Table 4.2 provides the ratio of yields at 0 and 5 degrees over a range of momenta. At low energies, the data are consistent with no angular dependence. At energies greater than 2 GeV, the

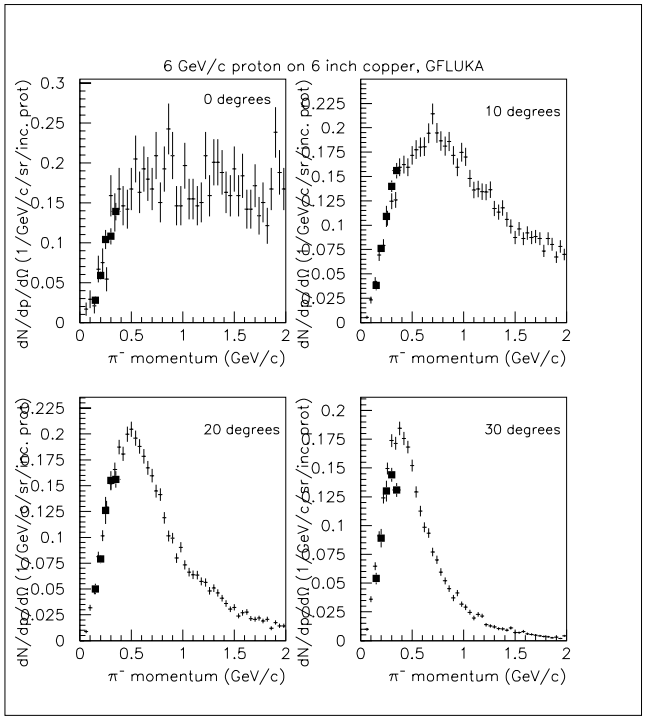

Figure 4.11: Pion production as predicted by FLUKA compared to existing data for 6 GeV protons incident on a 6 inch copper target. (Mokhov and Striganov)

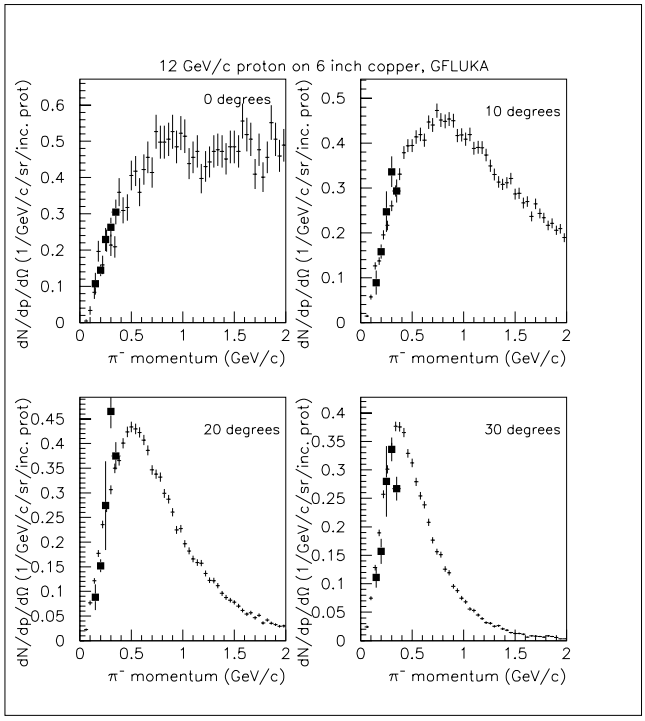

Figure 4.12: Pion production as predicted by FLUKA compared to existing data for 12 GeV protons incident on a 6 inch copper target. (Mokhov and Striganov)

data do show angular dependence. Fits to the data in this region describe the angular dependence to 10%.

Charged and neutral kaon production data have been analyzed in our energy range. It should be noted that kaon production is suppressed at low energies. Thus, the ν_μ flux does not show an obvious kaon peak as is seen for higher energy neutrino experiments such as NuTeV. The charged kaon ν_μ contribution can be isolated by cutting above 3 GeV as discussed below. A particularly useful set of K_S data that constrains the Monte Carlo production prediction is available from the KEK proton synchrotron[52] for 12 GeV/c protons on Cu measured at 3.5, 5.0, 6.5, 8.0 and 9.5 degrees.

For the final analysis we plan to use an improved Monte Carlo generator, under development at Fermilab by Sergei Striganov and Nikolai Mokhov, which models the low energy production data.[47] This Monte Carlo is under development for the muon collider as well as for BooNE and is specifically designed for 8 GeV primary proton production. The program will interface to GEANT.

The body of knowledge associated with low energy particle production is expanding. The most important upcoming contribution is the data from BNL E910, 6 to 20 GeV proton interactions on heavy targets, including copper.[53] This experiment has nearly 4π coverage, and reconstructs $\pi^\pm$, $K^\pm$ and K_S. As an example of the high statistics and large kinematic coverage of E910, figure 4.13 presents the preliminary π^- data as a function of transverse mass, over the wide rapidity range. These results will provide important constraints on the BooNE production Monte Carlo.

More production studies may be expected in the future. Physicists working on the development of the First Muon Collider, which would be fed from the Fermilab Booster, are considering proposing an experiment at the BNL AGS.[26] Although there are no immediate plans for a production experiment at Fermilab, the design of the BooNE beam line leaves open the possibility. Protons could be directed to a separate spectrometer, or a tiny part of the BooNE secondary beam could be allowed to pass through the dump into a small spectrometer. In short, there is sufficient interest in the subject that we expect further data will become available.

BooNE does not rely solely on production data from other experiments to constrain the secondary particle production. Very strong constraints come from using the neutrino spectrum in the detector to determine the secondary particle fractions. These analysis methods have been developed in previous neutrino experiments. For example, this technique has been successfully used to fix the charged π/K fraction in the NuTeV and E734 experiments and, thus, fix the ν_e background from K^+/K^- decay.[56] These methods are discussed in

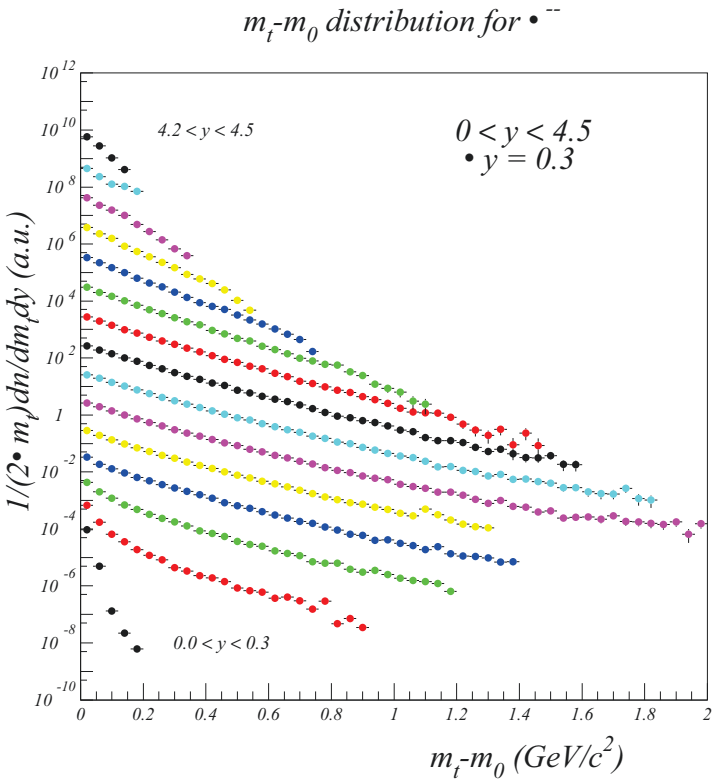

Figure 4.13: Preliminary results on π^- production from BNL E910. Data are shown as a function of difference between transverse mass and pion mass and as a function of rapidity. Analysis by H. Heijima.

the sections on systematics below.

4.4.2 Secondary Beam Simulation

The secondary beam simulation is based upon the GEANT321 [54] transport code with the standard FLUKA hadron interaction package activated. The horns are modeled after the BNL horn system [55] with some modifications for the lower beam energy and higher pulse repetition rate. The neutrino flux calculation is checked for the Brookhaven beam configuration by comparing with the Brookhaven experimental results [55]. Agreement between the predicted and measured fluxes, shown in figure 4.14, gives us confidence in the calculation. At low energies, before tuning the simulation with the most recent low energy production data, the agreement is ∼10%, which is the systematic error we quote for the flux from Monte Carlo production. The disagreement at low energy may be due to simulation of a thinner horn (2 mm) than the horn used by the Brookhaven experiment (6 mm). At higher energies the agreement is excellent.

The default configuration for the BooNE secondary beam has a decay path from the beginning of the target of 50m. The target is a titanium rod of length 55cm and radius 4mm. The horn wall thickness is assumed to be 2mm Al equivalent around the target with a magnetic field region beginning at 1.35 mm radius from the center of the target, consistent with ohmic heating constraints. The horn current of 250kA is the same as in the BNL horns. The proton beam on target is consistent with the 10π mm-mrad emittance expected from the Fermilab Booster. The angular divergence and transverse spread on target are set to .1 degrees and 1.5 mm respectively in both the horizontal and vertical directions.

A study of the variation in the neutrino flux with beam parameters has been carried out. The fluxes as a function of beam position on target, target radius, target length, horn material thickness, and inner horn diameter are shown in Table 4.3.

4.4.3 ν_μ Flux and Systematics

The main contribution to the ν_μ flux is from pion decay, as kaon production is suppressed at 8 GeV compared to higher energies. Above 3 GeV, the ν_μ's are mostly from K^+ decays, and this region will be used to constrain the kaon content of the beam.

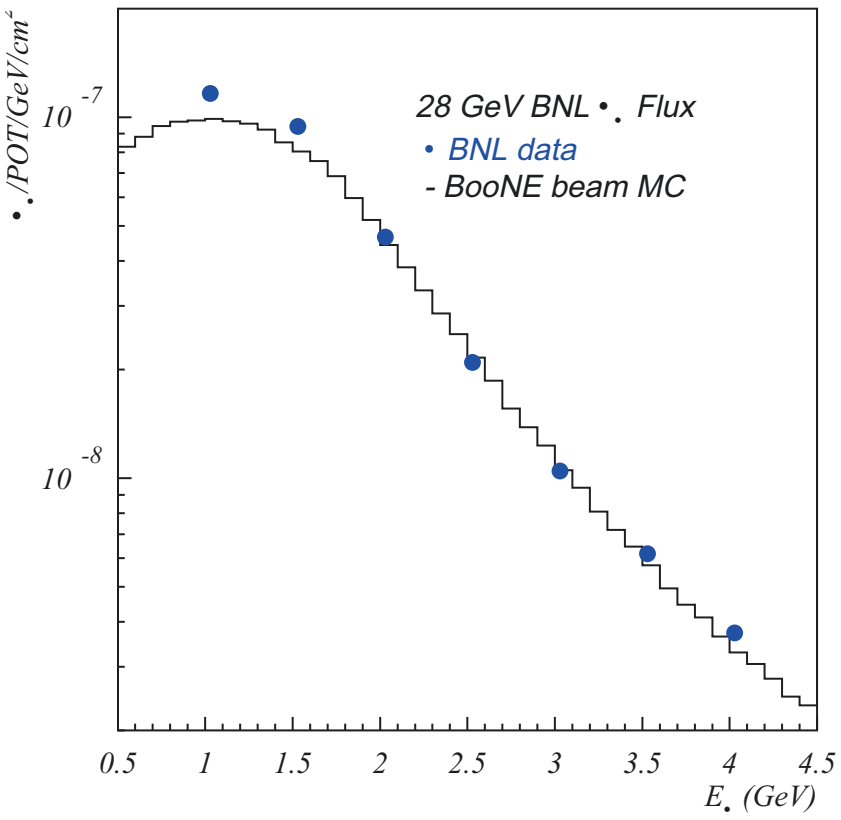

Figure 4.14: The BNL measured flux for 28 GeV protons on target compared to the flux from the GEANT BNL simulation.

Table 4.3: Flux predictions as a function of various beam parameters. Nominal values are in bold face. The values are in units of $\nu/proton/cm^2$, averaged over a 3 meter radius disk at a distance of 500 meters from the target. There is approximately a 3% statistical error on each calculation.

Target Radius:	2mm	3mm	**4mm**	6mm
	1.08	1.64	1.88	1.83
Target Length:	15cm	27cm	40cm	**55cm**
	1.32	1.72	1.81	1.88
Horn Wall:	0mm	**2mm**	4mm	6mm
	2.03	1.88	1.69	1.50
Beam displacement:	**0mm**	1mm	2mm	3mm
	1.88	1.88	1.63	1.37
Horn Inner Radius:	6mm	8mm	10mm	**13.5mm**
	2.16	1.95	2.21	1.88
Horn Current:	200kA	**250kA**	300kA	
	1.95	1.88	1.96	

Neutrino Flux Angular and r Dependence

Fig. 4.15 shows the neutrino flux as a function of neutrino energy and $\cos\theta$, where θ is the angle of the neutrino relative to the incident proton direction. Although the total neutrino flux peaks at $\theta = 0$, for a given neutrino energy the maximum neutrino flux varies as a function of θ. For example, for $E_\nu = 0.6$ GeV the neutrino flux peaks at $\cos\theta = 0.999$ and for $E_\nu = 0.4$ GeV the peak flux occurs at $\cos\theta = 0.998$, or $\theta = 63$ mrad. Therefore, we could offset the detector from the forward direction in order to decrease the higher energy neutrino flux and increase the lower energy neutrino flux. Our present design has no offset.

In the second phase of BooNE, when interactions in two detectors are compared to determine the oscillation parameters, it is important that the flux show a simple $1/r^2$ spatial dependence. The beam line has been designed with this in mind. The neutrino flux, as shown in Fig. 4.10 at 500 and 1000 m, has a $1/r^2$ spatial dependence to very good approximation. Fig. 4.16 shows the ratio of the neutrino flux passing through the MiniBooNE detector at 1000 m compared to 500 m as a function of neutrino energy. Although some deviation is observed between 1.5 and 2.5 GeV where the neutrino flux is mostly due to kaon decays and the flux is low (Fig. 4.16a), no deviation from a pure $1/r^2$ dependence is observed for neutrino energies less than 1.5 GeV, which is the range that will be used in the analysis (Fig. 4.16b). Averaged over the entire

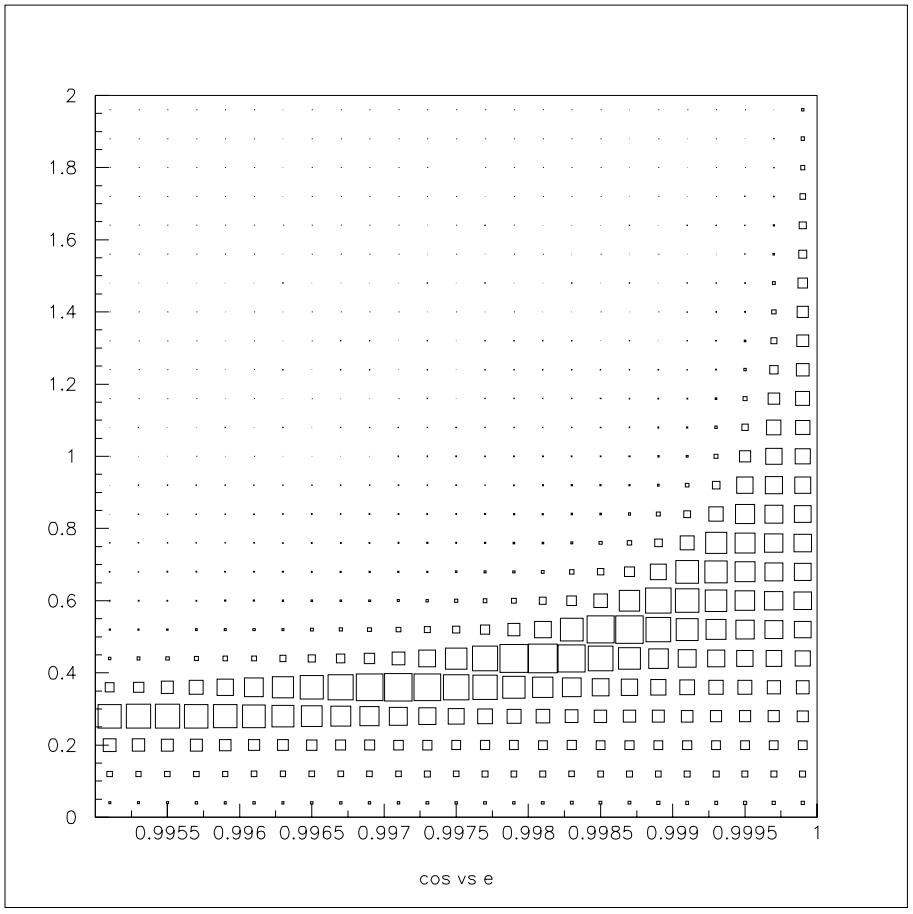

Figure 4.15: The neutrino flux as a function of neutrino energy (GeV) and $\cos\theta$, where θ is the angle of the neutrino relative to the incident proton direction.

neutrino energy range, there are about 3.91 (instead of 4.00) times as many neutrinos passing through the detector at 500 m compared to 1000 m. This deviation from a pure $1/r^2$ dependence can be corrected for easily.

ν_μ Flux Systematics for this Proposal

For this proposal we have assumed a 10% error on our understanding of the ν_μ flux for the disappearance search. This can be achieved given the combined information from our beam monitoring and production data from other experiments (discussed in section 4.4.1).

Further Constraint on the ν_μ flux if a Disappearance Signal is Observed

If we see a ν_μ disappearance signal in MiniBooNE, we can obtain further verification by running in $\bar{\nu}_\mu$ mode. Here we describe a technique for constraining the ν_μ flux which relies upon the fact that quasi-elastic scattering off free protons has a well known cross section. Thus it can be used to reduce the systematic errors associated with scattering off neutrons and protons bound in ^{12}C. The method is described in detail elsewhere [57] and only the salient features are covered here.

There are two main points on which the method depends. First, the antineutrino cross section and its Q^2 dependence on free protons is known to about 2% in this energy and momentum transfer range, mostly because of well measured neutron decay and relatively little form factor dependence. Second, ^{12}C is a member of a highly symmetrical isotriplet, so nuclear physics effects cancel to high accuracy. In other words, scattering from bound protons and bound neutrons are closely the same in ^{12}C.

The $\bar{\nu}_\mu$ on CH_2 scattering events can be separated into scattering from bound and free protons using the different shapes of the respective Q^2 distributions. Since the $\bar{\nu}_\mu$ flux for these two samples is the same, one can then scale the bound proton cross section from the known free proton cross section. The Q^2 dependence of the free proton cross section is well known,[58] and the Q^2 shape of bound protons in ^{12}C is deduced from ν_μ scattering on bound neutrons. Figs. 4.17 and 4.18 show the expected Q^2 distributions for free and bound protons, using a Fermi gas model for the nuclear effects. (The Fermi gas model is just being used to indicate the expected difference in the two distributions. In the actual measurement, the Q^2 distributions will be determined from the data as discussed above.) The $\bar{\nu}_\mu - CH_2$ data is fit to the appropriate sum of the two distributions, giving the amplitudes for bound and free scattering. The amplitude of the free scattering gives an absolute value for the $\bar{\nu}_\mu$ flux. The amplitude of the bound scattering combined with this measured

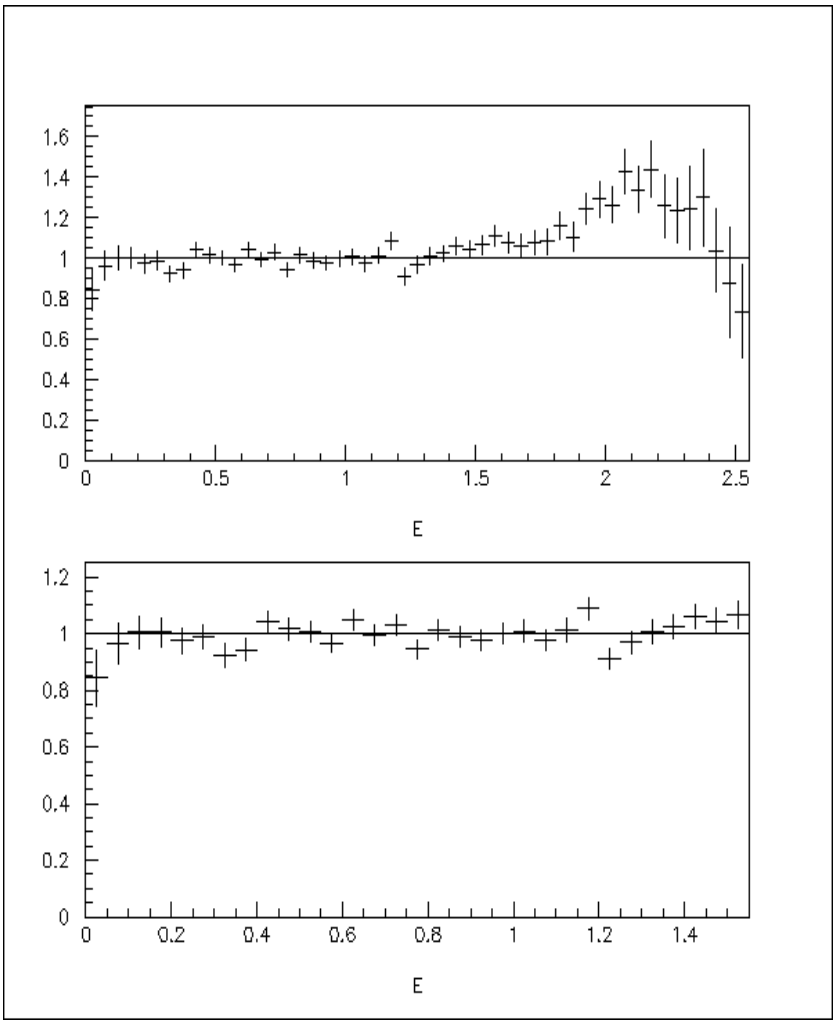

Figure 4.16: The ratio of the neutrino flux passing through the MiniBooNE detector at 1000 m compared to 500 m as a function of neutrino energy in GeV. The ratio is normalized such that it equals one for a pure $1/r^2$ dependence. The upper figure shows the full energy range, while the lower figure enlarges the region of interest.

Beam Particle	Avg. Decay Length (m)	Relative Prod. + Decay Rate	$\nu_e/\overline{\nu}_e$ B.R.
π^+	102	1.0	–
K^+	24	0.06	0.048
K_L	87	0.0025	0.388
μ^+	7120	0.0035	1.00

Table 4.4: Secondary particle decay properties and rates.

Source	ν_e Events	Background Fraction
μ decay	960	2.3×10^{-3}
K^+ decay	200	4.6×10^{-4}
K_L decay	110	2.5×10^{-4}

Table 4.5: Expected number of $\nu_e/\overline{\nu}_e$ events from various sources. The numbers correspond to 2.5×10^{20} pot.

$\bar{\nu}_\mu$ flux gives a measurement of an effective bound proton cross section. This cross section on bound protons can then be used to infer the related effective cross section for bound neutrons.

This method seems capable of yielding both neutrino and antineutrino fluxes at a level much better than previously obtained ($< 10\%$). Thus, this method can be used to determine the observed flux at the detector position. A comparison of this observed flux with predictions from the beam simulation can then be interpreted in terms of neutrino oscillations.

4.4.4 ν_e Background and Systematics

The intrinsic $\nu_e/\overline{\nu}_e$ background in the beam comes primarily from μ , K^+, and K_L decays in the decay pipe:

$$\pi^+/K^+ \rightarrow \nu_\mu \; \mu^+ \hookrightarrow e^+ \; \overline{\nu}_\mu \; \nu_e,$$

$$K^+ \rightarrow \pi^0 \, e^+ \, \nu_e,$$

$$K_L \rightarrow \pi^\pm \, e^\mp \, \overset{(-)}{\nu}_e \, .$$

μ decay is about three times larger than kaon decays and, therefore, systematic errors associated with μ decay need to be particularly minimized. The decay properties and relative rates are given in Table 4.4 and the $\nu_e/\overline{\nu}_e$ backgrounds are listed in Table 4.5

The $\nu_e/\overline{\nu}_e$ background can be calculated to better than 10% using a beam Monte Carlo that is tied to measured π and K production data as described in

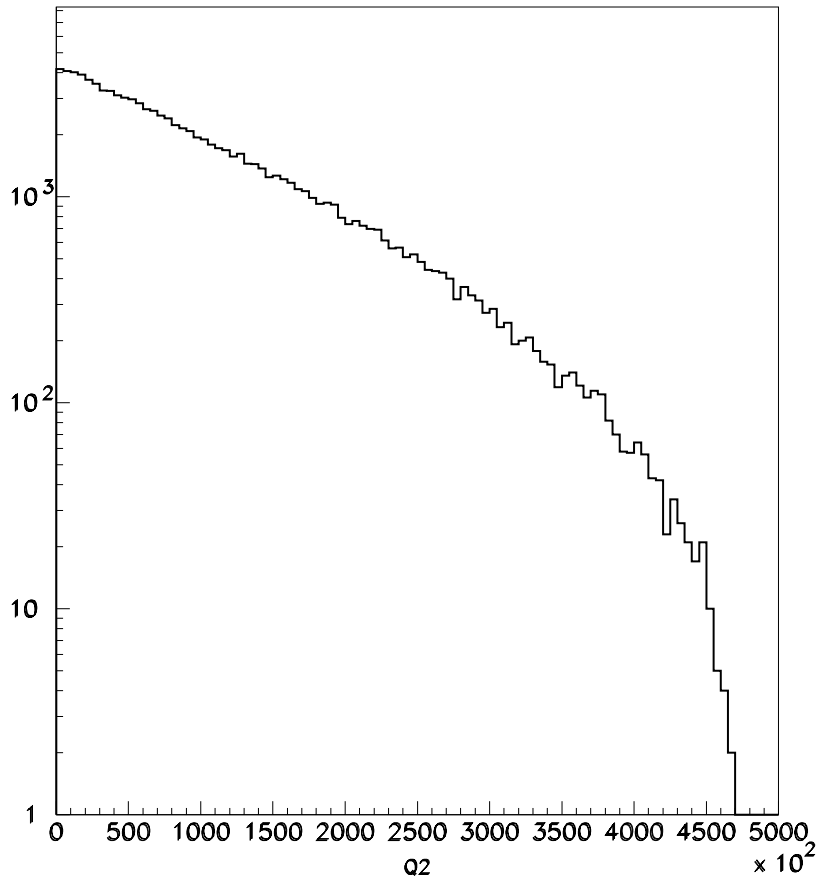

Figure 4.17: The Q^2 distribution for $\bar{\nu}_\mu p \rightarrow \mu^+ n$ scattering on free protons in units of $\mathrm{MeV}^2/\mathrm{c}^2$.

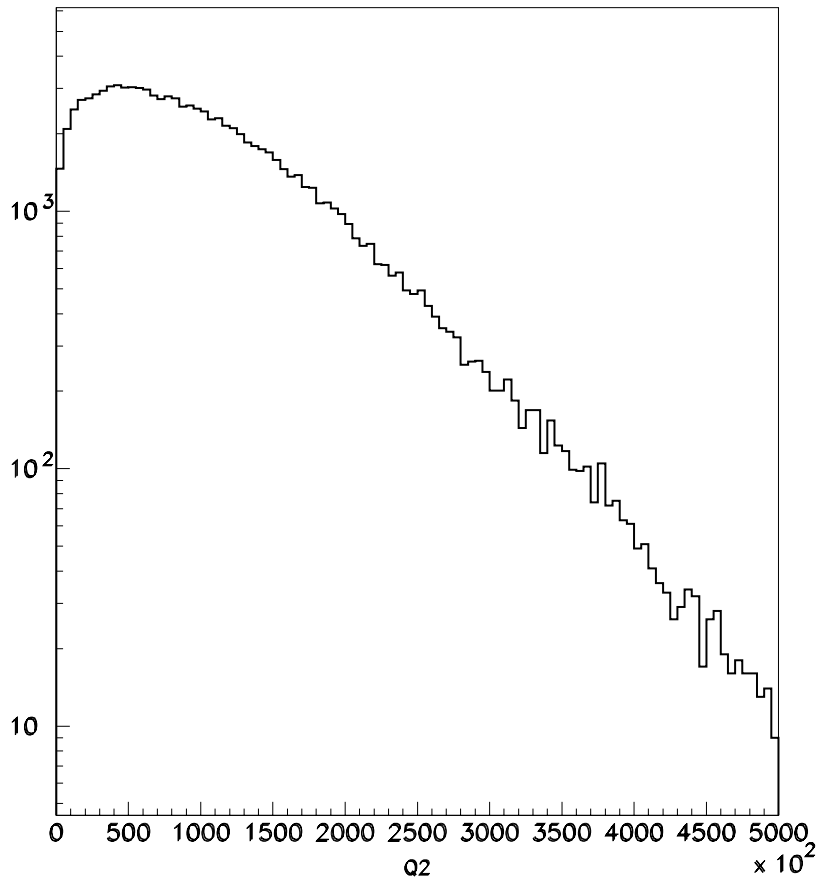

Figure 4.18: The Q^2 distribution for $\bar{\nu}_\mu C \rightarrow \mu^+ X$ scattering in units of $\mathrm{MeV}^2/\mathrm{c}^2$, using a Fermi gas model for the nuclear effects.

Section 4.4.1. Several other checks are also available to reduce the systematic uncertainty in these $\nu_e/\overline{\nu}_e$ background calculations:

- The observed ν_μ events provide a powerful constraint on the $\nu_e/\overline{\nu}_e$ background from μ decay.
- The change in the observed $\nu_e/\overline{\nu}_e$ rate with decay pipe length is sensitive to μ decay.

Constraints on the $\nu_e/\overline{\nu}_e$ background from the observed ν_μ events

The decay $\pi^+/K^+ \to \nu_\mu\,\mu^+$ followed by $\mu^+ \to e^+\,\overline{\nu}_\mu\,\nu_e$ is the main source of background ν_e events for the experiment. The observed ν_μ events in the detector are mainly from π^+ decay with less than 1% from K^+ and 3-body decays. The energy spectrum for π^+'s decaying in the decay pipe, those giving ν_μ events in the detector, and those that lead to ν_e events are shown in Fig. 4.19.

The energy of π^+'s that make ν_μ events in the detector are shifted to high energy due to the small solid angle in forward direction subtended by the detector. The detector covers an angle of about 10 mr, and the angular divergence of the pions that make ν_μ events peaks at 4 mr with a width of about 5mr as shown in Fig. 4.20. The ν_μ events observed in the detector therefore have decay angles with respect to the pion direction less than 10-20 mr. For pion energies between 1 and 5 GeV, restricting the decay angle produces a strong correlation between E_π and E_{ν_μ} since E_{ν_μ} has small variation near the forward direction. For the MiniBooNE setup, the ratio $\mathrm{E}_\pi/\mathrm{E}_{\nu_\mu} \approx 2.5 \pm 0.1$ for observed events in the detector. Fig. 4.21 shows a plot of the mean ratio of $\mathrm{E}_\pi/\mathrm{E}_{\nu_\mu}$ as a function of E_π for pions that produce ν_μ events in the detector; the ratio is fairly uniform with energy.

Since the E_{ν_μ} spectrum is closely tied to the E_π spectrum, one can use the observed E_{ν_μ} spectrum to make a correction to the E_π spectrum. A method has been developed that uses the ratio of the observed E_{ν_μ} spectrum to that predicted from the Monte Carlo to calculate a weight correction for the pion spectrum including the 2.5 scale factor.

$$Weight(E_\pi) = \frac{N^{obs}_{\nu_\mu}(E_\pi/2.5)}{N^{MC}_{\nu_\mu}(E_\pi/2.5)}$$

The $Weight(E_\pi)$ are fit to a simple quadratic function, and the function is used to weight a subsequent Monte Carlo run that should now agree with the observed ν_μ spectrum and, thus, give a better estimate of the ν_e background from muon decays.

Beam Modification	Observed ν_e/ν_μ Evt Ratio ($\times 10^{-3}$)	Change from Standard	Predicted ν_e/ν_μ Evt Ratio ($\times 10^{-3}$)	Difference
Standard	2.30 ± 0.03	—	—	—
$E_\pi \rightarrow E_\pi + 1\text{GeV}$	1.73 ± 0.02	$-25 \pm 2\%$	1.82 ± 0.02	$4.9 \pm 2\%$
$E_\pi \rightarrow E_\pi * 1.2$	1.98 ± 0.02	$-16 \pm 2\%$	1.91 ± 0.02	$-3.5 \pm 2\%$
$func(E_\pi)$	2.68 ± 0.02	$+17 \pm 2\%$	2.69 ± 0.02	$+0.4 \pm 2\%$
$\theta_\pi \rightarrow \theta_\pi * 2.0$	2.39 ± 0.04	$+\ 4 \pm 2\%$	2.36 ± 0.07	$-1.0 \pm 3\%$

Table 4.6: Results from the systematic studies of various beam modifications.

Monte Carlo studies have been made to test the systematic uncertainty associated with this method. These studies include the acceptance of the detector and a parameterization of the observed energy resolution ($\delta E/E$ changes linearly from 25% to 15% as E_ν changes from 0.5 to 1.0 GeV). The standard BNL pion and kaon beam file is modified by various methods to produce a simulated sample of observed data. The above method is then used to obtain weights by comparing ν_μ events to the standard BNL spectra. The predicted ν_e background is then compared to the simulated ν_e events to estimate the systematic uncertainty. Several modifications were considered to span the possible uncertainties in the beam spectrum.

1. $E_\pi \rightarrow E_\pi + 1.0$ GeV
2. $E_\pi \rightarrow E_\pi * 1.2$
3. $func(E_\pi) = \left(\begin{array}{ll} 2.0 * E_\pi & \text{for} \quad E_\pi < 0.75 \text{ GeV} \\ 0.2069 * (8.0 - E_\pi) & \text{for} \quad E_\pi \geq 0.75 \text{ GeV} \end{array} \right)$ This weighting changes both the mean and sigma of the distribution.
4. $\theta_\pi \rightarrow \theta_\pi * 2.0$

For case 1), the E_{ν_μ} and E_{ν_e} spectrum, before and after the weighting, is shown in Figs. 4.22 and 4.23. The results of these studies are summarized in Table 4.6 and indicate that the observed ν_μ spectrum can be used to constrain the ν_e background to $\approx 5\%$.

Systematic Uncertainties for the ν_μ Scaling Technique

Experimental uncertainties can affect how well the ν_e event prediction can be made using the observed ν_μ events. The scaling technique relies on the assumption that the true pion spectrum can be obtained from the ν_μ events and, therefore, uncertainties associated with the ν_μ measurements induce errors in

Source	Uncertainty	ν_e Prediction Error
Energy Calibration	$E_\nu \rightarrow 1.02\ E_\nu$	1.2%
Energy Non-linearity	$E_\nu \rightarrow E_\nu(1+0.02E_\nu)$	0.5%
Energy Offset	$E_\nu \rightarrow E_\nu + 10$ MeV	1.5%
$\nu_e/\nu_\mu\ \sigma(E_\nu)$	$\delta\sigma(E_\nu) = 0.1 \times (\sigma(\infty) - \sigma(E_\nu))$	2.0%
ν_μ Backgrounds	$N^{obs}_{\nu_\mu} = N^{real}_{\nu_\mu}(1+0.01E_\nu)$	0.9%
Relative ν_e/ν_μ Fid. Vol.	$\frac{\delta(\text{Fid.Vol.})}{\text{Fid. Vol.}} = 1\%$	1.0%

Table 4.7: Systematic uncertainties associated with various experimental errors. The last column give the percentage change in the predicted number of ν_e events in the observed energy range from 0.1 to 3.0 GeV.

this prediction. Most experimental uncertainties are common for both ν_e and ν_μ events and, therefore, the effects of these uncertainties tend to cancel. On the other hand, since the energy distributions of the ν_e and ν_μ events are different, energy dependent uncertainties can effect the two distributions differently. For example, a 2% absolute energy calibration error, ($E_\nu \rightarrow 1.02\ E_\nu$), will induce a 1.2% shift in the predicted ν_e to ν_μ ratio. The systematic uncertainties on the predicted ν_e rate between 0.1 and 3.0 GeV associated with several calibration errors are given in Table 4.7. In addition, there are uncertainties due to the neutrino cross section, backgrounds in the ν_μ event sample, and the determination of the relative fiducial volume for ν_e and ν_μ events. These uncertainties are also listed in Table 4.7. For the ν_e and ν_μ quasi-elastic cross section, an uncertainty of 10% on the value relative to the asymptotic cross section at high energy was assumed, $\delta\sigma(E_\nu) = 0.1 \times (\sigma(\infty) - \sigma(E_\nu))$.

Checks on the $\nu_e/\overline{\nu}_e$ background from variation of the decay pipe length

The sources of neutrino production in MiniBooNE have different dependences on the length of the decay pipe. For example, the main source of ν_e background comes from pion decay followed by muon decay. For all muon energies of interest, the decay pipe length, $L = 50m$, is much smaller than the muon decay length, $\lambda_\mu \approx 7100m$. The muon decay probability is then $\frac{(L-x)}{\lambda_\mu}$ where x is the point where the pion decays. Integrating over x from 0 to L and weighting by the pion decay probability, $\frac{e^{-\frac{x}{\lambda_\pi}}}{\lambda_\pi}$, yields a ν_e background rate that is proportional to $L^2/\lambda_\mu\lambda_\pi$. On the other hand, the $\pi_{\mu 2}$ source of detected ν_μ events and, thus, an oscillation signal would be proportional to L since $\lambda_\pi > L$. The smaller K^+_{e3} and K^L_{e3} sources of ν_e background are constant and proportional to L, respectively. Fig. 4.24 shows the variation in ν_e flux from

Decay Pipe Length (m)	ν_μ events	$\nu_\mu \to \nu_e$ oscillation events	mistake in ν_e bkgnd. from $\pi \to \mu \to \nu_e$
50	700,000	600 ± 50	600 ± 50
25	390,000	334 ± 35	174 ± 32

Table 4.8: Dependence of neutrino events on decay pipe length for observed ν_μ events, a possible oscillation signal, and a mistake in the ν_e background.

the Monte Carlo with decay length from μ, K^+ and K_L decays and for the oscillation signal.

A variation of the decay pipe length can, therefore, provide proof that an observed oscillation signal is not from ν_e background. The secondary dump at the end of the end of the decay pipe is being designed to move. If an oscillation signal is observed after 1×10^7 s of running, we would plan to move the dump from the $50m$ to a $25m$ position. A true oscillation signal should be reduced by a factor of 1.8 as opposed to a factor of 3.4 for a false signal associated with the muon decay background. An example scenario is shown in Table 4.8.

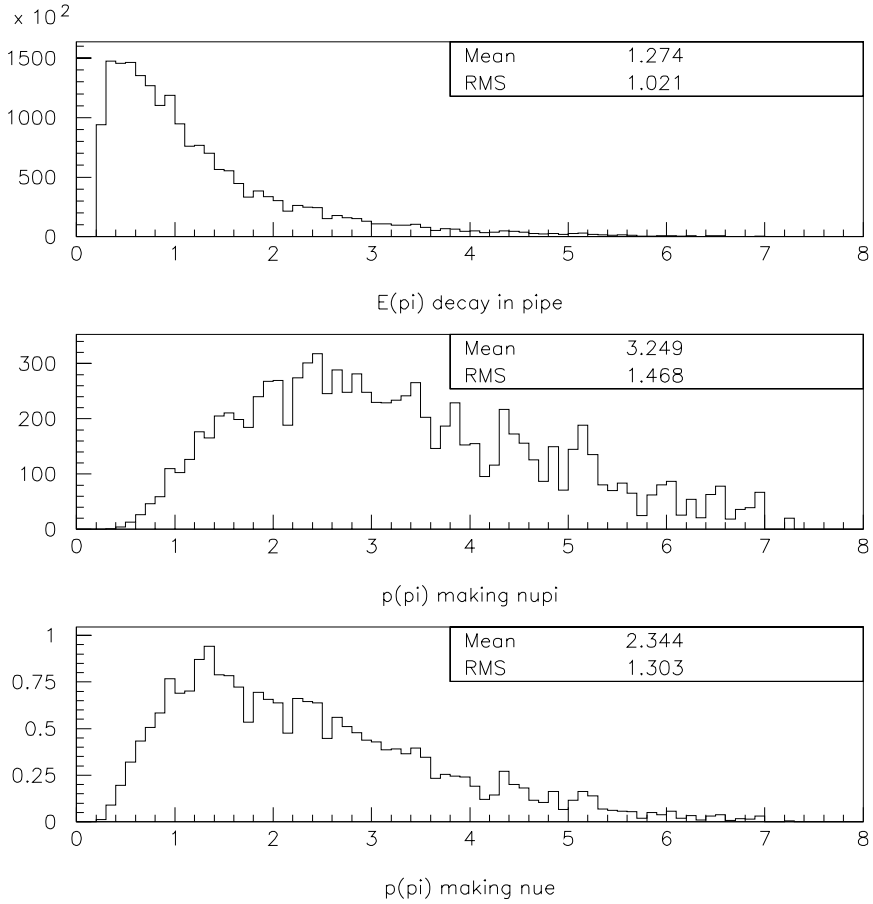

Figure 4.19: Pion energy distributions for: a) all pions that decay in the decay pipe, b) pions that lead to ν_μ, or c) ν_e events in the detector.

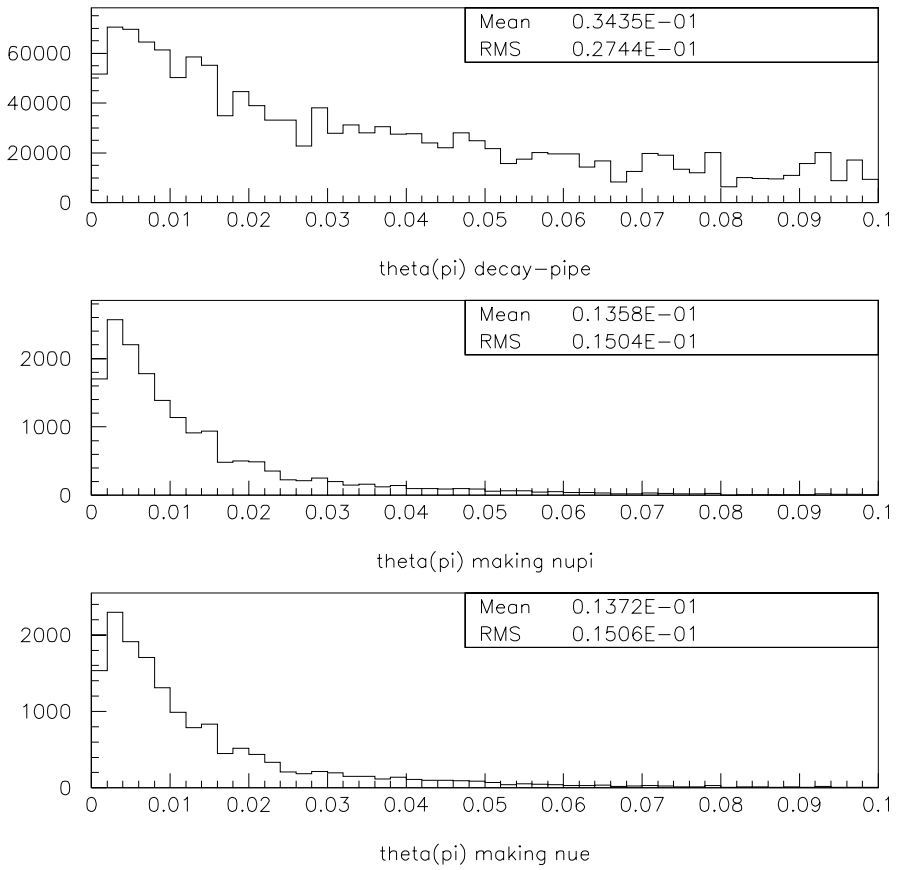

Figure 4.20: Pion angular distributions after the horn for: a) all pions that decay in the decay pipe, and pions that lead to events in the detector b) from ν_μ or c) from ν_e.

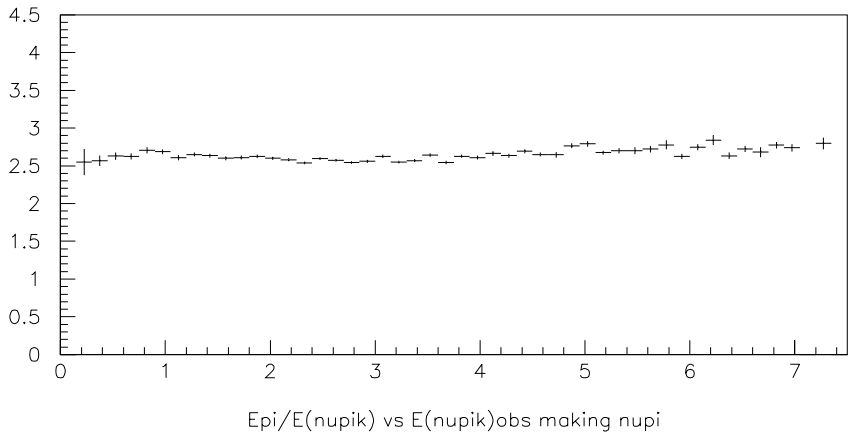

Figure 4.21: The average ratio of pion to observed ν_μ energy for bins of pion energy.

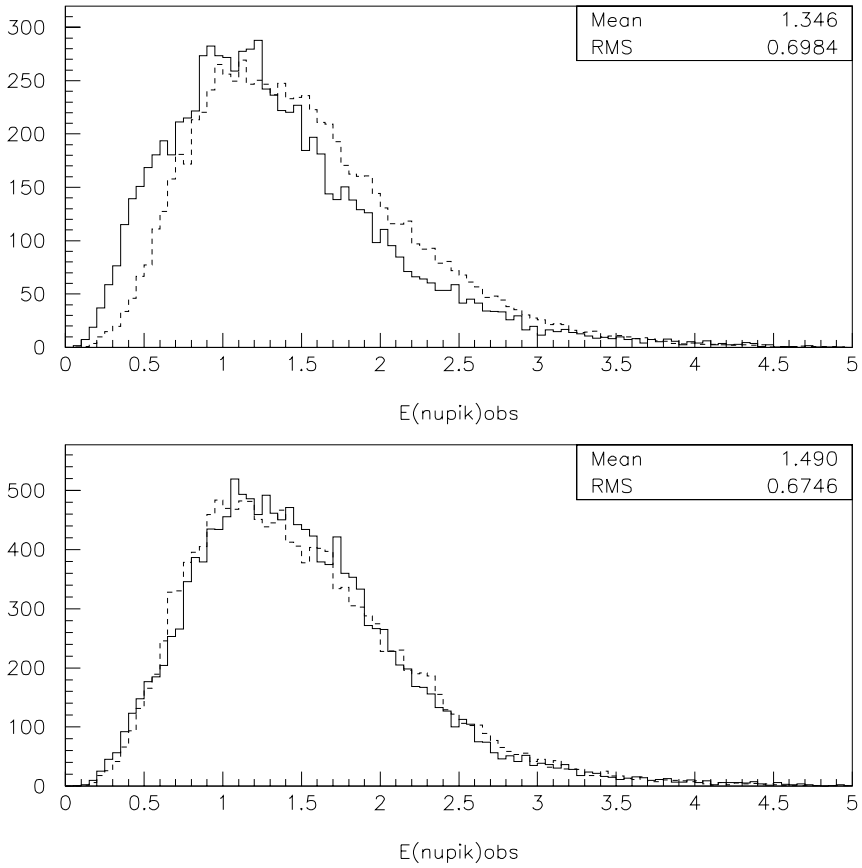

Figure 4.22: The observed and predicted energy distribution for ν_μ events a) before weighting and b) after weighting.

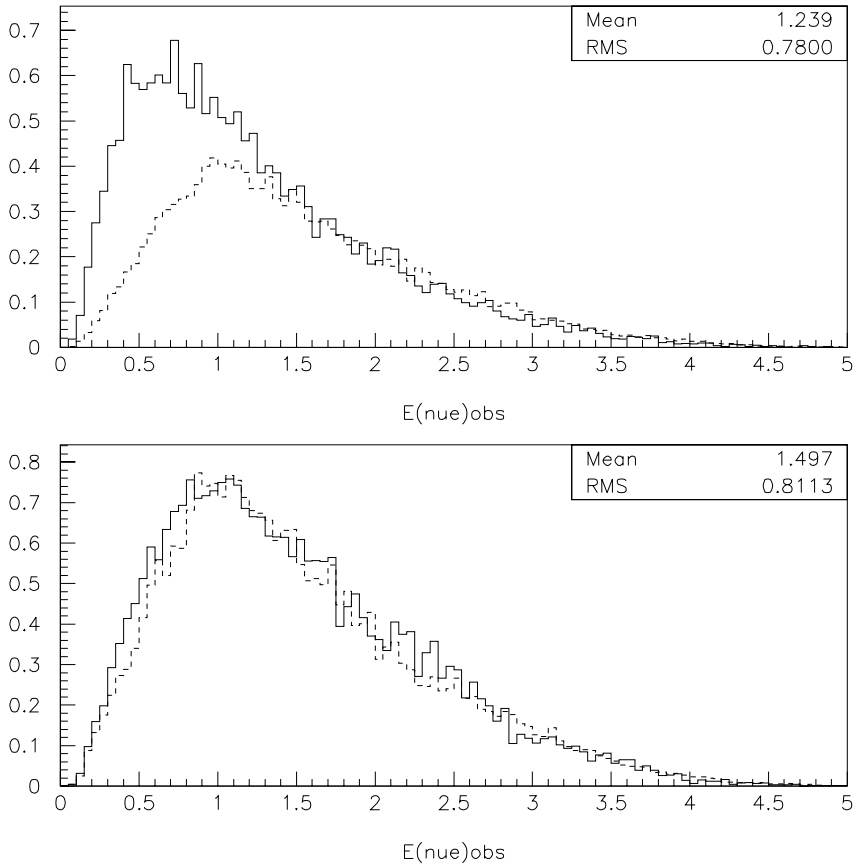

Figure 4.23: The observed and predicted energy distribution for ν_e events a) before weighting and b) after weighting.

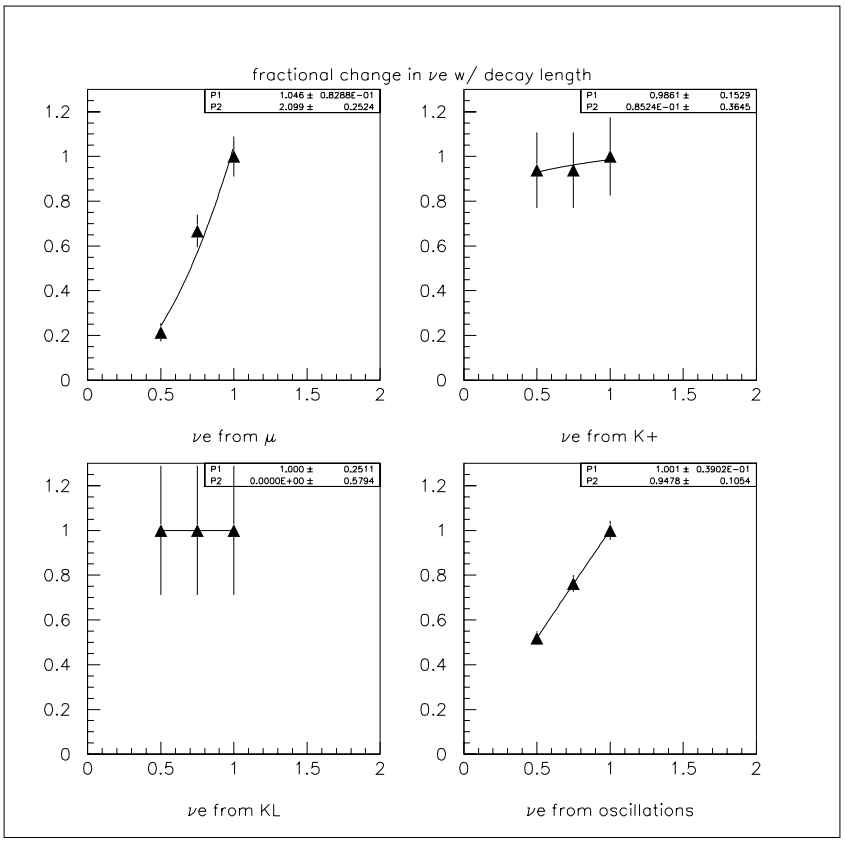

Figure 4.24: The variation of the Monte Carlo ν_e flux with fractional decay pipe length. Normalized fluxes for μ, K^+ and K_L decays and for an oscillation signal at $sin^2 2\theta$=0.002 and Δm^2=2 eV^2 are shown. The data are fit to the form $P_1 x^{P_2}$, where x is the fractional length of the decay pipe. Fractional lengths of 1/2, 3/4 and full length are presented to constrain the fits, although MiniBooNE plans to run with only the 1/2 and full length configurations.

Chapter 5

Detector Design and Simulation

The MiniBooNE detector will consist of a 12.0 m diameter spherical tank that is filled with 769 tons of mineral oil and covered on the inside with 1220 eight-inch phototubes (10% coverage). The outer volume of the tank will serve as a veto for outgoing and incoming particles.

The MiniBooNE experiment consists of a 769 ton imaging Čerenkov detector. The detector will be placed 500 m from the neutrino source, such that the energy distributions of $\nu_e C \rightarrow e^- X$ and $\nu_\mu C \rightarrow \mu^- X$ quasi-elastic events in the detector determine Δm^2 . Characteristics of the detector are shown in Table 5.1. The conceptual design of the proposed detector is shown in Fig. 5.1, while the detector location is shown in Fig. 2.5. The detector is a spherical tank 12 m in diameter. The outer 50 cm volume is optically isolated from the main volume and serves as a veto shield for uncontained events and cosmic rays. The inner (main detector) volume has a radius of 5.5 m and is filled with pure mineral oil such that 75% of the light generated by electrons in the tank is Čerenkov light and 25% is scintillation light. A total of 1220 eight-inch photomultiplier tubes (PMTs) cover 10% of the area of the inner tank.

The outer (veto) volume is equally important for identifying uncontained events and for vetoing cosmic rays. The mineral oil in this region will be optically isolated from the main volume and viewed by 292 PMTs pointing outward. The veto volume is separated from the main detector volume by a 1 cm thick opaque barrier.

In this chapter, details of the detector design are explained. Issues related to the construction are considered, and the electronics and data acquisition

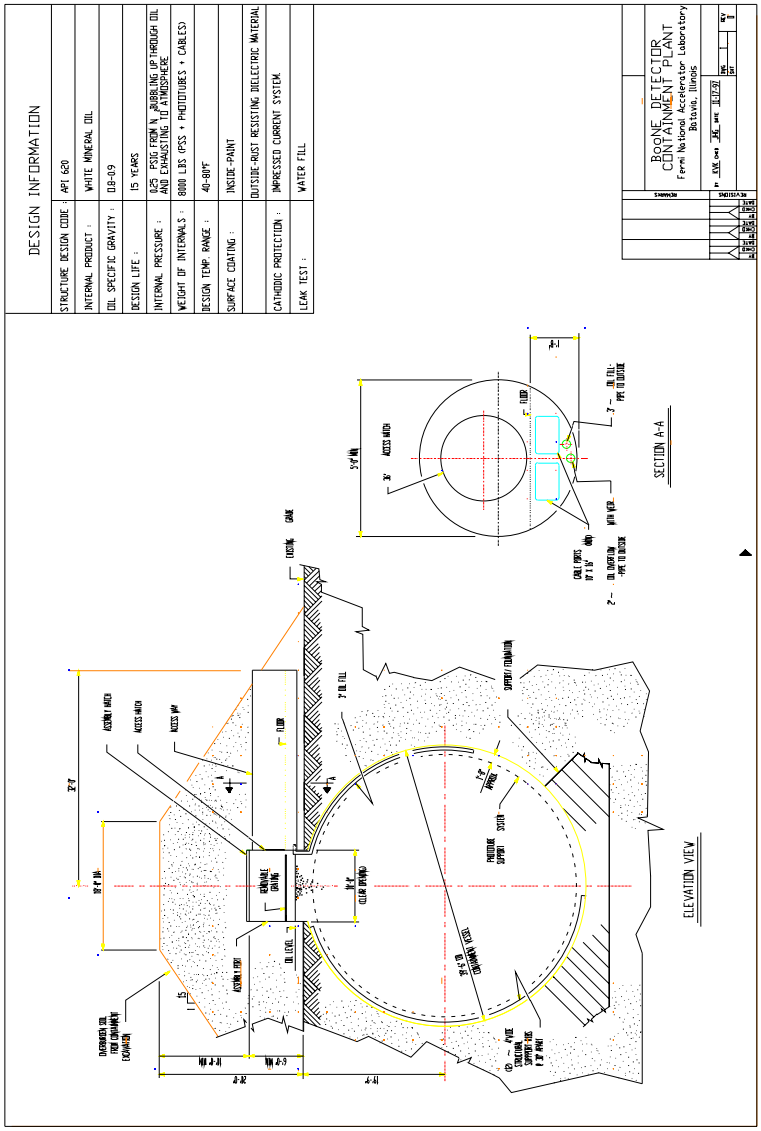

Figure 5.1: The conceptual design of the spherical tank.

Table 5.1: The characteristics of the MiniBooNE detector.

	Detector	Veto
Volume	697 m^3	208 m^3
Mass	592 t	177 t
PMTs	1220(10%)	292
Fiducial Volume	524 m^3	
Fiducial Mass	445 t	

are described. The PMTs, electronics, and data acquisition will be the same as those used for the LSND experiment.

5.1 Detector Construction Issues

The conceptual design for the spherical tank is shown in Fig. 5.1. The tank will be constructed from carbon steel. All portions of the tank exposed to oil will be painted with white epoxy paint. In the design shown, phototube cables exit the tanks through the manhole at the top. In the inner tank, the phototubes will be mounted on the opaque barrier that separates the veto volume from the main detector volume. Veto phototubes will also be mounted on the opaque barrier facing outward. The tank will rest on some minimal foundation, perhaps a gravel bed.

The detector will be placed below ground such that the top of the tank is at ground level. In order to provide protection from weather and dirt while phototubes are installed, an inflatable temporary dome will be placed over the top of the tank. This will be connected to a temporary Porta Kamp where supplies can be stored. After installation of the phototubes, the tank will be filled with mineral oil, and the dome and Porta Kamp will be removed. Finally, a 20' dirt embankment forming a hill over the tank will be restored to provide shielding for the above-ground-level portion of the detector. Electronics will be located in a trailer near to the detector.

In this proposal, the cost estimates for the construction of the tank system are from the Chicago Bridge and Iron Company of Plainfield, Illinois and are for the tank design shown in Fig. 5.1. [61]

5.2 Electronics and DAQ

The front-end electronics and the data acquisition system for MiniBooNE must record the time of occurrence and the charge in each photomultiplier tube pulse,

define a trigger for event selection, and provide for efficient event building. The system must provide time recording resolution of ~ 0.2 ns and charge resolution of ~ 0.2 pe. The system must span time scales of millisecond durations to allow for the correlations of prompt events with signals from subsequent decays. The dynamic range of the charge digitizer must be adequate to meet the needs of the event fitter and the energies that are expected from the neutrino scattering processes. Finally, the system must be low cost and fabricated with appropriate technologies. Since neutrino experiments tend to run for long periods, the system must operate reliably with low maintenance. An updated version of the LSND architecture can meet these requirements. In the following paragraphs the relevant features of the LSND electronics and data acquisition system are reviewed and the updates and modifications for the MiniBooNE experiment are described.

The LSND data acquisition architecture, illustrated in Fig. 5.2, consists of a fast analog front end, a flash analog to digital conversion (FADC) stage, and digital memories to store and sort the digitized data. A block diagram of this system as modified for MiniBooNE is shown in Fig. 5.3. The system operates synchronously with a GPS-referenced clock which provides the 100ns time base. This clock is scaled by a binary counter, the output of which is used as the address to store the digitized PMT data.

Each photomultiplier tube signal is connected to a channel that performs a leading edge time interval determination (the interval being between the PMT pulse and the following edge of the global clock) and an integration of the pulses. The signal acquisition and data timing are shown in Fig. 5.4. These signals are sampled every 100ns by FADCs and the digitized data are written into dual ported memories addressed by the global time base. At each clock tick the charge and time analog voltages are digitized by the FADCs and written into the dual ported memory. The address is then incremented and the cycle repeated. This part of the acquisition system is free running. The memories hold a finite time history (for LSND 204.8 μs with 100 ns resolution). They are configured as circular buffers, that is, the memory is overwritten after the clock has cycled through the address space of the memory. This provides for temporary storage of the immediate past history for a time long enough for a trigger decision to be made by a monoboard computer. It also allows for a pretrigger to determine the state of the detector prior to the arrival of an event, that is, it can "look backwards in time".

Data are extracted from the front-end dual-ported memories and built into events by the trigger system. Each front-end leading-edge discriminator provides a digital pulse to a global summation module, which computes the digital sum of all of the tubes that fired in the previous global-clock interval.

A bank of digital comparators signal when the sum exceeds a preset value and the global-clock time when this happens is loaded into a FIFO memory. The trigger monoboard computer (for LSND it was an MVME-167) continually reads this FIFO. From the resulting times series of multiplicity data the trigger determines the candidate events and initiates an event build by broadcasting those global-clock times when the particular event took place to the other address port of the dual-ported memories that contain the PMT charge and time data. The system transfers the data at these "event time stamps" from their temporary location to FIFOs located adjacent to the dual-ported memories, where the data resides until read by other monoboard computers. These computers (MVME-167) calibrate and compact the data, assemble them into ethernet packets, and send them to the experiment's analysis computer. A system configuration diagram is shown in Fig. 5.5.

Modifications to this system for MiniBooNE would include the design of the appropriate trigger hardware and the modifications to the trigger acquisition code. The front-end electronics is being redesigned to make use of faster, cheaper memory to allow a larger circular buffer for a longer recorded history. A revision of the digital architecture (all components reside in VME crates) is being undertaken to simplify the dedicated data and addressing lines and keep compatibility with the VME standards. This aims to improve the reliability and reduce system costs. A new, all digital time interpolator is in design to enhance the time resolution to the 0.2 ns specification. Finally, a 10-bit or 12-bit FADC is being considered to meet the resolution-dynamic range requirements on the charge measurement. Alternatively, a dual slope analog front end is being designed that has piecewise linear gains and which matches the desired low pulse height sensitivity and large pulse height dynamic range onto the 2V range of the FADCs.

The size of each PMT time window is determined by the trigger computer software, as is the triggering decision. It is straightforward to modify the trigger code to configure the above system for running with the beam time structure of the Fermilab Booster. For example, the front-end electronics would be left free running so that the prehistory could be acquired. When the Booster delivers a proton pulse to the target, a timing pulse would be generated and sent to an unused "PMT input" in the DAQ system. This would allow a precise time determination of when to begin considering events as neutrino candidates. The front end continues to record the activities in the detector, then after all anticipated events are finished, the trigger would read all of the data in the dual-ported memories. (It is more likely that such a read would begin sooner to remove any time overhead, but this is a detail in the design. The LSND system runs continuously and only reads that part of memory that

contains a window 500 ns wide around a candidate event's time stamp. The LSND system notes whether or not the accelerator has spilled beam on the neutrino production target by recording the beam status through an unused "PMT channel" as described above. Beam off events are handled identically to beam on events. The trigger does not know if the accelerator is off or on and as such is unbiased. This also allows a large sample of the background to be collected, which has been of great importance for LSND. It is not as critical to the MiniBooNE experiment, which takes place at higher energies. It may be relevant to ν-p elastic scattering studies, however.

5.3 Trigger Operating Modes

The data transfer rate on the VME backplane of a QT crate is set by the monoboard computer (MBC). For LSND a Motorola MVME167 was used and had a maximum transfer rate of 20 MBytes/s, which was realized by one VME bus cycle every 200 ns. With this rate it required 13 μs to collect one time-stamp record of a full loaded QT crate, consisting of 128 PMT channels plus one header long word (260 bytes of data). To collect the six time-stamp records of an event molecule required 78 μs.

Conventional LSND DAQ operates with the trigger controlling the event builds and only selected event molecules being read from QT memory into MBC memory. In this mode the VME back plane traffic is low. In view of the (relatively) low repetition rate of the Booster, several alternative modes of operation are possible. A "zero-threshold mode" that records the full detector history and a hybrid scheme that expands the history window are possible, as is a reduced threshold mode that would provide some data sparsification at the trigger level. For example, the MiniBooNE DAQ could operate in several different scenarios:

1. LSND-mode where by an initiating "high-threshold trigger" flags a"low-threshold mode" and selected events are built. This has low back plane traffic, but at the cost of a threshold for events.

2. Zero threshold-mode where the front-end clock is enabled $\sim 50\mu$s before the proton spill begins, the time of the spill is recorded, and the clock is allowed to run for (204.8-50.0) μs before being shut off and the entire QT memory is read into MBC memory. This mode collects the entire time history of the detector from $\sim 50\mu$s prior to the spill to $\sim 150\mu$s after the spill. It requires between 13 ms to 26 ms of back plane time to read the QT memory into the MBC. Assuming a worst case of a repetition rate of 15 spills per second (66 ms per spill), this mode allows for an overhead of at least 40ms between spills for MBC processing and full event building to the main acquisition computer.

3. A hybrid scheme that takes advantage of the buffering capability of the LSND front-end memory system. This scheme leaves the front-end clock running continuously and initiates QT-memory-to-FIFO transfers $\sim 20\mu$s before the spill. This QT-memory-to-FIFO link is maintained until the FIFOs are half full, where upon the trigger interrupts this link and operates now in the LSND-low-threshold mode. The QT-FIFO readout is begun by the MBC as soon as there is data in the FIFOs, which would occur at the $\sim 20\mu$s before spill time. Notice that the data flow is event driven with throttling controls (N.B., the use of the half-full flags on the QT FIFOs) and FIFO buffer capacity to allow for smooth transfer between the no-threshold and low-threshold modes of operation.
4. A modified hybrid scheme which combines the timing with respect to the beam spill with a low threshold (but not zero) to collect events that had, e.g., greater than 4 PMTs on, rather than collect everything, which would be mostly zeroes and burden the data acquisition for no good reason.

To implement these schemes on the LSND DAQ system requires the addition of a hardware card to signal the proton spill timing and the writing of new trigger software.

5.4 Calibration System

The calibration system is designed to (1) provide information on the phototube (PMT) response that is needed as input for the event reconstruction and particle identification calculations and (2) calibrate the position, energy and direction determination of the reconstruction program using stopping cosmic ray muons and decay electrons.

5.4.1 The Laser Calibration System

A laser calibration system similar to the ones successfully employed on the LSND and CHOOZ [62] experiments will be used. The primary purpose of this system is to quantify and monitor pertinent properties of each individual PMT including PMT gain, pulse height vs. photoelectron linearity, and timing. Other system functions include the monitoring of light attenuation of the oil over the lifetime of the experiment and the reconstruction of the light source location. The system will consist of a laser light distribution system, several (≥ 7) light dispersion flasks fixed at various locations in the detector, and long ($\geq 20\ m$) fiber optic cables that carry the laser light from the distribution system to each flask.

The laser light distribution system will be housed in an enclosure in close

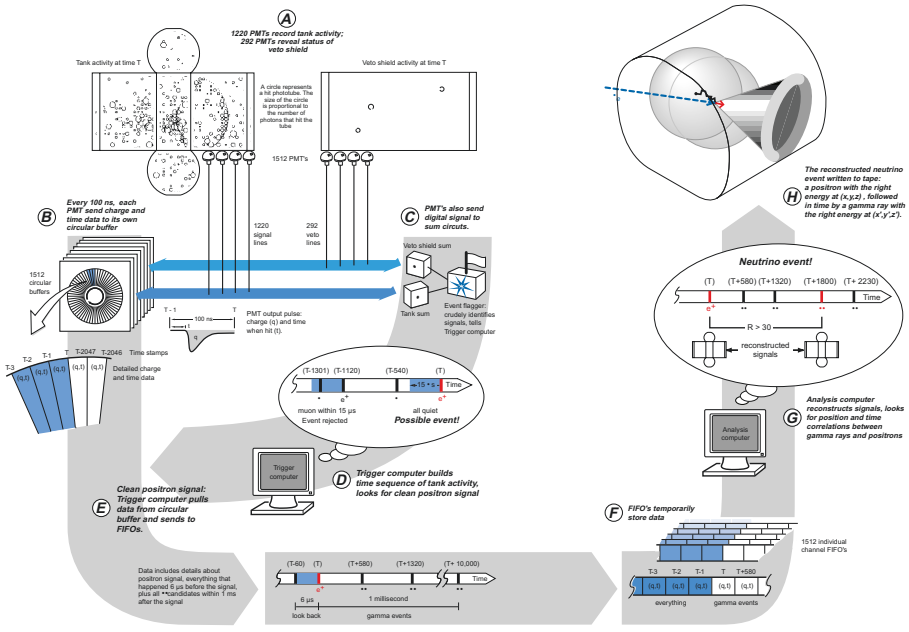

Figure 5.2: The LSND DAQ system.

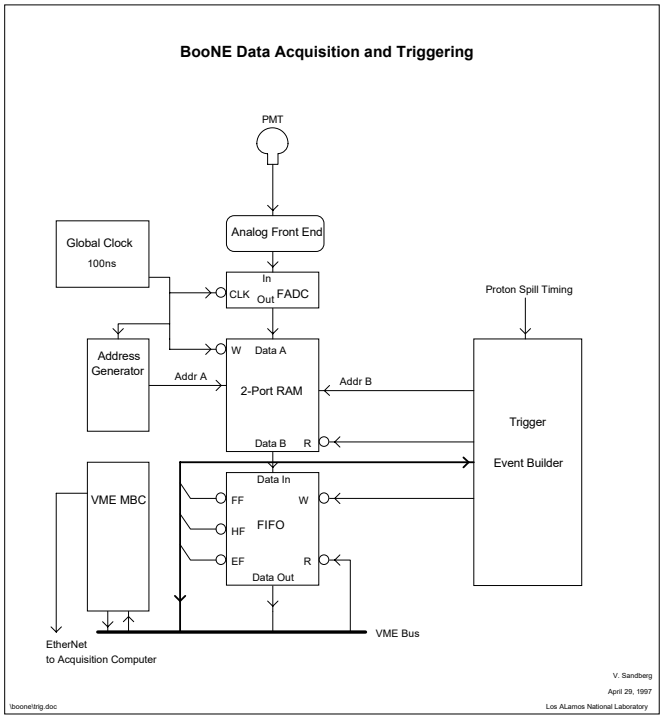

Figure 5.3: The proposed MiniBooNE PMT channel data acquisition.

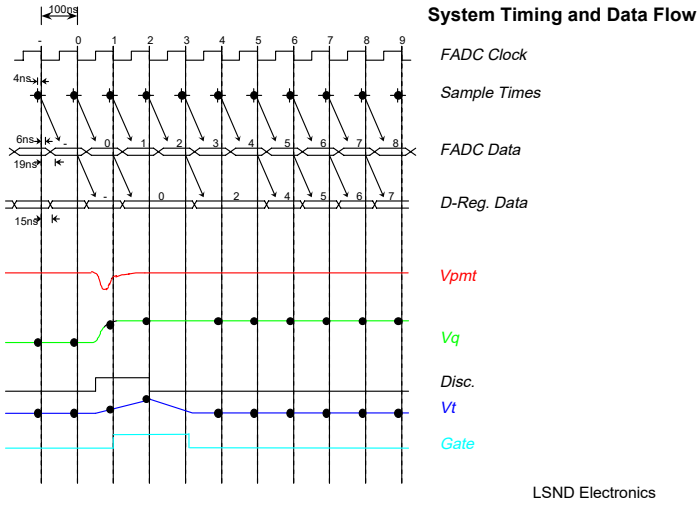

Figure 5.4: PMT pulse acquisition and signal timing relationships.

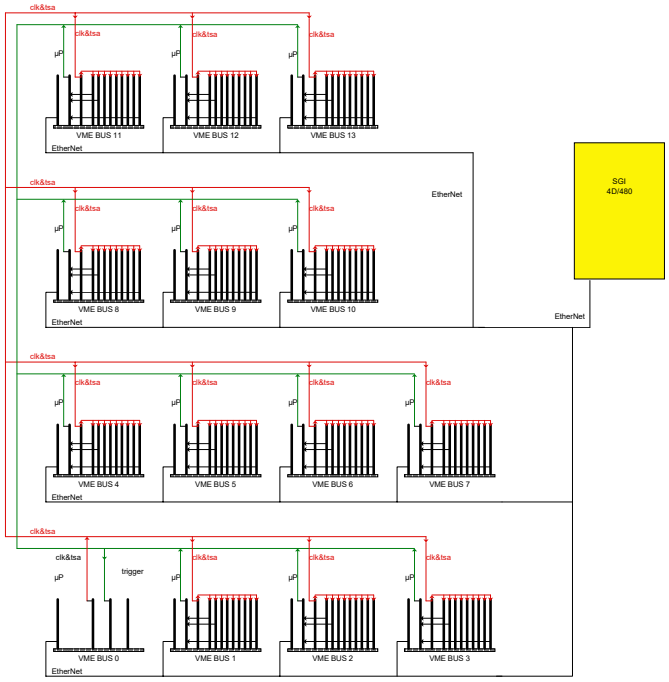

Figure 5.5: System configuration of the individual VME QT crates and their interconnections.

proximity to the detector. It will consist of a nitrogen laser generating ≤ 5 ns pulses, a motor-controlled attenuation system, reference photodiodes, and a mechanical splitter device that determines which fiber gets light. Two mechanical splitters under consideration are a motor-driven movable mirror which would direct the laser light to individual optical fibers and a remote-controlled shutter blocking system. Because nitrogen laser systems are notoriously noisy, part or all of the laser light distribution system will be enclosed in a Faraday Cage.

The light will be carried to the dispersion flasks by 200 micron quartz optical fibers. Each flask will be a spherical glass bulb with an inner diameter of ≥ 6 cm.The exact size and method of connection of the flask to the optical fiber is to be determined. The flasks will be filled with a dispersive medium such as Ludox or liquid scintillator, which are used by LSND and CHOOZ respectively.

A stand-alone control system would operate the laser system running a real-time control program, such as LabView, on a dedicated PC. The reference phototubes or photodiodes would provide a tag signal for the MiniBooNE DAQ. The reference photosensors would be calibrated with low activity radioactive sources. As was done in the LSND experiment, the laser could be pulsed at ~ 0.1 Hz continuously and asynchronously with the accelerator during normal data taking and at 20-30 Hz during beam off periods for special runs. Gain calibrations could be obtained from low light intensity runs by fitting the resolved single photoelectron peak for each individual PMT. The special runs could be with high light levels to provide timing offsets for all channels. Timing information from all the channels would be used to calculate a mean time slewing correction to be applied to each PMT.

5.4.2 The Stopping Muon Calibration System

The stopping muon calibration system will use stopping muons and their decay electrons to calibrate the event reconstruction program. This calibration system will provide a precision calibration of the energy, direction and position of muons for the complete range of muon energies of interest in the experiment. It will also provide a calibration for 50 MeV electrons from the observed decay electron energy spectrum. A muon tracker located above the detector will be used to determine the entering positions and directions of muons which stop in the detector. The stopping positions can be determined from the locations of the decay electrons. The muon energy can then be obtained from the muon range with an uncertainty due to range straggling of approximately 3%. The determination of muon energy from range is a well established technique in

this energy region.

Six scintillation spheres described below will be used to obtain samples of stopping muons and decay electrons for which the absolute stopping positions are known with uncertainties of less than 3 cm. For these samples the uncertainties in the muon energies will arise almost entirely from range straggling. In addition, these spheres will provide an absolute calibration of the positions obtained with the event reconstruction program at these six locations.

The muon tracker will cover an area of approximately 10 m^2 above the detector and will be used to determine the positions and directions of muons entering the detector. The tracker will be located in the small room that is at the center of the horizontal access tunnel. A satisfactory tracker can be built relatively easily using either chambers or scintillation counters. Due to multiple scattering of the muons in the detector it is only useful to measure the entering muons with a position resolution of 5 cm (RMS) and with an angular resolution of 0.1 radians (RMS). We plan to build a scintillation tracker with these resolutions. There will be 6 planes of scintillator (3 for x and 3 for y). Each plane will have 24 strips $5''$ wide and $10'$ long. There will be two $2''$ PMT per strip, one on each end. The signals from both ends will be added and then discriminated. The status of the 144 discriminator channels will be recorded for each event.

The present plan is for the muon tracker to consist of six $10' \times 10'$ planes of liquid scintillator. Each plane would be a single tank, $2''$ thick, with optical dividers every $5''$ providing the desired segmentation. Existing supplies of liquid scintillator would be used. It would also be possible to use plastic scintillators with fiber readout similar to the scheme adopted by MINOS. This might make sense if coordination with MINOS resulted in low cost for the components.

Six optically isolated scintillation spheres will be permanently located in the detector below the muon tracker. Each sphere will be 3 cm in radius and will have optical fiber or photodiode readout. Over 500 muons per month will stop in each sphere and decay. The positions of the spheres in the detector will vary from 30 cm to 500 cm from the detector surface so that stopping muons from 100 MeV to 1 GeV can be measured. For such events we will measure the muons with the muon tracker, with the detector and with the scintillation sphere. The decay electrons will be measured in delayed coincidence in both the scintillation sphere and in the detector. The muon range inside the detector will be extremely well determined for these events so that the muon energy resolution should be close to the 3% uncertainty arising from range straggling. The absolute energy calibration obtained by averaging over many events, will have a systematic uncertainty of approximately $\pm 1\%$.

These six spheres will also provide an absolute position calibration for muons and decay electrons at their locations in the detector. The locations of the spheres at various depths in the detector will allow us to determine and correct for any systematic bias in the position determination. For this purpose, all muons which stop in the spheres can be used, whether or not they traverse the muon tracker. The positions of the reconstructed stopping muons and decay electrons will be compared with the known sphere position. A trigger for these events would be the presence of both muon and electron pulses in sequence. This calibration will be performed as a function of particle energy and direction. We will also obtain position resolutions as a function of particle energy. In summary, this calibration will provide a very useful test of the performance of the event reconstruction program.

5.5 Pure Mineral Oil Tests

Data were taken in August of 1993 with the LSND tank filled with pure mineral oil before the b-PBD scintillator was added. The trigger for this first data run of LSND consisted of a stopping cosmic-ray muon trigger that required a cosmic-ray muon that fired the veto shield followed by a decay electron. Figs. 5.6 and 5.7 are event displays for a typical stopping cosmic-ray muon and correlated decay electron. The tank has been unfolded onto two dimensions, and each circle corresponds to a hit PMT with area proportional to the PMT charge. Note that the 40 MeV electron in Fig. 5.7 is, roughly speaking, similar to what a 100 MeV electron will look like in MiniBooNE because the LSND and MiniBooNE PMT area coverages are 25% and 10%, respectively. Fig. 5.8 shows the muon decay time and the phototube charge and multiplicity distributions for the triggered decay electrons, while Fig. 5.9 shows the x,y,z spatial distributions of these decay electrons, where y is vertical and z is approximately along the neutrino direction. The measured charge per electron energy was about 10 photoelectrons/MeV, which is about 1/3 the light output of the final LSND mixture of mineral oil plus 0.031 g/l of b-PBD. Fig. 5.10 shows the time distribution of the measured light relative to the fitted event time. About 3/4 of the light is in the main Čerenkov peak, while 1/4 of the light is scintillation light with a time constant of ~ 35 ns. This information is included in the detector simulation that is discussed in the following chapter. Note that mineral oil scintillates due to impurities that necessarily occur in the oil. The 3 to 1 ratio of Čerenkov to scintillation light is close to optimal for event reconstruction and particle identification. There is sufficient late light to measure the scintillation light fraction but sufficiently little isotropic light so as not to obscure the Čerenkov cone. We have the capability of adding b-

PBD scintillator to the oil to increase the scintillation fraction, and the precise amount of scintillation light over time can be determined from the fraction of late PMT hits.

The issue of whether or not "pure" mineral oil (MO) produces scintillation light appears to have no simple answer as MO is not a well characterized substance. The linear chains that constitute the bulk of a MO sample do not facilitate the development and propagation of visible light arising from the stopping of charged particles via collisions with electrons in the oil. However, if traces of benzene-like rings are present in the MO sample, it is possible that scintillation light will be produced and the material will be transparent to light at this wavelength. Such scintillation light would be particular to the sample being tested and can not be taken as quantitatively characteristic of MO. The material's history and trace contaminates will dominate the scintillation light characteristics.

To investigate its suitability for MiniBooNE, measurements of the scintillation light produced by the MO used as the base in LSND were carried out. This sample of MO contained no known additives and had been in storage under dry nitrogen at Los Alamos for about 5 years.

The samples were exposed to 120 MeV deuterons from the Texas A&M Cyclotron and the light detected in a 5cm diameter Phillips XP2232B PMT. Fig. 5.11 illustrates the set up. The deuteron beam (1500 d/sec) emerged from the beam pipe, passed through a thin (1mm) trigger scintillator and then traversed the 5 cm inner diameter of the cylinder containing the MO. The 120 MeV deuterons lost an average of 57 MeV in the MO. A trigger pulse associated with each beam particle gated the ADC recording the integrated charge from the PMT. Fig. 5.12 shows the recorded charge with the beam directed along a diameter 1 cm in front of the face of the PMT, with the cylinder filled with air, water, and MO respectively. There is a clear signal of scintillation light from MO and none from the air or water. Fig. 5.13 shows the measured charge as a function of distance between the beam trajectory and the face of the PMT expressed as the average number of detected photoelectrons (PE). The number of detected PEs is observed to be directly proportional to the solid angle of the beam path subtended by the PMT. A fit to the data reveals 0.83 ± 0.07 PEs/MeV of beam energy loss. The average number of PEs created by these traversing deuterons is approximately 14% of the number created by Čerenkov radiation from a fully relativistic particle traveling the same path. Fig. 5.14 is the PMT output for a single passage of a beam particle as recorded by a Tektronix TDS 620. The upper trace is the signal from the trigger while the lower trace shows the PEs from the MO sample. The horizontal scale is 20ns/div. The PE time distribution is consistent with a scintillation decay

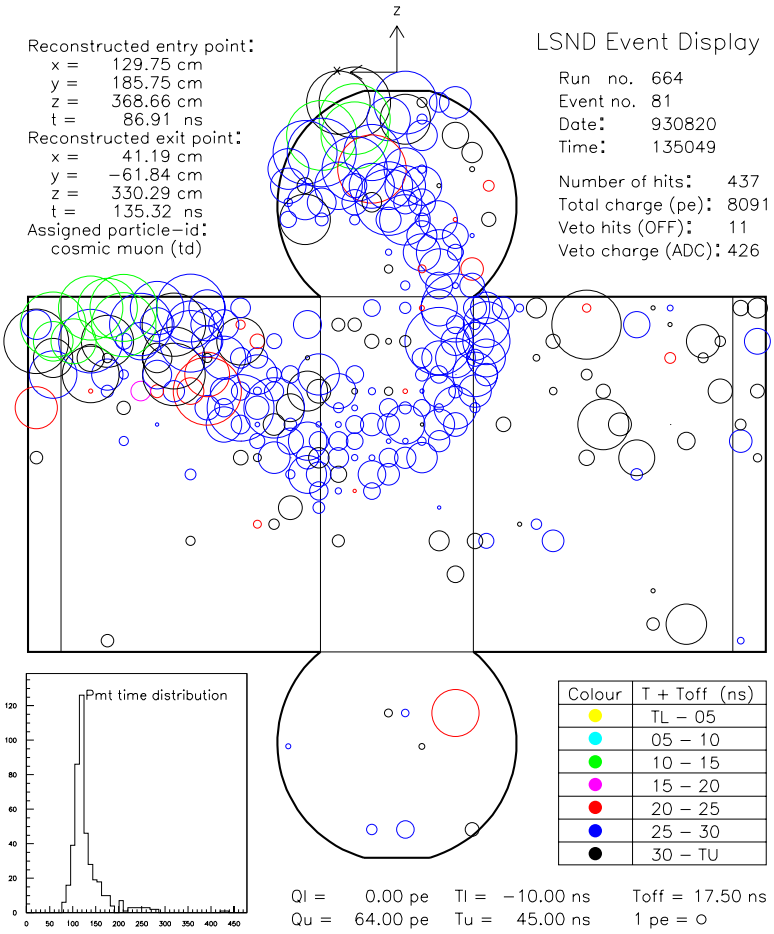

Figure 5.6: The event display for a typical stopping cosmic-ray muon. The tank has been unfolded onto two dimensions, and each circle corresponds to a hit PMT with area proportional to the PMT charge.

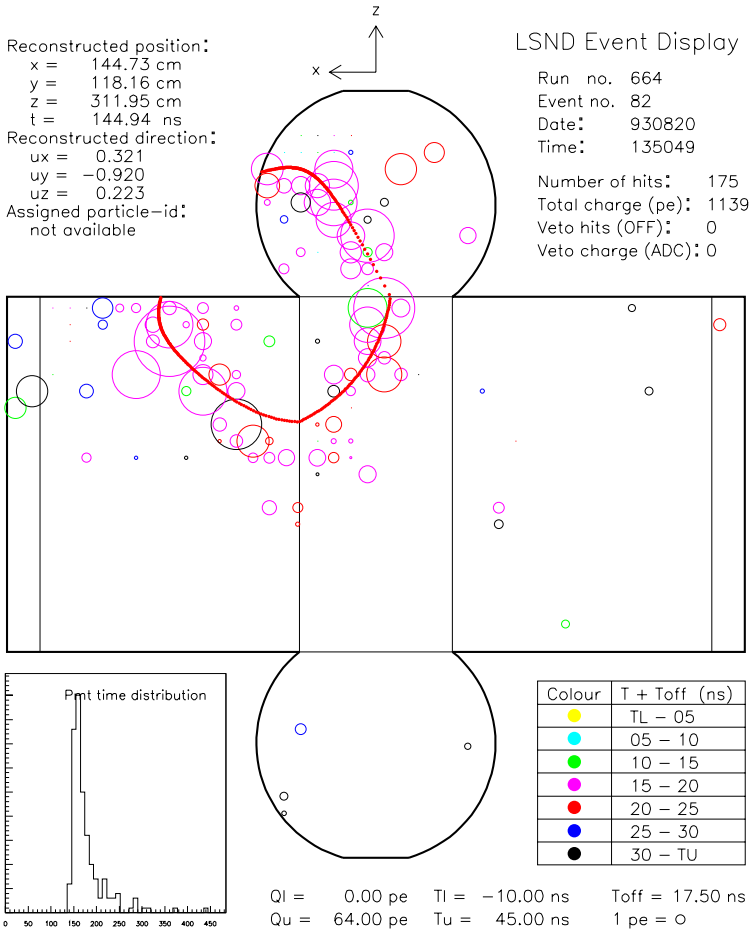

Figure 5.7: The event display for a typical decay electron. The tank has been unfolded onto two dimensions, and each circle corresponds to a hit PMT with area proportional to the PMT charge.

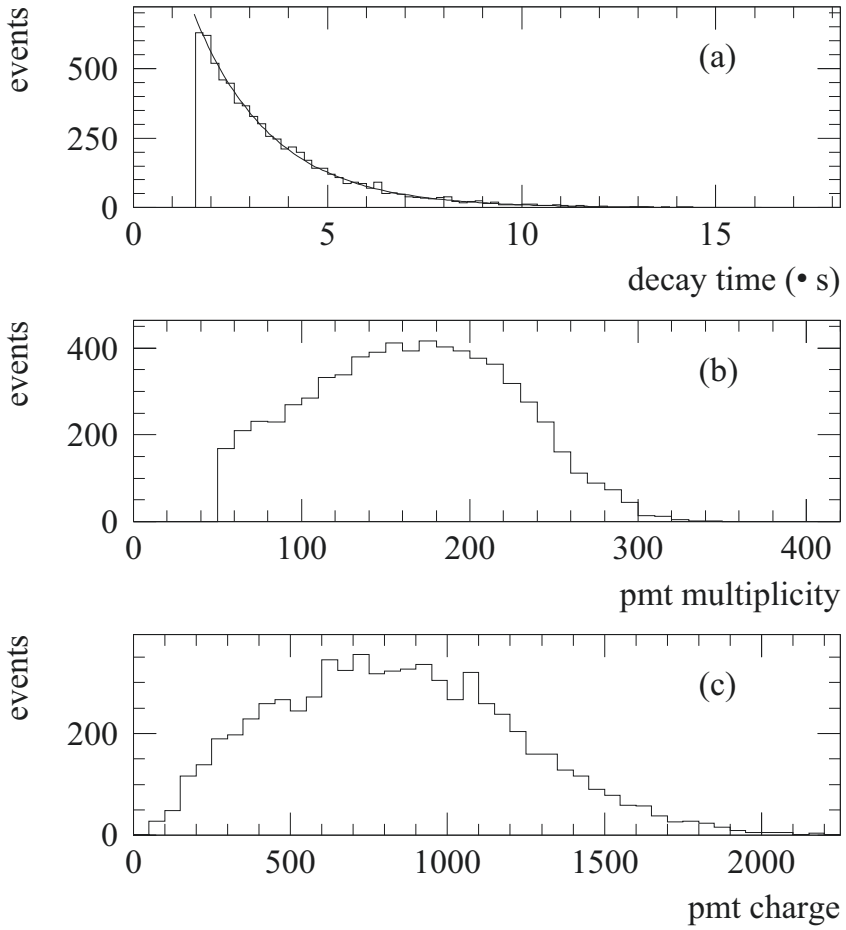

Figure 5.8: The muon decay time and the phototube multiplicity and charge distributions for the triggered electrons from muon decay.

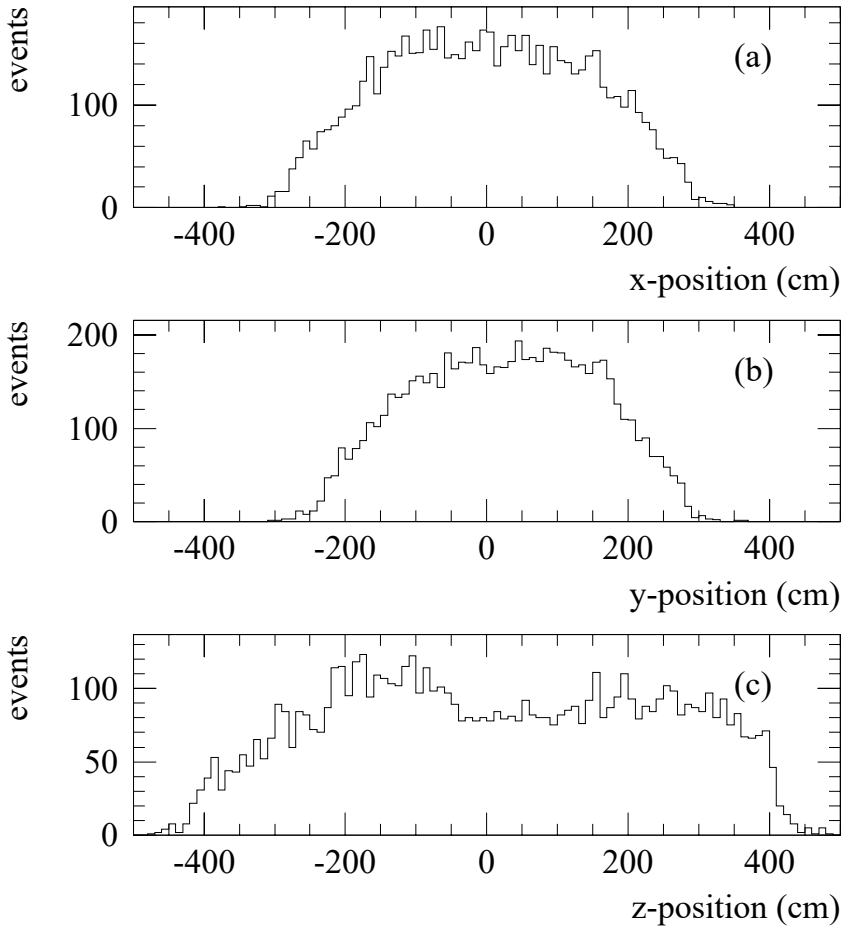

Figure 5.9: The x,y,z spatial distributions of the electrons from muon decay, where y is vertical and z is approximately along the neutrino direction.

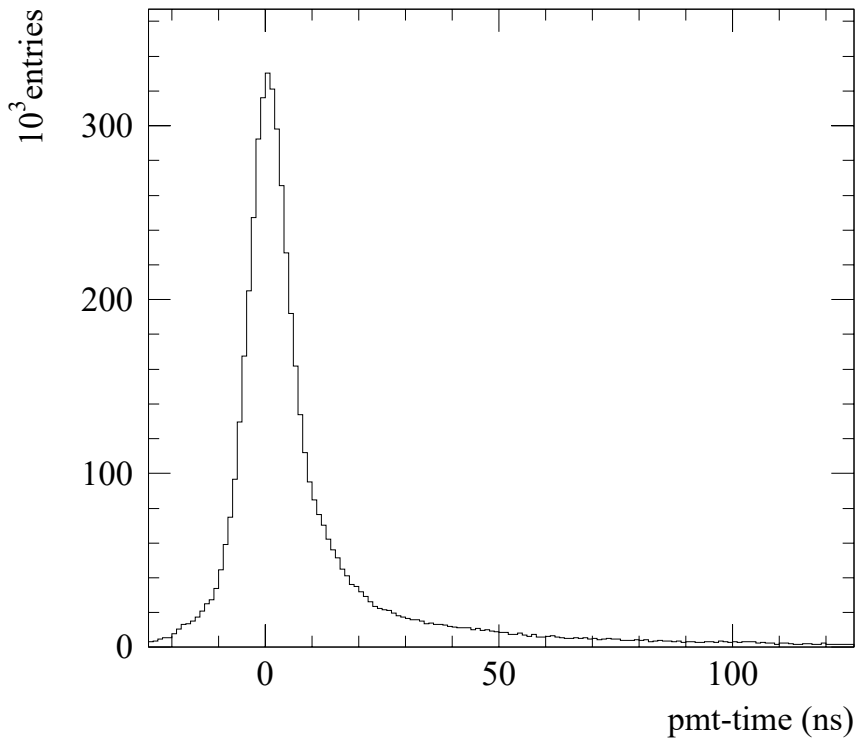

Figure 5.10: The time distribution of the measured light of electrons from muon decay relative to the fitted event time.

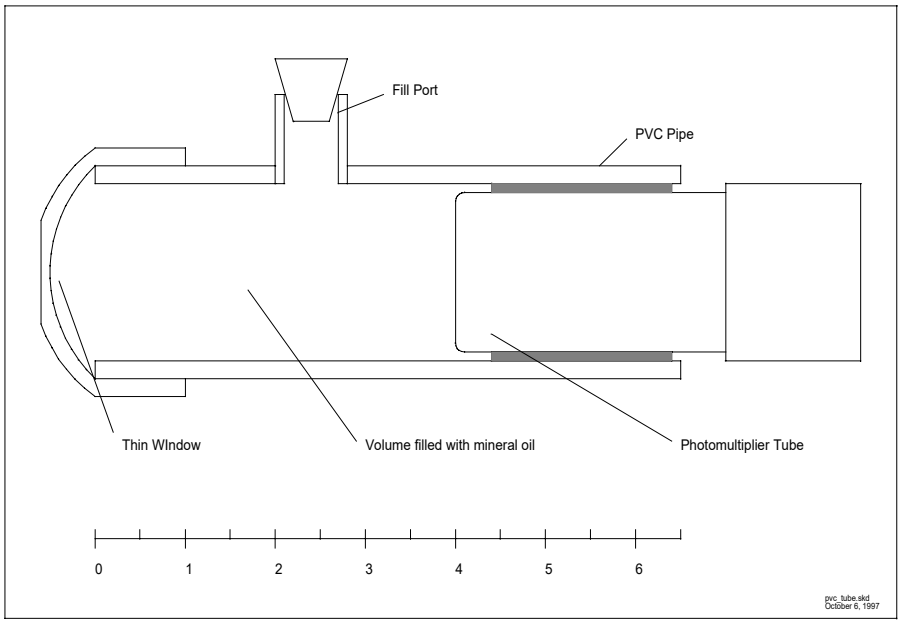

Figure 5.11: An illustration of the setup for the tests at the Texas A&M Cyclotron.

time of ~ 30 ns .

Another sample of MO from an entirely different source was tested and it produced similar results except that the light output was 3 times lower. However, the decay time of the scintillation light was approximately 30 ns, consistent with the above sample. Thus, it appears that commercial samples of MO do scintillate and the scintillation light will be appreciably delayed relative to prompt Čerenkov light, although the amount of light varies depending on the sample and will have to be measured before use in an experiment such as MiniBooNE.

5.6 GEANT Simulation of the Detector

The proposed MiniBooNE detector was simulated using the GEANT Monte Carlo package. A spherical tank filled with mineral oil was coded into the program with dimensions as described at the beginning of this Chapter and in Table. 5.1. An approximation of a PMT was modeled and multiple copies were positioned as shown in Fig. 5.15.

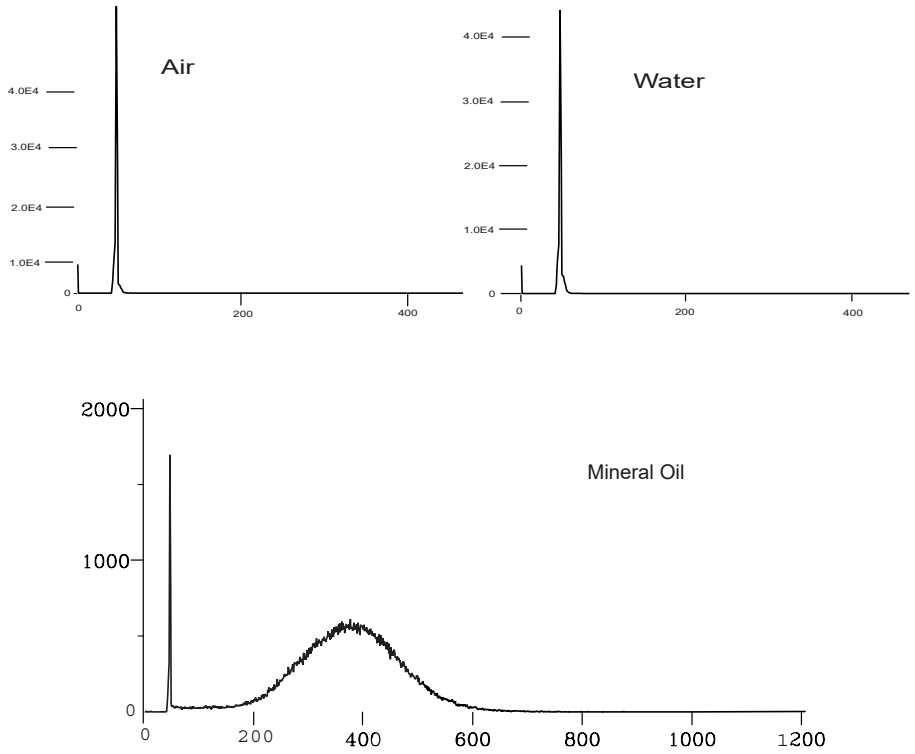

Figure 5.12: The recorded charge with the beam directed along a diameter 1 cm in front of the face of the PMT, with the cylinder filled with air, water, and MO respectively.

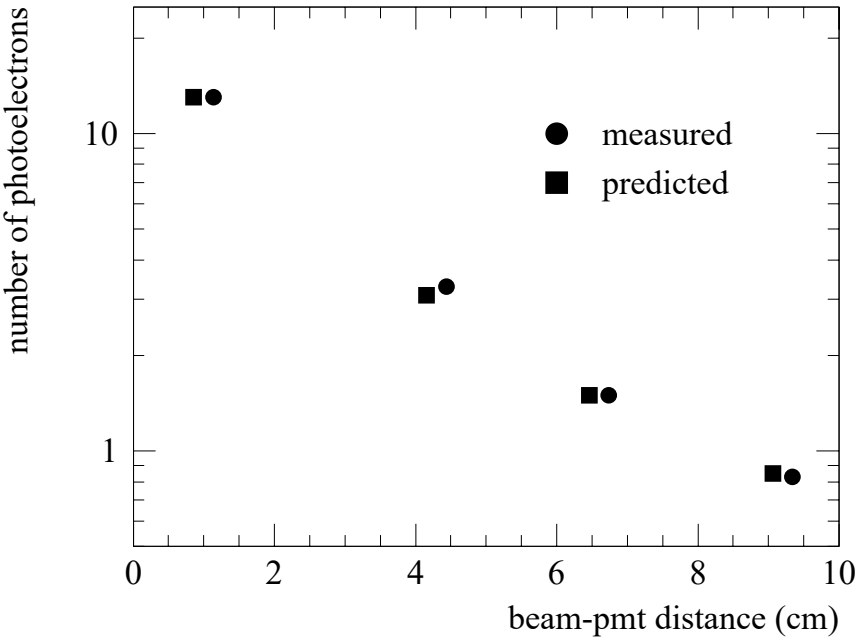

Figure 5.13: The measured charge as a function of distance between the beam trajectory and the face of the PMT expressed as the average number of detected photoelectrons (PE).

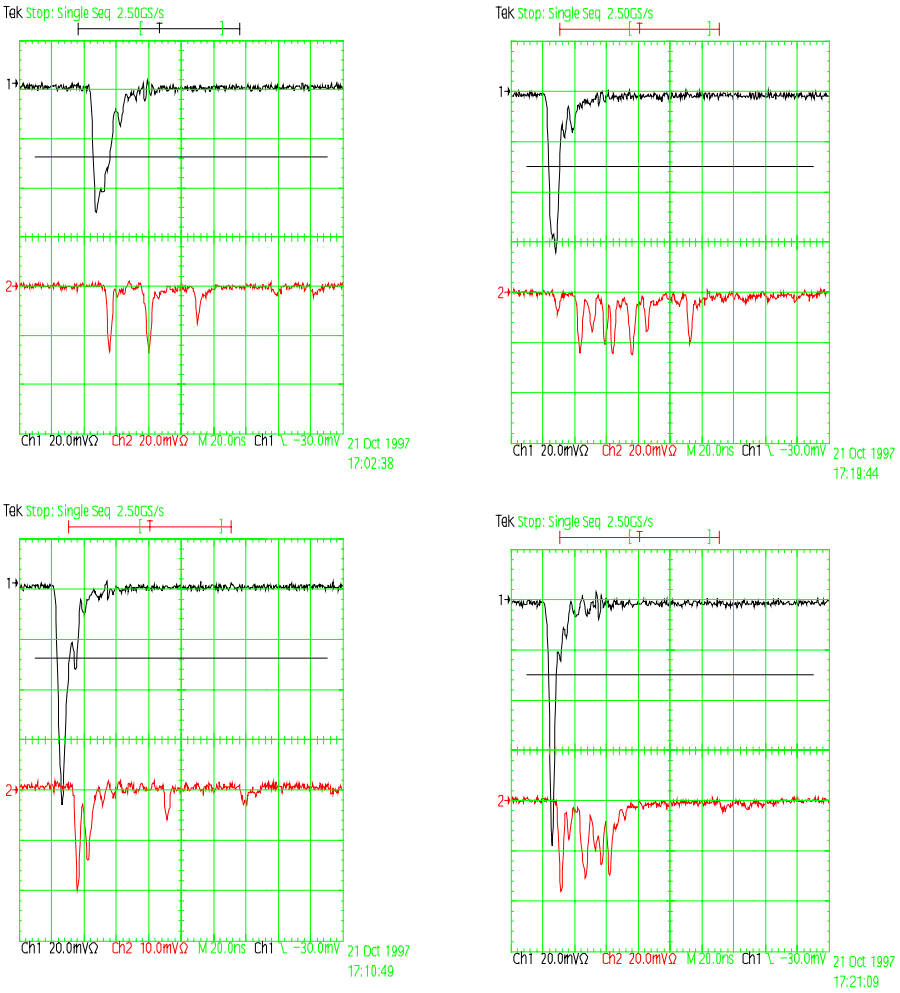

Figure 5.14: The PMT output for a single passage of a beam particle as recorded by a Tektronix TDS 620. The upper trace is the signal from the trigger while the lower trace shows the PEs from the MO sample. The horizontal scale is 20ns/div.

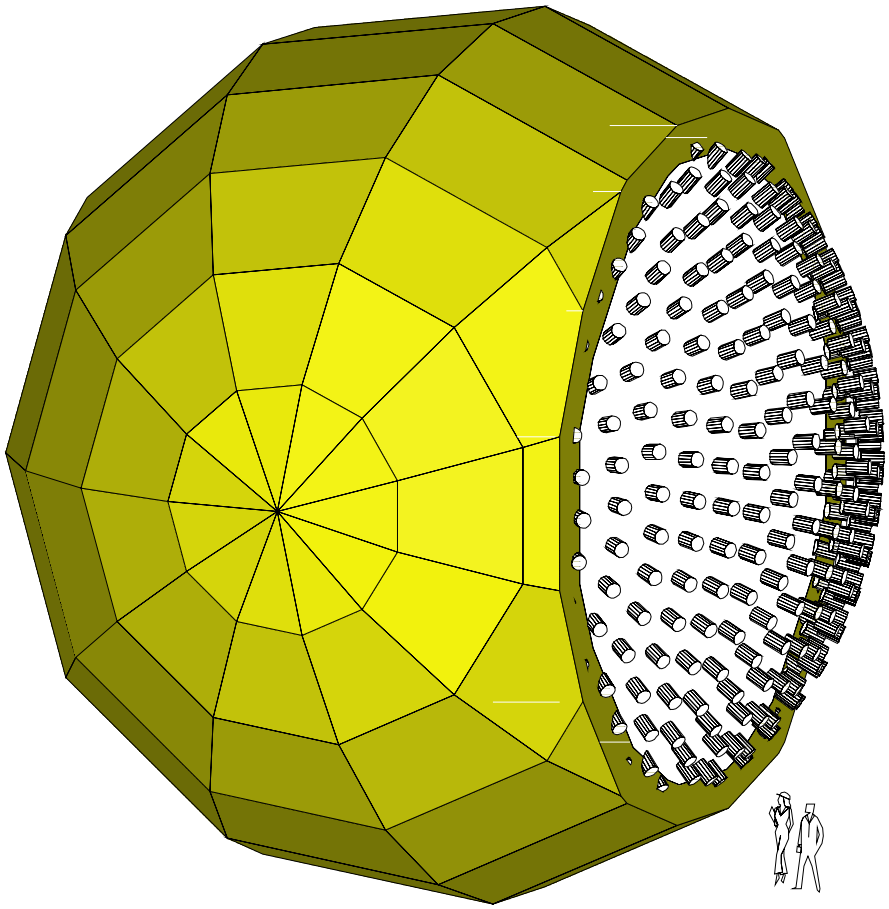

Figure 5.15: GEANT-generated schematic of the proposed detector.

The GEANT implementation (V3.21) simulates the production of Čerenkov light for particles with velocities above threshold and tracks this light through the media using the (wavelength-dependent) optical properties of the mineral oil. This optical photon tracking was also used to track scintillation photons that were generated isotropically and in proportion to the amount of energy lost by charged particles in the mineral oil. These optical photons were tagged as Čerenkov or scintillation photons so that the amount of scintillation light could be adjusted in the reconstruction phase. If an optical photon intersected the photocathode surface of the PMT volume, it was "detected" with an efficiency equal to the wavelength-dependent quantum efficiency of the PMT. These PMT "hits" were written to an ntuple along with the veto and input particle information.

In order to study the response of the proposed detector, first, single particle ($\mu^{\pm}, e^{\pm}, \pi^0$) events were generated isotropically over a range of energies (50-2000 MeV) within the mineral oil volume of the inner tank. Then, to better understand the relative rates for the signal and background reactions, multi-particle events of interest to the MiniBooNE experiment were simulated. The most important reactions studied were: $\nu_e C \to e^- X$, $\nu_\mu C \to \mu^- X$, and $\nu_\mu C \to \nu_\mu \pi^0 X$. The final states of these reactions often include an energetic proton which was included in the simulation. These events were generated within the fiducial volume of the inner tank and were weighted by the estimated cross sections and neutrino fluxes.

Chapter 6

Event Analysis

The GEANT-based detector Monte Carlo package accurately simulates events in the detector and allows the determination of the event reconstruction resolutions and the particle identification efficiencies. All of these techniques have been developed and tested at the LSND experiment.

This chapter describes the event analysis. The first section gives an introduction to the expected signals from particles in the detector. This section describes the expectation in very general terms. The second section provides the specific technical details of the chi-squares which are minimized in order to reconstruct an event and perform particle identification. The third and fourth sections discuss electron resolutions and particle identification. Systematic uncertainties are described in section five. Finally, a maximum likelihood charge and timing event reconstruction is described in the last section.

6.1 Introduction to Events in the Detector

The purpose of this section is to provide an intuitive understanding of events in the detector. The technical description of how this information is used is found in the following sections of this chapter. The general ideas behind event reconstruction in Čerenkov counters have been developed in a wide range of experiments, including LSND, IMB, Kamioka and Super Kamiokande.

This detector records information on:

- The phototube which was hit
- The timing of the initial hit for each tube

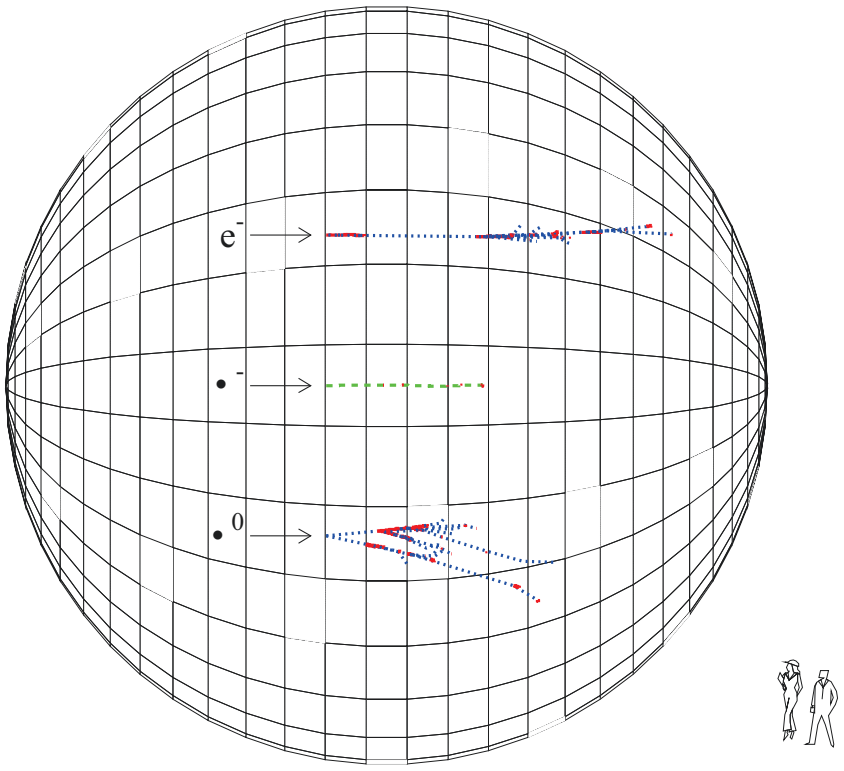

Figure 6.1: Example topologies of 500 MeV electrons, muons, and neutral pions in the detector tank.

Table 6.1: Some principles of particle ID in MiniBooNE

	Čerenkov Ring	Track Extent	Timing of hits
electrons	• $\beta \approx 1 \rightarrow \alpha = 47°$ Ring is "fuzzy" due to due to multiple scattering and bremsstrahlung	short track	More prompt (Čerenkov) than late (Scintillation) light
muons	Sharp outer edge of Čerenkov ring, diffuse inner edge of ring	Long track (Many exit detector)	high fraction of late light (less time above threshold)
π^0s	Two rings	Extended source region	Energetic recoil proton produces scint. light

- The number of photoelectrons
- The veto hits in an event.

Based on this information, events can be reconstructed, (*i.e.* mean track position and direction determined) and particles identified, as summarized in Table 6.1. The mean position of the track is required to be within the fiducial volume of the detector.

The main goal of the event reconstruction and particle identification is to separate quasi-elastic ν_e scatters producing an electron from the background of muons and single π^0s. As illustrated in Fig. 6.1, electrons, muons, and neutral pions have quite different topologies in the tank. In general, most muons are identified by the veto. Most muons which stop in the detector will decay, however 8% will be captured. Decay muons are identified by two tracks (as shown in fig. 6.1). Stopped muons which capture must be identified by their signature of photons in the tank, as discussed below. Those muons which are not cut represent a background to the analysis. In general, neutral pions are identified as having two electromagnetic tracks, one from each photon. Highly asymmetric decays represent a background to the analysis.

Čerenkov and scintillation light are produced by charged particles above threshold in the detector. For the case of electrons, the detector sees ∼75% Čerenkov light and ∼25% scintillation light. The Čerenkov light will form a ring while the scintillation light is isotropic. Because the scintillation light results from atomic transitions, these photons have a high probability of arriving at the phototubes later than the Čerenkov light in an event, which is, therefore, described as "prompt." Thus both the ring and the timing distinguish the scintillation light from the Čerenkov photons.

The direction and angle of the track can be reconstructed based on minimizing the difference between timing and position of phototube hits with respect to a hypothesis track. Consider a track which is traveling faster than the speed of light in the oil. For the case of tubes downstream of the track, photons from the downstream end of the track will arrive before those from the upstream end. Also, the Čerenkov ring will have a smaller radius for photons from the downstream end compared to the upstream end. When discussing "late" or "early" hits, this is with respect to the timing of the midpoint of the reconstructed track. Thus for an extended track, photons from the downstream end are most likely to arrive early. Typically, a charged particle will produce thousands of photons.

Intuitive information can be gained from considering event displays. An event display has not been written for MiniBooNE, however the LSND event display is instructive for electrons (fig. 5.7) and muons (fig. 5.6). These data were taken with pure mineral oil in the LSND detector, as discussed in section 5.5, above. Hits are color coded to represent timing information.

Electrons have relatively short tracks and are at $\beta \approx 1$. So naively one would expect these particles to produce well defined Čerenkov rings with opening angle $\alpha = 47°$ in mineral oil. However, multiple scattering and bremsstrahlung typically smear the ring associated with an electron. The electron remains above Čerenkov threshold throughout most of its path in the detector, thus the photons are predominately prompt.

The track length is useful for identifying muons. Many muons will exit the detector firing the veto tubes. The timing and position information for the hits associated with a muon will combine to indicate an extended source or, in other words, a long track. Muons which traverse the detector produce hits in nearly all of the phototubes. Lower energy muons may decay within the detector. In this case, the track reconstruction will indicate the presence of the initial track followed by the secondary track from the electron.

When running with a neutrino beam, μ^- are produced by the quasi-elastic scattering process and 8% of these muons are captured in the oil. These muons can be distinguished from electrons through the distinctive Čerenkov and scintillation signatures. Initially, most muons will be of sufficiently high energy that $\beta \approx 1$, producing a Čerenkov ring consistent with $\alpha = 47°$. Because muons suffer less multiple scattering than electrons, the outside edge of this Čerenkov ring remains sharp. However, as the muon slows in the oil, the Čerenkov angle becomes smaller, thus the inner region of the ring "fills in" with photons. The muons will drop below threshold earlier than the electrons, resulting in a larger fraction of late to prompt light in a muon event. The hits can be compared in Figs. 5.7 and 5.6 for data from LSND.

Recoil protons from the quasi-elastic interactions are below Čerenkov threshold. Thus they produce only scintillation light.

Showers from photons and electrons are indistinguishable in the detector. However, there are several handles for separating π^0 events with two photons from the electron events which form the signal. In most cases, the opening angle is sufficiently large to produce two distinctive Čerenkov rings in the detector. The photons may convert at some distance from the interaction vertex. As a result, the source of the photons is reconstructed to be from an extended vertex region. Also, single pion production events typically have more energetic recoil protons than quasi-elastic scatters, resulting in more scintillation light in the event. These signatures allow identification of most of the single π^0 events, as discussed below, leaving those cases with a highly asymmetric decay and a low energy recoil proton.

6.2 Event Reconstruction

Events are reconstructed using a fitting algorithm developed for LSND. As in LSND, the chi square of the position and angle fits (χ_r and χ_a) are minimized to determine the event position and direction. In addition, these minimized chi squares, together with the fraction of PMTs with late hits (χ_t) or early hits (χ_{t0}), provide excellent particle identification and low $\mu^{\pm} - e^{\pm}$ and $\pi^0 - e^{\pm}$ misidentification.

To determine the event position and time (corresponding to the midpoint of the track), the position chi square, χ_r, is minimized. χ_r is defined as

$$\chi_r = \sum q_i \times (t_i - t_o - r_i/v)^2/Q \ ,$$

where q_i is the charge of hit phototube i, t_i is the time of hit phototube i, t_o is the fitted event time, r_i is the distance between the fitted position and phototube i, v is the velocity of light in oil (20.4 cm/ns), Q is the total number of photoelectrons in the event, and the sum is over all hit phototubes. Similarly, the event direction (for particles above Čerenkov threshold) is determined by minimizing the angle chi square, χ_a. χ_a is defined as

$$\chi_a = \sum q_i \times (\alpha_i - 47^o)^2/Q \ ,$$

where α_i is the angle between the fitted direction and the line segment extending from the fitted position to hit phototube i, 47^o is the Čerenkov angle for $\beta \sim 1$ particles in mineral oil, and the sum is over all hit phototubes. Note that for both χ_r and χ_a, any PMTs that are dead or arcing are ignored.

With the track direction determined, the initial event vertex is found by using the measured track energy (which is proportional to the total number of photoelectrons in the event) to extrapolate back to the vertex.

6.3 Electron Resolutions

The event reconstruction algorithm has been tested by our detector simulation discussed above. A large sample of $\nu_e C \to e^- N$ electron events were generated uniformly in the tank in the energy range from 50 to 2000 MeV. Fig. 6.2 shows the resulting position, angular, and energy resolutions. As can be seen in the figure, the position resolution is about 34 cm, the angular resolution is about 6^o, and the energy resolution is about 10%. Note that for electron events there are about 3.8 photoelectrons per MeV.

6.4 Particle Identification

A typical event in MiniBooNE will cause hundreds of PMTs to be hit, where for each PMT hit there will be recorded the time of the first photoelectron and the total charge deposited. Excellent electron identification and muon and neutral pion rejection can then be obtained by using the fraction of late PMT hits (which measures the fraction of scintillation light), the fraction of early PMT hits, and the quality of the vertex and Čerenkov cone fits. Muons can be identified and rejected usually from the decay electron. However, $8 \pm 0.1\%$ of the μ^- will be captured before decaying. These captured muons are rejected for several reasons. First, quasi-elastic muon events have relatively more scintillation light than quasi-elastic electron events because of the muon mass (muons have a Čerenkov threshold of 38 MeV) and the recoil protons, which are more energetic on average than for quasi-elastic electron events. Also, muons travel farther than electrons, and this results in relatively more early and late PMT hits and a worse vertex position fit. Furthermore, muons have less multiple scattering and radiation than electrons, which causes the outside of the Čerenkov ring to be sharper for muons than for electrons. The inside of the Čerenkov ring will be somewhat filled in as the muons approach the Čerenkov threshold.

Neutral pions can also be rejected easily. First, neutral current π^0 events have relatively more scintillation light than quasi-elastic electron events because of the recoil protons, which are much more energetic on average than for quasi-elastic electron events. Also, π^0s are more spread out than electrons due to the radiation of the decay γs, and this results in relatively more early and late PMT hits and a worse vertex position fit. Furthermore, π^0s have two

Table 6.2: The number of events remaining after successive selections. The Veto,Time,Ring selection rejects events with more than 60 MeV of energy in the veto shield, reconstructed time more than 5 ns from the beam time, and a second Čerenkov ring within 23° of the first ring. Q is the total charge in the event, while χ_t, χ_{t0}, χ_r, χ_a, and r_q are described in the text.

Selection	# e^- Events	# μ^- Events	# π^0 Events
Total	4000	4000	4000
Veto,Time,Ring	2811	157	233
$\chi_t \times \chi_{t0} < 0.024$	2238	5	140
$\chi_r \times \chi_a / r_q < Q/1000 + 1$	1952	0	19

Čerenkov rings and relatively less charge in either of the rings than electron Čerenkov rings.

Therefore, electron events can be distinguished from muon events and neutral pion events by fitting the Čerenkov ring and event vertex and by measuring the fraction of PMTs with a late hit. Fig. 6.3 shows χ_t, the fraction of PMTs hit after 10 ns from the reconstructed time of the event, χ_{t0}, the fraction of PMTs hit before the reconstructed time of the event, $\chi_r \times \chi_a$, and r_q, the ratio of charge deposited in PMTs with $0.5 < \cos\theta < 0.7$ to $0.8 < \cos\theta < 1.0$ (θ is the angle between the PMT direction and the fitted event direction), for electron events (solid curve), muon events (dashed curve), and neutral pion events (dotted curve). Events have been rejected with more than 60 MeV of energy in the veto shield, reconstructed time more than 5 ns from the beam time, or a second Čerenkov ring within 23° of the first ring. The relative numbers of events are normalized to what will be observed in the detector, and a clear separation is observed between electron events, μ^- events and π^0 events. The number of events remaining after successive selections is shown in Table 6.2. With these selections, the efficiency for electron events as a function of visible charge is shown in Fig. 6.4, while Fig. 6.5 shows the π^0 efficiency and π^0/e^- efficiency ratio as a function of visible charge. The π^0 events are reduced by a factor of ~ 200, while maintaining a 50% efficiency for electron events Note that no μ^- events have passed the selection so far. The veto region is not crucial for the PID; however, it serves as a redundant tag for tracks leaving or entering the detector.

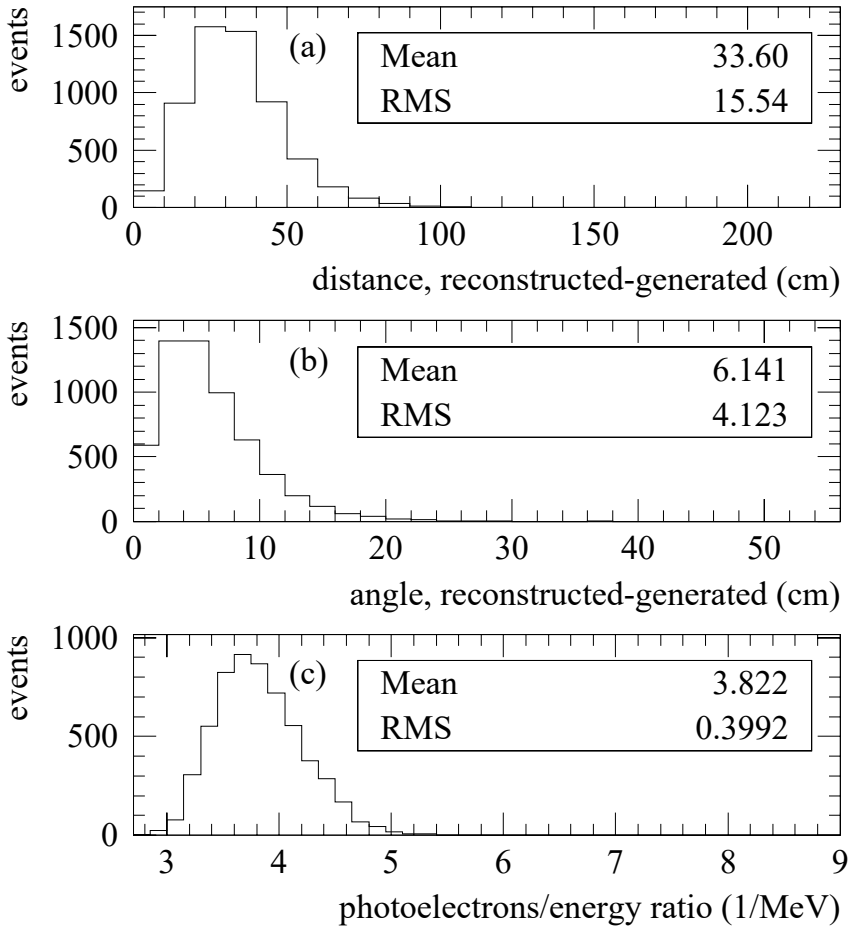

Figure 6.2: For $\nu_e C$ interactions, the (a) position (in cm), (b) angular, and (c) energy resolutions for a large sample of electrons generated in the tank by the detector simulation.

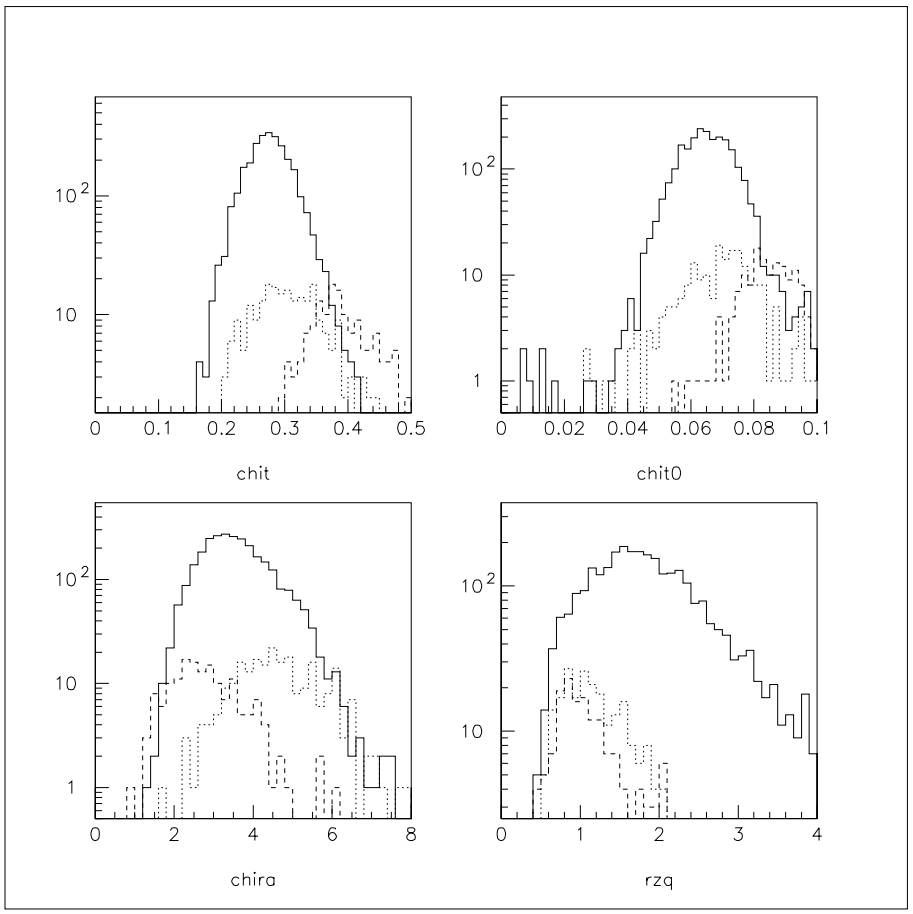

Figure 6.3: The (a) χ_t, (b) χ_{t0}, (c) $\chi_r \times \chi_a$, and (d) r_q distributions for electrons (solid curve), muons (dashed curve), and neutral pions (dotted curve). The relative numbers of events are normalized to what will be observed in the detector.

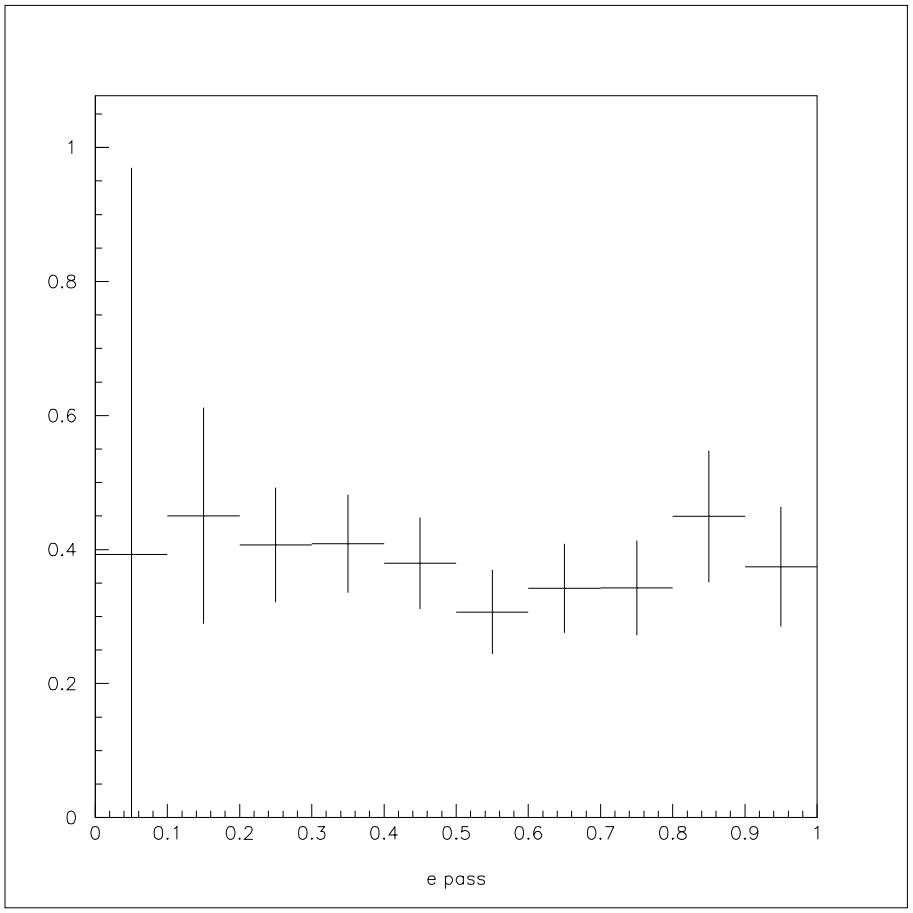

Figure 6.4: The electron reconstruction and PID efficiency as a function of visible charge.

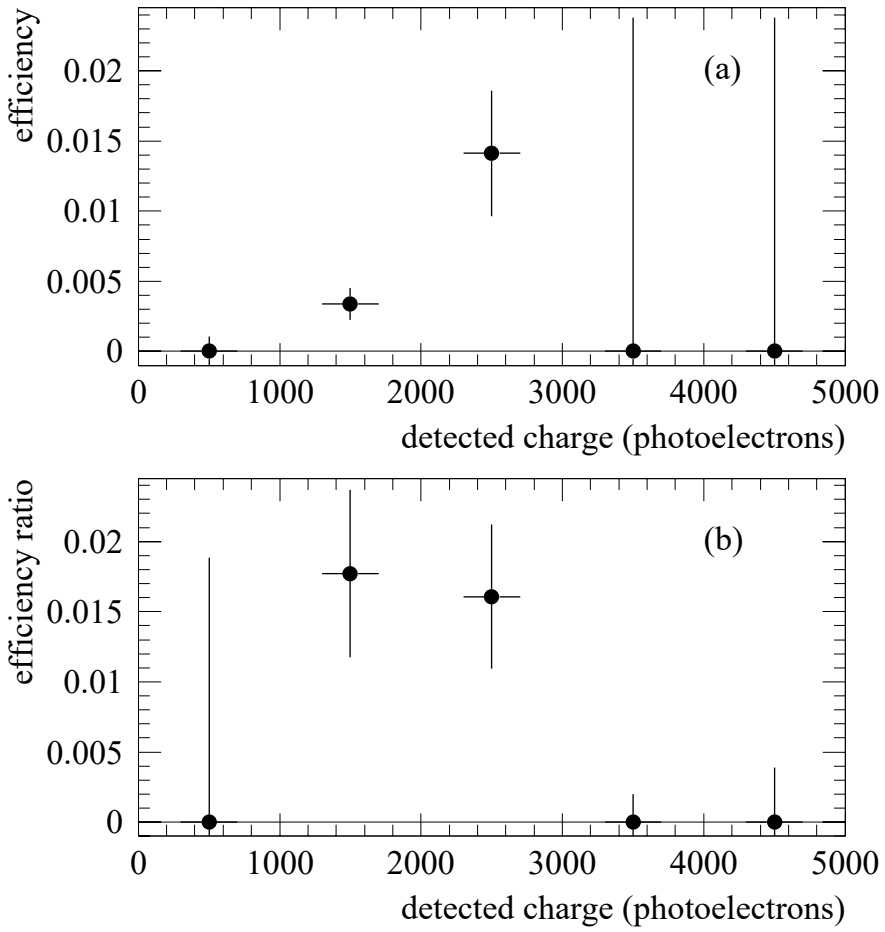

Figure 6.5: The (a) π^0 efficiency and (b) π^0/e^- efficiency ratio as a function of visible charge.

6.5 Systematic Uncertainty on the μ^- and π^0 Misidentification Background

As discussed in the previous section, the μ^- event and π^0 event misidentification as e^- event probabilities are approximately 0.0005 and 0.005, respectively. These misidentifications occur when the μ^- is captured in the oil before decaying (the probability of capture is $8 \pm 0.1\%$, while the decay electron inefficiency is $< 10^{-2}$) or when the π^0 decay is highly asymmetric. Therefore, we can measure the misidentification background by applying the PID selection on μ^- that decay, ignoring the decay electron, and by measuring the π^0 symmetric decays. Fig. 6.6 shows the cosine of the angle between the two fitted Čerenkov rings for π^0 decays (dashed curve) and electrons (solid curve). Although electrons should have only a single Čerenkov ring, multiple scattering and radiation by the electron will lead to a second ring. However, as shown in Fig. 6.6, the cosine of the angle distributions between the two rings have much different shapes, so that the π^0 background can be well measured. We, therefore, will be able to measure the μ^- event and π^0 event misidentification backgrounds with a systematic error of $\pm 5\%$.

6.5.1 Maximum Likelihood Event Reconstruction and Particle Identification

In parallel to the standard techniques described above, a maximum likelihood event reconstruction and particle identification is being developed for MiniBooNE. The algorithm has been originally developed for the LSND decay-in-flight analysis in order to fully utilize the capabilities of the detector. The basis for the reconstruction is a simple single track event model, parameterized by the track starting position and time (x, y, z, t), direction (φ, θ), energy (E), and length (l). For any given event defined by the set of parameters $\vec{\alpha}$,

$$\vec{\alpha} = (x, y, z, t, \varphi, \theta, E, l)\,, \tag{6.1}$$

the event likelihood for measuring a set of PMT charges (q_i) and times (t_i) $(i = 1, 1222)$ in the detector is the product over the 1222 individual charge and timing likelihood functions at the PMTs:

$$\mathcal{L}_{event} = \prod_{i=1}^{1222} \mathcal{L}_q(q_i; \vec{\alpha})\, \mathcal{L}_t(t_i; \vec{\alpha}). \tag{6.2}$$

Reversing the meaning of the likelihood function, $\mathcal{L}_{event}$ is the likelihood that the event is characterized by the set $\vec{\alpha}$, given the set of measured charges (q_i) and times (t_i). Maximizing the event likelihood $\mathcal{L}_{event}$ (or equivalently

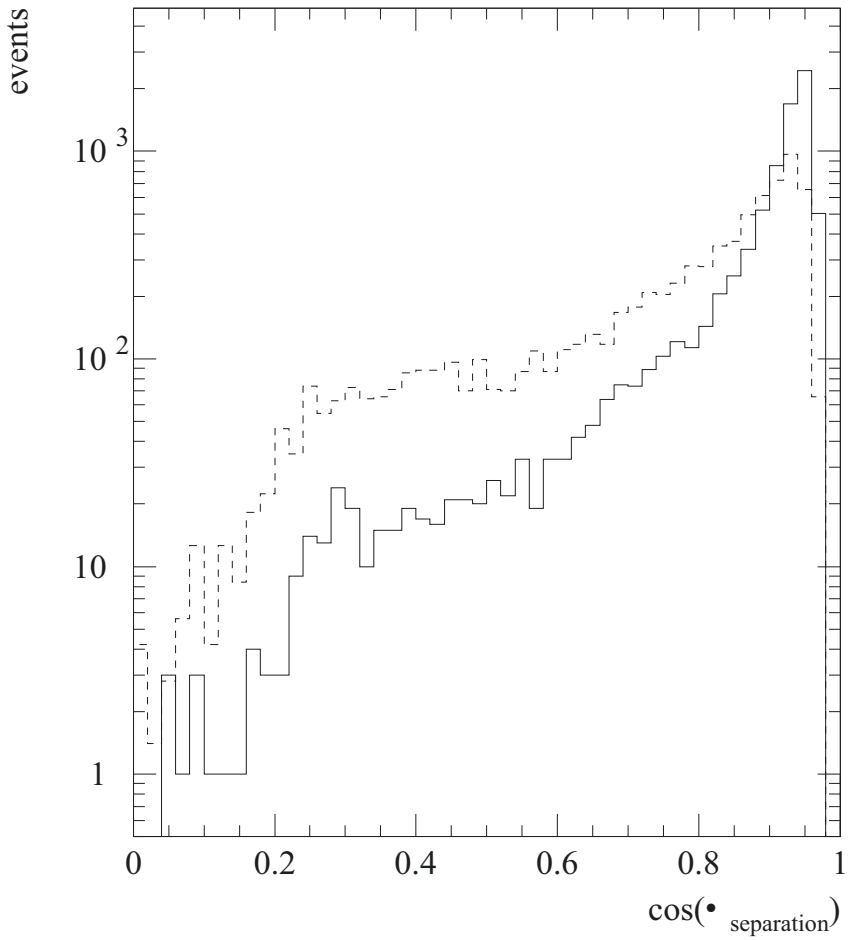

Figure 6.6: The cosine of the angle distribution between the two fitted Čerenkov rings for π^0 decays (dashed curve) and electrons (solid curve).

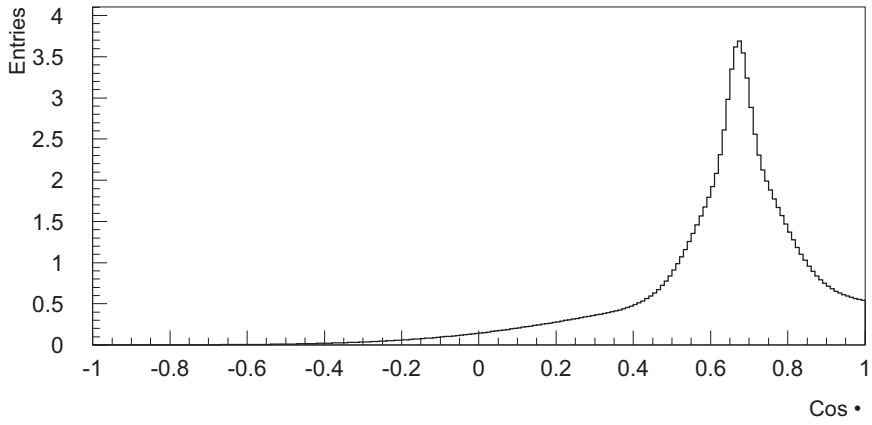

Figure 6.7: Čerenkov angular distribution for mono-energetic (40 MeV) Michel electron events.

minimizing $-\ln \mathcal{L}_{event}$) with respect to $\vec{\alpha}$ determines the optimal set of event parameters.

For a short track event we describe briefly the charge and time likelihoods in the following: The isotropic scintillation and scattered Čerenkov light have a strength Φ (photons per steradian), where Φ is proportional to the energy E of the event. The strength of the anisotropic direct Čerenkov light is parameterized as $\rho\Phi$, while the angular dependence is given by a function $f(\cos\theta_e)$, as illustrated in Fig. 6.7 for low energy electrons. The angle θ_e is the angle with respect to the event direction and the function is normalized such that

$$\int_0^\pi f(\cos\theta_e)\sin\theta_e\, d\theta_e = 1. \tag{6.3}$$

The average number of photoelectrons (PEs) μ expected at a phototube of quantum efficiency ε, at a distance r from the source, and subtending a solid angle Ω is given by

$$\mu = \varepsilon\,\Phi\,\Omega\,\left[e^{-r/\lambda_s} + \rho\, f(\cos\theta_e)\, e^{-r/\lambda_c}\right]. \tag{6.4}$$

The parameters λ_s and λ_c are the attenuation lengths for scintillation and direct Čerenkov light in the tank medium, respectively. Notice that although the individual quantum efficiencies of the PMTs as well as the attenuation

lengths are wave-length dependent, we use only global, effective values. All reconstruction parameters (attenuation lengths, solid angles and quantum efficiencies) are determined self-consistently from control data samples, in particular low energy Michel electrons from stopped cosmic-ray muon decays. The probability of measuring n PEs in the presence of the light source is then given by a Poisson distribution of mean value μ,

$$P(n;\mu) = \frac{1}{n!}\, e^{-\mu}\, \mu^n. \tag{6.5}$$

However, since the detector PMTs measure charge and not the number of PEs, the probability of measuring a charge q for a predicted value μ is given by

$$\mathcal{P}(q;\mu) = \sum_{n=0}^{\infty} P(q;n) P(n;\mu), \tag{6.6}$$

where the $P(q;n)$ functions are the charge response functions (CRFs) of the PMTs, i.e. the probability of measuring a charge q given a number of PEs n. Since μ depends directly on the set of event parameters $\vec{\alpha}$, the probability $\mathcal{P}(q;\mu)$ determines directly the charge likelihood $\mathcal{L}_q(q;\vec{\alpha})$ for the PMT. The CRFs are also measured directly from the data.

The corrected time t_{cor} of a PMT is defined as the measured PMT time after corrections for the event vertex time and light travel time from the event to the PMT surface. The time likelihood for any PMT is simply given by

$$\mathcal{L}(t_{cor};\vec{\alpha}) = w_c T_c(t_{cor}) + w_s T_s(t_{cor}), \tag{6.7}$$

where w_c and w_s are the fractional amounts of predicted Čerenkov and scintillation light, respectively, while T_c and T_s are the corrected timing distributions for the two light components, respectively. For prompt Čerenkov light T_c is a Gaussian centered at zero and approximately 1.5 ns wide. For scintillation light T_s is taken to be the convolution between an exponential decay with a time constant of 35 ns and a Gaussian of width 1.5 ns.

The extrapolation to high energy, long track events is achieved by allowing for multiple point-like sources along the track and also fitting for the total track length. Two different event reconstructions have been developed so far, for electron and muon events. The main differences between them are the parameterization of the Čerenkov angular distribution at different points along the track (i.e. at different energies), and also the timing along the track. As already mentioned earlier in this section, electrons are practically at $\beta = 1$ over the entire track length, which implies a Čerenkov angular distribution centered at $\cos\theta = 0.68$, but becoming narrower and narrower as the energy increases.

Muon events also have a relatively narrow Čerenkov angular distribution centered at $\cos\theta = 0.68$ at high energies ($\beta \approx 1$), but they slow down considerably along the track, thus continuously shifting the center of the Čerenkov angular distribution towards higher values of $\cos\theta$.

The performance of this new algorithm is illustrated in Fig. 6.8 for a sample of electron events from $\nu_e C \to e^- X$ and also for a sample of muon events from $\nu_\mu C \to \mu^- X$. The position resolution is 26 cm for electrons and 18 cm for muons, while the angular resolutions are 4.5° and 4.1°, respectively.

Electron identification is achieved by reconstructing the events under both hypotheses, i.e. electron- and muon-reconstruction, and building an electron-to-muon likelihood. This quantity is in turn based on the charge and timing likelihoods for PMTs in the forward, inner, and backward Čerenkov regions, to take advantage of the differences mentioned earlier. Similarly, a muon-to-electron likelihood is built for muon events reconstructed under both hypotheses, i.e. muon- and electron-reconstruction. The particle-id performance for electron events is shown in Fig. 6.9. A muon rejection of approximately 6×10^{-4} is achieved for an average electron efficiency of 0.71.

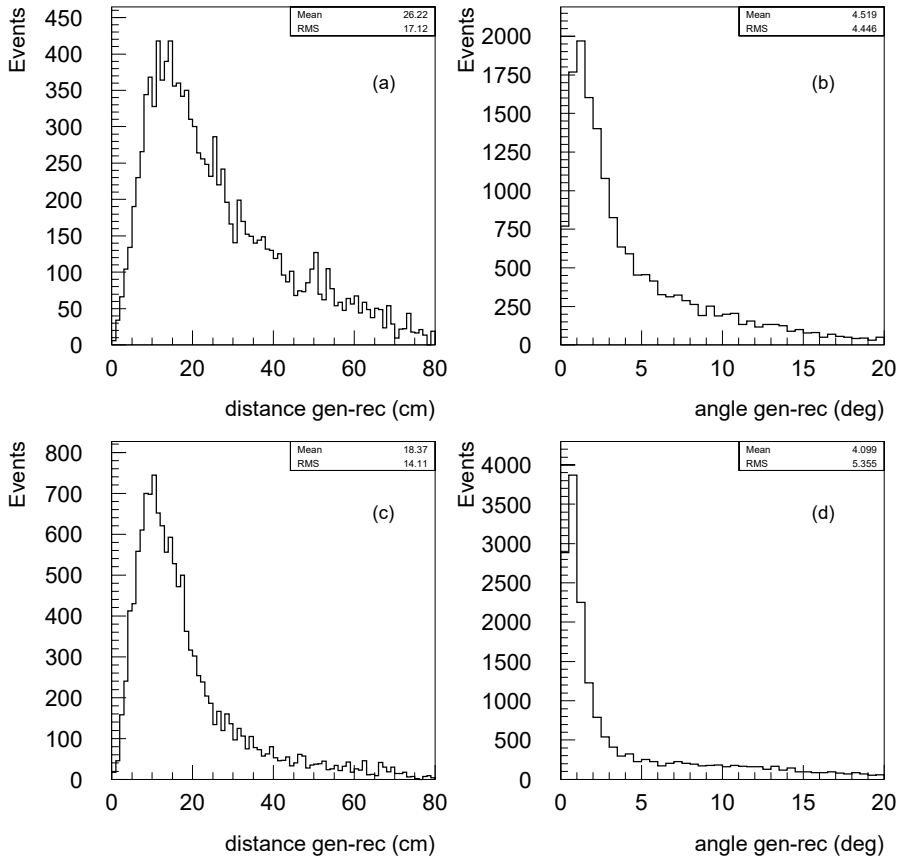

Figure 6.8: Position and angular resolution for Monte-Carlo electron events from $\nu_e C \rightarrow e^- X$ (top) and muon events from $\nu_\mu C \rightarrow \mu^- X$ (bottom).

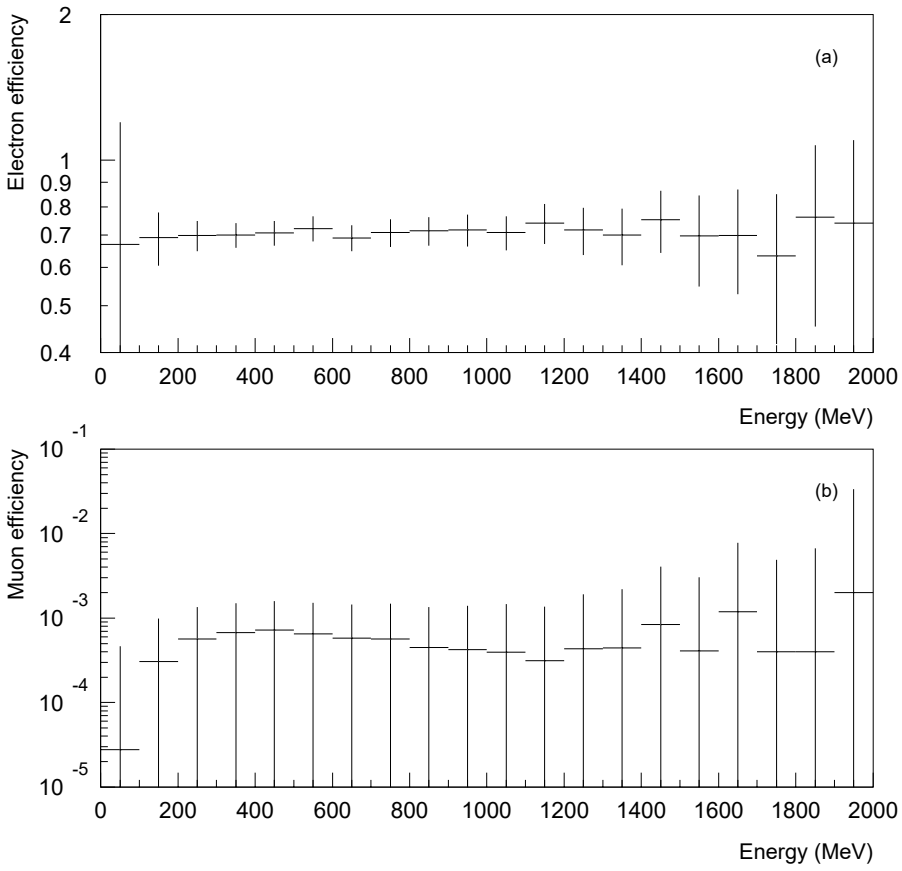

Figure 6.9: Electron (a) and muon (b) reconstruction and particle-id efficiency as a function of energy.

Chapter 7

The $\nu_\mu \rightarrow \nu_e$ Oscillation Search

The signature for $\nu_\mu \rightarrow \nu_e$ oscillations is ν_e quasi-elastic scattering off carbon nuclei. The main backgrounds come from intrinsic ν_e contamination in the beam, mis-identified ν_μ quasi-elastic scattering, and mis-identified neutral current π^0 production. The MiniBooNE experiment will be able to clearly observe neutrino oscillations in the > 0.1 eV^2 mass squared range for values of $\sin^2 2\theta > 10^{-3}$.

The expected sensitivity for the ν_e appearance search is shown in Fig. 2.1. The calculation is performed as a function of energy. Statistical and systematic errors are included. The number of events and the significance of the signal, again including both statistical and systematic errors, are shown in Fig. 2.2.

The quasi-elastic cross sections used to obtain the expectations are obtained from a modified Fermi-Gas calculation that agrees approximately with a more sophisticated continuum RPA calculation.[63] Also, the single pion cross sections are taken from Rein and Sehgal.[64] We estimate that there is an $\sim 20\%$ uncertainty in these cross sections.

7.1 The $\nu_\mu \rightarrow \nu_e$ Oscillation Signal

The neutrino oscillations ($\nu_\mu \rightarrow \nu_e$ and $\bar{\nu}_\mu \rightarrow \bar{\nu}_e$) are observed by $\nu_e C \rightarrow e^- N$ and $\bar{\nu}_e C \rightarrow e^+ B$ quasi-elastic scattering. The cross sections for these reactions[63] are shown in Fig. 7.1 and Tables 7.1 and 7.2 as a function of incident neutrino energy. Note that the cross sections rise rapidly with energy near

Table 7.1: Signal and background neutrino cross sections as a function of neutrino energy in MeV. The cross sections are for each C atom and are in units of 10^{-40} cm^2.

E_ν(MeV)	$\nu_e C \to e^- N$	$\nu_\mu C \to \mu^- N$	$\nu_\mu e^- \to \nu_\mu e^-$	$\nu_\mu C \to \nu_\mu \pi^0 X$	$\nu_\mu C \to \pi^\pm X$	$\nu_\mu C \to \mu^- \pi X$
100	13	0	0.01	0	0	0
200	106	63	0.03	0	0	0
300	249	213	0.04	1	0	0
400	369	341	0.05	8	1	10
500	458	435	0.06	20	8	71
600	520	501	0.08	34	17	135
700	563	546	0.09	50	24	203
800	593	575	0.10	65	32	267
900	613	596	0.11	77	39	325
1000	627	609	0.13	87	49	364
1100	636	619	0.14	92	52	394
1200	644	625	0.16	99	56	415
1300	650	629	0.17	101	57	442
1400	655	632	0.18	101	57	444
1500	659	634	0.20	102	58	450
1600	664	635	0.21	105	59	453
1700	667	636	0.22	105	59	460
1800	671	637	0.23	105	59	460
1900	675	638	0.25	105	59	460
2000	679	640	0.26	105	59	460

threshold and then taper off to a flat energy dependence well above threshold. Also, Fig. 7.2 shows the visible energy versus the neutrino energy, and Fig. 7.3 shows the recoil $e^\pm$ energy and $\cos\theta$ distributions after integrating over the incident neutrino energy spectrum. The angle θ is the reconstructed $e^\pm$ direction relative to the incident neutrino direction. Note that the $e^\pm$ has an energy on average that is about 2/3 the neutrino energy and a direction that becomes more forward peaked with energy.

7.2 The $\nu_\mu \to \nu_e$ Oscillation Background

A principal beam-related background is due to the intrinsic ν_e and $\bar{\nu}_e$ fluxes from kaon and muon decays discussed in chapter 5. This intrinsic background has the same reactions as the signal reactions described in section 8.1. The

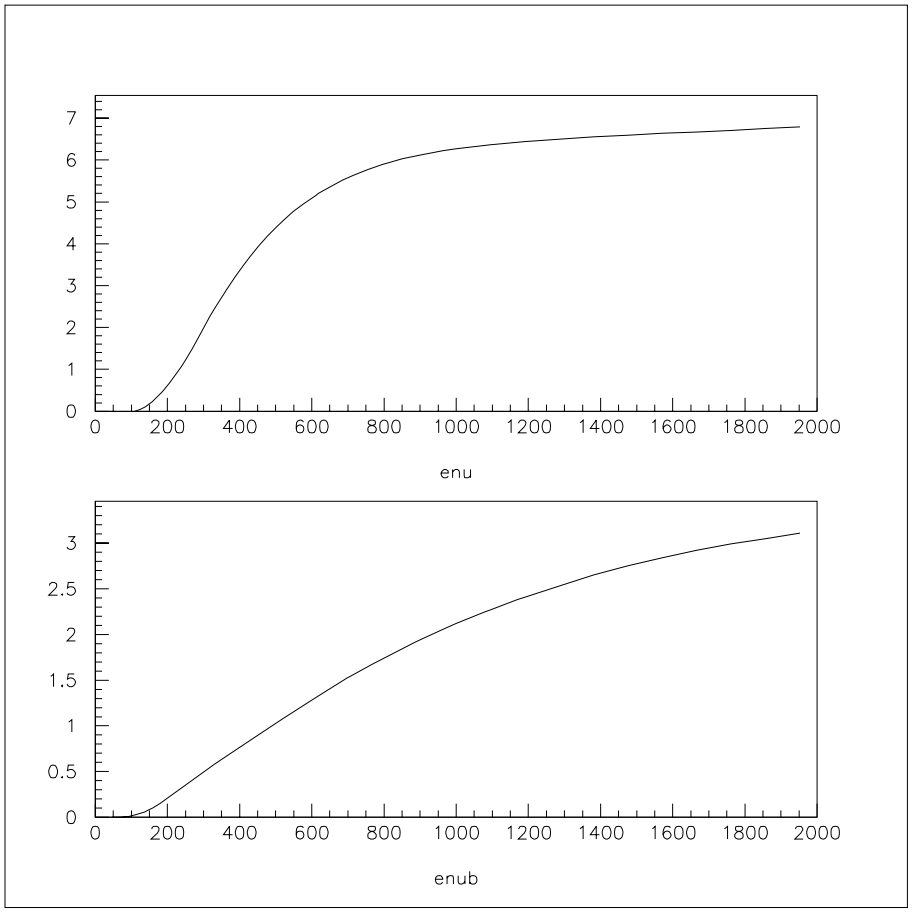

Figure 7.1: The cross sections (in units of 10^{-38} cm^2) for $\nu_e C \rightarrow e^- N$ and $\bar{\nu}_e C \rightarrow e^+ B$ quasi-elastic scattering as a function of incident neutrino energy in MeV.

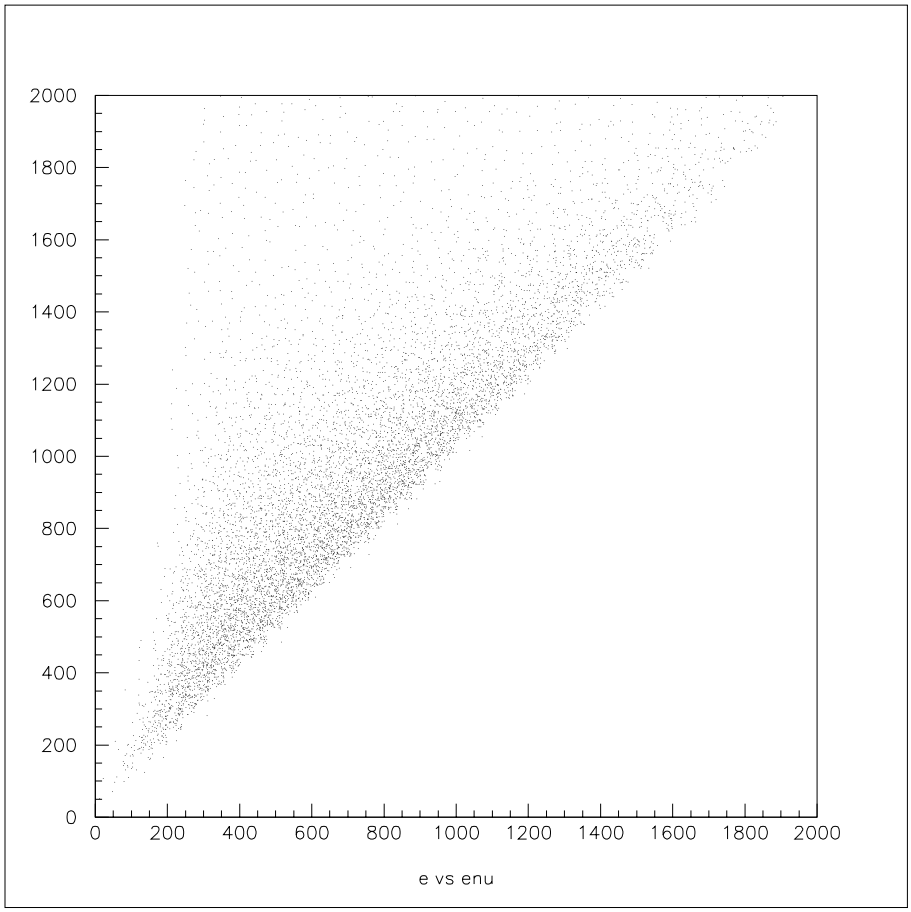

Figure 7.2: The visible energy versus the neutrino energy in GeV from $\nu_e C$ quasi-elastic scattering after integrating over the incident neutrino energy spectrum.

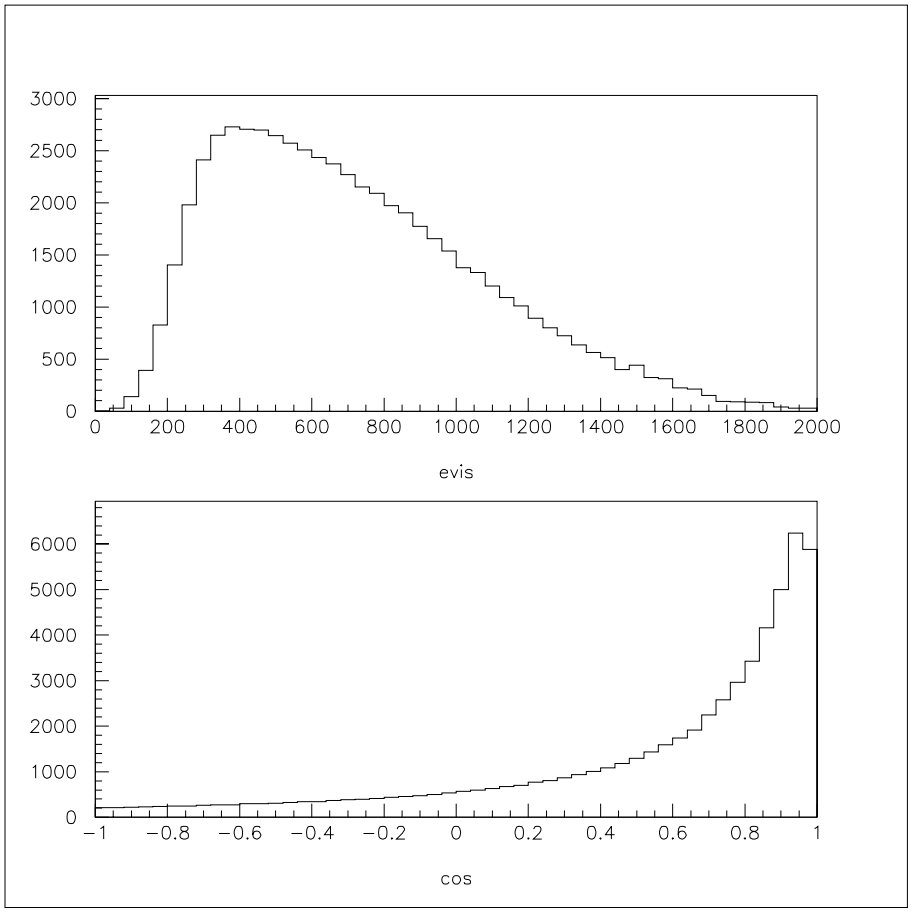

Figure 7.3: The recoil $e^{\pm}$ (a) energy in MeV and (b) $\cos\theta$ distributions from quasi-elastic scattering after integrating over the incident neutrino energy spectrum.

Table 7.2: Signal and background antineutrino cross sections as a function of antineutrino energy. The cross sections are for each C atom (the numbers in parentheses are the cross sections for free protons) and are in units of 10^{-40} cm^2.

$E_{\bar{\nu}}$(MeV)	$\bar{\nu}_e C \to e^+ B$	$\bar{\nu}_\mu C \to \mu^+ B$	$\bar{\nu}_\mu e^- \to \bar{\nu}_\mu e^-$	$\bar{\nu}_\mu C \to \bar{\nu}_\mu \pi^0 X$	$\bar{\nu}_\mu C \to \pi^\pm X$	$\bar{\nu}_\mu C \to \mu^+ \pi X$
100	7 (4)	0 (0)	0.01	0	0	0
200	32 (10)	22 (8)	0.02	0	0	0
300	59 (15)	53 (14)	0.03	1	0	0
400	84 (19)	80 (18)	0.04	5	0	4
500	109 (24)	106 (23)	0.05	11	4	31
600	133 (28)	130 (27)	0.06	18	8	59
700	156 (32)	153 (31)	0.07	26	11	89
800	176 (35)	174 (34)	0.08	34	14	117
900	195 (39)	193 (38)	0.09	40	18	142
1000	212 (42)	210 (41)	0.10	45	22	160
1100	227 (44)	226 (43)	0.11	48	23	177
1200	241 (47)	240 (46)	0.12	54	26	191
1300	253 (49)	253 (48)	0.13	56	27	213
1400	265 (51)	265 (50)	0.14	57	27	221
1500	275 (53)	275 (52)	0.15	59	29	224
1600	284 (55)	285 (54)	0.16	63	31	231
1700	292 (57)	293 (56)	0.17	65	32	246
1800	299 (58)	301 (57)	0.18	66	32	250
1900	305 (60)	307 (59)	0.19	67	33	256
2000	311 (61)	313 (60)	0.20	68	33	261

other main beam-on backgrounds are due to neutrino reactions that produce a $\mu^\pm$ or π^0 in the final state. The MiniBooNE design goal is to have particle identification sufficient to suppress muon misidentification as an electron by a factor of 1000 and π^0 misidentification as an electron by a factor of 100. As shown in section 7, these suppression factors are achieved. Other backgrounds that are considered are $\pi^\pm$ production and $\nu e \to \nu e$ elastic scattering. A list of all of these background reactions is shown in Table 7.3, and the cross sections are given in Tables 7.1 and 7.2 as a function of incident neutrino energy. Note that the non-beam-related backgrounds are expected to be very small due to the very low duty factor and can be subtracted precisely by a beam-on minus beam-off subtraction.

1. $\nu_\mu C \to \mu^- N$ The first background is due to $\nu_\mu C \to \mu^- N$ and $\bar{\nu}_\mu C \to \mu^+ B$

Table 7.3: A list of the background neutrino reactions for $\nu_\mu \to \nu_e$ appearance. Also shown is the factor that these backgrounds can be suppressed relative to $\nu_e C \to e^- X$ scattering and the approximate background level for the appearance oscillation search.

Reaction	Suppression Factor	Background Level
$\nu_\mu C \to \mu^- X$	10^{-3}	10^{-3}
$\nu_\mu C \to \nu_\mu \pi^0 X$	10^{-2}	10^{-3}
$\nu_\mu C \to \mu^- \pi X$	10^{-4}	10^{-4}
$\nu_\mu C \to \nu_\mu \pi^\pm X$	10^{-3}	10^{-4}
$\nu_\mu e^- \to \nu_\mu e^-$	10^{-1}	10^{-4}

scattering, where the $\mu^\pm$ is misidentified as an electron. The cross sections for these reactions as a function of incident neutrino energy are shown in Fig. 7.4. Because these cross sections are comparable to the cross sections of the neutrino oscillation signal reactions discussed in section 7.1 above, we must be able to reject these events by a factor of ~ 1000 in order to achieve a neutrino oscillation sensitivity of $\sim 10^{-3}$.

2. $\nu_\mu C \to \nu_\mu \pi^0 X$ The second background is due to $\nu_\mu C \to \nu_\mu \pi^0 X$ and $\bar{\nu}_\mu C \to \bar{\nu}_\mu \pi^0 X$ scattering. Fig. 7.5 shows the cross sections for these reactions as a function of incident neutrino energy. By comparing with the signal cross sections, it is clear that we must be able to reject these events by a factor of ~ 100 in order to achieve a neutrino oscillation sensitivity of $\sim 10^{-3}$.

3. $\nu_\mu C \to \nu_\mu \pi^\pm X$ The next background is due to $\nu_\mu C \to \nu_\mu \pi^\pm X$ and $\bar{\nu}_\mu C \to \bar{\nu}_\mu \pi^\pm X$ scattering. Fig. 7.6 shows the cross sections for these reactions as a function of incident neutrino energy. By comparing with the signal cross sections, it is clear that we must be able to reject these events by a factor of ~ 100 in order to achieve a neutrino oscillation sensitivity of $\sim 10^{-3}$.

4. $\nu_\mu C \to \mu^- \pi X$ Another background is due to $\nu_\mu C \to \mu^- \pi X$ and $\bar{\nu}_\mu C \to \mu^+ \pi X$ scattering, where the recoil π is a π^0 or $\pi^\pm$. Fig. 7.7 shows the cross sections for these reactions as a function of incident neutrino energy. By comparing with the signal cross sections, it is clear that we must be able to reject these events by a factor of ~ 1000 in order to achieve a neutrino oscillation sensitivity of $\sim 10^{-3}$.

5. $\nu_\mu e^- \to \nu_\mu e^-$ The final background that we consider is $\nu_\mu e^- \to \nu_\mu e^-$ and $\bar{\nu}_\mu e^- \to \bar{\nu}_\mu e^-$ elastic scattering. The cross section for this reaction is proportional to the neutrino energy and can be expressed as $\sigma(\nu_\mu e^- \to \nu_\mu e^-) = 1.6 \times E_\nu \times 10^{-42}$ cm^2, where the neutrino energy is in GeV. This background

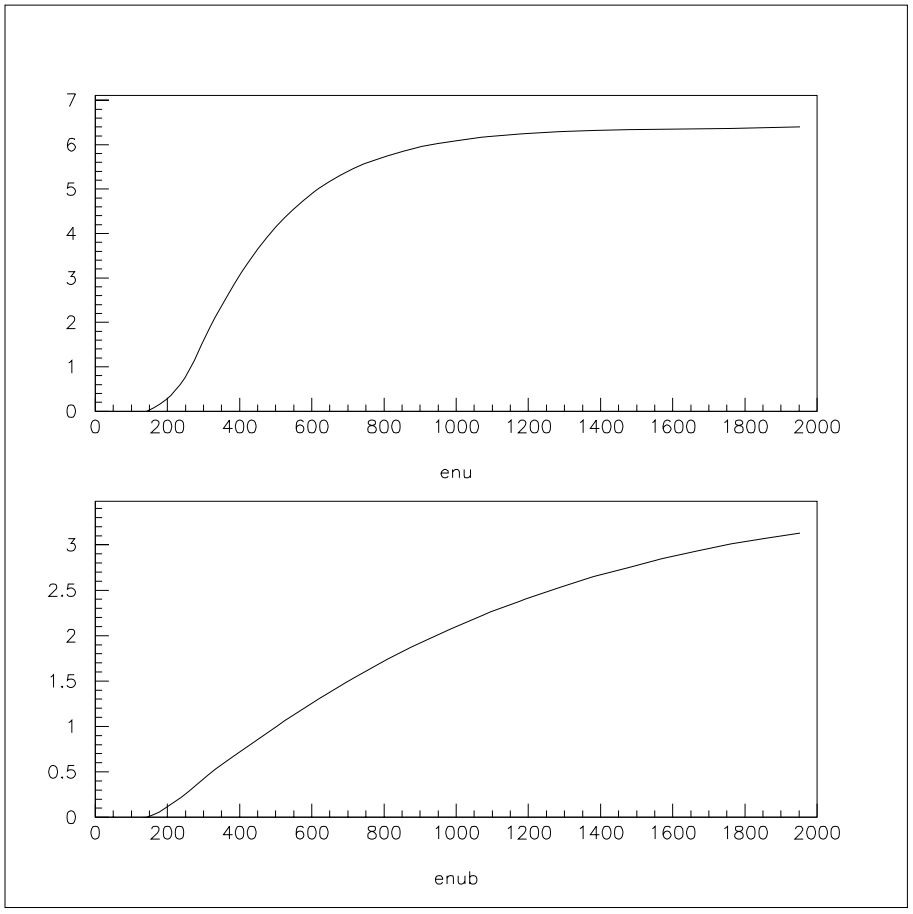

Figure 7.4: The cross sections (in units of 10^{-38} cm^2) for $\nu_\mu C$ and $\bar{\nu}_\mu C$ quasi-elastic scattering as a function of incident neutrino energy in MeV.

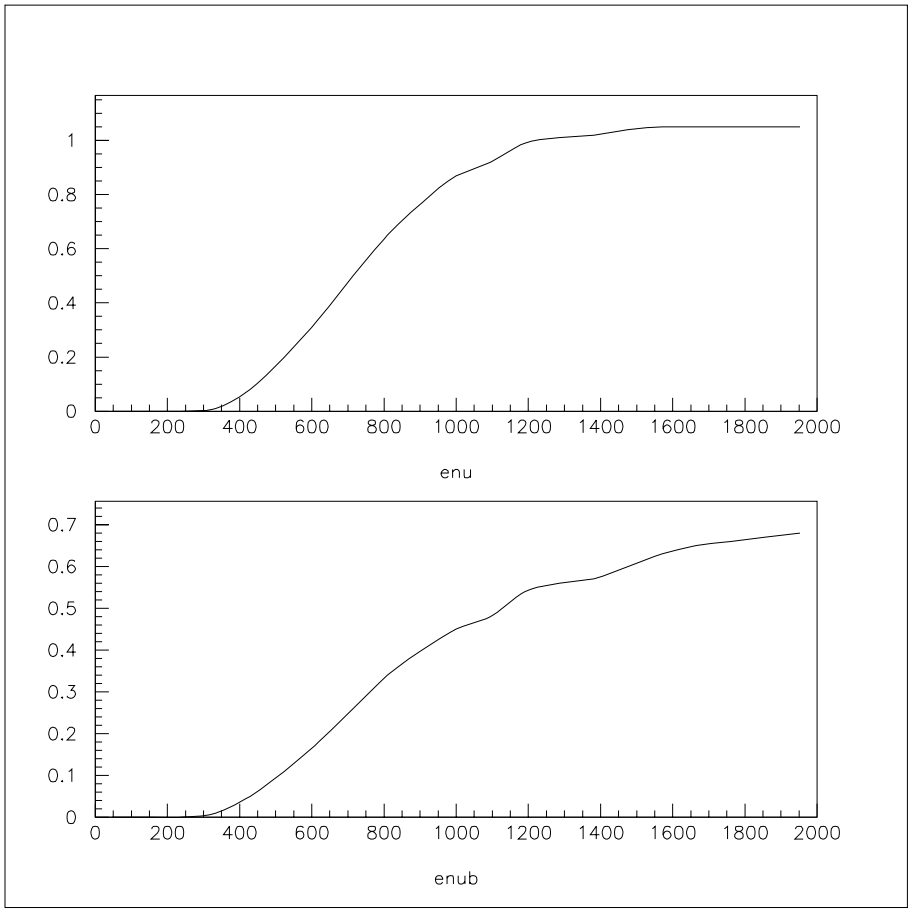

Figure 7.5: The cross sections (in units of 10^{-38} cm^2) for $\nu_\mu C$ and $\bar{\nu}_\mu C$ neutral current π^0 production as a function of incident neutrino energy in MeV.

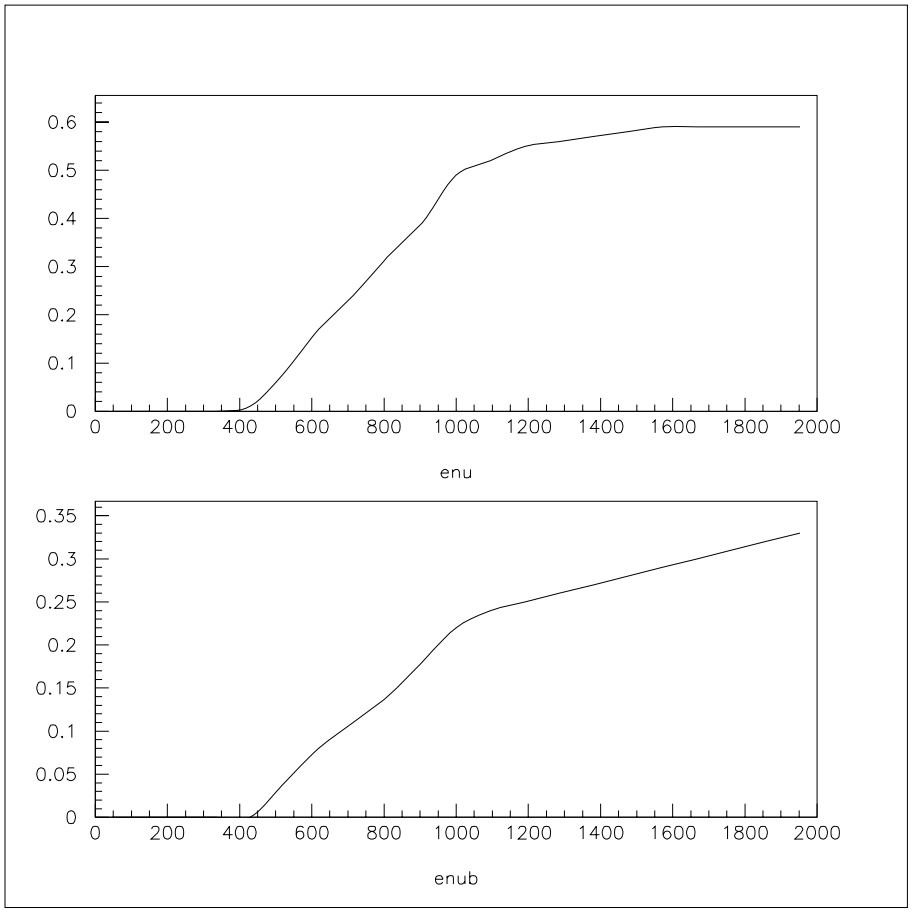

Figure 7.6: The cross sections (in units of 10^{-38} cm^2) for $\nu_\mu C$ and $\bar{\nu}_\mu C$ neutral current $\pi^\pm$ production as a function of incident neutrino energy in MeV.

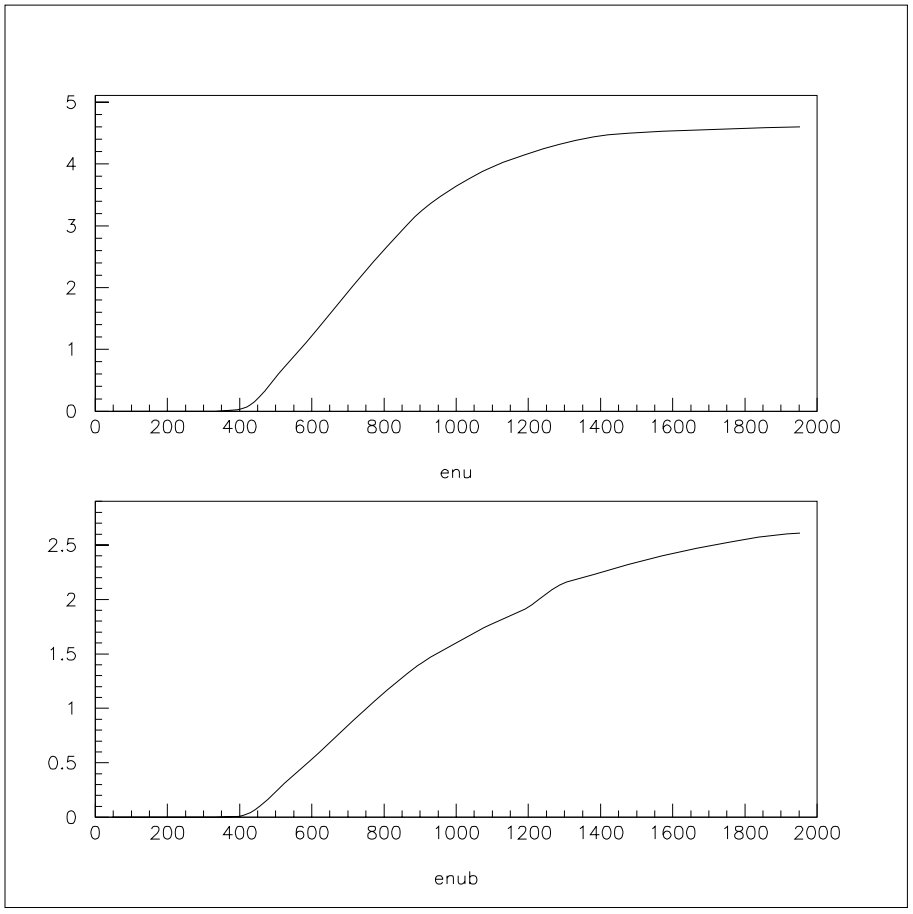

Figure 7.7: The cross sections (in units of 10^{-38} cm^2) for $\nu_\mu C$ and $\bar{\nu}_\mu C$ charged current pion production as a function of incident neutrino energy in MeV.

is small and can be identified by the recoil electron direction and by the lack of a recoil proton, which results in relatively less Čerenkov light. The inefficiency due to this identification is negligible.

7.3 Rejection of Events with Muons and Pions

As described in chapter 6, events with a $\mu^{\pm}$, π^0, or $\pi^{\pm}$ in the final state are rejected by using the χ^2 of the position fit (χ_r) and the χ^2 of the angle fit (χ_a), by vetoing events with energy, E_v, in the veto shield, and by using χ_t, the fraction of PMTs with a late hit (> 10 ns), and χ_{t0}, the fraction of PMTs with a early hit (< 0 ns). We obtain a factor of ~ 1000 rejection of $\mu^{\pm}$ and $\pi^{\pm}$ and a factor of ~ 100 π^0 rejection relative to electrons (see Fig. 6.3). The $e^{\pm}$ efficiency is $\sim 50\%$. Fig. 7.8 shows the expected visible energy (electron equivalent) distributions from the intrinsic ν_e background (dashed curve), the $\nu_\mu C \rightarrow \mu^- X$ background (dotted curve), and from the $\nu_\mu C \rightarrow \nu_\mu \pi^0 X$ background (dot-dashed curve). Also shown is the expected distribution from $\nu_\mu \rightarrow \nu_e$ oscillations for 100% transmutation and for $\Delta m^2 = 0.4$ eV^2 and $\sin^2 2\theta = 0.04$ (data points). The bands show the size of the background systematic errors. The signal to background ratio is greater than one for oscillation probabilities greater than $\sim 0.5\%$.

7.4 Projected Oscillation Measurements and Sensitivity

For the estimation of event rates we make the following assumptions. First, we assume that the Booster operates at an energy of 8 GeV and at an average rate of 5 Hz (2.5×10^{13} protons/s) for one calendar year (2×10^7 s). Half of the data collection is with a 50 m decay volume and half is with a 25 m decay volume. Also, we assume that the fiducial volume of the detector is 445 t (1.9×10^{31} CH_2 molecules) and that the total electron and muon efficiencies, including PID, are 50%. The resulting numbers of quasi-elastic events are shown in Table 7.4 for the detector at a distance of 500 m from the neutrino source. The horn can be run in either polarity and we may choose to run antineutrinos in the future. Therefore both neutrino and antineutrino scattering are shown. The muon-neutrino quasi-elastic scattering estimates assume no oscillations, while the electron-neutrino quasi-elastic scattering estimates assume 100% $\nu_\mu \rightarrow \nu_e$ transmutation.

The detector located at 500 m from the neutrino source will measure the ν_e energy spectrum through quasi-elastic scattering as described in chapters 8 and 9. The event energy distribution in the detector will provide proof that neutrino oscillations are occurring and will allow the determination of

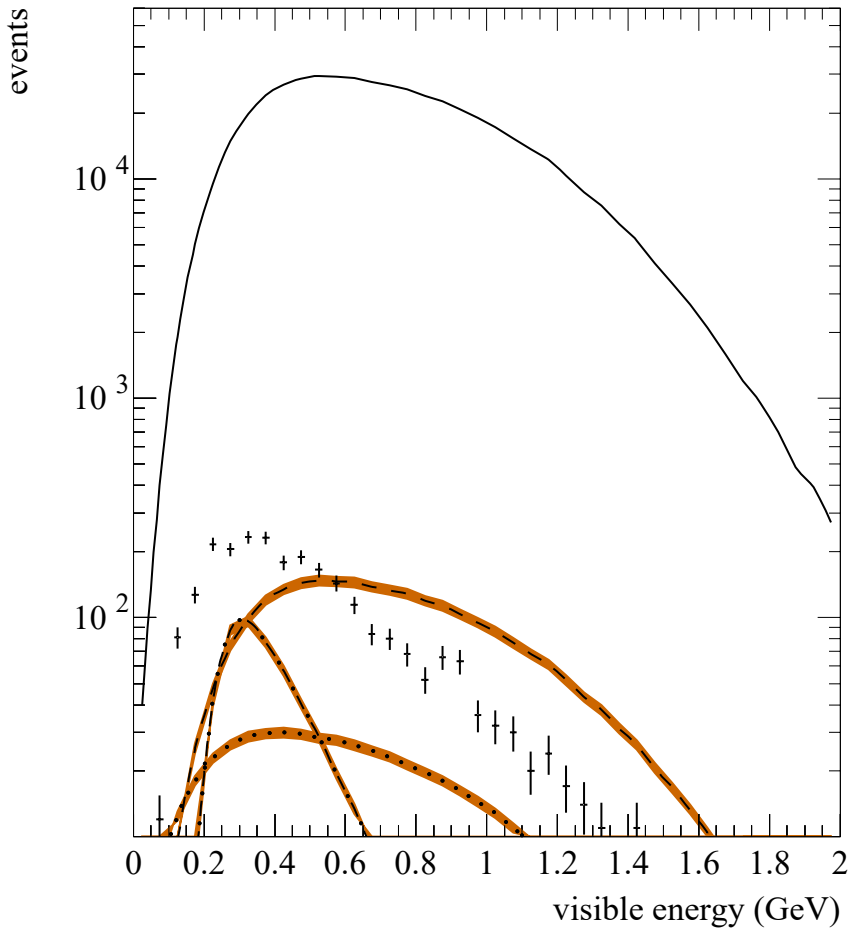

Figure 7.8: The expected visible energy (electron equivalent) distributions in MeV from the intrinsic ν_e background (dashed curve), the $\nu_\mu C \to \mu^- X$ background (dotted curve), and from the $\nu_\mu C \to \nu_\mu \pi^0 X$ background (dot-dashed curve). Also shown is the expected distribution from $\nu_\mu \to \nu_e$ oscillations for 100% transmutation (solid curve) and for $\Delta m^2 = 0.4$ eV^2 and $\sin^2 2\theta = 0.04$ (data points). The bands show the size of the background systematic errors.

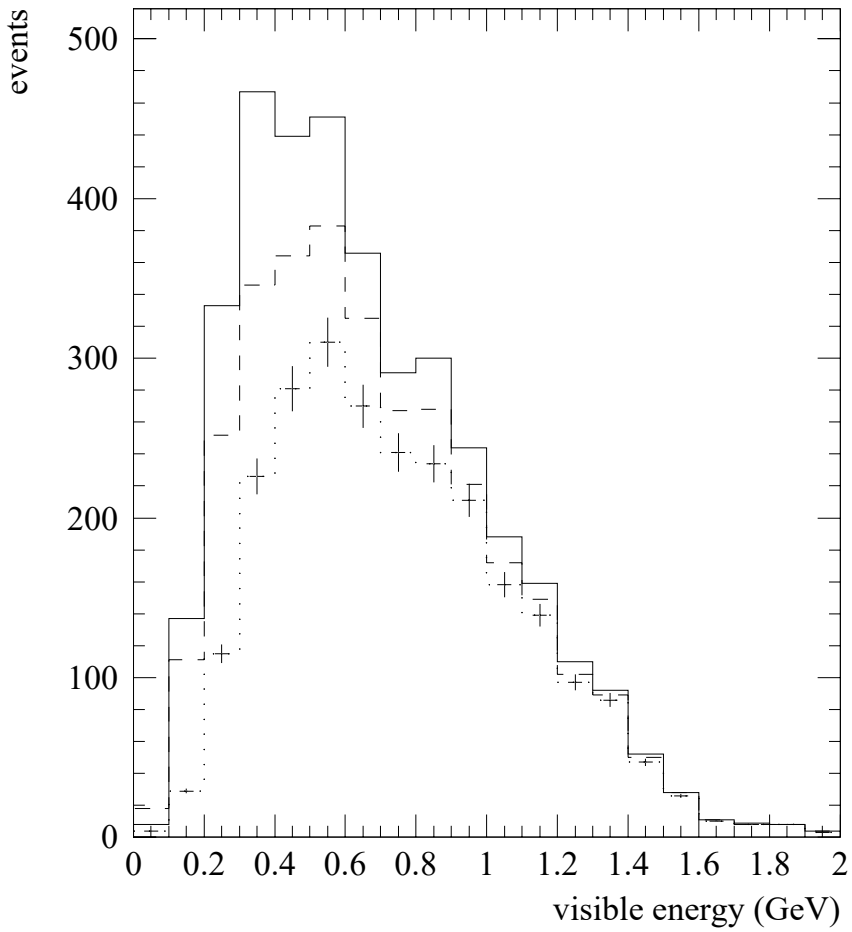

Figure 7.9: The ν_e quasi-elastic visible energy distribution in GeV, including oscillations and background sources, for two different possible oscillation parameters (motivated by LSND): $\Delta m^2 = 0.2$ eV^2 and $\sin^2 2\theta = 0.04$ (dashed) and $\Delta m^2 = 0.4$ eV^2 and $\sin^2 2\theta = 0.02$ (solid). Also shown in the figure is a dotted line giving the expectations for no oscillations. The two oscillation histograms include the background of the no oscillation histogram.

Table 7.4: The estimated numbers of contained quasi-elastic events for both neutrino and antineutrino scattering and for the detector at a distance of 500 m from the neutrino source. The muon-neutrino quasi-elastic scattering estimates assume no oscillations, while the electron-neutrino quasi-elastic scattering estimates assume 100% $\nu_\mu \to \nu_e$ transmutation.

Reaction	Number of Events
$\nu_\mu C \to \mu^- X$	590,000
$\bar{\nu}_\mu C \to \mu^+ X$	110,000
$\nu_e C \to e^- X$	617,000
$\bar{\nu}_e C \to e^+ X$	115,000

the neutrino oscillation parameters (assuming that the LSND signal is indeed due to neutrino oscillations). Fig. 7.9 shows the ν_e quasi-elastic event energy distribution for two different possible oscillation parameters (motivated by LSND): $\Delta m^2 = 0.2$ eV^2 and $\sin^2 2\theta = 0.04$ (dashed) and $\Delta m^2 = 0.4$ eV^2 and $\sin^2 2\theta = 0.02$ (solid). Also shown in the figure is a dotted line giving the expectations for no oscillations. Table 7.5 shows the number of oscillation events expected for these various scenarios, together with the expected number of background events from μ^- and π^0 mis-identification and from the intrinsic ν_e component in the beam. Note that neutrino oscillations can be shown to occur by observing an excess of $\nu_e C$ quasi-elastic events over what is expected. However, by fitting the excess of events as a function of visible energy, Δm^2 can be determined with an uncertainty of < 0.2 eV^2 and $\sin^2 2\theta$ with an uncertainty of $< 50\%$. The neutrino oscillation analysis will, therefore, consist of several steps: (1) Measurement of the ν_μ spectrum by using $\nu_\mu C \to \mu^- N$ quasi-elastic events; (2) Tuning the beam Monte Carlo to reproduce the measured data; (3) Measurement of the μ^- and π^0 misidentification backgrounds; (4) Determination of the total background with statistical and systematic errors; (5) Extracting the oscillation parameters by fitting the excess of observed events as a function of visible energy.

7.5 Verification of a Signal in MiniBooNE

There are several techniques for verifying an observed signal in the MiniBooNE experiment. The strongest confirmation will come from installing a second detector at the appropriate L indicated by the initial MiniBooNE data. This is referred to as the BooNE Experiment and is discussed at length in chapter 10. Here we discuss other possible options:

- Vary the decay pipe length

Table 7.5: The estimated number of $\nu_e C \to e^- N$ oscillation events for various scenarios, together with the expected number of background events from μ^- and π^0 mis-identification and from the intrinsic ν_e component in the beam.

Process	Number of Events
Oscillations with $\Delta m^2 = 0.2$ eV^2 and $\sin^2 2\theta = 0.04$	675
Oscillations with $\Delta m^2 = 0.4$ eV^2 and $\sin^2 2\theta = 0.02$	1200
μ^- Misidentification	600
π^0 Misidentification	600
Intrinsic ν_e Background	1800

- Run in $\overline{\nu}$ mode
- Vary the beam energy

As described in section 4.4.4, variation of the decay pipe length provides a strong confirmation of an oscillation signal. The most significant contribution to the intrinsic ν_e background of the beam is due to μ decays. This ν_e flux is expected to vary quadratically with fractional decay length. On the other hand, the signal from ν_μ oscillations will vary linearly with decay length. Consider the case where a 600 ± 50 event excess is observed after running for 1×10^7 s with a 50 m decay pipe. If the decay pipe is reduced to 25 m, then in the same running time one expects 334 ± 35 events if this is an oscillation signal, while only 174 ± 32 events if the excess is due to a mistake in the intrinsic background estimate. The advantage of this method is that it changes the experimental design in a well controlled and predictable fashion.

Alternatively, data can be taken in antineutrino mode. The horn is designed to run in either polarity. The μ^+ produced by quasi-elastic scattering are not captured in the oil. Thus, the muon mis-identification background is greatly reduced. The beam energy distribution is softer, allowing a test of the expected L/E variation. Also, the lower beam energy suppresses the π^0 background. It should also be noted that running in antineutrino mode is advantageous to the ν_μ disappearance search, as discussed in section 4.4.3. The reduction in event rate due to the lower flux magnitude in antineutrino mode is the main disadvantage, resulting in $\sim 10^8$ s of running to match the neutrino statistics.

Varying the beam energy while running in neutrino mode is theoretically attractive because it maintains a high event rate; however, it is operationally modestly difficult. One could replace the horn with one designed to focus lower energy particles. Ability to replace the horn system is built into the

Target Hall design. This is a better option than simply changing the current of the horn from the initial run because the horn shapes and separations are matched to the current. Thus significantly changing the current will result in a loss of flux. Alternatively, one could change the primary proton energy. This is not such a far-fetched possibility because the present permanent magnet 8 GeV extraction line will need to be replaced to allow Booster energy upgrades under consideration at FNAL. The new magnets for such a line exist and all utilities are already available in the extraction line. Lowering the primary beam energy to 6 GeV results in a loss of flux by a factor of four. Under either of these scenarios, the expected L/E dependence of a signal could be tested.

7.6 Search for CP Violation in the Lepton Sector

Assuming that $\nu_\mu \to \nu_e$ and $\bar{\nu}_\mu \to \bar{\nu}_e$ oscillations are observed, then, by comparing the neutrino and antineutrino oscillation parameters, it will be possible to make a test for CP violation in the lepton sector. CP violation may appear as a difference in the measured values of $\sin^2 2\theta$ (or even Δm^2, because in general all three different Δm^2 values can contribute to an oscillation signal) for neutrinos compared to antineutrinos. CP violation will be observed easily if the violation is large ($> 50\%$).

Chapter 8

The ν_μ Disappearance Search

The signature for ν_μ disappearance is ν_μ quasi-elastic scattering off carbon nuclei. The MiniBooNE experiment will be able to clearly observe neutrino oscillations in the 0.1 - 0.5 eV^2 mass range for values of $\sin^2 2\theta \sim 0.5$.

Fig. 2.4 shows the sensitivity for ν_μ disappearance. Statistical and systematic errors were taken into account in the calculation. A 25% uncertainty in the overall normalization and a 10% bin-to-bin shape uncertainty in the energy distribution was assumed. The energy dependence of the expected signal, efficiency, and backgrounds were included.

8.1 The ν_μ Disappearance Signal

The neutrino oscillations due to ν_μ disappearance are observed by looking for distortions in the energy spectrum of $\nu_\mu C \rightarrow \mu^- N$ and $\bar{\nu}_\mu C \rightarrow \mu^+ B$ quasi-elastic scattering. The cross sections for these reactions[63] are shown in Fig. 7.4 and Tables 7.1 and 7.2 as a function of incident neutrino energy. Note that the cross sections rise rapidly with energy near threshold and then taper off to a flat energy dependence well above threshold. Also, Fig. 8.1 shows the visible energy versus the neutrino energy, and Fig. 8.2 shows the recoil $\mu^\pm$ energy and $\cos\theta$ distributions after integrating over the incident neutrino energy spectrum. The angle θ is the reconstructed $\mu^\pm$ direction relative to the incident neutrino direction. Note that the $\mu^\pm$ has an energy on average that is about 2/3 the neutrino energy and a direction that becomes more forward

peaked with energy.

8.2 The ν_μ Disappearance Backgrounds

The main background to ν_μ quasi-elastic scattering is due to single charged pion production, where the pion is mistaken as a muon. For this to happen the pion must decay and not interact or capture, because the $\mu \to e$ decay is the signature for a muon. Also, the pion must be a π^+ and not a π^- because π^- always capture when they come to rest. The single π^+ cross section is only about 4% of the quasi-elastic cross section. Furthermore, as the collision length in oil is about 60 cm, the π^+ will typically interact or scatter before coming to rest. Therefore, the π^+ background in the ν_μ quasi-elastic sample is $< 2\%$ of the sample and is negligible. Other backgrounds, such as $\nu_\mu C \to \mu^- \pi X$ scattering, will have additional Čerenkov cones and are also negligible.

8.3 Projected Oscillation Measurements and Sensitivity

The detector located at 500 m from the neutrino source will measure the ν_μ energy spectrum through quasi-elastic scattering. The event energy distribution can provide proof for ν_μ disappearance oscillations and determine the neutrino oscillation parameters if the atmospheric neutrino problem is due to ν_μ disappearance with $\Delta m^2 > 0.1$ eV^2. Fig. 8.3 shows the ν_μ quasi-elastic energy distribution for two different possible oscillation parameters (motivated by the atmospheric neutrino problem): $\Delta m^2 = 0.2$ eV^2 and $\sin^2 2\theta = 0.5$ (dashed) and $\Delta m^2 = 0.4$ eV^2 and $\sin^2 2\theta = 0.5$ (dotted). Also shown in the figure is a solid line giving the expectations for no oscillations. Note that, as discussed in chapter 5, the neutrino flux varies as r^{-2} to an excellent approximation for $r > 250$ m and for detectors of the size proposed. As is shown in the figure, neutrino oscillations can be clearly measured by observing a variation in the number of $\nu_\mu C \to \mu^- X$ quasi-elastic events as a function of energy. We assume that the overall cross section is known to 25% and that the bin to bin variation in the energy spectrum is known to 10%. We estimate that, for the oscillation parameters above, Δm^2 can be determined with an uncertainty of < 0.2 eV^2 and $\sin^2 2\theta$ with an uncertainty of $< 50\%$.

8.4 An Oscillation Analysis with Reduced Systematic Errors

Another strategy for an oscillation analysis with reduced systematic errors is to divide the $\nu_e C \to e^- X$ visible energy distribution by the $\nu_\mu C \to \mu^- X$ visible energy distribution. This division removes uncertainties associated with the

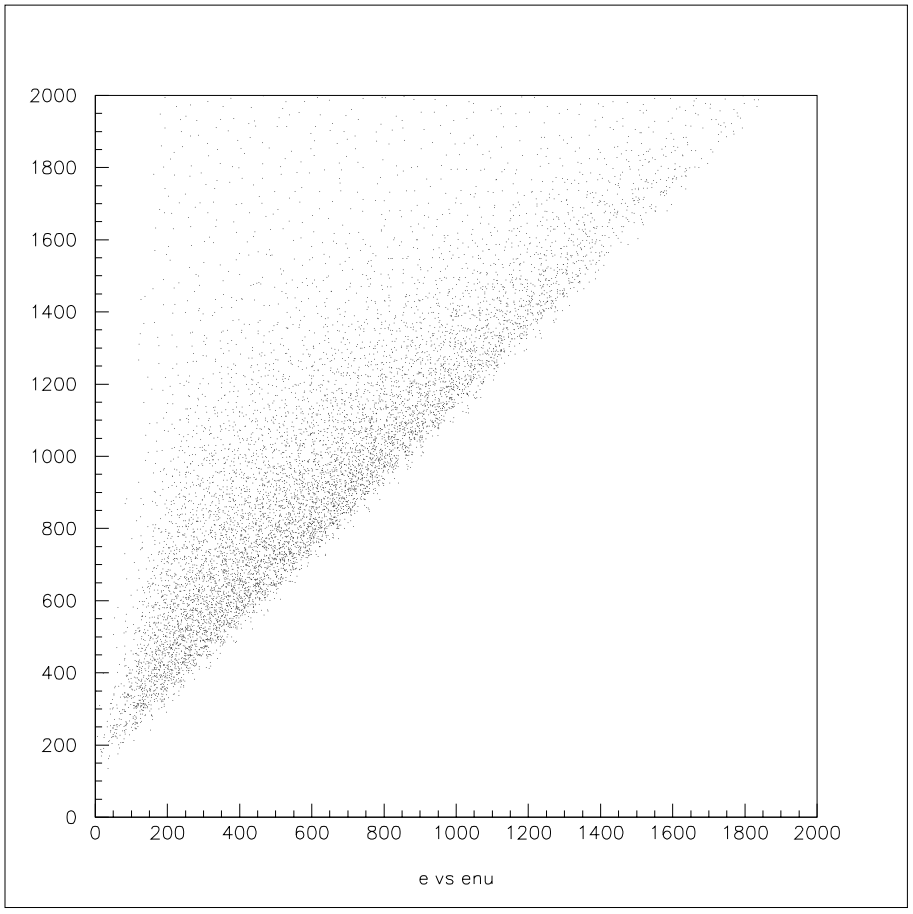

Figure 8.1: The visible energy versus the neutrino energy in MeV from $\nu_\mu C$ quasi-elastic scattering after integrating over the incident neutrino energy spectrum.

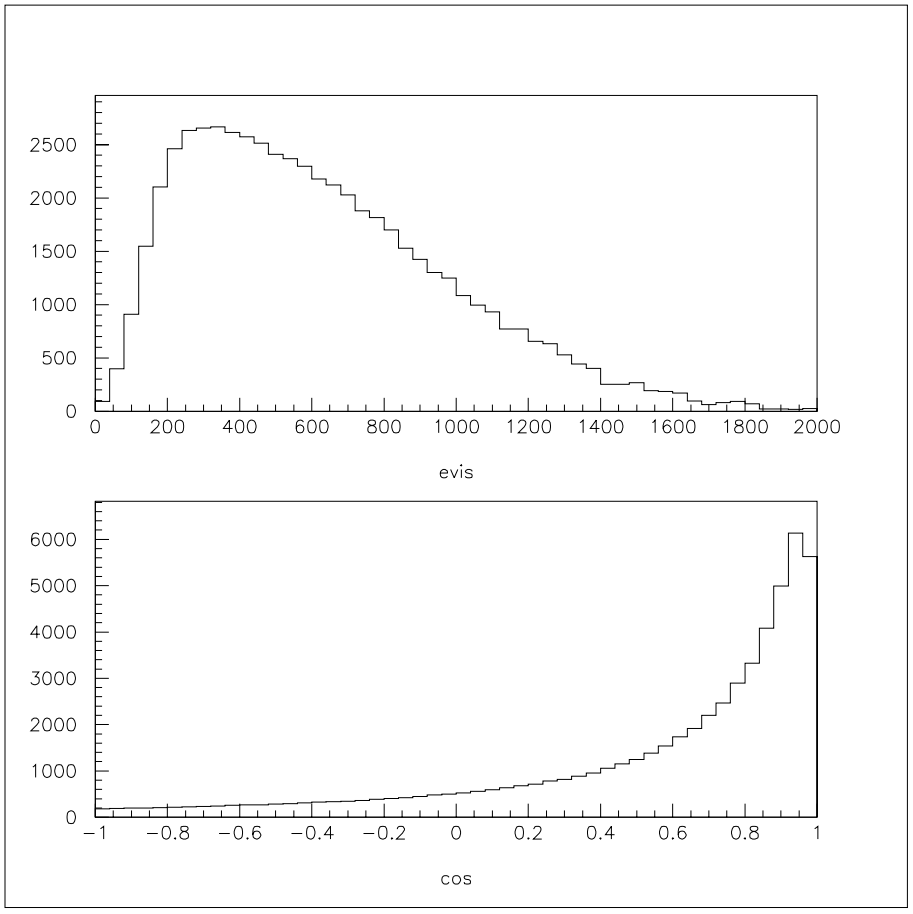

Figure 8.2: The recoil $\mu^{\pm}$ (a) energy in MeV and (b) $\cos\theta$ distributions from quasi-elastic scattering after integrating over the incident neutrino energy spectrum.

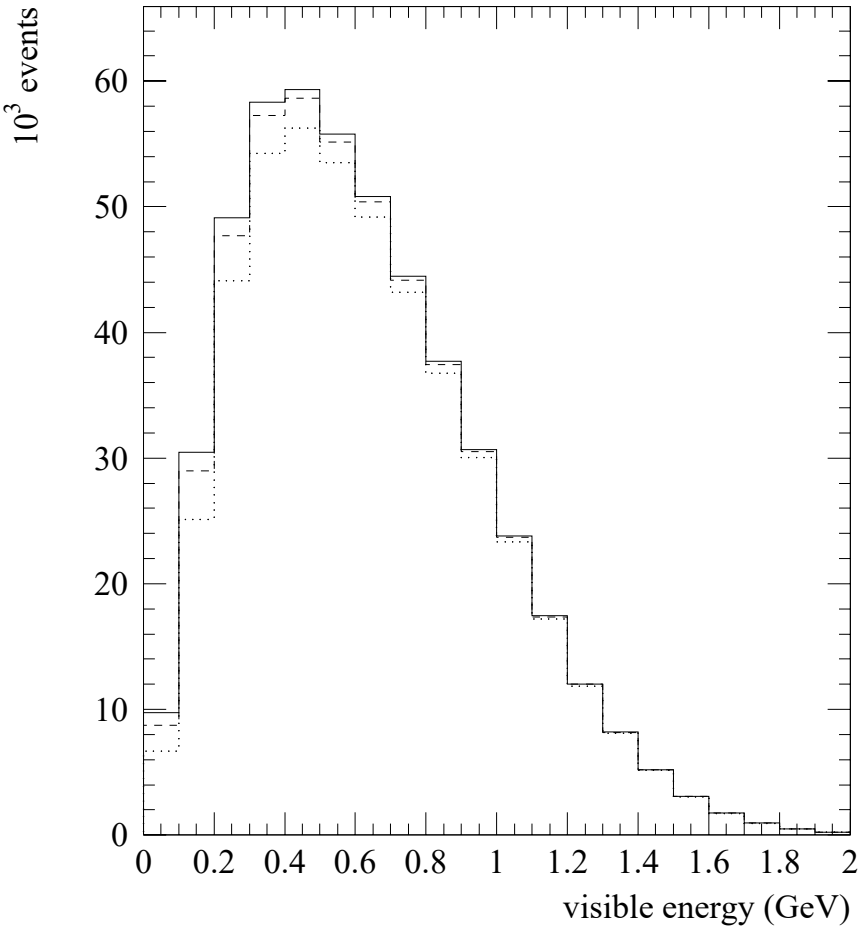

Figure 8.3: The ν_μ quasi-elastic visible energy distribution in MeV for two different possible oscillation parameters (motivated by the atmospheric neutrino problem): $\Delta m^2 = 0.2$ eV^2 and $\sin^2 2\theta = 0.5$ (dashed) and $\Delta m^2 = 0.4$ eV^2 and $\sin^2 2\theta = 0.5$ (dotted). Also shown in the figure is a solid line giving the expectations for no oscillations.

neutrino flux and cross sections, and, furthermore, the effect of oscillations is amplified if both $\nu_\mu \to \nu_e$ appearance and ν_μ disappearance are occurring at the same Δm^2. Fig. 8.4 shows the ratio of the $\nu_e C \to e^- X$ and $\nu_\mu C \to \mu^- X$ visible energy distributions (see Figs. 7.9 and 8.3) for: (a) $\Delta m^2 = 0.2$ eV^2, appearance $\sin^2 2\theta = 0.04$ and disappearance $\sin^2 2\theta = 0.5$ (solid curve); (b) $\Delta m^2 = 0.4$ eV^2, appearance $\sin^2 2\theta = 0.02$ and disappearance $\sin^2 2\theta = 0.5$ (dashed curve); and (c) no oscillations (dotted curve). Neutrino oscillations with the above parameters can be clearly distinguished from no oscillations.

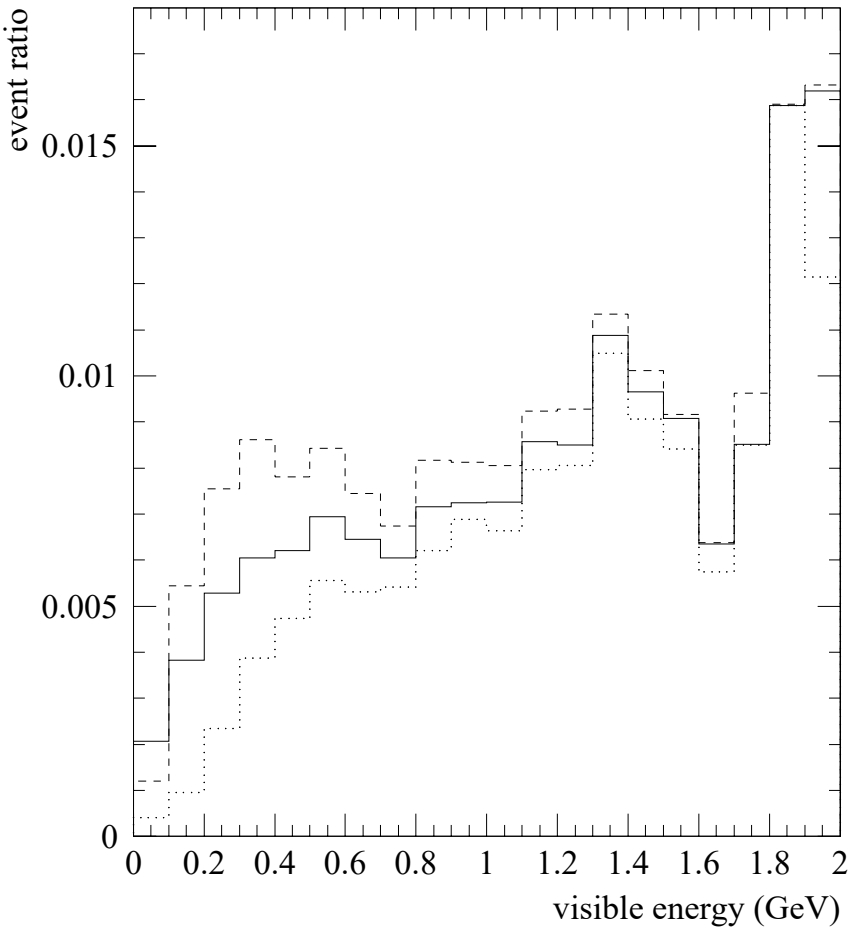

Figure 8.4: The ratio of the $\nu_e C \to e^- X$ and $\nu_\mu C \to \mu^- X$ visible energy distributions in MeV for: (a) $\Delta m^2 = 0.2$ eV^2, appearance $\sin^2 2\theta = 0.04$ and disappearance $\sin^2 2\theta = 0.5$ (solid curve); (b) $\Delta m^2 = 0.4$ eV^2, appearance $\sin^2 2\theta = 0.02$ and disappearance $\sin^2 2\theta = 0.5$ (dashed curve); and (c) no oscillations (dotted curve).

Chapter 9

Non-oscillation Neutrino Physics with MiniBooNE

With the MiniBooNE detector and FNAL Booster neutrino source, a plethora of nuclear and particle physics using the neutrino as a probe could be investigated. These topics include the role of strangeness in the proton, the behavior of the axial vector mass and coupling constant in nuclear matter, the helicity structure of the weak neutral current, and the neutrino magnetic moment.

The large-mass MiniBooNE detector along with the intense Booster neutrino source will create unprecedented neutrino reaction rates at these energies. The number of expected events for several interesting channels are listed in Table 9.1. These numbers are calculated assuming one year of running (2×10^7 s) at each polarity at an average rate of 2.5×10^{13} protons/s. The fiducial detector contains of 1.9×10^{31} CH_2 molecules and all particle ID efficiencies are assumed to be 50%.

The list below outlines some of the interesting physics that may be investigated with MiniBooNE. Several of the channels (namely, $\nu_\mu C \to \mu^- N$ and $\nu_\mu C \to \nu_\mu \pi^0 X$) will need to be understood thoroughly for neutrino oscillation background estimates. The others, while not potential backgrounds, have the possibility of yielding exciting physics. More detailed feasibility studies are currently underway.

- Neutrino-Nucleon Elastic Scattering and a Measurement of G_s

  The $\nu p \to \nu p$ and $\nu n \to \nu n$ reactions (where ν is a ν_μ or a $\bar{\nu}_\mu$) offer the possibility of extracting G_s, the strange quark axial form factor of

Table 9.1: Expected number of detected events in 1 year of running at each horn polarity for selected neutrino channels in the MiniBooNE detector.

ν_μ reaction	events	$\bar{\nu}_\mu$ reaction	events
$\nu_\mu C \to \mu^- N$	510,000	$\bar{\nu}_\mu C \to \mu^+ B$	150,000
$\nu_\mu e \to \nu_\mu e$	130	$\bar{\nu}_\mu e \to \bar{\nu}_\mu e$	60
$\nu_\mu C \to \mu^- \pi^0 X$	65,000	$\bar{\nu}_\mu C \to \mu^+ \pi^0 X$	21,000
$\nu_\mu n, p \to \nu_\mu n, p$	72,000	$\bar{\nu}_\mu n, p \to \bar{\nu}_\mu n, p$	18,000

the nucleon. The ratio of neutrino elastic scattering events producing a proton to those producing a neutron on the isoscalar carbon nucleus is a sensitive measure of G_s and dependent only weakly upon the F_2^s form factor[65]. More exactly, if this ratio is measured for both antineutrinos and neutrinos, G_s and F_2^s are separable[66]. A precision measurement of this ratio will be difficult with MiniBooNE due to the difficulty of separating neutrons and protons and perhaps a dedicated experiment closer to the neutrino source would be required. However, it may be possible to extract information on the strange form factors through the neutral-current/charge-current neutrino-antineutrino asymmetry[67]. This method is currently under study.

- Neutrino Charged-Current Scattering

  The ${\nu_\mu}^{12}C \to {\mu^-}^{12}N$ and ${\bar{\nu}_\mu}^{12}C \to {\mu^+}^{12}B$ reactions will be measured to high precision with MiniBooNE. An attempt will be made to measure M_A, the axial-vector dipole mass, by comparing the two as a function of Q^2, which allows a separation of the free protons from the bound protons in the $\bar{\nu}_\mu$ channel.

- Neutral-Current π^0 Production

  A measure of $\nu_\mu C \to \nu_\mu \pi^0 X$ is a sensitive probe of the structure of the weak neutral-current. Significant gains in precision will be achieved over previous experiments in this energy region. This will enable a test of the standard model prediction of the helicity structure of the weak neutral-current.

- Neutrino-Electron Neutral-Current Scattering

  By measuring the $\nu_\mu e^- \to \nu_\mu e^-$ cross section and its behavior at low-Q^2, we will search for evidence of a magnetic moment of the muon-neutrino. If the neutrino is a Majorana particle (and CPT holds) the neutrino must have no magnetic moment. Thus, a measurement of a non-vanishing

magnetic moment is proof that the neutrino is a Dirac particle. This is a difficult measurement due to the small cross section for this process, however, an non-zero magnetic moment could be of relevance in the solar neutrino problem.

Chapter 10

BooNE: A Future Upgrade to Two Detectors

Given an oscillation signal in the MiniBooNE experiment, a second detector will be added to determine the oscillation parameters. This also permits an initial search for CP violation in the lepton sector.

Given that an oscillation signal is observed in MiniBooNE, then the next goals would be:

- to determine the oscillation parameters for both $\nu_\mu \to \nu_e$ and ν_μ disappearance.
- to search for CP violation in the Lepton Sector.

A natural upgrade to the MiniBooNE experiment that addresses these goals is to add a second detector at a different distance. The energy dependence of the ratio of neutrino events in the two detectors determines the oscillation parameters with very low systematic uncertainty. Comparison of results from running in neutrino mode to antineutrino mode investigates CP violation. A summary of the expectations of this two-detector experiment is provided here.

The second detector will be a spherical tank of the same design as the MiniBooNE detector. The outer volume serves as a veto shield for uncontained events and is optically isolated from the main detector volume. The inner (main detector) volume has a diameter of 11 m and is filled with mineral oil. The inner detector has 1220 eight-inch photomultiplier tubes of the type used for the MILAGRO experiment (Hammamatsu R5912). The electronics and

Table 10.1: The estimated numbers of contained quasi-elastic events for both neutrino and antineutrino scattering and for both the near (500 m) and far (1000 m) detectors. The muon-neutrino quasi-elastic scattering estimates assume no oscillations, while the electron-neutrino quasi-elastic scattering estimates assume 100% $\nu_\mu \to \nu_e$ transmutation.

Reaction	Near Detector	Far Detector
$\nu_\mu C \to \mu^- X$	1,180,000	295,000
$\bar{\nu}_\mu C \to \mu^+ X$	220,000	55,000
$\nu_e C \to e^- X$	1,234,000	309,000
$\bar{\nu}_e C \to e^+ X$	230,000	58,000

data acquisition would be similar to the LSND design. The tank would be placed underground, with 20' of dirt overburden to reduce the rate of cosmic ray muons and eliminate the cosmic ray hadronic component. An approximate cost estimate for this detector is given in the chapter on costs and schedule.

The new, far detector will be placed approximately 1000 meters from the neutrino source. The MiniBooNE detector would be used as the near detector, located at 500 meters from the beam line target. These distances are chosen to provide the optimum comparison between the rate of events in the near and far detector, as discussed below. The MiniBooNE beam line will be used to provide the neutrino and antineutrino beams for both detectors.

10.1 Event Rates for BooNE

For the estimation of event rates we make the following assumptions. First, we assume that the Booster operates at an energy of 8 GeV and at an average rate of 5 Hz (2.5×10^{13} protons/s) for 2 calendar years of operation (4×10^7 s) at the positive focusing polarity. Also, we assume that the fiducial volume of the detector is 445 t (1.9×10^{31} CH_2 molecules) and that the total electron and muon efficiencies, including PID, are 50%. The resulting numbers of quasi-elastic events are shown in Table 10.1 for both neutrino and antineutrino scattering and for both the near (500 m) and far (1000 m) detectors. The muon-neutrino quasi-elastic scattering estimates assume no oscillations, while the electron-neutrino quasi-elastic scattering estimates assume 100% $\nu_\mu \to \nu_e$ transmutation.

10.2 $\nu_\mu \to \nu_e$ Appearance

The two detectors located at 500 m and 1000 m from the neutrino source will measure the ν_e energy spectrum through quasi-elastic scattering as described in sections 7 and 8. The energy-dependent ratio of event rates from the two detectors will provide proof that neutrino oscillations are occurring and will allow the determination of the neutrino oscillation parameters (assuming that the LSND signal is indeed due to neutrino oscillations). Fig. 10.1 shows the ratio of ν_e quasi-elastic events from the detectors at 500 m and 1000 m as a function of visible energy for four different possible oscillation parameters (motivated by LSND): (a) $\Delta m^2 = 0.2$ eV^2 and $\sin^2 2\theta = 0.04$; (b) $\Delta m^2 = 0.4$ eV^2 and $\sin^2 2\theta = 0.02$; (c) $\Delta m^2 = 0.6$ eV^2 and $\sin^2 2\theta = 0.01$; (d) $\Delta m^2 = 0.8$ eV^2 and $\sin^2 2\theta = 0.008$. For each set of oscillation parameters it is assumed that the total background rate from all sources (intrinsic ν_e component in the beam, π^0 background, μ background, etc.) is 0.5% of the $\nu_\mu \to \nu_e$ 100% transmutation rate. Also shown in the figures (at a ratio of 1) are solid lines giving the expectations for no oscillations. Note that, as discussed in chapter 4, the neutrino flux varies as r^{-2} to an excellent approximation for $r > 250$ m. As is shown in the figures, neutrino oscillations can be clearly observed and measured. We estimate that, for the oscillation parameters above, Δm^2 can be determined with an uncertainty of < 0.1 eV^2 and $\sin^2 2\theta$ with an uncertainty of $< 25\%$.

10.3 ν_μ Disappearance

The two detectors located at 500 m and 1000 m from the neutrino source also will measure the ν_μ energy spectrum through quasi-elastic scattering as described in sections 8 and 9. The energy-dependent ratio of event rates from the two detectors can be used to observe ν_μ disappearance oscillations and determine the neutrino oscillation parameters. Figs. 10.2 and 10.3 show how the visible energy will change with Δm^2 for full mixing for the 500 m and 1000 m detectors, respectively. Fig. 10.4, shows the ratio for full mixing. Motivated by the atmospheric neutrino problem, Fig. 10.5 shows the ratio of ν_μ quasi-elastic events from the detectors at 1000 m and 500 m as a function of visible energy for: (a) $\Delta m^2 = 0.1$ eV^2 and $\sin^2 2\theta = 0.5$; (b) $\Delta m^2 = 0.2$ eV^2 and $\sin^2 2\theta = 0.5$; (c) $\Delta m^2 = 0.4$ eV^2 and $\sin^2 2\theta = 0.5$. Also shown in these figures (at a ratio of 1) are solid lines giving the expectations for no oscillations. Note that, as discussed in chapter 5, the neutrino flux varies as r^{-2} to an excellent approximation for $r > 250$ m. As is shown in the figures, neutrino oscillations can be clearly observed and measured. We estimate that, for the oscillation

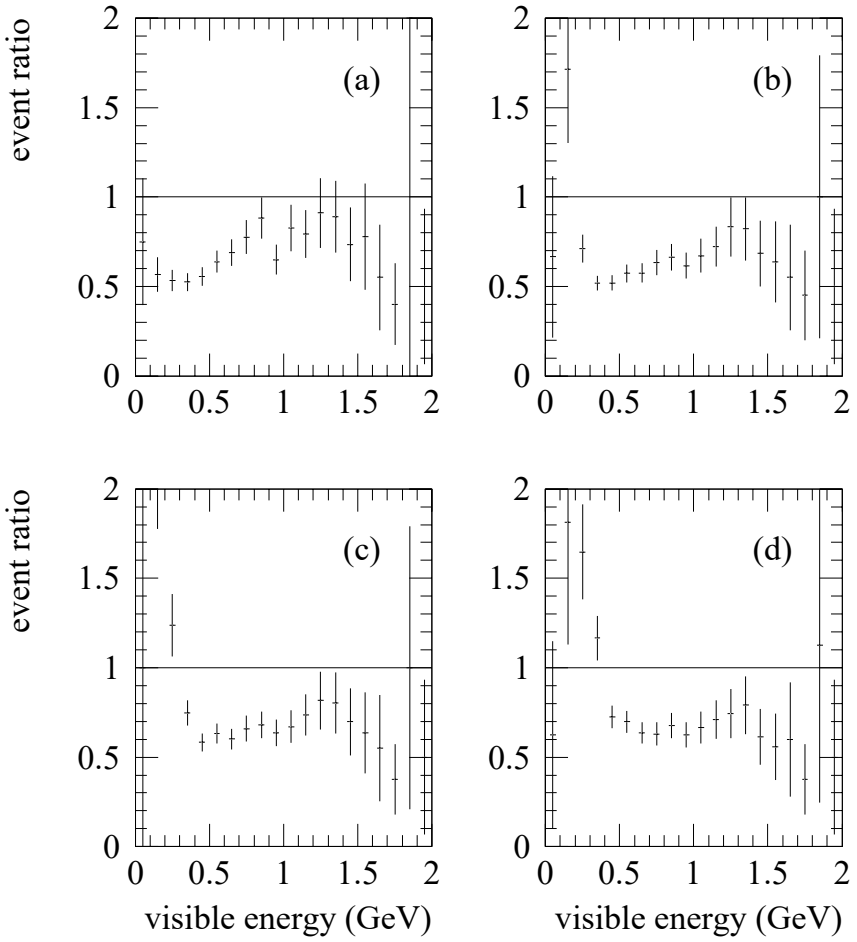

Figure 10.1: The ratio of ν_e quasi-elastic events from the detectors at 500 m and 1000 m as a function of visible energy in GeV for four different possible oscillation parameters (motivated by LSND): (a) $\Delta m^2 = 0.2$ eV^2 and $\sin^2 2\theta = 0.04$; (b) $\Delta m^2 = 0.4$ eV^2 and $\sin^2 2\theta = 0.02$; (c) $\Delta m^2 = 0.6$ eV^2 and $\sin^2 2\theta = 0.01$; (d) $\Delta m^2 = 0.8$ eV^2 and $\sin^2 2\theta = 0.008$. Also shown in the figures (at a ratio of 1) are solid lines giving the expectations for no oscillations.

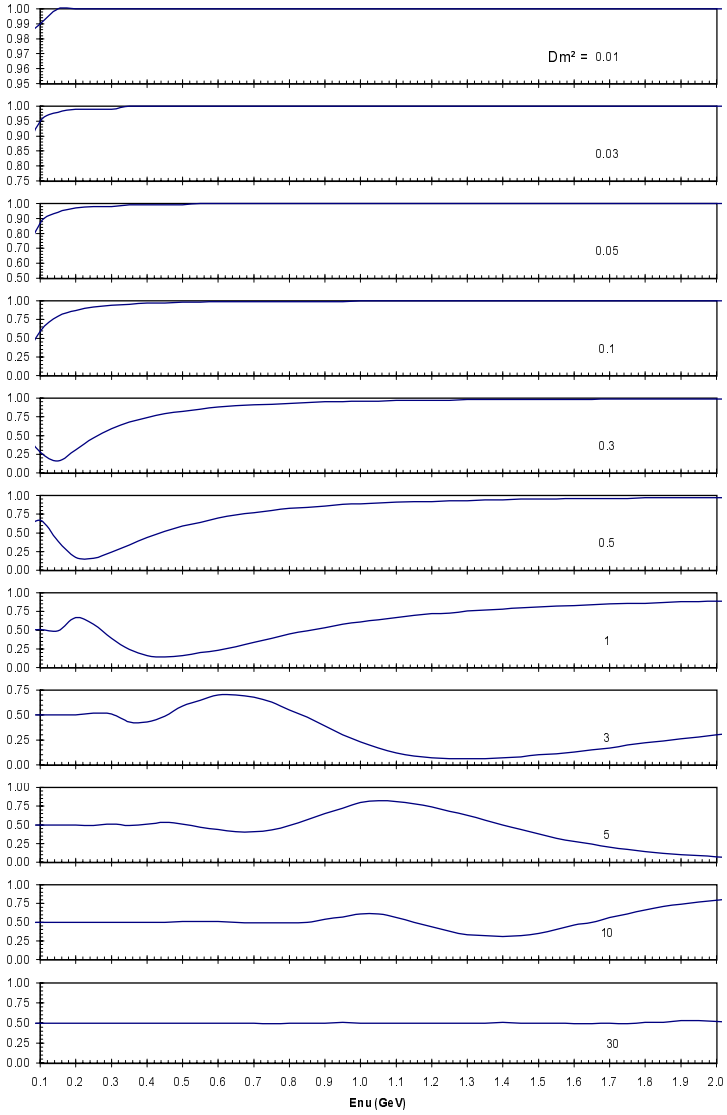

Figure 10.2: The dependence on energy of events at the near (500 m) detector for full mixing and various Δm^2 values.

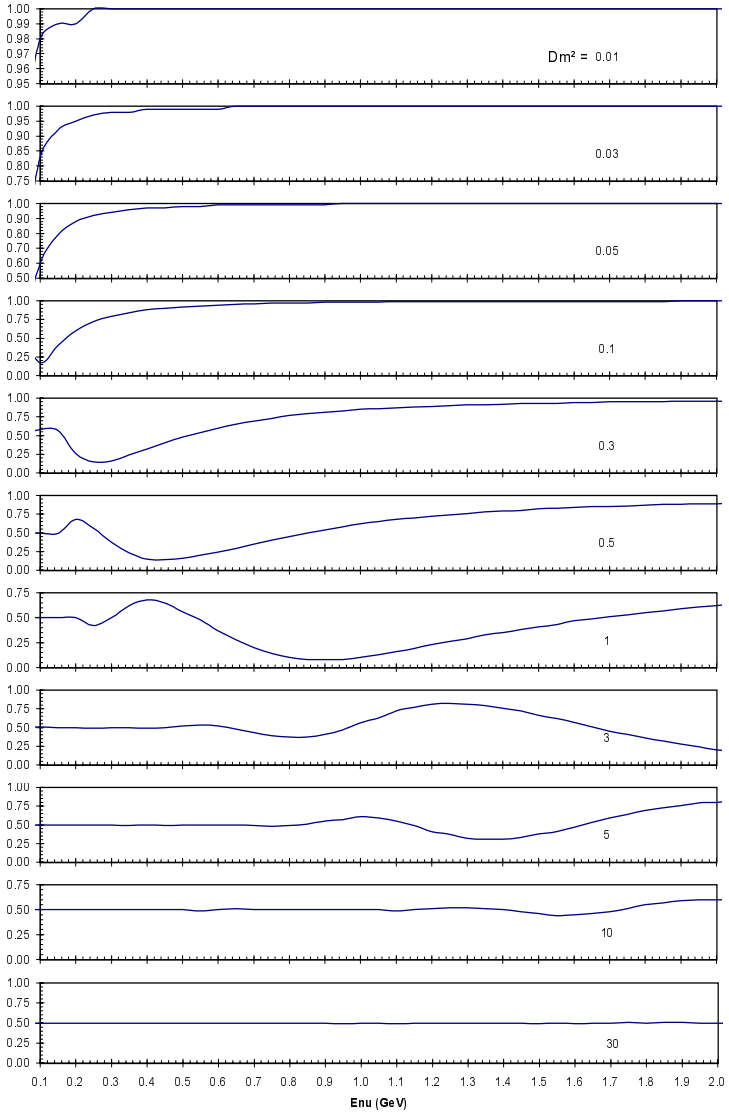

Figure 10.3: The dependence on energy of events at the far (1000 m) detector for full mixing and various Δm^2 values.

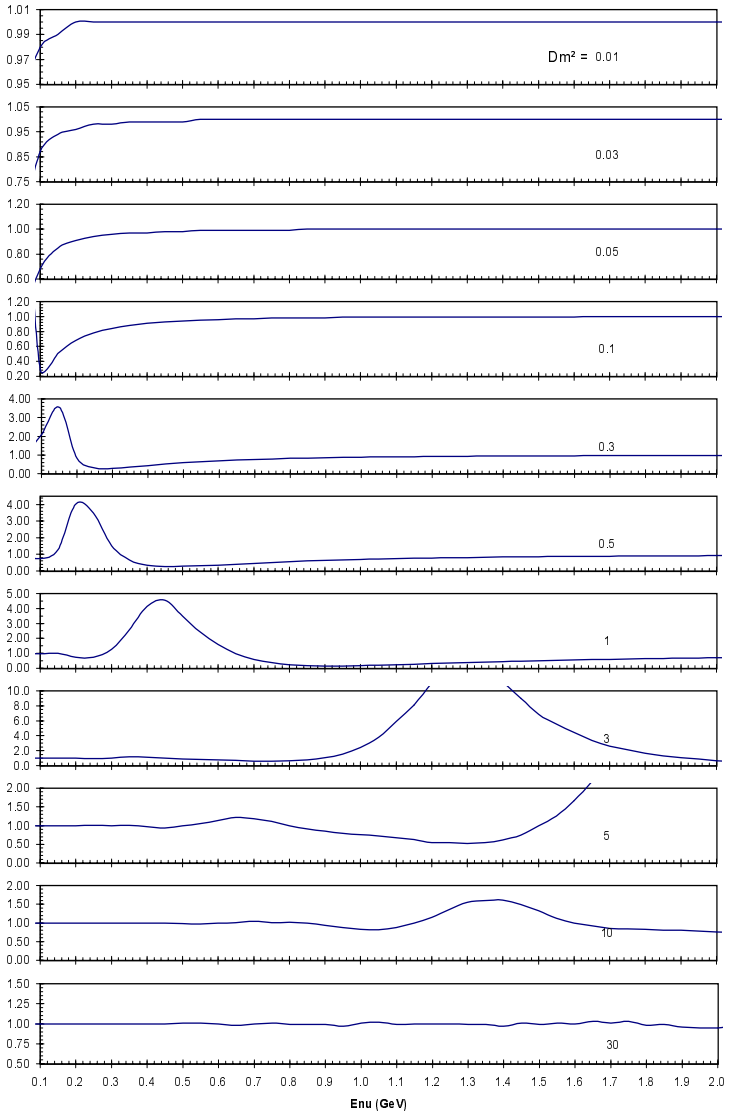

Figure 10.4: The ratio of events at the near (500 m) and far (1000 m) detectors as a function of energy for full mixing and various Δm^2 values.

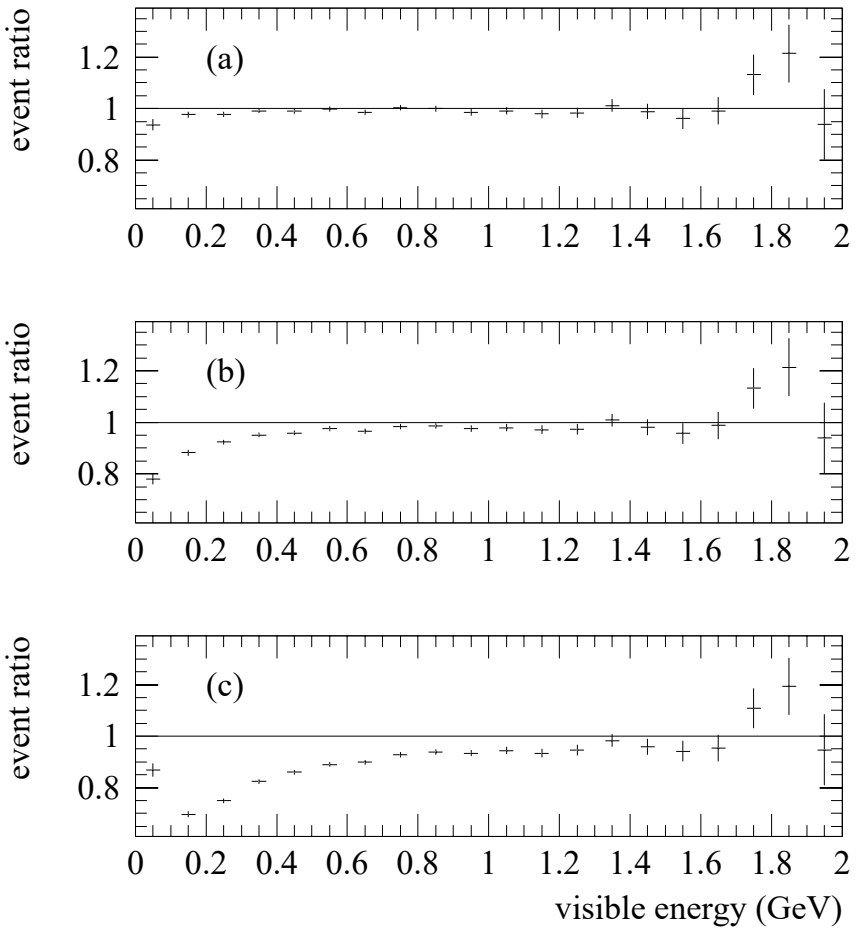

Figure 10.5: The ratio of ν_μ quasi-elastic events from the detectors at 1000 m and 500 m as a function of visible energy in GeV for three different possible oscillation parameters (motivated by the atmospheric neutrino problem): (a) $\Delta m^2 = 0.1$ eV^2 and $\sin^2 2\theta = 0.5$; (b) $\Delta m^2 = 0.2$ eV^2 and $\sin^2 2\theta = 0.5$; (c) $\Delta m^2 = 0.4$ eV^2 and $\sin^2 2\theta = 0.5$. Also shown in the figures (at a ratio of 1) are solid lines giving the expectations for no oscillations.

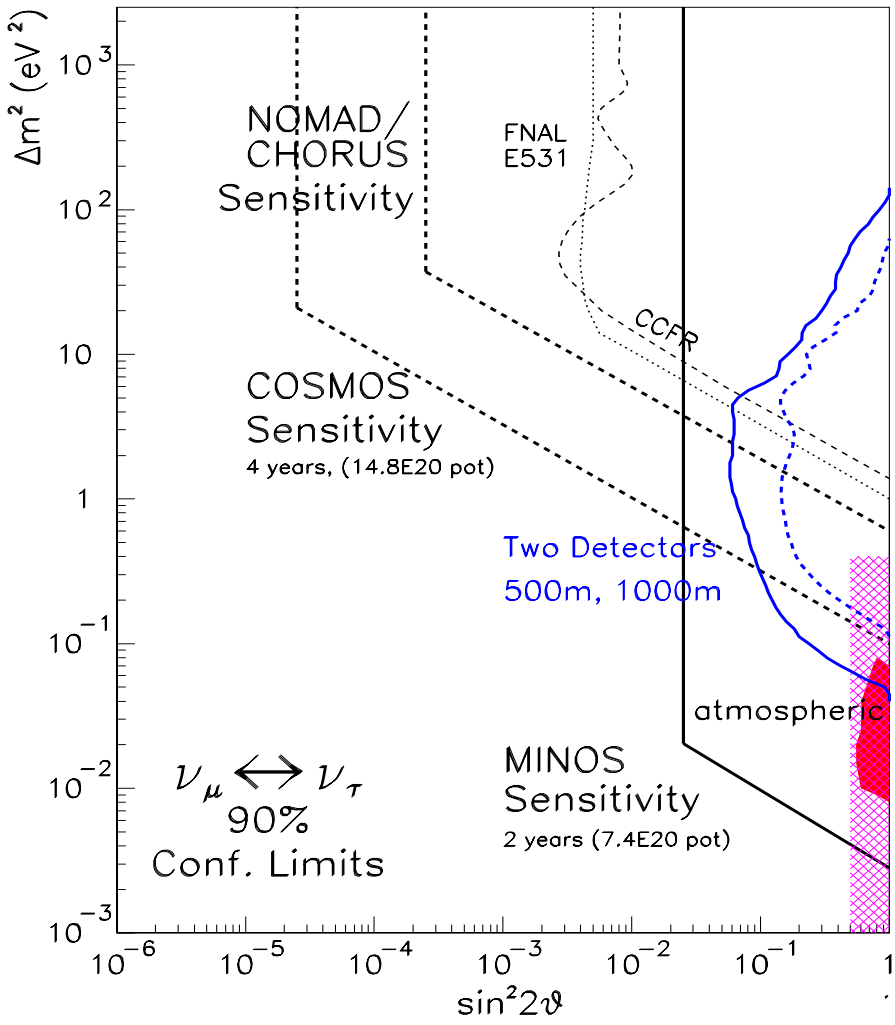

Figure 10.6: Summary of results from past experiments (narrow, dashed and dotted), future approved experiments (wide, dashed) and 90% C.L. limit expected for the two-detector configuration, BooNE, (solid) for ν_μ disappearance after one calendar year of running at 0.5 km and 1 km. Solid region indicates the favored region for the atmospheric neutrino deficit from the Kamiokande experiment. No zenith angle dependence would extend the favored region to higher Δm^2 as indicated by the hatched region.

parameters above, Δm^2 can be determined with an uncertainty of < 0.1 eV^2 and $\sin^2 2\theta$ with an uncertainty of $< 25\%$. The expected limits if no signal is observed is shown in Fig. 10.6.

10.4 Search for CP Violation in the Lepton Sector

Assuming that $\nu_\mu \to \nu_e$ and $\bar{\nu}_\mu \to \bar{\nu}_e$ oscillations are observed, then, by comparing the neutrino and antineutrino oscillation parameters, it will be possible to make a test for CP violation in the lepton sector. CP violation may appear as a difference in the measured values of $\sin^2 2\theta$ (or even Δm^2, because in general all three different Δm^2 values can contribute to an oscillation signal) for neutrinos compared to antineutrinos. We estimate that CP violation can be observed easily if the violation is unexpectedly large ($> 25\%$).

Chapter 11

Overview of Cost and Schedule

The cost of the MiniBooNE detector and neutrino beam line are estimated to be $2.21M and $3.92M (or $3.07M and $6.25M with contingency and escalation), respectively. A reasonable time scale is the commencement of data taking in 2001.

In Figs. 11.1 and 11.2 are shown the cost and schedule for design and construction of the detector summary tasks. In Appendix C a full cost and schedule is shown with dependent tasks defined. The time of each summary task has been estimated and the duration in days is shown in the diagram. The dependence on predecessor tasks is explicit. It is assumed that all tasks are started as soon as predecessor functions are complete and that labor of appropriate skill will be available as soon as necessary. (Therefore, this schedule is optimistic in that sense.) In addition, it is assumed that funding will be available as soon as parts acquisition is possible (i.e. design of components is complete). In reality, both funding and labor will have a substantial impact on the actual schedule, but enough is uncertain at this time that an unconstrained schedule seems to be the most useful planning device.

The cost estimate for the civil construction of the beamline tunnel and Target Hall are given in the Project Definition Cost Estimate (PDCE) prepared by the Facility Engineering Services Section. The rollup of that estimate is reproduced in Figure 11.3. The estimate is based on the construction schedule given in the PDCE, which is also reproduced in Figure 11.4, along with the schedule for construction and installation of the technical components. The

ID	Task Name	Duration	Start	Finish	Cost	Predecessors
1	1 Detector Conceptual Design	324d	Mon 8/18/97	Thu 11/12/98	$20,000.00	
2	1.1 Site Plan	168d	Mon 8/18/97	Wed 4/8/98	$0.00	
3	1.1.1 Detector Position	47d	Mon 8/18/97	Tue 10/21/97	$0.00	
7	1.1.2 Site Elements	121d	Wed 10/22/97	Wed 4/8/98	$0.00	3
13	1.2 Containment	124d	Mon 8/18/97	Thu 2/5/98	$20,000.00	
21	1.3 Tennis Dome	30d	Fri 2/6/98	Thu 3/19/98	$0.00	19
25	1.4 Penetrations	70d	Fri 2/6/98	Thu 5/14/98	$0.00	19
32	1.5 Outside Access	40d	Fri 3/20/98	Thu 5/14/98	$0.00	23
38	1.6 Containment Specification	30d	Fri 5/15/98	Thu 6/25/98	$0.00	13,25
41	1.7 Containment Internal Structure	100d	Fri 6/26/98	Thu 11/12/98	$0.00	39
51	2 Detector Detailed Design	160d	Fri 5/15/98	Thu 12/24/98	$0.00	
52	2.1 System Layout	150d	Fri 5/15/98	Thu 12/10/98	$0.00	
60	2.2 Containment	30d	Fri 11/13/98	Thu 12/24/98	$0.00	49
70	2.3 External Services	30d	Fri 5/15/98	Thu 6/25/98	$0.00	32

Figure 11.1: Page 1 of the cost and schedule for design and construction of the detector summary tasks.

ID	Task Name	Duration	Start	Finish	Cost	Predecessors
84	4 Containment Construction	270d	Fri 1/8/99	Thu 1/20/00	$850,000.00	82
86	4.2 Bid Process	10d	Fri 1/8/99	Thu 1/21/99	$0.00	
88	4.3 Excavation	120d	Fri 3/5/99	Thu 8/19/99	$0.00	87FS+30d
92	4.4 Tennis Dome Construction	90d	Fri 9/17/99	Thu 1/20/00	$50,000.00	91FS+20d
97	5 Detector Component Fabrication	90d	Fri 11/13/98	Thu 3/18/99	$15,900.00	68
98	5.1 Cable Plant	90d	Fri 11/13/98	Thu 3/18/99	$15,900.00	
100	5.1.2 Laser Calibration	15d	Fri 11/13/98	Thu 12/3/98	$5,700.00	
106	5.1.3 Imlay Bulbs	45d	Fri 12/4/98	Thu 2/4/99	$3,000.00	101
110	5.1.4 Attenuation Length Tester	30d	Fri 2/5/99	Thu 3/18/99	$2,200.00	109
115	6 Detector Internal Installation	85d	Fri 1/21/00	Thu 5/18/00	$40,000.00	95,113
121	7 PMTs	503d	Tue 12/1/98	Thu 11/2/00	$18,000.00	
123	7.2 LANL Detector	433d	Tue 1/26/99	Thu 9/21/00	$12,000.00	
129	7.3 LANL Veto	473d	Tue 12/1/98	Thu 9/21/00	$6,000.00	122
137	8 Caboose	280d	Tue 12/1/98	Mon 12/27/99	$192,000.00	122
138	8.1 Layout	280d	Tue 12/1/98	Mon 12/27/99	$192,000.00	
139	8.1.1 Preamps	60d	Tue 12/1/98	Mon 2/22/99	$2,000.00	
141	8.1.2 Trigger System	241d	Tue 12/1/98	Tue 11/2/99	$70,000.00	
142	8.1.2.1 Local Tzero Generation	1d	Tue 12/1/98	Tue 12/1/98	$5,000.00	
147	8.1.3 Primary Channels (QT)	90d	Tue 2/23/99	Mon 6/28/99	$5,000.00	140
149	8.1.4 Crate structure	220d	Tue 2/23/99	Mon 12/27/99	$85,000.00	140
156	8.1.5 System Monitoring	90d	Tue 2/23/99	Mon 6/28/99	$30,000.00	140
157	8.1.5.1 Local System	90d	Tue 2/23/99	Mon 6/28/99	$20,000.00	
162	9 Local DAQ	40d	Tue 12/28/99	Mon 2/21/00	$115,000.00	137
163	9.1 Site Data Handling	40d	Tue 12/28/99	Mon 2/21/00	$105,000.00	
168	10 Lab E	60d	Tue 1/25/00	Mon 4/17/00	$2,500.00	166
174	11 Oil	85d	Fri 1/8/99	Thu 5/6/99	$550,000.00	82
181	12 Assembly & Commissioning	80d	Fri 11/3/00	Thu 2/22/01	$0.00	135,172
182	12.1 Pre Fill Operation	80d	Fri 11/3/00	Thu 2/22/01	$0.00	
185	12.1.3 Oil Filling	35d	Fri 12/29/00	Thu 2/15/01	$0.00	179,184

Figure 11.2: Page 2 of the cost and schedule for design and construction of the detector summary tasks.

cost estimate for the technical components is given in Figure 11.5. Note that escalation is not included in the cost estimates. If an escalation of 6.7% is used to mid-term year 00, the escalation would be $234,000 in the beamline civil cost estimate, and about $165,000 in the technical estimate. Overhead and G&A are excluded from all cost estimates at this time.

The civil construction for the beamline tunnel will have to coincide with a Main Injector shutdown of two months. This is to allow for construction that is near the Main Injector and cannot be adequately shielded for radiation. The construction of the Target Hall will include time for installation of the target pile steel and the beam absorber. Twenty one calendar days are provided for this activity. The civil construction associated with the detector is geographically separate from beamline construction, and will be carried out by a separate and independent contract.

Horn #1 and the horn power supply are technically challenging elements. Provision is made in the schedule for testing of horn #1 and the supply, so that the design can be thoroughly verified before installation in the Target Hall, and before the horn is exposed to beam and made radioactive. The contingency in both cost and schedule for this element is problematic at this stage of design, and may require revision when the ANSYS analysis is carried out and we have a better understanding of the degree of reliability we can incorporate into the final design. The conflict between the need for a thin inner conductor to minimize beam interactions, and the need for structural integrity is not fully understood at this time and will require further study.

Cost Breakdown

Project Cost		Equipment Cost
• Site Work	$635,000.	
• Concrete	$870,000.	
• Metal	$89,000.	$200,000.
• Woods and Plastics	$8,000.	
• Finishes	$48,000.	
• Mechanical	$78,000.	
• Electrical	$232,000.	
Subtotal	$1,960,000.	$200,000.
O&P @15%	$294,000.	
Total	$2,254,000.	$200,000.

EDIA

Project Cost		Other Costs	
		EDIA CDR @ 3%	$84,000.
EDIA Title 1 and 2 @14%	$316,000		
EDIA Title 3 @9%	$203,000		
Geotechnical	18,000.		
Total	$537,000.		$84,000.

Project Cost Summary

Project Cost

Subcontract	$2,254,000.
EDIA	$537,000.
Subtotal	$2,791,000.
Contingency & Mgnt. Rsv. @25%	$698,000.
Subtotal	$3,489,000.
Escalation to (June 2000) mid-point of construction @6.7%	$234,000.
Subtotal	$3,723,000.

Figure 11.3: Cost estimate for beamline civil construction.

Figure 11.4: Schedules for beamline civil construction, and construction and installation of the technical elements.

Monies in FY97 Dollars

Technical Component Cost Estimate Total Including Contingency: $ 2,550,032

WBS		M&CS	Labor	Total	M&CS Contingency % and $		Labor Contingency % and $		Total Contingency
	Technical Components	**864,641**	**1,151,600**	**2,016,241**		**215,349**		**328,780**	**533,791**
1	**Primary Beam Devices**	**28,000**	**66,421**	**94,421**		**8,400**		**19,926**	**28,326**
1.1.	New Devices			0	30%	0	30%	0	0
1.2.	Reclaimed Devices	28,000	28,611	56,611	30%	8,400	30%	8,583	16,983
1.14.	EDIA		2,352	2,352			30%	706	706
1.15.	Installation	0	35,458	35,458	30%	0	30%	10,637	10,637
2	**Neutrino Beam Devices**	**60,227**	**579,205**	**639,432**		**31,572**		**173,762**	**194,997**
2.1.	Target & Horn #1	36,400	24,900	61,300	30%	10,920	30%	7,470	18,390
2.2.	Horn #2	8,000	119,200	127,200	30%	2,400	30%	35,760	38,160
2.3.	Absorber	26,384	42,581	68,965	30%	7,915	30%	12,774	20,689
2.4.	Collimator	25,843	0	25,843	40%	10,337	40%	0	
2.5.	Target Pile Shielding	0	177,020	177,020	30%	0	30%	53,106	53,106
2.14.	EDIA		121,040	121,040			30%	36,312	36,312
2.15.	Installation	0	94,464	94,464	30%	0	30%	28,339	28,339
3	**Power Supplies**	**453,908**	**175,103**	**629,011**		**77,260**		**52,531**	**129,791**
3.1.	Magnet and Septa Power Supplies	61,158	0	61,158	30%	18,347	30%	0	18,347
3.2.	Horn Power Supplies	392,750	9,552	402,302	15%	58,913	30%	2,866	61,778
3.14.	EDIA		100,000	100,000			30%	30,000	30,000
3.15.	Installation	0	65,551	65,551	30%	0	30%	19,665	19,665
4	**Vacuum System**	**50,200**	**89,050**	**139,250**		**25,100**		**13,055**	**38,155**
4.1.	Materials & Contracted Services	50,200	0	50,200	50%	25,100	30%	0	25,100
4.14.	EDIA		78,676	78,676	30%		10%	7,868	7,868
4.15.	Installation	0	10,374	10,374	50%	0	50%	5,187	5,187
5	**Water Systems**	**86,750**	**30,400**	**117,150**		**17,350**		**6,080**	**23,430**
5.1.	Materials & Contracted Services	86,750	5,400	92,150	20%	17,350	20%	1,080	18,430
5.14.	EDIA		25,000	25,000			20%	5,000	5,000
5.15.	Installation	0	0	0	20%	0	20%	0	0
6	**Instrumentation**	**111,376**	**91,686**	**203,062**		**33,413**		**27,506**	**60,919**
6.1.	Primary Beam Devices	55,266	66,441	121,707	30%	16,580	30%	19,932	36,512
6.2.	Secondary Beam Devices	56,110	25,245	81,355	30%	16,833	30%	7,574	24,407
7	**Controls**	**52,100**	**100,515**	**152,615**		**15,630**		**30,155**	**45,785**
7.1.	Internet Rack Monitor	35,000	98,781	133,781	30%	10,500	30%	29,634	40,134
7.2.	SWIC Electronics	17,100	1,734	18,834	30%	5,130	30%	520	5,650
8	**Safety Interlocks**	**22,080**	**19,220**	**41,300**		**6,624**		**5,766**	**12,390**
8.1.	Materials & Contracted Services	22,080	0	22,080	30%	6,624	30%	0	6,624
8.14.	EDIA		7,000	7,000			30%	2,100	2,100
8.15.	Installation	0	12,220	12,220	30%	0	30%	3,666	3,666

Instrumentation & Controls (elements 6 and 7) include EDIA and Installation in the M&CS and Labor costs.

Figure 11.5: Cost estimate for the beamline technical elements.

Chapter 12

Conclusions

The MiniBooNE experiment will have the capability of observing both $\nu_\mu \to \nu_e$ appearance and ν_μ disappearance. It will also search for CP violation in the lepton sector.

We propose to construct and operate a neutrino detector system and broad band neutrino beam generated from the Fermilab Booster that has the capability of observing and measuring $\nu_\mu \to \nu_e$ oscillations and ν_μ disappearance over a wide range of Δm^2. The motivation for this experiment stems from the LSND neutrino oscillation result[1] and the atmospheric neutrino problem. The relatively low energy (0.1 - 2.0 GeV) neutrino beam combined with a detector distance of 500 m will cover the interesting Δm^2 region between 0.01 and 1.0 eV^2 for modest cost and effort. The proposed MiniBooNE experiment would start with a single detector with the goal of probing this mass region and establishing definitive indications of neutrino oscillations. If a positive signal is observed, a second stage, BooNE, would use two detectors at different distances in the same neutrino beam to accurately determine the oscillation parameters and investigate any CP violating $\nu_\mu/\bar{\nu}_\mu$ effects.

The MiniBooNE experiment will use one detector at a distance of 500 m from the neutrino beam source. The high intensity available from the Booster combined with an efficient horn-focused secondary beam will provide over 500,000 events per year in the $\sim$ 800 ton detector. With this setup, the intrinsic ν_e component of the beam is less than 3×10^{-3}. The totally active MiniBooNE detector has good particle identification capabilities and the expected mis-identification fraction is at the $< 2 \times 10^{-3}$ level. Comparisons of the observed ν_e and ν_μ energy distributions with expectations will allow a

sensitive search for $\nu_\mu \to \nu_e$ oscillations and ν_μ disappearance.

If oscillations exist at the LSND level, MiniBooNE should see approximately one thousand anomalous ν_e events over background and establish the signal at the $> 8\,\sigma$ level. From the energy dependence of the excess, the oscillation parameters can be determined in the LSND region with a Δm^2 ($\sin^2 2\theta$) uncertainty of < 0.2 eV^2 ($< 50\%$) respectively. Examining the signal with both incident ν_μ and $\bar{\nu}_\mu$ will allow a first look at possible CP violation effects in the lepton mixing matrix. On the other hand, if no oscillation signal is observed, the experiment will significantly extend the region probed for oscillations and exclude $\nu_\mu \to \nu_e$ oscillations with $\sin^2 2\theta > 3.8 \times 10^{-4}$ for large Δm^2 and $\Delta m^2 > 0.02$ eV^2 for $\sin^2 2\theta = 1$.

In summary, the MiniBooNE experiment will make a sensitive search for ν_e appearance and ν_μ disappearance from neutrino oscillations. The experiment has unique capabilities and sensitivity to measure oscillations in this region in a cost effective and timely manner.

Appendix A

Changes to the Design from the Letter of Intent

Although the concept of the experimental design has remained the same since the MiniBooNE Letter of Intent was submitted to the Fermilab PAC in May, 1997, several improvements have been made in order to maximize the physics, while maintaining a reasonable level of cost. The changes made to the design since the LOI are explained in this appendix.

A.1 Tank Geometry

The new tank design is a 6 m sphere. The spherical tank design was recommended over the cylindrical plan by tank engineering firms. A spherical design is straightforward to construct and economically feasible. For 10% phototube coverage, the spherical design increases the total fiducial volume of the detector from 382 t to 445 t. Two firms have been approached for preliminary cost estimates: Chicago Bridge and Iron and Pittsburgh-Des Moines. One firm will be retained for a conceptual design.

A.2 Pure Oil

Mineral oil which is not doped with scintillator will be used in the detector. Analysis of LSND run 664, data on oil which was not doped with scintillator, indicates a ratio of Čerenkov to scintillation light of 3 to 1. The fraction of "prompt" Čerenkov light to "late" scintillation light in an event is a useful input for particle identification. Doping with scintillator can obscure the Čerenkov

light, so undoped oil appears to be the best choice for particle identification. Tests of scintillation light from the undoped oil, performed at Texas A & M in late October, are described in the proposal.

A.3 Veto

GEANT studies indicate that a thick wall between the veto and tank is unnecessary. The veto and detector will be constructed as a single volume filled with undoped mineral oil. The 1220 detector phototubes will be mounted on an internal support structure. Opaque shields around the tubes will optically separate the veto and the detector. The 292 veto phototubes will be mounted on the same support structure, facing outward.

A.4 Systematic error from particle misidentification

The systematic error from misidentification of μs and π^0s is 5%. This level was determined by using the μ and π^0 events which are not misidentified to constrain the level of misidentified events.

A.5 Detector position relative to beam line

The detector will be positioned on axis with the beam, 6 m below ground level. This is a preferable design if further detectors are to be installed in-line in the future. This is economically feasible with the spherical tank design, which requires less excavation than a cylindrical design.

A.6 Detector position relative to target

The detector will be located at a distance of 500 m from the proton target. Three reasons led to the change in detector position. First, the 1 km position chosen for the LOI represented a balance between a lower reach in Δm^2 for the ν_μ disappearance search and statistics for the $\nu_\mu \to \nu_e$ oscillation search. Second, installation at 500 km leaves flexibility for the position of a "far" detector in the future if a $\nu_\mu \to \nu_e$ signal is observed. The L of the far detector will be chosen based on the observations from the initial tank. Third, the best design for a future two-tank experiment places the largest tank at the farthest distance. The size of initial tank is constrained by the requirement of 10% coverage with the 1220 LSND phototubes. Thus, it is best to design this tank to be the near detector.

A.7 Beamline Direction

The beam direction is now approximately along project north. Altering the beam direction allows the extraction line to avoid the main injector cooling ponds, places the first detector in a field which is easily accessible by a road, but not visible from Kirk road, and permits a second future detector to be placed on site at any L between 1 and 3 km.

A.8 8 GeV Beam Extraction

The 8 GeV proton transport will use EPB dipoles rather than permanent dipoles. This provides flexibility for the future if the Booster is upgraded in energy. The EPB dipoles and associated transrex power supplies are available.

A.9 Decay Length

The decay length will be adjustable by moving the beam absorber. This provides an important check of the oscillation signal, which is expected to vary significantly differently with decay length than the primary intrinsic ν_e background from muon decay (see Verification of Signal, below)

A.10 Systematic error from ν_e beam content

For the proposal, we will assume a 5% systematic error on the intrinsic ν_e beam content from muon decays. The observed ν_μ events place a strong constraint on intrinsic ν_e in the beam, allowing us to achieve this systematic error.

A.11 Verification of the signal with a one-detector setup

The adjustable decay pipe is most important if a signal is observed. The signal is expected to vary nearly linearly with fractional decay length while the background from muon decays will vary approximately quadratically. Other methods of verification include $\overline{\nu}$ running and varying the beam energy.

A.12 Expectations for Running Time

This proposal will present results for 2×10^7 s of running, which is obtainable in one calender year. Excluding scheduled shutdowns, the Booster downtime was 1.5% and the Linac downtime was 1.8%. The neutron therapy facility is presently requesting 14% of a calender year. Thus it is feasible to achieve

2×10^7 s (63%) running time in one calender year. We propose two runs for 1×10^7 s (or 2.5×10^{20} p.o.t.) with the beam absorber at 50 m and 25 m, respectively.

Appendix B

Beam Line Civil Design

In this appendix we present the civil design of the BooNE Beamline. These figures are from the Project Definition Cost Estimate for MiniBooNE, Nov. 1997, produced by FNAL Facilities Engineering Services Section. Cost estimates from this report were presented in Chapter 11. The Project Definition Cost Estimate Report is available upon request.

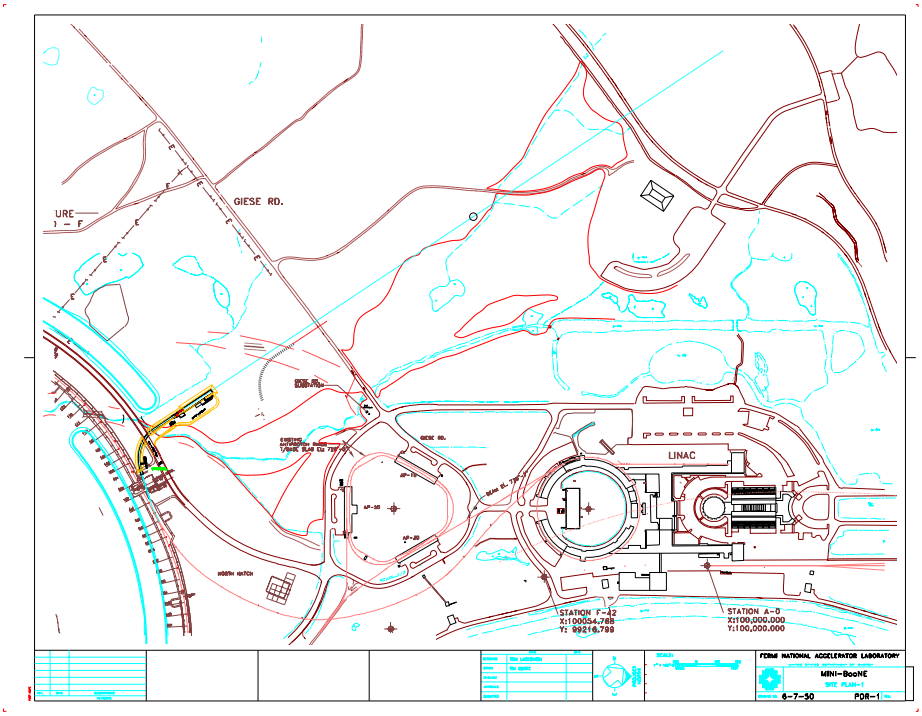

Figure B.1: Figure 1 of Project Design Report

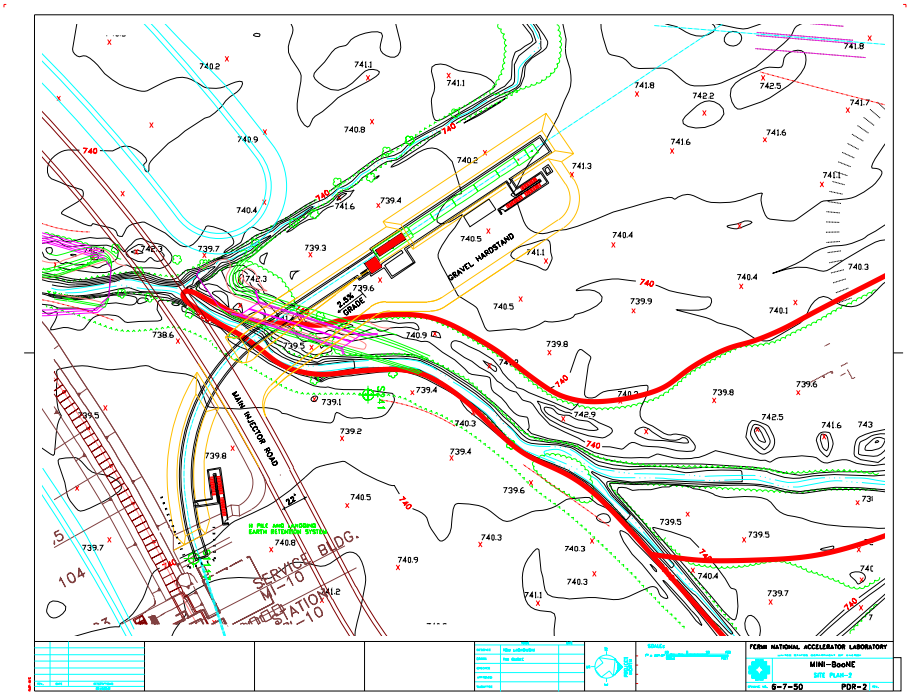

Figure B.2: Figure 2 of Project Design Report

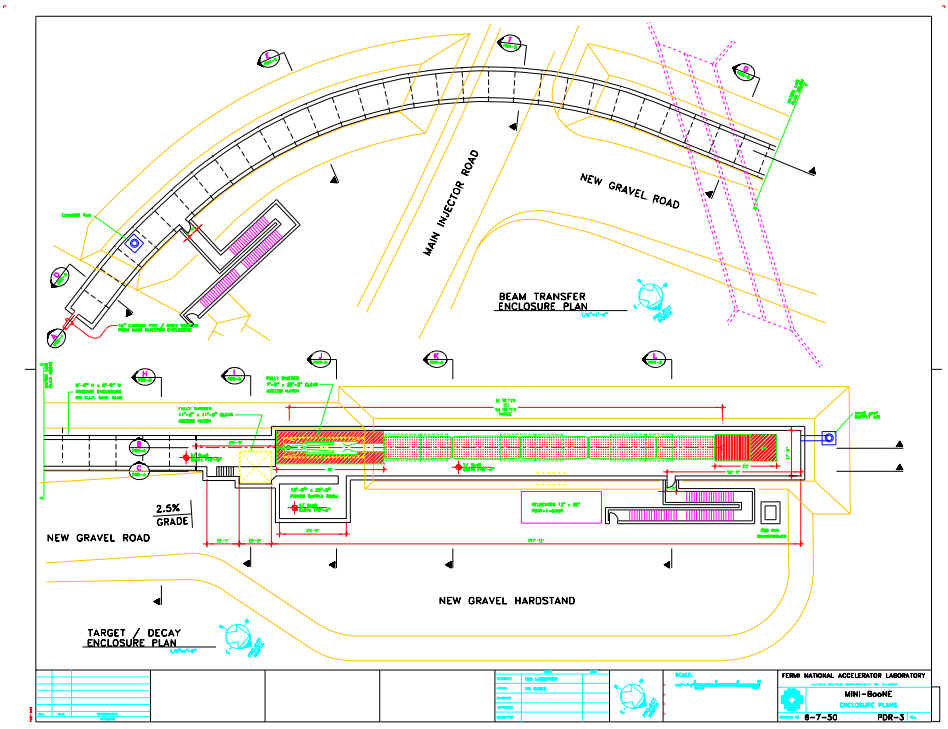

Figure B.3: Figure 3 of Project Design Report

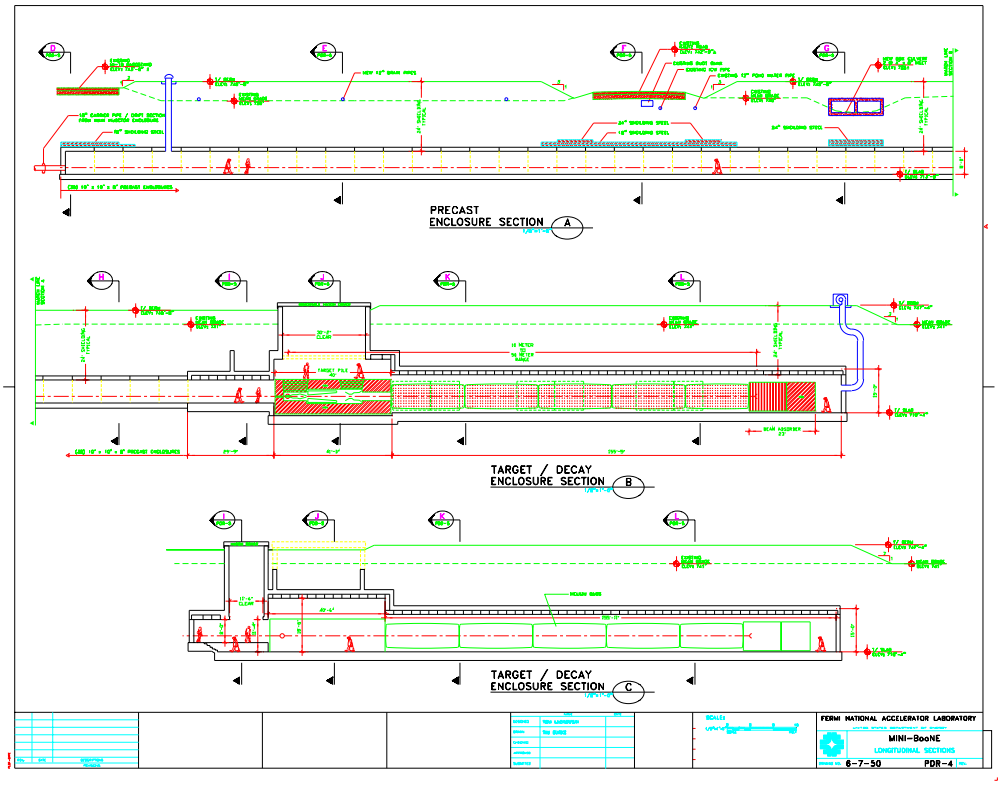

Figure B.4: Figure 4 of Project Design Report

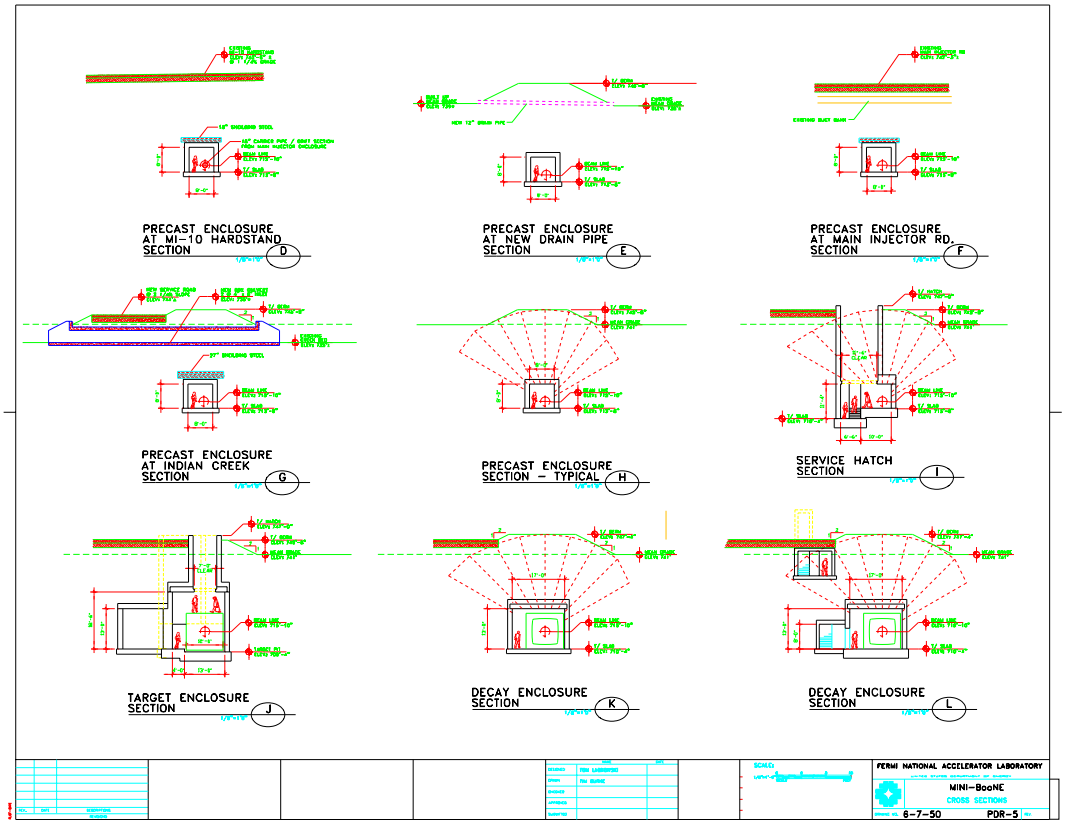

Figure B.5: Figure 5 of Project Design Report

Appendix C

The MiniBooNE Detector Work Breakdown Study: Costs and Schedule

In this appendix we present the Work Breakdown Study for the MiniBooNE Detector, including cost and schedule. The Work Breakdown study for the BooNE beamline is available as a separate document from this proposal, upon request.

Figure C.1: Page 1 of the detector WBS.

ID	Task Name	Duration	Start	Finish	Cost	Predecessors
34	1.5.2 Overburden	10d	Fri 4/3/98	Thu 4/16/98	$0.00	33
35	1.5.3 Caboose Location	10d	Fri 4/17/98	Thu 4/30/98	$0.00	34
36	1.5.4 Portakamp Location	10d	Fri 5/1/98	Thu 5/14/98	$0.00	35
37						
38	**1.6 Containment Specification**	**30d**	**Fri 5/15/98**	**Thu 6/25/98**	**$0.00**	**13,25**
39	1.6.1 Written Specification	30d	Fri 5/15/98	Thu 6/25/98	$0.00	
40						
41	**1.7 Containment Internal Structure**	**100d**	**Fri 6/26/98**	**Thu 11/12/98**	**$0.00**	**39**
42	1.7.1 Signal Cables	10d	Fri 6/26/98	Thu 7/9/98	$0.00	
43	1.7.2 Laser Bulbs	10d	Fri 7/10/98	Thu 7/23/98	$0.00	42
44	1.7.3 Imlay Bulbs	40d	Fri 7/24/98	Thu 9/17/98	$0.00	43
45	1.7.4 Attenuation Length Tester	10d	Fri 9/18/98	Thu 10/1/98	$0.00	44
46	1.7.5 Temperature Regulation	10d	Fri 10/2/98	Thu 10/15/98	$0.00	45
47	1.7.6 Oil Distribution	10d	Fri 10/16/98	Thu 10/29/98	$0.00	46
48	1.7.7 Nitrogen	10d	Fri 10/30/98	Thu 11/12/98	$0.00	47
49	1.7.8 Complete	0d	Thu 11/12/98	Thu 11/12/98	$0.00	48
50						
51	**2 Detector Detailed Design**	**160d**	**Fri 5/15/98**	**Thu 12/24/98**	**$0.00**	
52	**2.1 System Layout**	**150d**	**Fri 5/15/98**	**Thu 12/10/98**	**$0.00**	
53	2.1.1 Containment	20d	Fri 11/13/98	Thu 12/10/98	$0.00	41
54	2.1.2 Preamplifiers	20d	Fri 5/15/98	Thu 6/11/98	$0.00	32
55	2.1.3 Services, Oil etc	20d	Fri 5/15/98	Thu 6/11/98	$0.00	32
56	2.1.4 External Calibration System	20d	Fri 5/15/98	Thu 6/11/98	$0.00	32
57	2.1.5 Caboose	20d	Fri 5/15/98	Thu 6/11/98	$0.00	32
58	2.1.6 Complete	0d	Thu 6/11/98	Thu 6/11/98	$0.00	57
59						
60	**2.2 Containment**	**30d**	**Fri 11/13/98**	**Thu 12/24/98**	**$0.00**	**49**
61	2.2.1 Signal Cables	15d	Fri 11/13/98	Thu 12/3/98	$0.00	
62	2.2.2 Laser Bulbs	15d	Fri 11/13/98	Thu 12/3/98	$0.00	
63	2.2.3 Imlay Bulbs	30d	Fri 11/13/98	Thu 12/24/98	$0.00	
64	2.2.4 Attenuation Length Tester	15d	Fri 11/13/98	Thu 12/3/98	$0.00	
65	2.2.5 Temperature Regulation	15d	Fri 11/13/98	Thu 12/3/98	$0.00	
66	2.2.6 Oil Distribution	15d	Fri 11/13/98	Thu 12/3/98	$0.00	

Figure C.2: Page 2 of the detector WBS.

ID	Task Name	Duration	Start	Finish	Cost	Predecessors
67	2.2.7 Nitrogen	15d	Fri 11/13/98	Thu 12/3/98	$0.00	
68	2.2.8 Complete	0d	Fri 11/13/98	Fri 11/13/98	$0.00	
69						
70	**2.3 External Services**	**30d**	**Fri 5/15/98**	**Thu 6/25/98**	**$0.00**	**32**
71	2.3.1 Signal Cable Plant to Caboose	30d	Fri 5/15/98	Thu 6/25/98	$0.00	32
72	2.3.2 Preamplifier Setup	10d	Fri 5/15/98	Thu 5/28/98	$0.00	32
73	2.3.3 Laser and Drive Fiber System	20d	Fri 5/15/98	Thu 6/11/98	$0.00	32
74	2.3.4 Imlay Bulb Readout	20d	Fri 5/15/98	Thu 6/11/98	$0.00	32
75	2.3.5 Attenuation Length Readout	20d	Fri 5/15/98	Thu 6/11/98	$0.00	32
76	2.3.6 HV Supply System	20d	Fri 5/15/98	Thu 6/11/98	$0.00	32
77	2.3.7 Temperature Regulator and Plumi	20d	Fri 5/15/98	Thu 6/11/98	$0.00	32
78	2.3.8 Oil Handling System	20d	Fri 5/15/98	Thu 6/11/98	$0.00	32
79	2.3.9 Nitrogen Supply	20d	Fri 5/15/98	Thu 6/11/98	$0.00	32
80	2.3.10 Complete	0d	Fri 5/15/98	Fri 5/15/98	$0.00	32
81						
82	3 Construction Start	0d	Thu 1/7/99	Thu 1/7/99	$0.00	60FS+10d,80
83						

Figure C.3: Page 3 of the detector WBS.

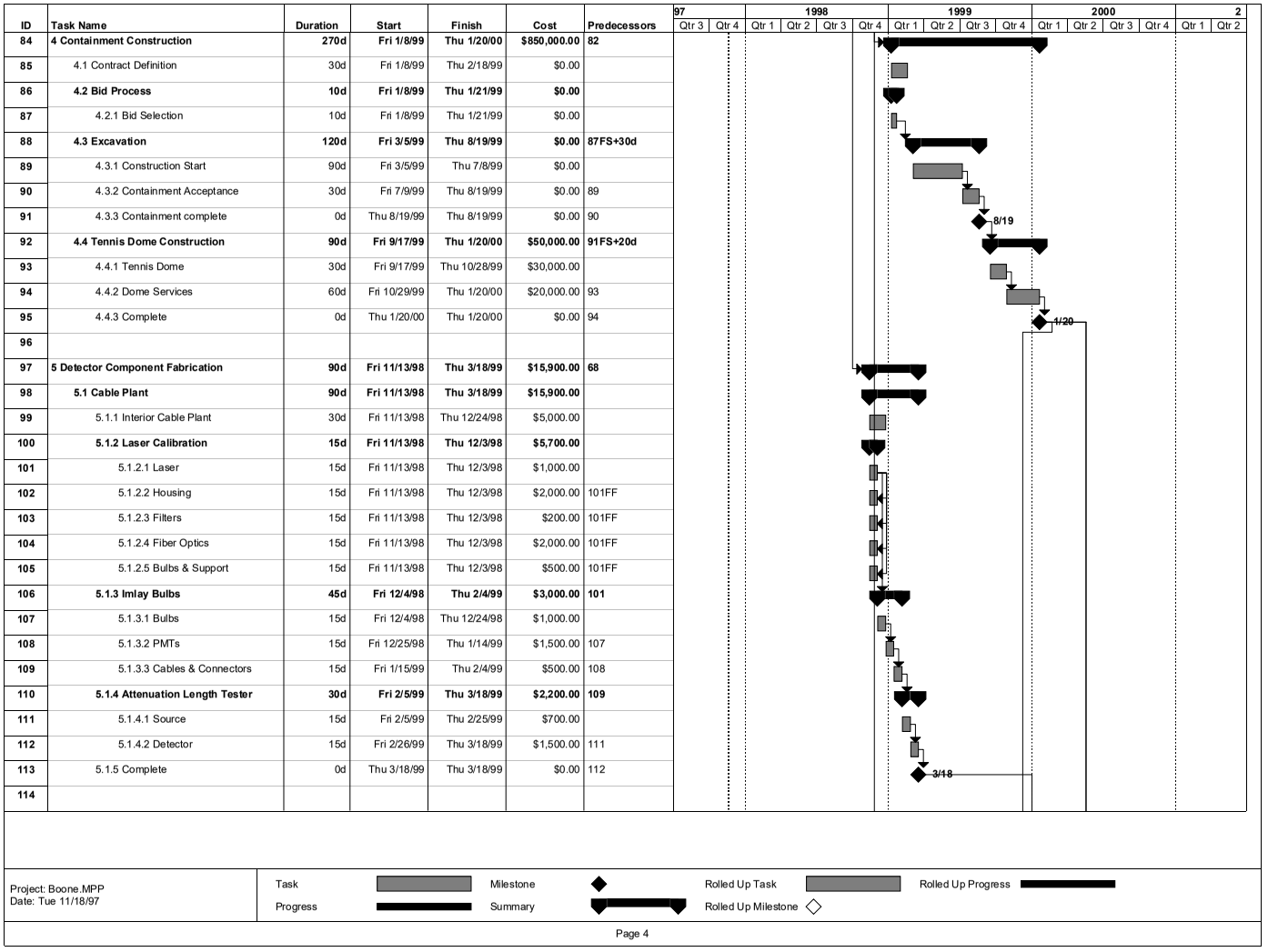

ID	Task Name	Duration	Start	Finish	Cost	Predecessors
84	**4 Containment Construction**	**270d**	**Fri 1/8/99**	**Thu 1/20/00**	**$850,000.00**	**82**
85	4.1 Contract Definition	30d	Fri 1/8/99	Thu 2/18/99	$0.00	
86	**4.2 Bid Process**	**10d**	**Fri 1/8/99**	**Thu 1/21/99**	**$0.00**	
87	4.2.1 Bid Selection	10d	Fri 1/8/99	Thu 1/21/99	$0.00	
88	**4.3 Excavation**	**120d**	**Fri 3/5/99**	**Thu 8/19/99**	**$0.00**	**87FS+30d**
89	4.3.1 Construction Start	90d	Fri 3/5/99	Thu 7/8/99	$0.00	
90	4.3.2 Containment Acceptance	30d	Fri 7/9/99	Thu 8/19/99	$0.00	89
91	4.3.3 Containment complete	0d	Thu 8/19/99	Thu 8/19/99	$0.00	90
92	**4.4 Tennis Dome Construction**	**90d**	**Fri 9/17/99**	**Thu 1/20/00**	**$50,000.00**	**91FS+20d**
93	4.4.1 Tennis Dome	30d	Fri 9/17/99	Thu 10/28/99	$30,000.00	
94	4.4.2 Dome Services	60d	Fri 10/29/99	Thu 1/20/00	$20,000.00	93
95	4.4.3 Complete	0d	Thu 1/20/00	Thu 1/20/00	$0.00	94
96						
97	**5 Detector Component Fabrication**	**90d**	**Fri 11/13/98**	**Thu 3/18/99**	**$15,900.00**	**68**
98	**5.1 Cable Plant**	**90d**	**Fri 11/13/98**	**Thu 3/18/99**	**$15,900.00**	
99	5.1.1 Interior Cable Plant	30d	Fri 11/13/98	Thu 12/24/98	$5,000.00	
100	**5.1.2 Laser Calibration**	**15d**	**Fri 11/13/98**	**Thu 12/3/98**	**$5,700.00**	
101	5.1.2.1 Laser	15d	Fri 11/13/98	Thu 12/3/98	$1,000.00	
102	5.1.2.2 Housing	15d	Fri 11/13/98	Thu 12/3/98	$2,000.00	101FF
103	5.1.2.3 Filters	15d	Fri 11/13/98	Thu 12/3/98	$200.00	101FF
104	5.1.2.4 Fiber Optics	15d	Fri 11/13/98	Thu 12/3/98	$2,000.00	101FF
105	5.1.2.5 Bulbs & Support	15d	Fri 11/13/98	Thu 12/3/98	$500.00	101FF
106	**5.1.3 Imlay Bulbs**	**45d**	**Fri 12/4/98**	**Thu 2/4/99**	**$3,000.00**	**101**
107	5.1.3.1 Bulbs	15d	Fri 12/4/98	Thu 12/24/98	$1,000.00	
108	5.1.3.2 PMTs	15d	Fri 12/25/98	Thu 1/14/99	$1,500.00	107
109	5.1.3.3 Cables & Connectors	15d	Fri 1/15/99	Thu 2/4/99	$500.00	108
110	**5.1.4 Attenuation Length Tester**	**30d**	**Fri 2/5/99**	**Thu 3/18/99**	**$2,200.00**	**109**
111	5.1.4.1 Source	15d	Fri 2/5/99	Thu 2/25/99	$700.00	
112	5.1.4.2 Detector	15d	Fri 2/26/99	Thu 3/18/99	$1,500.00	111
113	5.1.5 Complete	0d	Thu 3/18/99	Thu 3/18/99	$0.00	112
114						

Figure C.4: Page 4 of the detector WBS.

ID	Task Name	Duration	Start	Finish	Cost	Predecessors
115	**6 Detector Internal Installation**	**85d**	**Fri 1/21/00**	**Thu 5/18/00**	**$40,000.00**	**95,113**
116	6.1 Interior Cable Installation	30d	Fri 1/21/00	Thu 3/2/00	$0.00	
117	6.2 PMT Supports	30d	Fri 3/3/00	Thu 4/13/00	$15,000.00	116
118	6.3 Veto Separator	25d	Fri 4/14/00	Thu 5/18/00	$25,000.00	117
119	6.4 PMT Installation Start	0d	Thu 5/18/00	Thu 5/18/00	$0.00	118
120						
121	**7 PMTs**	**503d**	**Tue 12/1/98**	**Thu 11/2/00**	**$18,000.00**	
122	7.1 Decommission LSND	0d	Tue 12/1/98	Tue 12/1/98	$0.00	
123	**7.2 LANL Detector**	**433d**	**Tue 1/26/99**	**Thu 9/21/00**	**$12,000.00**	
124	7.2.1 Remove from Detector	60d	Tue 1/26/99	Mon 4/19/99	$0.00	131
125	7.2.2 Clean & Retest	30d	Tue 4/20/99	Mon 5/31/99	$1,000.00	124
126	7.2.3 Repackage	20d	Tue 3/23/99	Tue 4/20/99	$10,000.00	125SF
127	7.2.4 Transport	10d	Tue 4/20/99	Mon 5/3/99	$1,000.00	126
128	7.2.5 Installation @ Fermilab	90d	Fri 5/19/00	Thu 9/21/00	$0.00	127,95,115
129	**7.3 LANL Veto**	**473d**	**Tue 12/1/98**	**Thu 9/21/00**	**$6,000.00**	**122**
130	7.3.1 Remove from Detector	20d	Tue 12/1/98	Mon 12/28/98	$0.00	
131	7.3.2 Clean & Retest	20d	Tue 12/29/98	Mon 1/25/99	$1,000.00	130
132	7.3.3 Repackage	20d	Tue 1/26/99	Mon 2/22/99	$4,000.00	131
133	7.3.4 Transport	10d	Tue 4/20/99	Mon 5/3/99	$1,000.00	127SS
134	7.3.5 Installation @ Fermilab	90d	Fri 5/19/00	Thu 9/21/00	$0.00	133,95,115
135	7.4 Dismantle Tennis & Backfill	30d	Fri 9/22/00	Thu 11/2/00	$0.00	128,134
136						

Figure C.5: Page 5 of the detector WBS.

ID	Task Name	Duration	Start	Finish	Cost	Predecessors
137	**8 Caboose**	**280d**	**Tue 12/1/98**	**Mon 12/27/99**	**$192,000.00**	**122**
138	**8.1 Layout**	**280d**	**Tue 12/1/98**	**Mon 12/27/99**	**$192,000.00**	
139	**8.1.1 Preamps**	**60d**	**Tue 12/1/98**	**Mon 2/22/99**	**$2,000.00**	
140	8.1.1.1 System Refurbish	60d	Tue 12/1/98	Mon 2/22/99	$2,000.00	
141	**8.1.2 Trigger System**	**241d**	**Tue 12/1/98**	**Tue 11/2/99**	**$70,000.00**	
142	**8.1.2.1 Local Tzero Generation**	**1d**	**Tue 12/1/98**	**Tue 12/1/98**	**$5,000.00**	
143	8.1.2.1.1 Trigger Broadcast	1d	Tue 12/1/98	Tue 12/1/98	$0.00	
144	8.1.2.2 Crate Receiver Cards	90d	Wed 12/2/98	Tue 4/6/99	$5,000.00	143
145	8.1.2.3 Monoboard Spares	60d	Wed 4/7/99	Tue 6/29/99	$5,000.00	144
146	8.1.2.4 Event Assembly	90d	Wed 6/30/99	Tue 11/2/99	$5,000.00	145
147	**8.1.3 Primary Channels (QT)**	**90d**	**Tue 2/23/99**	**Mon 6/28/99**	**$5,000.00**	**140**
148	8.1.3.1 LANL Card Refurbish	90d	Tue 2/23/99	Mon 6/28/99	$5,000.00	
149	**8.1.4 Crate structure**	**220d**	**Tue 2/23/99**	**Mon 12/27/99**	**$85,000.00**	**140**
150	8.1.4.1 Backplanes	90d	Tue 2/23/99	Mon 6/28/99	$10,000.00	
151	8.1.4.2 Local Processing Spares	60d	Tue 6/29/99	Mon 9/20/99	$20,000.00	150
152	8.1.4.3 GPS & Clock Generation	30d	Tue 9/21/99	Mon 11/1/99	$5,000.00	151
153	8.1.4.4 Diagnostics	40d	Tue 11/2/99	Mon 12/27/99	$10,000.00	152
154	8.1.4.5 Low Voltage Replacement	1d	Tue 2/23/99	Tue 2/23/99	$15,000.00	
155	8.1.4.6 High Voltage Replacement	1d	Tue 2/23/99	Tue 2/23/99	$25,000.00	
156	**8.1.5 System Monitoring**	**90d**	**Tue 2/23/99**	**Mon 6/28/99**	**$30,000.00**	**140**
157	**8.1.5.1 Local System**	**90d**	**Tue 2/23/99**	**Mon 6/28/99**	**$20,000.00**	
158	8.1.5.1.1 Oil Level	30d	Tue 2/23/99	Mon 4/5/99	$0.00	
159	8.1.5.1.2 Temperature	30d	Tue 4/6/99	Mon 5/17/99	$0.00	158
160	8.1.5.1.3 Laser	30d	Tue 5/18/99	Mon 6/28/99	$0.00	159
161						
162	**9 Local DAQ**	**40d**	**Tue 12/28/99**	**Mon 2/21/00**	**$115,000.00**	**137**
163	**9.1 Site Data Handling**	**40d**	**Tue 12/28/99**	**Mon 2/21/00**	**$105,000.00**	
164	9.1.1 Acquisition computers	40d	Tue 12/28/99	Mon 2/21/00	$90,000.00	
165	9.1.2 Taper	35d	Tue 12/28/99	Mon 2/14/00	$15,000.00	
166	9.2 Transmission to Lab E	20d	Tue 12/28/99	Mon 1/24/00	$10,000.00	
167						

Project: Boone.MPP
Date: Tue 11/18/97

Task
Progress
Milestone
Summary
Rolled Up Task
Rolled Up Milestone
Rolled Up Progress

Page 6

Figure C.6: Page 6 of the detector WBS.

ID	Task Name	Duration	Start	Finish	Cost	Predecessors
168	**10 Lab E**	**60d**	**Tue 1/25/00**	**Mon 4/17/00**	**$2,500.00**	**166**
169	10.1 Reception at Lab E	20d	Tue 1/25/00	Mon 2/21/00	$2,500.00	
170	10.2 Data Handling at Lab E	40d	Tue 1/25/00	Mon 3/20/00	$0.00	169FF
171	10.3 Remote Process	60d	Tue 1/25/00	Mon 4/17/00	$0.00	169FF
172	10.4 Monitoring & Analysis	40d	Tue 1/25/00	Mon 3/20/00	$0.00	169FF
173						
174	**11 Oil**	**85d**	**Fri 1/8/99**	**Thu 5/6/99**	**$550,000.00**	**82**
175	11.1 Procurement	40d	Fri 1/8/99	Thu 3/4/99	$0.00	
176	11.2 Production	5d	Fri 3/5/99	Thu 3/11/99	$0.00	175
177	11.3 Delivery	10d	Fri 3/12/99	Thu 3/25/99	$0.00	176
178	11.4 Testing & Installation	30d	Fri 3/26/99	Thu 5/6/99	$0.00	177
179	11.5 Completion	0d	Thu 5/6/99	Thu 5/6/99	$0.00	178
180						
181	**12 Assembly & Commissioning**	**80d**	**Fri 11/3/00**	**Thu 2/22/01**	**$0.00**	**135,172**
182	**12.1 Pre Fill Operation**	**80d**	**Fri 11/3/00**	**Thu 2/22/01**	**$0.00**	
183	12.1.1 Tube Preoperation	20d	Fri 11/3/00	Thu 11/30/00	$0.00	
184	12.1.2 Dummy Calibration	20d	Fri 12/1/00	Thu 12/28/00	$0.00	183
185	**12.1.3 Oil Filling**	**35d**	**Fri 12/29/00**	**Thu 2/15/01**	**$0.00**	**179,184**
186	12.1.3.1 Oil Fill	30d	Fri 12/29/00	Thu 2/8/01	$0.00	
187	12.1.3.2 Level Regulation Test	5d	Fri 2/9/01	Thu 2/15/01	$0.00	186
188	12.1.4 Temperature Regulation	5d	Fri 2/16/01	Thu 2/22/01	$0.00	187
189	12.1.5 Detector Operational	0d	Thu 2/22/01	Thu 2/22/01	$0.00	188

Figure C.7: Page 7 of the detector WBS.

Appendix D

Support from Divisions of the Laboratory

The purpose of this appendix is to describe the scope of our requests to the lab. Equipment requested from the laboratory are listed below. The MiniBooNE experiment will also request tasks of the laboratory. The following is an attempt to begin to enumerate these tasks. Further requests beyond those listed here are possible.

D.1 Beams Division

Alignment The Survey and Alignment group will need to assist in construction control, installation of the magnet alignment network (including transfer of the network from the MI enclosure into the MiniBooNE pretarget enclosure), marking of device locations, and final magnet alignment.

Magnets The Technical Division will need to refurbish the EPB dipoles, electromagnet quadrupoles, trim dipoles, and any additional magnets required for the beam line. The Technical Division will also need to design and fabricate the permanent magnet quadrupoles for the beam line; the design is expected to draw heavily upon the Recycler production.

Vacuum The Beams Division will need to design, procure and coordinate the installation of the vacuum system components, including ion pumps and their power supplies, gauges and valves. Following the actual installation (Davis-Bacon), leak-checking will need to be performed.

Power Supplies The Beams Division will need to locate existing power supplies, arrange for their installation, along with electrical connections and controls. Installation of cables to the magnets will need to be specified and coordinated (Davis-Bacon). In particular, the design of the switching device which deflects the beam for MiniBooNE into the beam line channel will need considerable attention, and, if necessary, the switching magnet will need to be fabricated either by Beams Division or Technical Division personnel.

Instrumentation Beamline instrumentation will need to be specified, procured and installed by the Beams Division.

Safety System The Beams Division will need to design and install the electrical and radiation safety system interlocks.

Controls The Beams Division will need to provide the necessary power supply controls and read-backs, instrumentation (beam position monitor, beam loss monitor and beam profile) controls and read backs, associated with operation of the beam line. Timing information will need to be provided to the experiment.

Utilities The Beams Division will need to provide cooling water for the magnets and power supplies. This includes design of the connections into the existing LCW system, piping in the MI and pretarget enclosure, and connections to the magnets.

Installation The Beams Division will need to design and procure magnet stands for all magnets in the beam line, and coordinate the installation of magnet stands and magnets (Davis-Bacon).

Civil Construction FESS will need to design, or to interact with an outside A&E firm, as appropriate, the beam line and target station enclosure, the connection with the MI enclosure, the target station building,the experimental facility, and the necessary infrastructure (electrical power, lighting, roads, feeders, power lines, sumps, cable trays, etc.) They will have to provide construction supervision and coordination during construction, and shielding-assessment drawings upon completion.

D.2 Particle Physics Division

The Particle Physics Division will be asked to support the detector construction and installation. This will involve work with LANL to support development

of the specifications for the detector tank. This work has already begun and involves the Mechanical Support Group. As plans and schedules for the detector evolve, the PPD Mechanical Support Department will be asked to help to assure that the collaboration meets Fermilab standards and policies.

Civil construction will also be required for the detector tank. This work will be coordinated with the help of PPD and the Facility Engineering Services Section. We will ask the PPD Mechanical Support Department to coordinate and develop the specifications for civil construction with FESS. The issues involved include road access to the construction site, location of the Caboose and small reservoir tank, and supply of utilities to the detector area.

The design of the focusing horns will involve computer modeling to map out the mechanical stresses in the inner conductor. The modeling is also needed to determine the thickness of the conductor, which affects beam interactions in the horn, and horn cooling requirements. We will call upon the PPD Engineering Analysis Group to help with this work.

The entire project, including the Target Hall and beamline enclosures, will require an environmental evaluation. This work will be carried out with close cooperation of the ES&H Section. The PPD will be involved in that portion of the EA that includes the detector area.

The installation and operation of the detector will require technical support from the PPD. We will be asking the PPD to support the experiment with two technicians that will help to supervise the installation effort. Temporary technicians will be needed during the construction phase of the detector for preparing and installing phototubes, running cables, and hooking up electronics.

D.3 Computing Division

MiniBooNE requests the computing division to provide equipment support for setting up and running the experiment as well as computational resources for analysis and simulations.

Equipment estimates appear in table D.3. Although there is $174K worth of equipment listed, all but $79K is equipment already in the ELS pool.

We will be bringing the VME crates, phototube power supplies and VME electronics from the LSND experiment, so these items are not part of our request.

The first three items are for computer equipment to be used for data acquisition. Data will be acquired from the experiment VME crates over 100 Mbit/s ethernet into the four CPU processor. LSND used a Silicon Graphics system with eight R4400 CPUs for this purpose. By the time MiniBooNE runs,

Table D.1: Equipment for MiniBooNE

Quantity	Item	Cost	New
1	Four CPU system for data acquisition	50K	•
1	five cartridge DLT tape stacker	20K	•
1	DLT tape drive	5K	•
4	9 Gb disk drives	4K	•
5	X terminals (color and mono)	10K	
10	NIM Crates and Power supplies	10K	
60	NIM modules	6K	
4	CAMAC crates and Power supplies	10K	
20	CAMAC modules	24K	
2	Lecroy digital oscilloscopes	20K	
3	Tektronics analog oscilloscopes	15K	

this system will be obsolete by several generations so a new system must be purchased. The system requested is a four processor Silicon Graphics Origin which is acceptable, but which will almost certainly be out of date by the time the experiment runs.

Analysis software will filter this data and write candidate events onto disk. A job will run periodically to transfer data from disk onto DLT tape. The use of the tape stacker will allow the experiment to run with minimal intervention for long periods of time as was the case for LSND.

The NIM and CAMAC electronics will be for miscellaneous interface functions. Oscilloscopes will be used during the commissioning of the experiment to check signals and noise levels.

We will need the computing division datacomm group to set up networking in the electronics hut. We envision one 100 Mb ethernet branch between the data acquisition computer and the VME crates containing the front end electronics. Separate from that would be another ethernet carried in one strand of the fiber optic cable which connects with the Target Hall and MI10. We would like this segment to then connect to the lab backbone and be isolated behind a router/gateway to minimize the impact of network traffic on both sides since we would also use this as a data path for our beam line information.

The computational resources for analysis will be small. The total data sample will be on the order of 500K events. Using the LSND experience of about a second/event for reconstruction, on a Silicon Graphics Origin CPU, this works out to be 140 hours of CPU time. The farms and batch system technology will have been upgraded many times by the time this becomes an issue. We do not expect MiniBooNE usage to be a large consumer of central

computing resources.

References

1. C. Athanassopoulos *et. al.* , Phys. Rev. Lett. **75**, 2650 (1995); C. Athanassopoulos *et. al.* , Phys. Rev. Lett. **77**, 3082 (1996); C. Athanassopoulos *et. al.* , Phys. Rev. C. **54**, 2685 (1996).
2. B. Bodmann *et. al.* , Phys. Lett. B **267**, 321 (1991); B. Bodmann *et. al.* , Phys. Lett. B **280**, 198 (1992); B. Zeitnitz *et. al.* , Prog. Part. Nucl. Phys., **32** 351 (1994).
3. W. C. Louis, representing LSND, to appear in the Proceedings of the Erice School on Nucl. Physics, 19th course, "Neutrinos in Astro, Particle and Nuclear Physics", 16-24 September 1997.
4. C. Athanassopoulos *et. al.* , LA-UR-97-1998, submitted to Phys. Rev. C.
5. K. Eitel, "Recent results and upgrade from KARMEN," Presented at Workshop on Fixed Target Physics at the Main Injector, May, 1997, and private communications.
6. K. Eitel, thesis, Universitat und Forschungszeutrum Karlsruhe (1995); Forschungszeutrum Karlsruhe report FZKA 5684 (1995).
7. D. Michael, MINOS Collaboration, private communication, July 31, 1997. For updates on the MINOS prospects, see: http://www.hep.anl.gov/NDK/Hypertext/numi_notes.html
8. MINOS Collaboration, P875, "A Long Baseline Neutrino Oscillation Experiment at Fermilab, February, 1995; Dave Ayres for the MINOS collaboration, "Summary of the MINOS proposal, A Long Baseline Neutrino Oscillation Experiment at Fermilab", March 1995; NuMI note: NuMI-L-71, see: http://www.hep.anl.gov/NDK/Hypertext/numi_notes.html
9. N. Armenise, *et. al.* , "Search For Muon Neutrino $\rightarrow$ Electron Neutrino Oscillation at the CERN-PS", CERN-SPSC-97-21, Oct 1997.
10. D. Autiero, *et. al.* , "A Medium Baseline Facility for ν_μ Oscillations", CERN-SPSC-97-23, Oct 1997.
11. K. S. Hirata *et. al.* , Phys. Lett. B**280**, 146 (1992).
12. R. Becker-Szendy *et. al.* , Phys. Rev. D**46**, 3720 (1992).
13. R. Clark *et. al.* , Phys. Rev. Lett. **79**, 345 (1997).
14. Y. Hirata *et. al.* , Phys. Lett. B**335**, 237 (1994).
15. Y.Totsuka, "Neutrino Physics (Nonaccelerator)," presented at the Lepton Photon Symposium 1997, Hamburg, July, 1997, see: http://www-sk.icrr.u-tokyo.ac.jp/doc/sk/pub/pub_sk.html
16. B. Achkar *et. al.* , Nucl. Phys. **B434**, 503 (1995).

17. M. Apollonio *et. al.* , hep-ex/9711002, submitted to Phys. Lett. B.
18. F. Dydak *et. al.* , Phys. Lett. B **134**, 281 (1984).
19. C. Cardall and G. M. Fuller, Phys. Rev. D **53**, 3532(1996); G. L. Fogli, E. Lisi, and G. Scioscia, hep-ph/9702298.
20. C. Cardall and G. Fuller,Nucl. Phys. Proc. Suppl. **51B** (1996)
21. C. Cardall and G. Fuller, *18th Texas Symposium of Relativistic Astrophysics* (1996).
22. Y. Qian and G. Fuller , Phys. Rev. Lett.**71 1965-1968**,(1993)
23. P. Spentzouris, "Summary of Working Group on Non-oscillation Physics at the Main Injector," Workshop on Fixed Target Physics at the Main Injector, May 1-4, 1997;
http://www.fnal.gov/projects/numi/workshop/summaries/summaries.html
24. D. Christian, private communication, Oct 29, 1997.
25. W. Molzon for the MECO Collaboration, Communication to Fermi National Accelerator Laboratory, June 26, 1997.
26. R. Palmer, A. Tollestrup, A. Sessler, "Status Report of a High Luminosity Muon Collider and Future Research and Development Plans," available from:
http://www.fnal.gov/projects/muon_collider.
27. T. Diehl and W. Molson, Stopped Muon Physics Working Group; G. Gutierrez and L. Littenberg, Physics with Low Energy Hadrons Working Group; Workshop on Physics at the First Muon Collider and at the Front End of a Muon Collider, November 6 - 9, 1997.
http://fnphyx-www.fnal.gov/conferences/femcpw97/workshop.html
28. R. Davis, Prog. Part. Nucl. Phys. **32**, 13 (1994).
29. J. N. Abdurashitov *et. al.* , Phys. Lett. B **328**, 234 (1994); P. Anselmanni *et. al.* , Phys. Lett. B **328**, 377 (1994).
30. Y. Fukuda *et. al.* , Phys. Lett. B **335**, 237 (1994).
31. N. Hata and P. Langacker, Phys. Rev. D **50**, 632(1994); N. Hata and P. Langacker, IASSNS-AST 97/29, UPR-751T (1997).
32. J. N. Bahcall and M. M. Pinsonneault, Rev. Mod. Phys. **64**, 885 (1992).
33. A. Cumming and W. C. Haxton, Phys. Rev. Letter **77**, 4286 (1996).
34. T. Gaisser and M. Goodman, Proceedings of the 1994 Snowmass Summer Study, Particle and Nuclear Astrophysics in the Next Millennium; E. W. Kolb R. D. Peccei eds, World Scientific 1994
35. T. K. Gaisser and J. S. O'Connell, Phys. Rev. D **34**, 822 (1986); W. M. McDonald, E. T. Dressler and J. S. O'Connell, Phys. Rev. C **19**, 455 (1979). The ^{12}C nucleus is modeled with binding energy 25 MeV, Fermi momentum 220 MeV/c, and six neutrons.
36. P.F. Harrison, D.H. Perkins, and W.G Scott, Phys. Lett. B349 (1995)

137; e-Print Archive: hep-ph/9702243, submitted to Phys. Lett. B.
37. See for example, D. Michael, "Summary of Neutrino Oscillation Experiments," talk presented at the Fermilab Users Meeting, 1997. Slides are available from the Fermilab User's Office upon request.
38. Presented at the October 17, 1997, PAC meeting by S. Wojcicki. Slides are available from the Fermilab Director's Office upon request.
39. CERN SPSC 81-20/P178, SPSC 82-20/P178.
40. CERN SPSC 97-21/1216.
41. L. A. Ahrens *et. al.* , Phys. Rev. D **34**, 75 (1986).
42. See TM-632
43. Reference supporting use of EPB for pulsed application. To be supplied. George Krafczyk, private communication.
44. R. Drucker, R. Ford, G. Tassotto; Secondary Emission Detectors for Fixed Target Experiments at Fermilab, Paper presented at the Third European Workshop on Beam Diagnostics and Instrumentation for Particle Accelerators (DIPAC 97), Frascati, Italy,1997.
45. Ferioli, Jung; Evolution of the Secondary Emission Efficiencies of Various Materials Measured in the CERN SPS Secondary Beam Lines, Paper presented at DIPAC 97, Frascati, Italy, 1997.
46. Monte Carlo simulation developed by Robert B. Drucker, University of Oregon, The NuTeV Collaboration. Private communication.
47. N. Mokhov and S. Striganov, talks presented at the Sept. 18, 1997 BooNE meeting, slides are available.
48. M.F.Audus, *et. al.* , Il Nuovo Cimento XLVI A 3 p. 502 (1966).
49. J.D. Davies, *et. al.* , Il Nuovo Cimento LIV A 3 p. 608 (1968).
50. D. Berely, *et. al.* , IEEE Transactions on Nuclear Science NS-20 3, 997 (1973).
51. D. Berely, *et. al.* , IEEE Transactions on Nuclear Science NS-20 3, 997 (1973).
52. Abe, *et. al.* , Phys. ReV. D36, 1302.
53. H. Kirk, presentation at Snowmass96 Workshop; B. Cole, private communication;
http://www.nevis1.nevis.columbia.edu/heavyion/e910.
54. CERN Program Library, GEANT V3.21.
55. L.A. Ahrens *et. al.* Physical Review **D34** 75 (1986).
56. B. King, thesis, Columbia University, Nevis-283 (1994).
57. D. H. White, LSND TN-114 (1997).
58. C. H. Llewellyn Smith, Physics Reports **3**, 262 (1972); P. Vogel, Phys. Rev. D **29**, 1918 (1984); E. J. Beise and R. D. McKeown, Comm. Nucl. Part. Phys. **20**, 105 (1991).

59. R. Becker-Szendy *et. al.* , Phys. Rev. D**46**, 3720 (1992).
60. M. C. Goodman, Nucl. Phys. B (Proc. Suppl.) **38**, 337 (1995).
61. N. Bacon, Business Development Manager, Chicago Bridge and Iron Company.
62. Jean George and Byron Dieterle, The CHOOZ Collaboration, Private Communications, August, 1997.
63. E. Kolbe, K. Langanke, and S. Krewald, Phys. Rev. C **49**, 1122 (1994); (K. Langanke, private communication).
64. D. Rein and L. M. Sehgal, Ann. of Phys. **133**, 79 (1981); D. Rein and L. M. Sehgal, Nucl. Phys. **B223**, 29 (1983).
65. G. Garvey, E. Kolbe, K. Langanke, and S. Krewald, Phys. Lett. B **289**, 249 (1992).
66. G. Garvey, E. Kolbe, K. Langanke, and S. Krewald, Phys. Rev. C **48**, 1919 (1993).
67. W. M. Alberico et al., (hep-ph/@xxx.lanl.gov, March 1997).

898

April 15, 1998

Response to the FNAL PAC

The BooNE Collaboration

Thank you for your comments from the January PAC meeting regarding the BooNE proposal. In section 1, we provide a response to the one question posed by the PAC in January:

> "The Committee would also like to see further analysis work which fully exploits the shape of the energy distribution which would be measured by the experiments."

In section 2 of this response, we discuss new information which strengthens our case for approval, including new physics results from the LSND experiment.

We request Stage I approval in May:

- Because of the importance and timeliness of the physics goals.
- In order to move forward on funding issues. The BooNE collaboration has proceeded with efforts to arrange funding. We are involved in discussions with DOE/OHENP and with NSF. In the case of NSF, we have a number of proposals submitted which are being held pending approval. We are happy to answer questions concerning our arrangements at the closed session of the PAC meeting. At this point, we can go no further on seeking funding from either NSF or DOE until we have received Stage I approval.
- In order to maintain our strong collaboration with the momentum necessary to complete the first stage of the experiment in a timely manner. The university groups are now prepared to make strong contributions to BooNE, including the Booster studies, as soon as the experiment is approved. If the experiment is delayed, however, university resources will tend to be diverted to other projects, and several of the university groups, which will have their support reviewed this summer and fall, will find it difficult to remain committed to BooNE.
- In order to hire postdocs, engineers and technicians and start construction of the detector in FY1999. Without approval in May this will be difficult for our institutions.

1 Energy Dependent Oscillation Analyses

Question from January PAC Response :

> "The Committee would also like to see further analysis work which fully exploits the shape of the energy distribution which would be measured by the experiments."

1.1 Energy Dependent Fits Including Systematic Uncertainties

The MiniBooNE proposal submitted in Jan. 98 included estimates of sensitivity for the experiment based on using the total number of observed events over background. This method is a conservative estimate of the experiment's sensitive region since it does not depend on knowing the energy distributions of the various background sources. As pointed out by the Committee, this method does not take full advantage of all the information available in the data. In this section, we describe alternative estimates of the MiniBooNE sensitivity from an energy dependent analysis.

The energy dependent analysis uses a standard χ^2 method where systematic uncertainties in the backgrounds are included through additional fit parameters constrained by their assumed errors. With this technique, the bin-to-bin energy correlations for the systematic uncertainties in the backgrounds are automatically included. For this method, χ^2 is given by:

$$\chi^2 = \sum_{i=E \text{ bins}} \frac{\left(n^{obs}(E_i) - n_{osc}^{pred}\left(\Delta m^2, \sin^2 2\theta, E_i\right) - \sum_{j=bkgnd} (1-\delta_j)\, n_j^{bkgnd}(E_i) \right)^2}{\left(\sigma_i^{obs}\right)^2} + \sum_{j=bkgnd} \left(\frac{\delta_j}{\sigma_j^{syst}} \right)^2$$

where n^{obs} is the number of observed events, n_{osc}^{pred} is the number of predicted $\nu_\mu \rightarrow \nu_e$ oscillation events for the given $\Delta m^2, \sin^2 2\theta$ values, and n_j^{bkgnd} is the number of background events from source j . The five background sources considered, as described in the proposal, were ν_e from μ^+, K_L, and K^+ decay (with systematic errors, σ^{syst}, of 0.05, 0.1, and 0.1 respectively) and misidentification backgrounds from outgoing μ's or π^0's (with systematic errors

of 0.05). The δ_i parameters allow the background level to shift within the systematic uncertainties, σ_j^{syst}.

In addition, the procedure includes systematic uncertainties in the background shape. These energy dependent uncertainties in the background should be small since most of the backgrounds are determined directly from the data. For example, the mis-identification backgrounds are measured as a function of energy using the observed μ and π^0 events which are extended into the unobservable region. Also, the primary source of ν_e's from μ decay is determined with little systematic uncertainty from the observed ν_μ events as described in the proposal. Thus, only the small ν_e background from K decay is not tied directly to MiniBooNE data. We believe that this source also will have reduced energy dependent systematic uncertainties when the new K production data from Brookhaven are used as a constraint. As an estimate of these uncertainties, we have used an energy dependent weighting function given by $\left(1 + \left|1 - \frac{E_i}{E_0}\right| \delta_E^j\right)$ where δ_E^j is the systematic parameter with uncertainty σ_E, and E_0 is the mean energy for each of the five backgrounds. This function effectively changes the width of the distribution keeping the mean value relatively constant. The E_0 parameter for ν_e's from kaons and muon were 1.4 and 1.1 GeV respectively and for the μ and π^0 mis-identification events were 0.7 and 1.35 GeV respectively. The uncertainty, σ_E, was assumed to be 0.1 for all backgrounds thus changing the shape of the background by about 10% over the energy range spanned by each of the background distributions.

1.2 MiniBooNE Sensitivity with Energy Dependent Fits

The sensitivity of the experiment to oscillations can be found by forcing

$$n^{obs}(E_i) = \sum_{j=bkgnd} n_j^{bkgnd}(E_i)$$

$$\text{with } \left(\sigma_i^{obs}\right)^2 = n^{obs}(E_i).$$

Using the same event statistics and backgrounds as presented in the proposal for one year of running, 5×10^{20} protons on target, the energy dependent fit yields the 90% CL ($\chi^2 > 1.64$) region shown in Fig. 1 along with the previous proposal result labeled as "Total Events". As shown, the energy-dependent analysis is about a factor of two more restrictive at high Δm^2 and, for low Δm^2, is $\sqrt{2}$ better. Also shown in Fig. 1 is the region where MiniBooNE will see a 5σ or greater signal above background and make a conclusive measurement.

The ability of the MiniBooNE experiment to isolate a ν_e appearance oscillation signal and measure the parameters for the signal can be estimated from

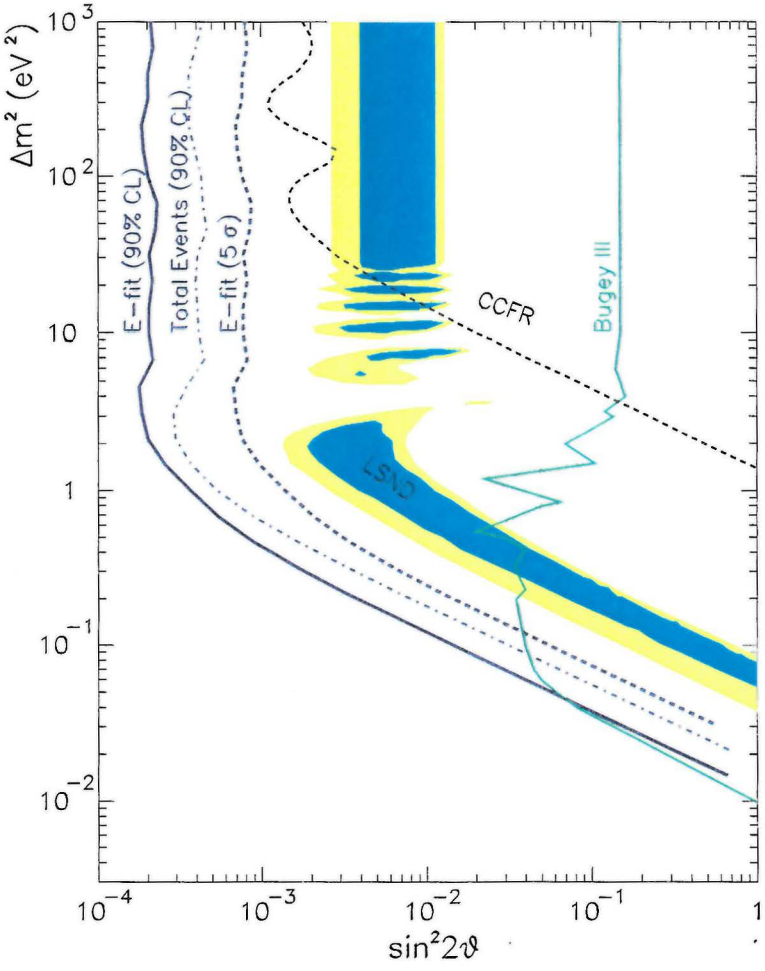

Figure 1: Sensitivity regions for the MiniBooNE experiment with 5×10^{20} protons on target. The solid (dashed) curve is the 90% CL (5σ) region using the energy fit method and the dashed-dot curve is the 90% CL region using the total event method from the proposal.

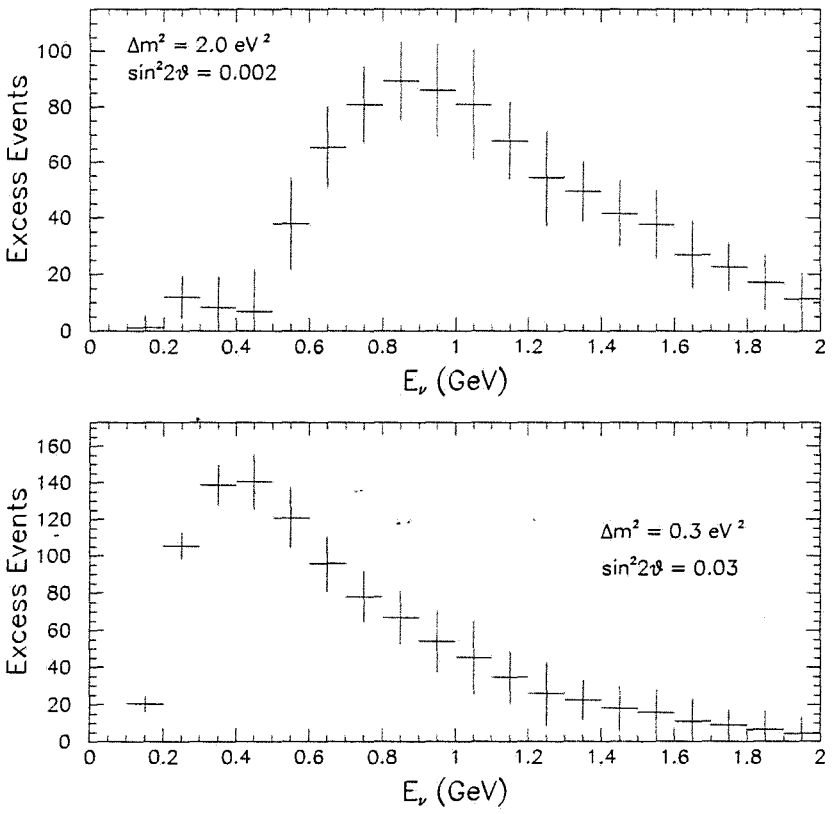

Figure 2: The energy distribution of excess events over background for two example oscillation signals. The error bars include the statistical and systematic uncertainties in the background. (Note the errors are correlated from bin to bin for the systematic uncertainties.) The statistical sample corresponds to one year of MiniBooNE running with 5×10^{20} protons on target.

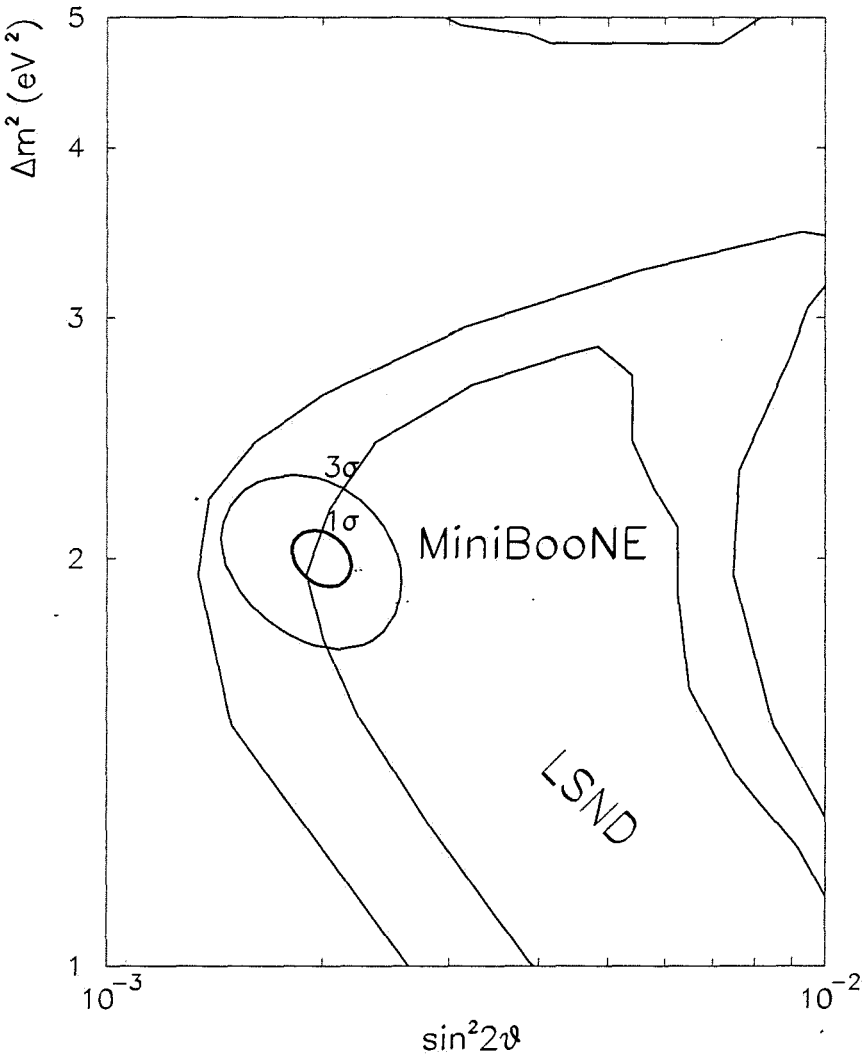

Figure 3: Results of the fit for the $\Delta m^2 = 2\ eV^2$ and $\sin^2 2\theta = 0.002$ data. The plot shows the 1 σ and 3 σ contours from the fit along with the LSND 90% and 99% regions.

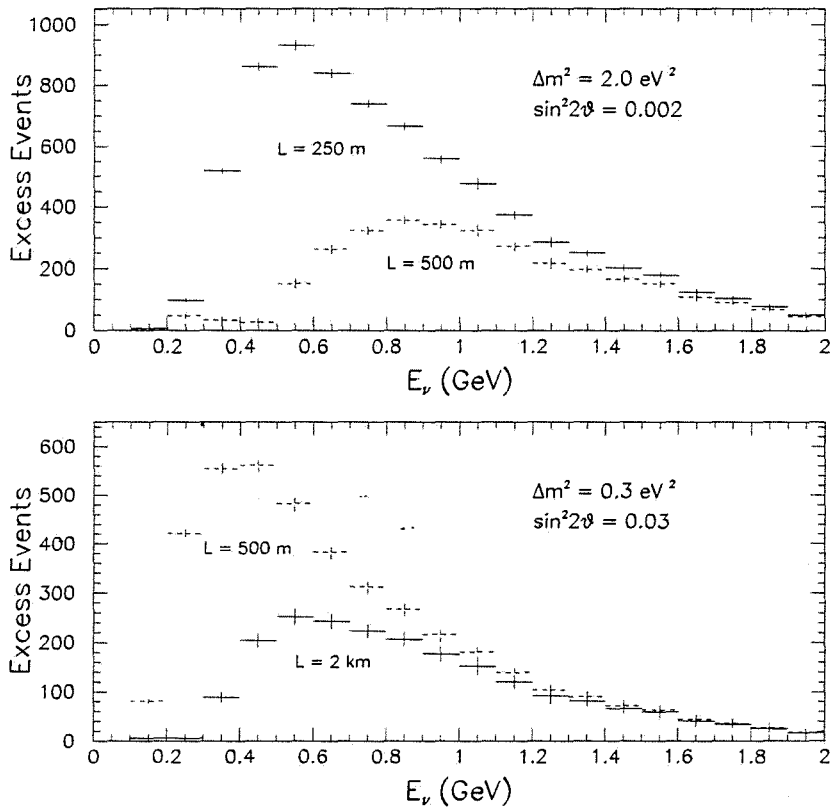

Figure 4: The energy distribution of excess events over background for two example oscillation signals and several distances for the detector. The solid (dashed) points in the top plot are for $\Delta m^2 = 2\ eV^2$, $\sin^2 2\theta = 0.002$ at a distance of 250 m (500 m). The solid (dashed) points in the bottom plot are for $\Delta m^2 = 0.3\ eV^2$, $\sin^2 2\theta = 0.03$ at a distance of 2 km (500 m). The statistical sample corresponds to an increased BooNE sample corresponding to 2×10^{21} protons on target.

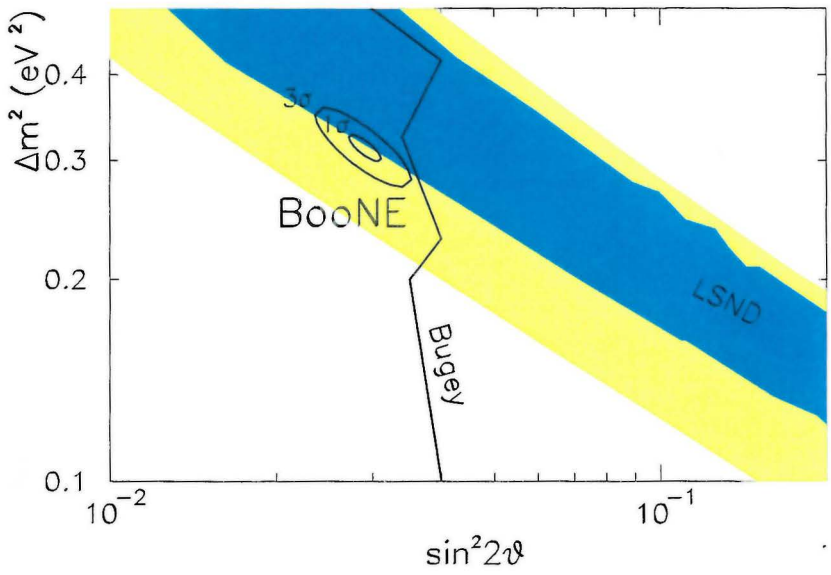

Figure 5: Allowed region for the full two detector experiment (BooNE) from fits to simulated data with $\Delta m^2 = 0.3$ eV^2 and $\sin^2 2\theta = 0.03$. The plot shows the 1σ and 3σ contours for a data sample corresponding to 5×10^{20} protons on target.

Table 1: Energy dependent fits for two example oscillation signals. The statistical sample corresponds to one year of MiniBooNE running with 5×10^{20} protons on target.

Δm_0^2	$\sin^2 2\theta_0$	$\delta(\Delta m^2)$	$\delta(\sin^2 2\theta)$	$\chi^2_{\text{No Osc}}/51\ df$	Signal Significance
0.3 (eV^2)	0.03	0.10 (eV^2)	0.02	441	44 σ
2.0 (eV^2)	0.002	0.10 (eV^2)	0.0002	152	15 σ

energy dependent fits to fake data generated with given input parameters. For these studies, the fake data is set by the equation,

$$n^{obs}(E_i) = n_{osc}(\Delta m_0^2, \sin^2 2\theta_0, E_i) + \sum_{j=bkgnd} n_j^{bkgnd}(E_i)$$

again with a statistical sample corresponding to one year of running with 5×10^{20} protons on target. Table 1 shows the fit results for two sets of parameters that span the allowed edge of the LSND 90% CL region. Plots of the number of excess events over background for these two cases are also shown in Fig. 2. In both cases, MiniBooNE will establish an oscillation signal at greater than 15 standard deviations.

The 2 eV^2 example is at the maximum sensitivity of the MiniBooNE experiment where the experiment can determine the oscillation parameters with greatest precision. Here, fits to the energy distributions of the excess events maps out a fairly restrictive region in the $\Delta m^2, \sin^2 2\theta$ plane as shown in Fig. 3. In the low Δm^2 region of the MiniBooNE sensitivity, as displayed in the 0.3 eV^2 example, the fit parameters Δm^2 and $\sin^2 2\theta$ are highly correlated. This is due to the fact that the oscillation probability is approximately proportional to $\sin^2 2\theta \cdot (\Delta m^2)^2$ and, therefore, the fit can only determine the combination of the two parameters. The fit can clearly establish an oscillation signal (at the 30 σ level) but only restricts Δm^2 to the 30 to 50 % level.

From the above analysis, it is clear that the MiniBooNE experiment can establish a signal in the LSND region. If a signal is observed, Δm^2 will be determined with sufficient accuracy $(\approx 0.1\ \text{eV}^2)$ to indicate where a second detector should be placed for the follow-up two detector BooNE experiment. For example, if $\Delta m^2 \approx 0.3\ \text{eV}^2$ (2.0 eV^2) then the second detector should be placed at 2 km (0.25 km) to best determine the oscillation parameters as indicated in Fig. 4.

As an example of the expectations for BooNE (the full 2 detector experiment), consider the case of low Δm^2 where the second detector is placed at

2 km. Fig. 5 shows the expected 1 σ and 3 σ contours. BooNE will measure Δm^2 to ± 0.014 eV^2 and $\sin^2 2\theta$ to ± 0.002 for 5×10^{20} protons on target.

2 Additional Information

Below we discuss recent developments that have occured since we submitted our detailed proposal in January.

2.1 New physics results affecting BooNE

The physics motivation for BooNE has been strengthened by new preliminary data from LSND which reinforces the evidence for neutrino oscillations. Fig. 6 shows the energy distribution for electron events with a correlated photon ($R > 30$) from the full 1993-1997 data sample. The points with errors are the data after a beam on-off subtraction has been performed. The data are clearly in excess of the background expected from normal neutrino interactions and in agreement with the signal expected from background plus neutrino oscillations at low values of Δm^2. The $\cos\theta$ distribution for events with $R > 30$ and $36 < E < 60$ MeV is shown in Fig. 7, where θ is the angle between the incident neutrino direction and the outgoing electron. The data are consistent with the slightly forward-peaked distribution expected from $\bar{\nu}_e p \rightarrow e^+ n$ interactions. We observe an average $\cos\theta = 0.24 \pm 0.12$, which is in agreement with the value of 0.16 expected from neutrino oscillations. Finally, Fig. 8 shows the LSND Δm^2 versus $\sin^2 2\theta$ favored regions from the $\bar{\nu}_\mu \rightarrow \bar{\nu}_e$ oscillation analysis, together with limits from other experiments. The light and dark shaded regions correspond to 90% and 99% likelihood regions from a likelihood fit of all of the data that makes use of the electron energy, angle, and distance distributions and the photon multiplicity, distance, and time distributions. The likelihood regions include a $\pm 12\%$ systematic uncertainty. The most favored region is a band that stretches from $\Delta m^2 = 2$ eV^2 down to $\Delta m^2 = 0.2$ eV^2.

Of the hints for neutrino oscillations, the LSND signal is the most amenable to systematic study at accelerators due to the larger Δm^2 values involved: > 0.1 eV^2 compared to $10^{-2} - 10^{-3}$ eV^2 for the atmospheric neutrino problem and $10^{-4} - 10^{-5}$ eV^2 for the solar neutrino problem. Thus, in studying the LSND signal, detectors can be placed much closer to the neutrino source, so that it is much easier to observe a clear sinusoidal variation as a function of ℓ/E and prove that neutrino oscillations occur.

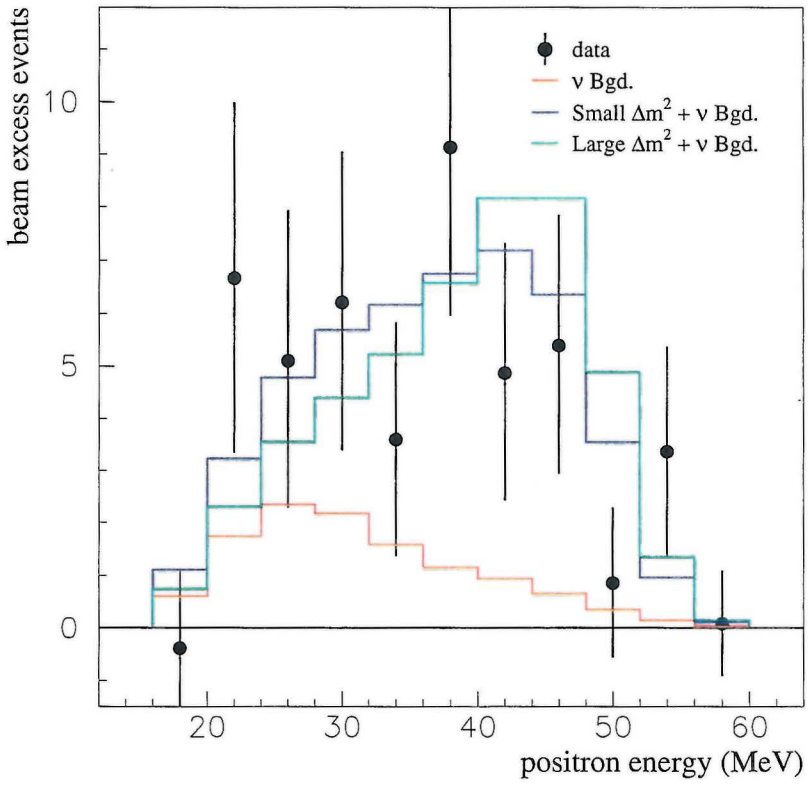

Figure 6: The preliminary LSND energy distribution for electron events with a correlated photon ($R > 30$) from the full 1993-1997 data sample.

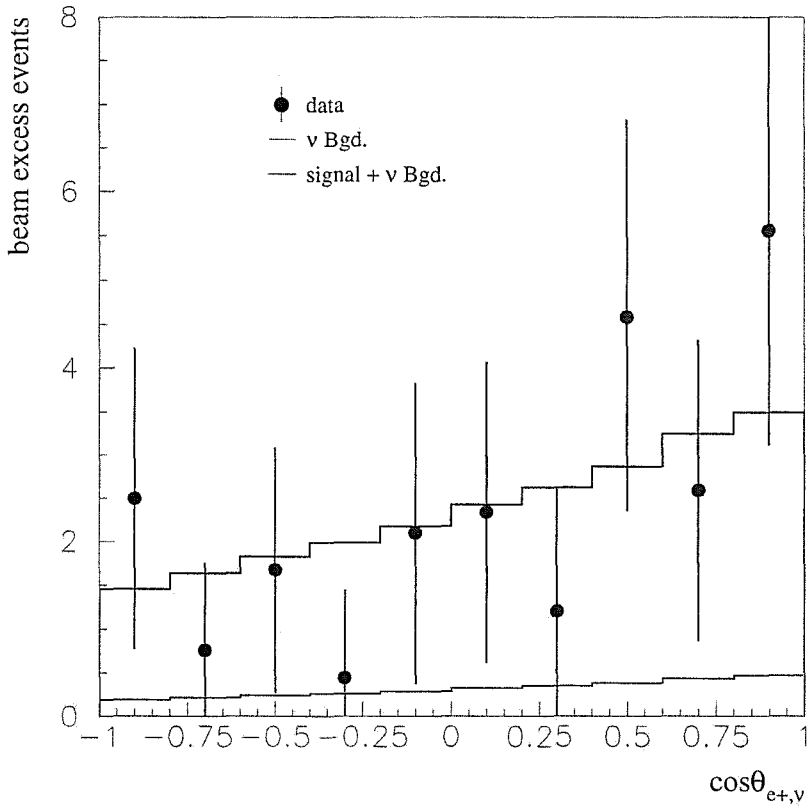

Figure 7: The preliminary LSND $\cos\theta$ distribution from the full 1993-1997 data sample for events with $R > 30$ and $36 < E < 60$ MeV, where θ is the angle between the incident neutrino direction and the outgoing electron.

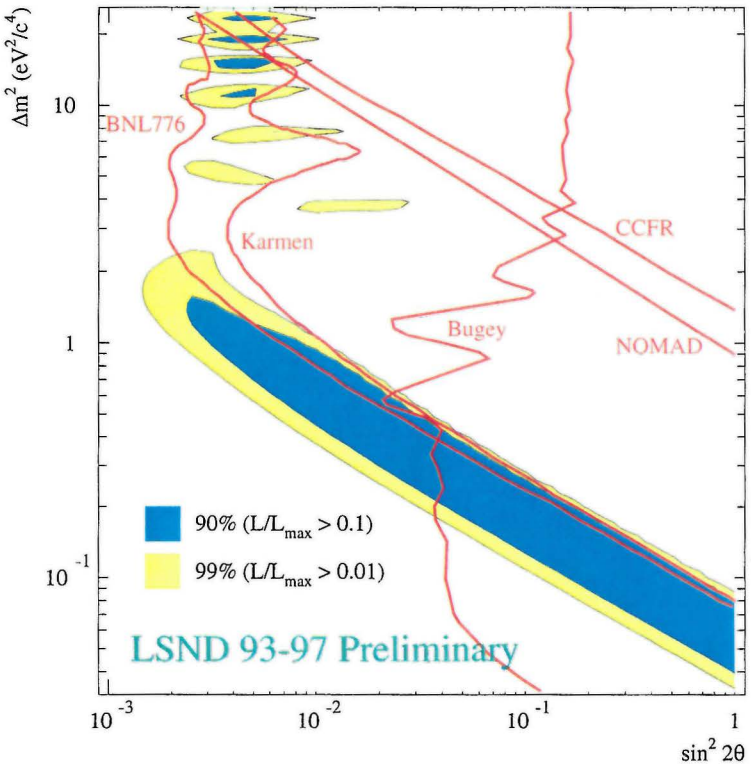

Figure 8: The preliminary LSND Δm^2 versus $\sin^2 2\theta$ favored regions from the full 1993-1997 data sample, together with limits from other experiments.

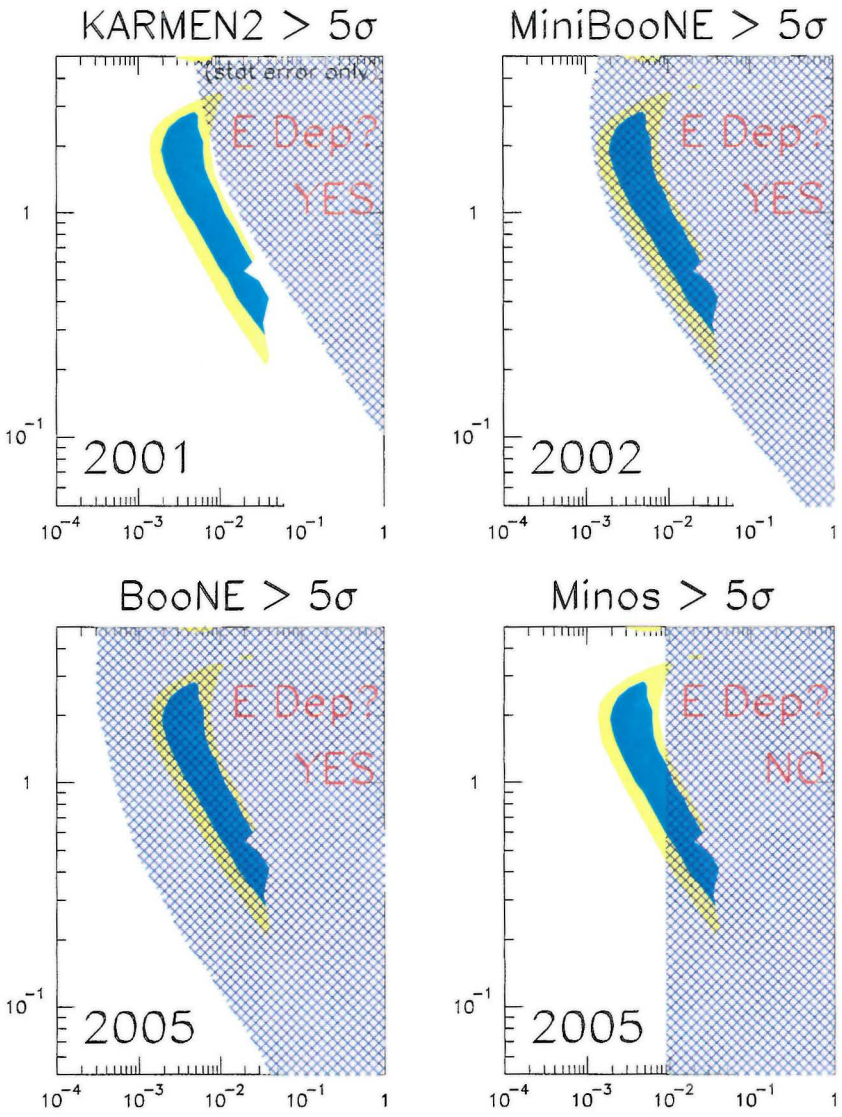

Figure 9: The discovery potential of MiniBooNE and BooNE compared to KARMEN2 and MINOS. The allowed LSND region is shaded. The cross-hatched region indicates where each experiment has sensitivity greater than 5 σ, where σ is calculated by summing over energy bins.

2.2 BooNE and other neutrino experiments

Evidence for neutrino oscillations comes from the solar and atmospheric neutrino problems in addition to the LSND signal. It is important to realize that there are at least three neutrinos, so that the solar, atmospheric, and LSND effects may all be different manifestations of three-generation mixing. For example, a recent paper by Teshima *et al.* (hep-ph/9801276) explains all of the data with three neutrinos and a small Δm^2 of $\sim 3 \times 10^{-5}$ eV^2 and a large Δm^2 of $\sim 2 \times 10^{-1}$ eV^2.

While there are multiple experiments addressing the solar and atmospheric neutrino questions, there is, as yet, no experiment which conclusively addresses the LSND signal. The BooNE proposal continues to be a unique and timely opportunity to address the entire LSND favored region at a modest cost. MiniBooNE has two important capabilities:

1. Coverage of the entire LSND range with a greater than 5σ signal expected, hence the experiment has "discovery potential." Fig. 9 indicates the regions in $sin^2 2\theta$ and Δm^2 where MiniBooNE and BooNE have greater than 5σ signals expected (cross-hatched).

2. Sensitivity to the characteristic energy dependence associated with oscillations.

No other proposed or approved experiment has these capabilities, although a Letter of Intent (LOI SPSC/I 216, see http://chorus01.cern.ch/~pzucchel/loi) has been submitted to CERN that proposes mounting an experiment in the old PS neutrino beam that would have sensitivity similar to BooNE.

We emphasize that BooNE is complementary to the MINOS experiment. The main goal of MINOS is the study of the atmospheric neutrino deficit, although this experiment does have $\nu_\mu \to \nu_e$ capability. MINOS, at a distance of 730 km, covers well the $10^{-3} < \Delta m^2 < 10^{-1}$ eV^2 range, while BooNE, at a distance of 0.5 km, is sensitive to $\Delta m^2 > 10^{-1}$ eV^2. MINOS only partially covers the LSND signal at the 5σ level (see Fig. 9). Because any ℓ/E sinusoidal variation will be averaged over at such a large distance for $\Delta m^2 > 10^{-1}$ eV^2, MINOS will be unable to observe the characteristic energy dependence associated with oscillations in the LSND region.

Fermilab will have a stronger neutrino program with both BooNE and MINOS than with just one of these experiments.

2.3 Progress on Technical Issues

BooNE has made exceptional progress over the last three months. We have discussed funding with both DOE and NSF; we have performed further anal-

ysis that fully exploits the shape of the energy distribution; we have helped considerably with the Booster radiation measurements and shielding issues; we have carefully examined the design of the Target Hall from the perspective of the maintenance and repair of very radioactive components; with the help of the Director we have selected new locations for the Target Hall and detectors that take into account the Margaret Pearson Prairie and the muon collider development work; we have studied the design of the underground oil tanks so that the requirements of the DOE and Illinois EPA are fully satisfied; and we have completed the EENP (environmental evaluation notification form) which is the first step to getting the environmental assessment.